# Alma Mater Studiorum – Università di Bologna

## DOTTORATO DI RICERCA IN

## ASTROFISICA

Ciclo XXX

**Settore Concorsuale:** 02/C1

**Settore Scientifico Disciplinare:** FIS/05

## "The Exotic Zoo of Millisecond Pulsars in Globular Clusters: a multi-wavelength study"

**Presentata da:** Mario Cadelano

| **Coordinatore Dottorato** | **Supervisore** |
|---|---|
| Chiar.mo Prof. F. R. Ferraro | Chiar.mo Prof. F. R. Ferraro |

**Co-Relatrici**

Chiar.ma Prof.ssa B. Lanzoni
Dr.ssa C. Pallanca

**Esame finale anno 2018**

# Abstract

This thesis work is focused on the study of millisecond pulsars in globular cluster by using multi-wavelength observations obtained with radio and optical telescopes. Radio observations have been used to search for and timing the pulsars. While classical search routines are based on the analysis of single and long time sequence of data, we present here an alternative method. This method exploits the large amount of available archival radio data to search for very faint pulsars by stacking all the daily power spectra. This method led to the discovery of three new pulsars in the stellar system Terzan 5.

The update of the timing solutions of 9 (out of 12) pulsars in the globular cluster M28 is then presented. The timing solutions now cover a data span of about 10 years and provide precise spin, astrometric and orbital properties for all the analyzed systems. For the case of the eccentric and relativistic binaries M28C and M28D, post-Keplerian corrections to the orbit have been measured in order to derive the masses of both the binary components. The measurement of the pulsar proper motions allowed to constrain the cluster motion as a whole, which has been used to infer its orbit in the Galaxy gravitational field. Finally, the pulsar spin and orbital period derivatives have been used to measure their accelerations induced by the cluster potential field. It turned out that a classical King model is able to reproduce all the measured accelerations. However, two systems show anomalous "jerk" values that suggest perturbations by nearby orbiting stars.

Optical observations have been exploited to search for millisecond pulsar optical counterparts, whose emission is totally dominated by the companion stars. Six new companion stars have been discovered, thus increasing by $\sim$40% the total number of companions identified in globular clusters. In particular, four companions turned out to be He white dwarfs, as expected from the canonical formation scenario. One companion turned out to be a very faint and non-degenerate object, showing a strong variability which is likely the result of a strong heating of the stellar side exposed to the pulsar injected flux. Its position in the color-magnitude diagram, not compatible with that of any evolutionary sequence of the cluster, also confirms that this system underwent a non-canonical evolution. Finally, one companion is a main-sequence star which shows a strong H$\alpha$ emission likely due to a low-level accretion probably from a residual disk. This system can be located in an early evolutive stage, immediately preceding the reactivation of an already re-accelerated pulsar. Furthermore, we identified the companion star to a transient low-mass X-ray binary. This companion turned out to be a sub-giant branch star and therefore this system is likely in a very early phase of the mass accretion stage, when an expanding secondary star is filling its Roche-Lobe and transferring material that eventually spins-up the NS.

Conclusion are drawn in the final chapter, where the evolution of millisecond pulsars is discussed and possible future developments are suggested.

*To my Walden...*

*When we become the enfolders of those orbs,*
*and the pleasure and knowledge of every thing in them,*
*shall we be fill'd and satisfied then?*

*No, we but level that lift to pass and continue beyond.*


- Walt Whitman, *Leaves of Grass* -

Pulsars (PSRs) are rapidly spinning and highly magnetized neutron stars (NSs), mostly known as emitters of pulsating radiation in the radio bands. Their characteristic pulsated emission is the result of a collimated beam of radiation located in correspondence of the magnetic poles, misaligned with respect to the spinning axis. Therefore, the observer receives a pulsed signal every time the emission beams sweep past the line of sight, once per rotation. This is the so-called "lighthouse effect".

The first PSR was discovered about 50 years ago by Jocelyn Bell Burnell, who observed an intense source of pulsation in the sky with a stable period of 1.33 s (Hewish et al., 1968), later confirmed to be a rapidly spinning NS by Franco Pacini and Thomas Gold (Gold, 1968). Both of them independently proposed that such a rotating and magnetized star, made mostly of neutrons and formed after the supernova explosion of a high-mass star, could emit a radiation similar to that observed by Jocelyn Bell Burnell.

To date, ∼ 2600 PSRs have been discovered throughout he Galaxy[1]. The vast majority of them are isolated systems spinning at periods of about 1 s. However, a second important class, populated by ∼ 400 objects, shows very short spin periods (around 5 ms) and are usually called "millisecond pulsars" (MSPs). They are old NSs, reaccelerated by mass and angular momentum accretion from an evolving companion star and therefore they are commonly observed in binary systems with an exhausted and deeply peeled secondary star, usually a white dwarf (WD) with a He core (e.g., Stairs, 2004).

Being highly collisional systems, globular clusters (GCs) are the ideal habitat for the formation of MSPs (Verbunt, Hut, 1987; Hut et al., 1991; Ransom et al., 2005; Hessels et al., 2007). Indeed, about 40% of MSPs are found in these systems, despite the Galaxy is ∼ $10^3$ times more massive than the entire GC system. This can be explained taking into account that MSPs in GCs are the outcome not only of the standard evolution of primordial binary systems, but also of non primordial binaries created through stellar dynamical encounters in the dense internal region of GCs. Before this thesis work, 146 MSPs were known in 28 GCs [2]. However, population synthesis models suggest that the next generation of radio telescopes will unveil few hundreds or even few thousands of new MSPs within the 150 Galactic GCs. Such a large population will

---

[1]http://www.atnf.csiro.au/people/pulsar/psrcat/
[2]http://www.naic.edu/~pfreire/GCpsr.html

hopefully include holy grails of PSR astronomy such as MSP-MSP binaries or even MSP-black hole binaries, expected to be formed exclusively in the extreme environments of GC cores through dynamical interactions (Freire et al., 2004; Verbunt, Freire, 2014).

MSPs in GCs can provide a wealth of science spacing in many different fields, from stellar evolution to accretion physics, from dynamics to general relativity tests. In the following we briefly introduce some of the science that can be performed by studying these objects. Some of this aspects will be discussed with more details throughout the thesis:

- Thanks to the stability of their signal over time, MSPs are extremely precise clocks. Deviations from their precision can be caused by their acceleration induced by the host GC potential field. Thus such deviations can be exploited to study the structure of the cluster itself, its physical characteristics, dynamical status, possibly probing or excluding the presence of an intermediate-mass black hole in the center (e.g., Prager et al., 2017). Moreover, the measurements of MSP proper motions allow to constrain the orbit of the host cluster within the Galaxy, shedding light on the formation and evolution of these stellar systems and the Milky Way itself across their $\sim 12$ Gyr lifetime.

- The study of MSPs in GCs can be used to improve out understanding of the dynamical evolution of these dense stellar systems. For instance, the identification of a large population of MSPs is crucial to constrain the rate of ejection and the NS retention fraction in the early stage of GC evolution. Furthermore, different GCs show differences in the properties of their MSP population. For example, the numerous population of MSPs in 47 Tucanae shows properties basically identical to those of the Galactic field population, while M15 shows a population composed exclusively of exotic systems, such as isolated MSPs and double NS systems. This is tightly related to the cluster dynamical status which can therefore be constrained identifying as many MSPs as possible in many different GCs (Verbunt, Freire, 2014).

- Since MSPs are mostly located in binary systems, their companion stars, identifiable through optical observations, provide a complementary view on the properties of these systems. Indeed, according to the canonical formation scenario, MSP companions are expected to be WDs with a He core. However, several deviations from this scenario can occur. These deviations are usually imprinted on the characteristics of the companion stars and thus the identification of the optical counterparts can help shedding light on the MSP evolutionary paths (Ferraro et al., 2001b, 2003a; Pallanca et al., 2010, 2014; Mucciarelli et al., 2013). The identification and characterization of MSP optical counterparts is also a powerful tool to study stellar evolution under extreme conditions (due to the MSP energetic emission), as well as the accretion mechanism and the physical processes occurring in the intra-binary space, where the interplay between the PSR wind of relativistic particles

and material lost from the outer envelope of the companion star becomes dominant (e.g., Bogdanov et al., 2005).

- MSPs can be used to test general relativity on small scales thanks to independent measurements (through PSR timing) of different relativistic orbital properties of the binaries, so-called "post-Keplerian parameters" (e.g., Burgay et al., 2003; Kramer et al., 2006; Breton et al., 2008). The number of systems clearly showing such effects is enhanced in GCs thanks to perturbations of the binaries due to close encounters with other stars. Binary MSPs also provided in the past the first indirect evidence of gravitational waves emission through the measurement of the orbital period decay of a double NS system (Hulse, Taylor, 1975). Finally, mass measurements through PSR timing and spectroscopy of the companion star could in principle be used to measure NS masses with high precision, thus possibly setting constraints on the equation of state of ultra-dense matter, which is a still open question in fundamental physics (Freire et al., 2008b; Demorest et al., 2010).

This thesis presents a multi-wavelength study of MSPs in GCs performed through radio and optical observations. These observations have been exploited through different approaches aimed to discovering new and extremely faint objects, obtain long-term highly precise timing solution and identify the optical counterparts to systems experiencing different evolutionary stages. The thesis is organized as follows:

- In Chapter 1 we provide a theoretical background on PSR properties, emission physics and evolution to the stage of MSPs. The properties of the different families of MSPs are then presented. Finally, we show why GCs are the ideal habitat for the formation of these systems and what kind of science has been (and can be) done by studying their population of MSPs.

- In Chapter 2 we present the main radio and optical methodologies used to study MSPs in GCs, from the techniques used to search for them and timing their signals in the radio bands, to the identification and characterization of their optical counterparts through optical observations.

- In Chapter 3 we report on the discovery of three new MSPs in the stellar system Terzan 5. These have been identified not though classical search routines, but using a different approach which exploits the large archival observations of this cluster, which has been routinely monitored in the past years.

- In Chapter 4 we analyze the long-term timing solutions of the MSPs in the GC M28. The timing solutions have been updated by using observations performed in the past 6 years and used to constrain the properties of each systems, evaluate the cluster proper motion and measure the acceleration induced by the GC potential field.

- In Chapter 5 we present the optical identification and characterization of the companion star to the black-widow system M71A. Black-widows are a sub-class of MSPs showing eclipses of the radio signal. They largely deviate from the canonical formation scenario and the companion star is expected to be very different from the "typical" He WD.

- In Chapter 6 we report on the identification and characterization of the optical counterparts to four MSPs in the GC 47 Tucanae. All the discovered companion stars are He WD, as expected from the standard formation scenario. Their properties are analyzed and discussed.

- In Chapter 7 we focus our attention on the optical counterpart to an accreting MSP system in the GC NGC 6440. Accreting MSPs are a sub-class of transient low-mass X-ray binaries showing pulsations from an already recycled NS, which is however still inactive as a radio MSP. The optical counterpart gives us the chance to probe the properties of the companion star in a system experiencing an evolutionary stage immediately preceding that of radio MSPs.

- In Chapter 8 we report on the identification of the optical counterpart to EXO 1745-248, a low-mass X-ray binary in the stellar system Terzan 5. This binary is characterized by recurrent outburst episodes triggered by active mass accretion from an evolving secondary star to the NS. The characterization of such a system allows to get insights on the very early stages of NS binary evolution, where the re-acceleration of a slow and inactive pulsar is still on-going.

- Finally, in the Conclusion chapter, we summarize the results obtained in this work, we draw our final conclusions and future prospects on the study of PSRs in GCs.

# FROM NEUTRON STARS TO MILLISECOND PULSARS

This chapter is aimed at providing a general theoretical background for a proper study of the population of millisecond pulsars in globular clusters. We will present a general view on the neutron star properties and on the pulsar phenomenology, focusing on the physical processes that characterize their peculiar signals. Then, we will show what is and how forms a millisecond pulsar, presenting the number of different evolutionary scenarios that create the exotic zoo of these objects. We will conclude showing why globular clusters are the ideal site for the formation of millisecond pulsars and what kind of science can be performed with a multi-wavelength approach.

## 1.1 Neutron Stars

Neutron stars (NSs) are rapidly spinning and magnetized compact stars composed mostly of neutrons. They are the core remnant of the gravitational collapse of massive stars ($M > 11 \, \mathrm{M_\odot}$) which eject their envelopes through supernova explosions.

The primary energy source of a star is given by thermonuclear fusion reactions, which can sustain the stellar structure until the exhaustion of the thermonuclear fuel (i.e. H, He and heavier elements till, at most, the iron group elements like Fe and Ni). Once this is exhausted, the only stellar energy source left is the gravitational one. This phenomenon has different outcomes depending on the original mass of the star:

- Stars with masses smaller than $\sim 11 \, \mathrm{M_\odot}$ end their life as white dwarfs (WDs): compact ($\sim \mathrm{R_\oplus}$) and hot ($\sim 10^{4-5} \, \mathrm{K}$) stars sustained by the pressure of degenerate electrons and mostly made of C and O or, possibly, of O, Ne and Mg.

- Stars with masses between $\sim 11 \, \mathrm{M_\odot}$ and $\sim 25 \, \mathrm{M_\odot}$ become NSs: extremely compact objects ($\sim 10 \, \mathrm{km}$), sustained by the pressure of degenerate neutrons.

- For stars with masses larger than $\sim 25 \, \mathrm{M_\odot}$, the gravitational collapse leads directly to the formation of a black hole.

While the processes leading to the formation of a WD are relatively steady and smooth events, the formation of a NS is preceded by the violent emission of most of the star gravitational energy through an explosion known as "core-collapse supernova". During this process, the outer envelopes of the star are blown away, while only a small inner core is left, formed from the collapse of the previous star nucleus, mostly composed of iron group elements and degenerate electrons (vaguely resembling a WD composed of Fe nuclei). This nucleus is subject to free fall collapse since its mass is expected to exceed the Chandrasekhar limit[1] of $\sim 1.4 \, \mathrm{M_\odot}$ and a remnant composed mostly of neutrons is formed. In fact, during this phase, the density in the stellar core is large enough that neutronization of matter is favored through $\beta-$decay reactions:

$$(1.1) \qquad\qquad p^+ + e^- \rightarrow n + \nu_e$$

This process results in the formation of a tremendous amount of neutrons. As a rough estimate, the ratio between the stellar nucleus mass (close to the Chandrasekhar limit of $\sim 1.4 \, \mathrm{M_\odot}$) and the neutron mass ($\sim 1.7 \times 10^{-24} \, \mathrm{g}$) is of the order of $10^{57}$, thus easily explaining why these remnants are called "neutron stars".

NSs are extremely compact stars. Assuming that in a NS the speed of sound is smaller than the speed of light, it has been demonstrated (Lattimer et al., 1990) that the minimum radius is

---

[1]It is the mass limit below which a system supported by the pressure of degenerate electrons (such as a WD) is stable. Above this value, the pressure can no longer sustain the gravitational collapse.

about 1.5 times its Schwarzschild radius ($R_S$):

$$(1.2) \qquad R_{min} \simeq 1.5\,R_S = \frac{3GM}{c^2} = 6.2\,\mathrm{km}\left(\frac{M}{1.4\,\mathrm{M_\odot}}\right)$$

where $G$ is the gravitational constant, $c$ the speed of light and $M$ the NS mass. On the other hand, a maximum radius can be obtained assuming that the rotating star is stable against centrifugal forces. For a NS with rotational period $P$, we find:

$$(1.3) \qquad R_{max} \simeq \left(\frac{GMP^2}{4\pi^2}\right)^{1/3} = 16.8\,\mathrm{km}\left(\frac{M}{1.4\,\mathrm{M_\odot}}\right)^{1/3}\left(\frac{P}{\mathrm{ms}}\right)^{2/3}$$

The fastest known rotating NS (PSR J1748−2446ad; Hessels et al., 2006) spins with a period of ∼ 1.39 ms, implying a maximum radius of ∼ 21 km for a typical mass of $1.4\,\mathrm{M_\odot}$. Assuming that the NS is born from the collapse of a WD-like structure with a radius ∼ $R_\oplus$, it follows that its final radius can be up to ∼ 500 times smaller than that of the progenitor one. Indeed, most models predict NSs to have a radius of $10\,\mathrm{km} - 20\,\mathrm{km}$ (Lattimer, Prakash, 2001). Although such measurements are observationally challenging, high-energy data are confirming this range of values (e.g., Guillot et al., 2013; Güver, Özel, 2013). This can also explain why NSs are observed as rapidly rotating stars: under the (weak) assumption that during the gravitational collapse there is no mass and/or angular momentum loss in the stellar core and that the NS is a sphere of uniform density, applying the conservation of angular momentum law before and after the collapse we find:

$$(1.4) \qquad I_i\Omega_i = I_f\Omega_f \implies \Omega_f = \Omega_i\frac{R_i^2}{R_f^2}$$

where $I = \frac{2}{5}MR^2$ and $\Omega = 2\pi/P$ are the moment of inertia and angular velocity of the NS (or of the stellar nucleus, before the collapse), respectively. Setting $R_i = 500\,R_f$, we find that $P_f = 10^{-6}P_i$. Considering a typical $P_i \approx 10^3$ s, it results that $P_f \approx 10^{-3}$ s.

Shortly after their formation, NSs are extremely hot objects with temperature as high as $10^{11}$ K. However, very efficient cooling mechanisms allow the star to reach, in a time-scale of $10^5$ years, a typical temperature of about $10^6$ K (see Potekhin et al., 2015, and reference therein). Therefore the black-body emission of these objects is peaked at soft X-ray wavelengths, even though, as explained in the following, most of the NS radiation is emitted through non-thermal mechanisms.

A possible alternative NS formation mechanism is the so-called "Accretion Induced Collapse": if a massive WD in a binary system is accreting material from a standard evolving star, its mass can eventually exceed the Chandrasekhar limit. It follows a gravitational collapse that likely creates a NS (e.g. Freire, Tauris, 2014).

### 1.1.1 The Internal Structure of a Neutron Star

The NS structure is able to contrast the gravitational collapse thanks to the pressure granted by degenerate neutrons. As for any degenerate system, the stellar structure can be described by an equation of state, that provides a link between the density and the pressure of the star at different stellar radii.

Given the extreme physical properties of NSs, testing the equation of state in Earth laboratories is prohibitive. Indeed, for a typical NS with a mass of $1.4\,M_\odot$ and a radius of about 10 km, the average density is $\sim 6.7 \times 10^{14}$ g cm$^{-3}$, about the same order of magnitude of the density of an atomic nucleus. While the equation state of matter with density large as the nuclear density is known, beyond this value relativistic field theories have not been able, so far, to constrain this equation, due to our lack of knowledge of the properties of the strong force in such an extreme regime. Observational constraints can be obtained through the simultaneous measurement of NS radii and masses, which is, however, quite challenging (see, e.g., Lattimer, Prakash, 2001; Guillot, Rutledge, 2014).

A description of the different kinds of equation of state proposed so far by theoretical physicists is beyond the goals of this thesis. Briefly, in most of them a NS with a very short interval of radii ($10.5$ km $-12$ km) is expected to be found in the mass range from $0.5\,M_\odot$ to $2.5\,M_\odot$ (Lyne, Graham-Smith, 2012). The bulk of the NS population is known to have a mass around $1.35\,M_\odot$ (Stairs, 2004), corresponding to radii in the interval of 10.5 km and 11.2 km.

The maximum mass allowed to a system supported by the pressure of degenerate electrons is well known as the Chandrasekhar limit. The same value for a system supported by the pressure of degenerate neutrons is however unknown, as a consequence of our ignorance about the equation of state. A possible value, the so-called "Tolman-Oppenheimer-Volkov" limit, is of about $2.5\,M_\odot$ (Lattimer, Prakash, 2001). However, none of the NSs with a precise mass measurement reach such a value, although few candidates are known (Freire et al., 2008b; Demorest et al., 2010), especially among the class of recycled NSs (see Section 1.5).

A schematic representation of the NS structure is reported in Figure 1.1, where it can be seen that the star density varies by about 9 orders of magnitude between the surface ($\rho \sim 10^9$ g cm$^{-3}$) and the central regions ($\rho \sim 10^{18}$ g cm$^{-3}$). The most external regions of the crust are composed of a thin atmosphere of atomic nuclei and free electrons, whose typical thickness is of few meters. Below that, the matter already reach the typical density of a WD and it is composed of a solid lattice, mostly of Fe nuclei. Descending into the star interiors, the energetic of the system favors the neutronization of matter: the production of isotopes with a large number of neutrons (e.g. Ni$^{62}$, Ni$^{64}$, Ni$^{66}$), through $\beta$-decay reactions like in 1.1. Although such isotopes would be unstable in normal condition and neutrons would decade into protons, this cannot happen in a complete degenerate structure. Below the crust, where densities are very close to the nuclear ones, the matter is expected to be in an superfluid state, where heavy atomic nuclei are embedded in a
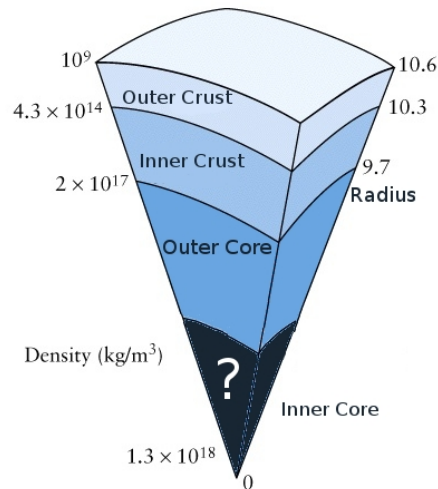
Figure 1.1: Schematic representation of the NS internal structure. Credits: A. Patruno.

sea of neutrons, with some protons and electrons. Finally, in the very central regions, where the composition of the matter is still extremely unclear, and the density overcomes the nuclear one, elementary particles can behave in unpredictable ways. Some models predict that the matter can be in exotic states, where the extreme densities force the disruption of neutrons into mesons and kaons, possibly also creating a solid inner core. Other models predict an interior composed of free quarks or a Bose-Einstein condensate. In any case, the real structure of NS interiors is still to be defined (see, e.g., Shapiro, Teukolsky, 1983).

## 1.2 Phenomenology of Pulsars

NSs are commonly observed as radio pulsars (PSRs), which are highly magnetized and rotating objects characterized by a peculiar emission of pulsated and stable radiation at radio wavelengths. As we will see, most of the PSR properties can be naturally explained in a scenario where charged particles, located in the NS surface, are accelerated in a highly magnetized and rotating structure.

### 1.2.1 Pulse Properties

The typical pulsed emission is the result of the so-called *lighthouse effect*, where an emission beam (or possibly two), located at the magnetic pole (or poles), sweep past our line of sight once per NS rotation. PSR spin periods cover a broad range of values: the slowest one is PSR J18414$-$0456 s with a spin period of 11.79 s (Dib, Kaspi, 2014), while the fastest one is PSR J1748$-$2446ad (Hessels et al., 2006), spinning at about 1.39 ms. Each PSR is characterized by a distinct pulse profile, which is usually very stable at the same observing frequency and therefore can be thought as a fingerprint of the PSR itself. Being very weak radio sources (typical flux densities are of the order of $10^{-5} - 1$ Jy), the pulse profile is obtained by summing together hundreds or thousands of

9
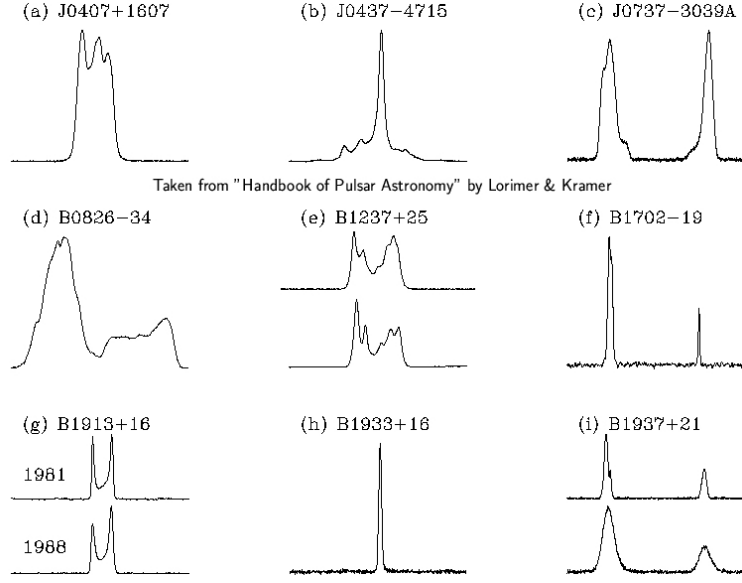
Figure 1.2: Integrated pulse profiles for a sample of PSRs.

pulses (this process is called "folding") creating an "integrated pulse profile" like those reported in Figure 1.2. The shape of each pulse profile is due to the size and geometry of the emission beam, as well as the angle between the line of sight and the beam. The main pulse profile is sometimes followed by a secondary pulse called "interpulse", separated by 180° from the main pulse and likely due to a secondary emission beam originate from the opposite magnetic pole.

The radio PSR emission is characterized by a strong dependence of the emitted flux density on the observing frequency. This dependence can be described by a simple power-law ($S_\nu \propto \nu^\alpha$) with a steep spectral index $0 \gtrsim \alpha \gtrsim -4$ (Maron et al., 2000).

## 1.2.2 Derivation of the Pulsar Physical Parameters

The emission of a PSR does not come for free, but at the expenses of a large reservoir of kinetic rotational energy. This is the reason why PSR periods are observed to increase with time. The spin-down rate ($\dot{P} = dP/dt$) is related to the rotational kinetic energy as follows (see Lorimer, Kramer, 2004, for more details):

$$\dot{E} \equiv -\frac{dE_{rot}}{dt} = -\frac{d(I\Omega^2/2)}{dt} = -I\Omega\dot{\Omega} = 4\pi^2 I \dot{P} P^{-3} \tag{1.5}$$

where $\dot{E}$ is the "spin-down luminosity" and represents the kinetic energy output emitted by the NS. Assuming a typical moment of inertia $I = 10^{45}$ g cm$^2$, we find:

$$\dot{E} \simeq 3.95 \times 10^{31} \text{ erg s}^{-1} \left(\frac{\dot{P}}{10^{-15}}\right)\left(\frac{P}{\text{s}}\right)^{-3} \tag{1.6}$$

Only a very small fraction of this spin-down luminosity is actually converted into radio emission. Most of it is converted into high energy radiation and relativistic wind of particles that heavily

interact with the interstellar medium (the so-called "PSR wind nebulae") or, if present, with a companion star (Kirk et al., 2009).

As we will see in the following, PSRs have strong dipole magnetic fields. A rotating magnetic dipole with a moment $|\mathbf{m}|$ emits electromagnetic waves at its rotation frequency. The radiation power is:

$$(1.7) \qquad \dot{E}_{dipole} = \frac{2}{3c^3} |\mathbf{m}|^2 \Omega^4 \sin^2 \alpha$$

where $\alpha$ is the angle between the magnetic and the spin axis. Equating equation (1.5) to equation (1.7), we find:

$$(1.8) \qquad \dot{\Omega} = -\left( \frac{2|\mathbf{m}|^2 \sin^2 \alpha}{3Ic^3} \right) \Omega^3$$

which shows the expected spin period evolution. By expressing this equation using a simple power-law and in terms of the rotational frequency $\nu$, this relation becomes:

$$(1.9) \qquad \dot{\nu} = -K\nu^n$$

where $n$ is called "breaking index" and $K$ is assumed to be a constant. For a pure magnetic dipole breaking, the index is $n = 3$. However, other dissipation mechanisms, such as the PSR wind, may carry away part of the rotational kinetic energy. The measured values of $n$ varies from 1.4 to 2.9 (Kaspi, Helfand, 2002), confirming that the pure magnetic dipole breaking is just a poor assumption.

Rearranging equation (1.9) in terms of the spin period derivative, a first order differential equation is obtained. Integrating this equation, assuming a constant $K$ and $n \neq 1$, a simple relation for the PSR age can be obtained:

$$(1.10) \qquad T = \frac{P}{(n-1)\dot{P}} \left[ 1 - \left( \frac{P_0}{P} \right)^{n-1} \right]$$

where $P_0$ is the PSR birth spin period. Assuming $P_0 << P$ and $n = 3$, this equation simplifies in the so-called "characteristic age":

$$(1.11) \qquad \tau_c \equiv \frac{P}{2\dot{P}} \simeq 15.8 \, \text{Myr} \left( \frac{P}{\text{s}} \right) \left( \frac{\dot{P}}{10^{-15}} \right)^{-1}$$

Such an age is easily measurable through observations. However, given the assumptions, its value is not a very reliable measurement of the true PSR age. Thus it should be treated carefully and only as a rough estimate. Rearranging the two latter equations, we find an equation for the spin period at birth:

$$(1.12) \qquad P_0 = P \left[ 1 - \left( \frac{n-1}{2} \right) \frac{T}{\tau_c} \right]^{\left( \frac{1}{n-1} \right)}$$

Therefore, if the breaking index is measured and the true age of the PSR is independently determined (e.g. by measuring the age of an associated supernova remnant), the PSR spin period at birth can be inferred. The range of possible PSR birth periods is still unclear. Some estimates suggest a broad range of values from tens to hundreds of milliseconds (e.g. Migliazzo et al., 2002; Kramer et al., 2003).

PSRs are highly magnetized systems. Although direct measurements of the magnetic field strength are not possible, an estimate of its intensity can be obtained from equation (1.8), since the magnetic field strength is related to the magnetic moment by the relation $B \approx |\mathbf{m}|/r^3$. It follows that the magnetic field strength at the NS surface ($B_S$) is:

$$(1.13) \qquad B_S = \sqrt{\frac{3Ic^3}{8\pi^2 R^6 \sin^2 \alpha} P\dot{P}}$$

Using the same typical $I$ as before, a typical radius $R = 10$ km and assuming $\alpha = 90°$, we find:

$$(1.14) \qquad B_S = 3.2 \times 10^{19}\, G\, \sqrt{P\dot{P}} \simeq 10^{12}\, G \left(\frac{\dot{P}}{10^{-15}}\right)^{1/2} \left(\frac{P}{s}\right)^{1/2}$$

As in the case of the characteristic age, given all the assumptions, this equation does not provide a precise measure of the true surface magnetic field, but only a rough estimate. As we shall see in Section 1.4, this characteristic surface magnetic field can cover a broad range of values from $\sim 10^8$ G to $\sim 10^{15}$ G.

## 1.3   Pulsar Magnetosphere and Emission Mechanism

In Section 1.1.1 we saw that the NS surface and atmosphere are composed of charged particles. These are subject to Lorentz forces much stronger than the gravitational ones. In a rotating and magnetized system such as a NS, this leads to the formation of a strong electric field able to extract plasma from the surface, which surrounds the NS following the magnetic field lines and creating the "PSR magnetosphere". A simple, yet very educative model of this phenomenon has been presented by Goldreich, Julian (1969) shortly after the discovery of the first PSR. This model assumes that the spin and magnetic axes of the PSR are aligned and shows that in any point of the sphere, the magnetic field $\mathbf{B}$ induces an electric field $\mathbf{E} = (\mathbf{\Omega} \times \mathbf{r}) \times \mathbf{B}$. In a perfectly conductive sphere this will be balanced by a distribution of charges that create an electric field able to grant, at any point $\mathbf{r}$, a force-free state. This can be mathematically expressed as follows:

$$(1.15) \qquad \mathbf{E} + \frac{1}{c}(\mathbf{\Omega} \times \mathbf{r}) \times \mathbf{B} = 0$$

Under the assumption that there is vacuum outside the sphere, the surface charges induce a quadrupole moment that corresponds to a surface electric field:

$$(1.16) \qquad E_{||} = \left.\frac{\mathbf{E} \cdot \mathbf{B}}{B}\right|_{r=R} = -\frac{\Omega B_S R}{c} \cos^3 \theta$$

Figure 1.3: Schematic representation of a rotating NS and its surrounding magnetosphere
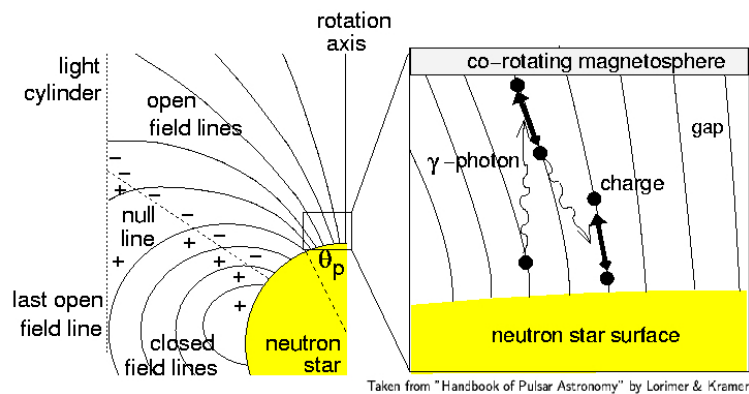


Figure 1.4: PSR magnetosphere according to the Goldreich-Julian model.

This field induces an electric force on charged particles that is stronger than the gravitational pull. As a consequence, charges are easily extracted from the surface to create a surrounding dense plasma. The charge distribution around the NS is arranged in such a way that the electric field $E_{||}$ is shielded and thus the force-free state (see equation 1.15) is maintained also outside the star. This plasma outside the NS is subjected to the same electromagnetic field as the NS interior and thus the charged particles are forced to rigidly co-rotate with the star. Co-rotation can however occur up to a distance where the plasma is rotating at a speed equal to the speed of light. This co-rotation limit defines a radius known as "light cylinder radius" and is given by:

$$(1.17) \qquad R_{LC} = \frac{c}{\Omega} = \frac{cP}{2\pi} \simeq 4.77 \times 10^4 \, \text{km} \left( \frac{P}{\text{s}} \right)$$

The existence of such a limiting radius divides the magnetosphere into two distinct regions as shown in Figures 1.3 and 1.4: the "closed field lines region" where the magnetic field lines close within the light cylinder and the "open field lines region" where the magnetic field lines cannot close.

The presence of the open field line region provides the physical ground for the NS to emit the pulsated radiation. Indeed, the radio beam, responsible of the pulsed signal, is confined within this region. The exact physical mechanism that produce the PSR emission is still poorly understood. However, the generally accepted model identifies the emitting region as a cone-shaped beam centered on the magnetic poles, within a so-called "inner acceleration gap" (see Figures 1.3 and 1.4). Here, the plasma extracted from the surface by a residual electric field, is accelerated along the open field lines, thus emitting photons in a direction tangential to that of the open field line at the point of emission. This mechanism is usually called "curvature emission" (Komesaroff, 1970) and the very high brightness temperatures measured imply that this mechanism is a coherent process, at least at radio wavelengths. Briefly, the charges extracted from the NS surface are accelerated, reaching relativistic energies ($\gamma \lesssim 10^7$), along the magnetic field lines where they emit $\gamma$-ray photons by curvature emission or inverse Compton scattering with lower-energy photons. These photons, due to the presence of the strong magnetic field, can split into an electron-positron pair if the initial energy is larger than twice the electron rest mass. In such a way, a new generation of particle is created and it will emit high energy photons and create pairs again. The net result is the creation of an avalanche of secondary pair plasma. This phenomenon results in the multiplication by a factor up to $10^4$ of the initial plasma density and it is believed that the acceleration of this secondary plasma produces the commonly observed radio emission (see Lorimer, Kramer, 2004, and reference therein, for more details). As a consequence, the opening angle of the radio beam is a function of both the width of the open field line region and the height where the emission occurs. However, it is worth reminding that the observed pulse shape is also a function of the structure of the emitting regions within the cone and of the portion of the emission cone crossed by the observer line of sight.

For the sake of completeness, we specify that the PSR pulsated emission has been observed also at higher energies, such as optical, X-ray and $\gamma$-ray wavelengths. The emission mechanism

in these bands is quite different from the radio one and likely located, as well as in the inner acceleration gap, also in an outer acceleration gap: a region in the outer magnetosphere close to the light cylinder (see Figure 1.3). High energy photons from these outer gaps are probably created through synchrotron and curvature emission (in a lower $B$ regime, with respect to the radio emission case), while high energy photons from the inner gap are likely due to inverse Compton scattering.

## 1.4 Pulsar Evolution

The evolution of a PSR can be described through a spin period vs spin period derivative ($P - \dot{P}$) diagram, reported in Figure 1.5 (Lorimer, Kramer, 2004). From the analysis of the plot, at least two distinct families of PSRs can be distinguished. The bulk of the PSR population is located at "long" spin periods, centered around 0.5 s, and spin-down rates of about $10^{-15}$: these are classical isolated NSs, spinning down after being formed in a supernova event. They are characterized by typical magnetic field of $10^{11-13}$ G and ages of about $10^{6-7}$ yr. A second family can be identified in those objects with extremely short spin periods, around 5 ms, and low spin-down rates around $10^{-20}$. Given their typical spin periods, these objects are called "millisecond pulsars" (MSPs). From equation (1.11) is it clear that this population is composed of PSR older than the bulk of the population, being older than $10^8$ yr and, on the basis of equation (1.14), having low magnetic field strength of about $10^{8-9}$ G. Furthermore, the vast majority of them is located in binary systems. Indeed, as we will see in the following, their formation requires the presence of a companion star.

According to the most plausible evolutionary scenarios (Lorimer, Kramer, 2004), PSRs are born with small spin periods around tens of milliseconds and large spin-down rates ($\lesssim 10^{-15}$), thus located in the upper left section of the $P - \dot{P}$ diagram. While they slow down, losing rotational kinetic energy, they move toward the bulk population with period around 0.5 s. This evolution is likely accompanied by a decay of the magnetic field strength and thus a decrease of the spin-down rate. The slow down process keeps moving the PSR toward the rightest regions of the diagram where they eventually cross the so-called "death line" and enter the "PSR graveyard". This is a region where the combination of spin periods and spin-down rates is not suitable to provide an efficient emission mechanism and therefore the NS is no more able to emit as a PSR.

The bulk of the PSR population is located close to the death line. This is because the evolutionary time scales from the birth region to this region of the diagram is quite fast, the typical timescale being of about $10^{5-6}$ yr. Indeed, young PSRs have short spin periods and strong magnetic fields that allow an efficient energy emission, and thus a rapid slow down. When they reach spin periods larger than $\sim 0.5$ s, this is not true anymore and the evolution in the $P - \dot{P}$ diagram is slowed down. After $10^7$ yr the emission eventually becomes too weak to be detectable and the PSR moves toward and beyond the death line.
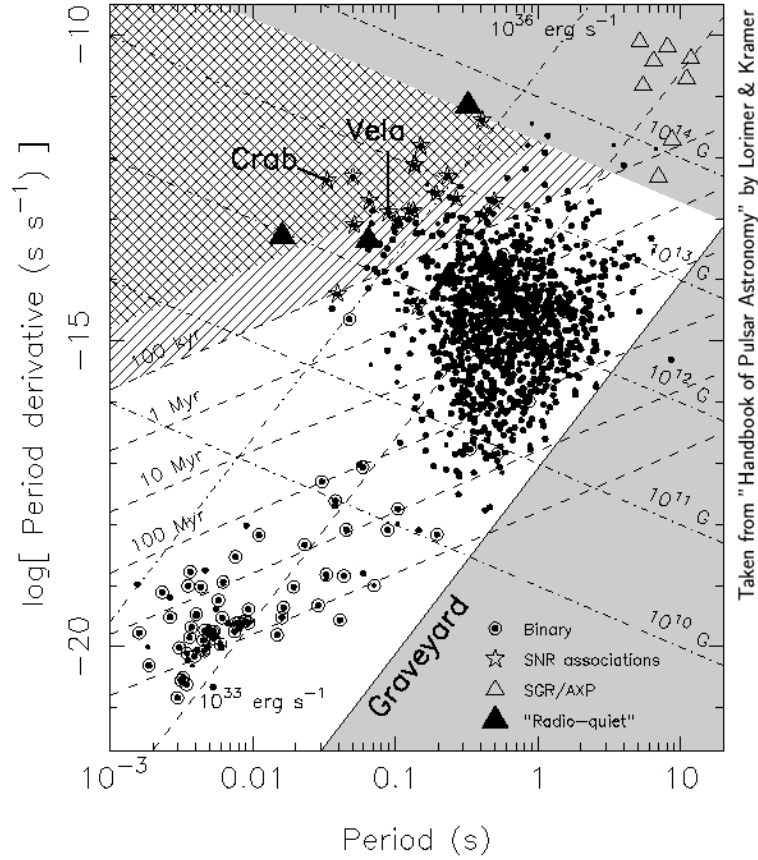
Figure 1.5: The $P - \dot{P}$ for a large sample of radio PSRs. Binary systems are highlighted with circles. PSRs associated to supernova remnants are plotted as empty stars, magnetars as empty triangles and radio quiet PSRs as filled triangles. Lines at constant magnetic field, characteristic age and spin-down luminosity are also plotted. The gray shaded area is the region called "graveyard" where the PSR is expected to be no more observable.

Across the death line, we should be no more able to see the PSR emission. However, if the dead NS is located in a binary system, accretion phenomena can transfer mass and angular momentum from the companion to the NS. This can spin-up the NS till periods of the order of milliseconds, where the emission mechanism can be reactivated and the NS can be visible again in the radio band as a MSP. The same mechanisms are also thought to be responsible of the burying of the magnetic field (Bisnovatyi-Kogan, Komberg, 1974): this is why MSPs are observed in the lower left region of the diagram, where objects with very low spin-down rates (and thus weak magnetic field) are located.

In the $P - \dot{P}$ diagram it can be also distinguised a third family of objects, composed by PSRs with long spin periods but very high spin-down rates (of $\sim 10^{-11}$) corresponding to strong

magnetic field strengths (around $10^{14-15}$ G). These objects are called "magnetars" or in some cases "Anomalous X-ray Pulsars" or "Soft Gamma-ray Repeaters" and they are characterized by high energy emission (Kaspi, Beloborodov, 2017). A description of this family of PSRs is beyond the goals of this thesis.

## 1.5 Millisecond Pulsars

As we saw in the previous section, MSPs represent an old and evolved population of NSs, resulting from mass accretion from a companion star onto a dead NS.

The first MSP, 4C21.53, was discovered in 1982 by Backer et al. (1982) and Alpar et al. (1982). It was long thought that this source could host a NS as primary star. However, no pulsations were discovered till the search was moved to very short spin periods, in a region where no PSR was known. In this way, it was discovered a 1.6 ms pulsation from this source, confirming its PSR nature, but with an unprecedented short spin period. To date, $\sim 400$ MSPs are known[2].

The formation of a MSP begins in a binary system where the massive star explodes as a supernova, creating a NS. This phenomenon can release an amount of energy large enough to unbound the binary. However, it can be shown, starting from the virial theorem and assuming spherical symmetry, that the binary system survives the explosion if the total amount of mass ejected during the supernova event is less than half the total mass of the binary system. After the explosion, if the binary system survives, it likely is on an eccentric orbit and the NS is visible as a classical PSR for about $10^{6-7}$ yr. The accretion phenomenon usually starts when the companion star evolves from the main sequence stage and becomes a red giant star. If in this stage the companion fills its Roche Lobe[3] (Figure 1.6), transfer of material from the surface of the companion toward the NS can occur through the stellar wind or, more commonly, through the Lagrange point $L1$ (see Figure 1.6). The mass transfer onto the NS implies also the transfer of angular momentum, thus resulting in the acceleration of the compact object. A limiting spin period is reached thanks to the equilibrium between the magnetic pressure of the accreting NS and the ram pressure of the in-falling matter (Bhattacharya, van den Heuvel, 1991). Its value is usually of few milliseconds and hence a MSP is formed. This phenomenon allows us to observe old NSs, whose emission should not be observable, having passed the death line. This is why MSPs are also known as "recycled PSRs" and the accretion/reacceleration stages as "recycling scenario".

Aside from the dominant radio pulsed emission, MSPs are also strong high energy emitters, both in the X-ray and in the $\gamma$-ray regimes (Rutledge et al., 2004; Bogdanov et al., 2011; Xing,

---

[2]See `https://apatruno.wordpress.com/about/millisecond-pulsar-catalogue/`

[3]The Roche Lobe is defined as the region, around a star in a binary system, within which orbiting material is gravitationally bound to that star.
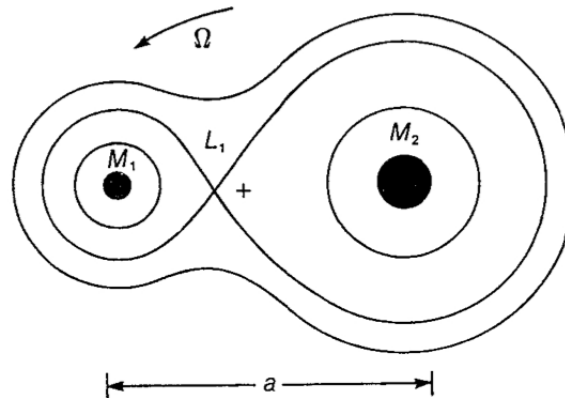
Figure 1.6: Surfaces of equal gravitational potential in a binary system, as seen from the equatorial plane. The two drop-like structures intersecting at the Lagrange point $L1$ are called Roche Lobes of the stars with masses $M_1$ and $M_2$, rotating around the center of gravity with angular velocity $\Omega$.

Wang, 2016). The high energy emission can be due both to thermal and non thermal processes, like the emission of photons in the surroundings of the MSP magnetosphere or to intra-binary shocks between the relativistic wind of particles emitted by the MSP and the material lost by the companion star. On the other hand, the optical emission of MSPs is dominated by the companion stars (e.g. Ferraro et al., 2001b, 2003a; Stappers et al., 2001; Breton et al., 2013) and thus optical observations are the only window to characterize the binary system properties from the secondary star point of view and to study the physics and the evolution of stars under the extreme conditions due to the presence of a NS.

### 1.5.1 Canonical Formation Scenarios

Canonical formation scenarios are quite branched and include many kind of MSPs. A simple but illustrative classification can be done on the basis of the companion mass. This quantity is not always easily measurable. In some cases its value can be constrained by the identification of the companion star in the optical bands while in the case of relativistic binary systems, PSR timing can provide precise mass measurements of both the primary and the secondary stars.

A schematic representation of the different possible evolutionary scenarios is presented in Figure 1.7 (see Stairs 2004). As can be seen, following the formation of the primary PSR and the subsequent accretion stages, the secondary object becomes an inactive system from the thermonuclear reactions point of view, usually a WD. We can distinguish three main MSP families on the basis of the companion mass:

- MSPs with low-mass companion stars: it is the most common class and the companion

**A**

Main–sequence stars, one > 8 M$_\odot$, one low–mass (~1M$_\odot$)

Primary explodes as supernova

Roche–Lobe overflow and accretion disk

Result: long–period binary system with a millisecond pulsar and a low–mass white dwarf companion
Example: PSR J1713+0747

**B**

Main–sequence stars, one > 8 M$_\odot$, one intermediate–mass (~5 M$_\odot$)

Primary explodes as supernova

Common–envelope evolution: the NS spirals into and expels the envelope of the companion

Result: mildly recycled pulsar (spin period tens of milliseconds) in a close orbit with a massive white dwarf (~1 M$_\odot$)
Example: PSR J1157–5112

**C**

Main–sequence stars, one ~7 M$_\odot$, one ~5 M$_\odot$

Mass transfer from the primary to the secondary

The primary has lost mass and shrinks to form a WD

Common envelope: the WD spirals into and expels the envelope of the secondary

WD—He–star binary

Secondary explodes as supernova

Result: young pulsar in orbit around a massive WD companion.
Example: PSR J1141–6545

**D**

Main–sequence stars, both >8 M$_\odot$

Primary explodes as supernova

Mass transfer to neutron star from companion wind

Common envelope: the NS spirals into and expels the envelope of the secondary

NS—He–star binary
Roche–Lobe overflow possible

Secondary explodes as supernova

Result: double–neutron–star system
Example: PSR B1913+16

Figure 1.7: Schematic representation of MSP canonical formation scenarios, taken from Stairs (2004). Panel A shows the evolutions of MSPs with low-mass companion stars, panel B and C the evolution of MSPs with intermediate-mass companions and finally panel D the evolution of MSPs with high-mass companion stars.

    stars are usually WD with a He core and mass $< 0.5\,\mathrm{M_\odot}$.

- MSPs with intermediate-mass companion stars. They usually have massive C-O WD companions with masses $\sim 1\,\mathrm{M_\odot}$.

- MSPs with high-mass companion stars, where the latter has a mass larger than $1\,\mathrm{M_\odot}$, typically another NS.

**MSPs with low-mass companion stars**

The vast majority of binary MSPs belongs to this class. They are formed from binary systems with a low-mass ($\sim 1\,\mathrm{M_\odot}$) secondary star. This scenario is depicted in section A of Figure 1.7.

Once the NS is formed and the secondary is evolved to the red giant phase, mass accretion can occur via Roche-Lobe overflow, through the formation of an accretion disk.

The accretion stages are commonly observed in systems called "Low-Mass X-ray Binaries" (LMXBs)[4], whose intense X-ray radiation is due to the accretion disk (Tauris, van den Heuvel, 2006). These systems have been long thought to be the progenitor of MSPs and this connection has been recently confirmed by the discovery of a new class of binary systems, the so-called "transitional MSP" (tMSPs), which we will describe in Section 1.5.3. The "low-mass" prefix is used to distinguish them from the class of "High-Mass X-ray Binaries", with more massive companion stars, that are thought to be the progenitors of double PSR systems (Stairs 2004, scenario D of Figure 1.7).

This phase can last as long as $\sim 1$ Gyr and thus the final result is a rapidly spinning MSP with spin periods usually shorter than 10 ms, and a companion star whose envelope has been completely stripped out, thus a low-mass WD ($\sim 0.1\,M_\odot - 0.2\,M_\odot$) with a He core or, more rarely, with a C-O core and an outer envelope of H and He.

**MSPs with intermediate-mass companion stars**

They are the outcome of the evolution of binary systems where the secondary star has a mass in the range $3\,M_\odot - 6\,M_\odot$. The evolutionary scheme is reported in sections B and C of Figure 1.7. In the former case, the primary star creates a NS and when the secondary evolves to be a red giant, a common envelope phase allows the NS to accrete material from the secondary and thus to spin the NS up. At the end, we find a mildly recycled MSP (spin periods of tens of ms) with a massive WD with a C-O core (see, e.g., Lorimer et al., 2006; Pallanca et al., 2013b). In the latter scenario, both the stars have masses lower than $\sim 8\,M_\odot$. The more massive one firstly becomes a red giant and starts to transfer mass to the secondary star via Roche-Lobe overflow. The primary becomes a massive WD with a C-O or O-Mg core. When the secondary evolves, a common envelope phase allows mass transfer from the secondary to the primary. Finally the secondary star, which has accreted matter in the early stages and lost its envelope in the later ones, explodes as a supernova and a young PSR is formed (see, e.g., Kaspi et al., 2000).

**MSPs with high-mass companion stars**

It is the scenario depicted in section D of Figure 1.7. Briefly, two main sequence stars, both with masses larger than $8\,M_\odot$, evolve. When the first NS is formed and the second one reaches the red giant phase, mass transfer onto the NS can occur via the stellar wind lost by the secondary star. After a common envelope phase, where the accretion can still occur, the secondary star explodes as a supernova and a second NS is formed. These systems are usually characterized by large spin periods ($\geq 20$ ms) and eccentric orbits ($0.1 \lesssim e \lesssim 0.9$). Double NS systems are known, like PSR

---

[4]For the sake of completeness, it is worth mentioning that it also exist a sub-class of LMXB with a stellar mass black hole as primary star with different properties with respect to those with a NS primary.

B1913+16 or B2127+11C (Jacoby et al., 2006; Weisberg et al., 2010), but only in one case the pulsations have been detected from both the NSs (Burgay et al., 2003). All of them are highly relativistic systems and thus suitable to be used as probes of general relativity (e.g. Hulse, Taylor, 1975).

### 1.5.2 The Spiders: Black-Widows and Redbacks

There is another class of MSPs with low-mass companion star, whose properties are not predicted by the canonical evolutionary scenario described before. These systems are named "spiders" and classified in two species: Black-Widows (BW) and Redbacks (RB, see, e.g., Fruchter et al., 1988; Ruderman et al., 1989; Ray et al., 2012; Roberts, 2013). They are also called "eclipsing MSPs" since they are characterized by periodical eclipses of the radio signal lasting for a significant fraction of the orbit, usually during the PSR superior conjunction. This phenomenon cannot be due to the occultation of the MSP by the companion star, but to absorption or scattering between the radio photons and ionized material located between the emitter and the observer. This material is likely produced from the ablation of the companion star surface by the relativistic wind of particles and high energy radiation emitted by the re-activated PSR (and so the name of the two murderous spiders). An artistic representation is reported in Figure 1.8.

Among a population of 402 MSPs, 22 RBs and 40 BWs are known so far[5]. The distinction between the BW and the RB classes is made on the basis of the companion star mass: while

[5]see https://apatruno.wordpress.com/about/millisecond-pulsar-catalogue/



Figure 1.8: An artistic representation of a spider MSP system. Credits: Ferraro F. R., ESO.

RB companions can have masses in the range $0.1\,\mathrm{M}_\odot - 0.5\,\mathrm{M}_\odot$, BWs have extremely low-mass companion stars, of the order of $\leq 0.05\,\mathrm{M}_\odot$ (see Figure 1.9). Both the kinds of companions are expected to be non-degenerate or, at least, semi-degenerate stars, as observationally confirmed by their optical identification (e.g. Stappers et al., 2001; Pallanca et al., 2010; Breton et al., 2013). Indeed, in the case of a WD companion, the surface gravity would be too strong and the projected radius too small to produce such a mass loss from its atmosphere. The typical orbital periods of spider MSPs can cover a range from few hours to a day (Figure 1.9) and so they always present very compact orbits with no measurable eccentricities, as a result of the strong tidal interaction between the two components of binary system. A strong tidal locking also forces the companion star to rotate around his rotational axis with the same period of the orbit and thus, as in the Earth-Moon case, the same region of the star is constantly exposed to the MSP. Interestingly, spider MSPs are X-ray and $\gamma$-ray emitters (e.g. Bogdanov et al., 2005; Ray et al., 2012). The bulk of the high energy radiation is due to non thermal emission from an intra-binary shock formed between the PSR wind and the material outflowing from the companion star (Roberts et al., 2014).

There are few cases of MSPs with an expected extremely low-mass companion that show no radio eclipses. The typical mass function of their companion star is around $10^{-5}\,\mathrm{M}_\odot$, while that of BW is usually $\geq 3 \cdot 10^{-4}\,\mathrm{M}_\odot$. Since the mass function depends on the orbital inclination angle as $\sin^3(i)$, it is reasonable that these systems are BWs seen at low inclination angle (Freire, 2005). Indeed, the eclipsing material is expected to be able to intercept the radio beam and our line of sight only at high inclination angles.

The physical mechanisms leading to the formation of these systems are still debated. Simulations by Chen et al. (2013) show that RBs and BWs are the outcome of different evolutionary paths, where the PSR irradiation efficiency is the discriminant factor. At odds with these results, the simulations by Benvenuto et al. (2014) show that the evolution of RBs is bifurcated, with some of them evolving into BWs and the others producing canonical MSPs with a He WD companion. Possibly, the progressive evaporation of BW companions could lead to their total disruption and thus to the formation of isolated MSPs.

### 1.5.3 Accreting and Transitional Millisecond Pulsars

The bridge between LMXBs and MSPs is found in a class of peculiar binaries called "Accreting Millisecond X-ray Pulsars" (AMXPs). These are a subgroup of transient LMXBs that show, during outbursts, X-ray pulsations from a rapidly rotating NS. During these outbursts, the matter lost from the non-degenerate companion star via Roche-Lobe overflow is channeled down from a truncated accretion disk onto the NS magnetic poles, producing X-ray pulsations at the rotational frequencies ($\nu \geq 100$ Hz) of a weakly magnetized ($B \sim 10^{8-9}$ G) NS (see Patruno, Watts, 2012, and references therein).
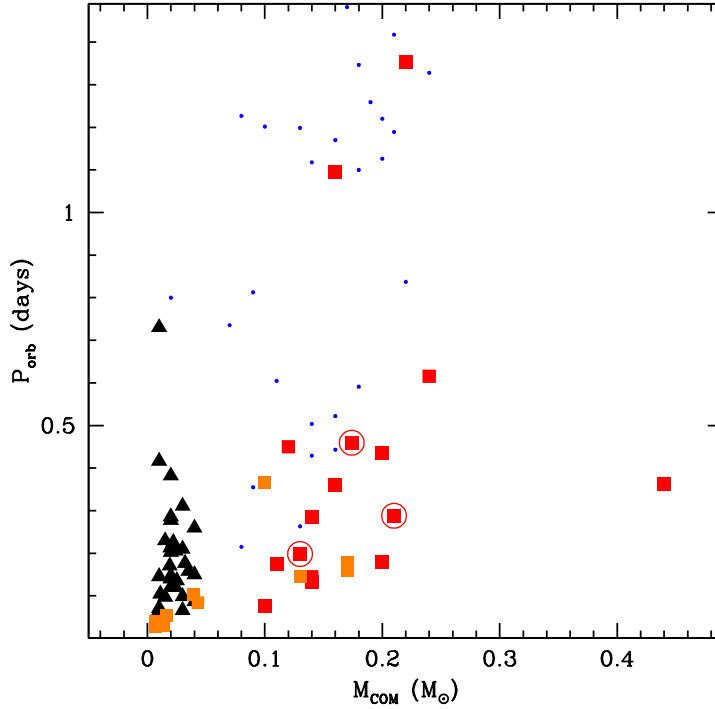
Figure 1.9: Orbital period as a function of the companion mass for a sample of MSPs. Blue points mark the position of a small sample of canonical MSPs with He WD companion stars. Black triangles, red and orange squares mark the positions of BWs, RBs and AMXPs, respectively. Finally, the three open circles around the red squares identify the three tMSPs.

AMXPs emission is powered by the accretion itself, at odds with that of classical MSPs, powered by the NS rotation. Indeed, the presence of active accretion halts the radio emission mechanism (and indeed pulsations have never been detected in these systems, despite deep radio searches; Patruno et al. 2009) and the pulsations are visible thanks to the heating of the inner acceleration gap due to the presence of accretion flow. Such a flow is however a non steady phenomenon and indeed, during quiescence, X-ray pulsations have never been observed. All AMXPs are transient systems, running through cycles of outburst and quiescence with recurrence times different among systems and with durations from few days to several years. The spin frequencies of these systems confirm that the re-acceleration of the dead NS already took place during previous stages.

The total number of AMXPs systems currently known is 20 (Patruno, Watts, 2012; Sanna et al., 2017b,a; Strohmayer, Keek, 2017). All of them are compact or even ultracompact binaries with orbital periods usually much shorter than 1 day and companion stars with masses usually smaller than $1\,M_\odot$, in a similar fashion to that of spider MSPs (see Figure 1.9). Given the range covered by the orbital periods, these systems are unlikely to be the progenitors of canonical MSPs,

while a tight connection with the spiders is obvious given their orbits and the properties of their companion stars.

The discovery of AMXPs has been an important validation for the MSP recycling scenario, probing that accretion of matter during the LMXB phase can indeed spin-up a slowly rotating NS. The final confirmation of this scenario arrived in 2013, almost 50 years after the discovery of the first binary PSR. Papitto et al. (2013) found that the transient X-ray source IGR J18245−2452 in the globular cluster (GC) M28 had an accretion outburst during March 2013, when it reached a luminosity larger than $10^{36}$ erg s$^{-1}$. They discovered that during this outburst the NS was emitting X-ray pulsations with a period of 3.9 ms. These have been used to obtain a timing solution that showed that the spin and orbital properties of this object were identical to that of PSR J1824−2452I, a RB system already known in the cluster. No radio pulsations have been detected during the outburst phase, while they reappeared less than two weeks after the end of the outburst, thus probing that this system was swinging between a pure accretion powered state, where it behaves like an AMXP, and a pure rotational powered state, where it behaves like an eclipsing radio MSP. These systems have been named "transitional MSPs" (tMSPs) and to date, only two more are known (Archibald et al., 2009; De Martino et al., 2015). All of them during the rotation powered state are classified as RBs (see Figure 1.9). The possibility that also BWs can swing to an accretion powered state is still open.

## 1.6 Globular Clusters: the Ideal Millisecond Pulsar Factories

GCs are gravitationally bound systems composed of up to $10^6$ stars and orbiting the Galaxy halo and bulge. The gravitational forces due to the ensemble of stars results in systems with spherical symmetry and high central densities. They are very old systems with typical ages of $\sim 12$ Gyr and metallicities $-2.0 \lesssim [\text{Fe/H}] \lesssim -1.0$, but up to solar values for the systems in the Galactic bulge (e.g. Terzan 5).

The central high densities are high enough that GC are the only place in the universe where dynamical interactions between stars occur in a timescale much shorter than the stellar ages. Therefore, the stars within the cluster, during their lifetime, are subjected to a large number of dynamical interactions such as exchange interactions, fly-byes, collisions, creation and disruption of binary systems. This results in the production of a large number of exotic objects such as MSPs, LMXBs, blue straggler stars and cataclysmic variables.

Although the absolute number of MSPs in the Galactic field is larger than that in GCs (252 vs 149), their number per unit mass is larger in the latter. In other words, $\sim 40\%$ of MSPs are found in GCs, despite the Galaxy is $\gtrsim 10^3$ times more massive than the entire GC system. This is easily explainable in a scenario in which MSPs in the field are the outcome of the evolution of primordial
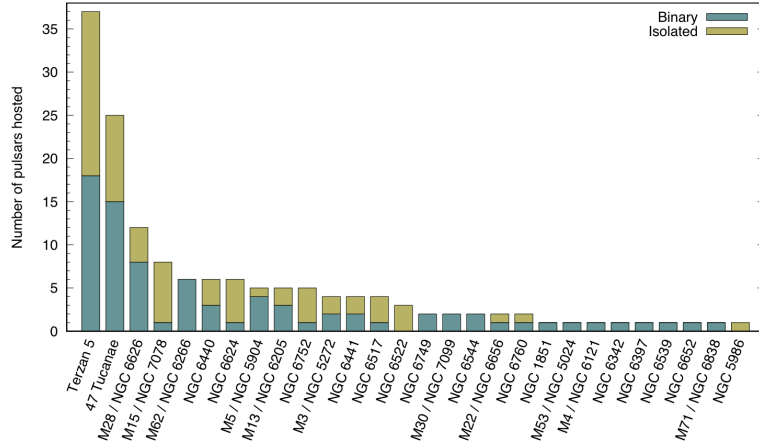
Figure 1.10: Number of MSPs identified in each GCs. The results shown in Chapter 3 are already included here. Courtesy of A. Ridolfi.

binary systems, while those in GCs can be the result of the evolution of both primordial systems and new binary systems formed later through dynamical interactions.

Figure 1.10 shows the number of MSPs in each cluster. As can be seen, half of the population is located in only three GCs: Terzan 5, 47 Tucanae and M28. The first system alone hosts ~ 25% of the entire population, thus suggesting an environment particularly suitable for creating new binaries. Most of these MSPs are likely the outcome the canonical evolutionary scenario, although the population properties are quite different than that in the Galactic field. As can be seen in Figure 1.11, the distribution of spin periods in GCs shows a distribution similar to that of Galactic field MSPs, but with a significant number of cases of long spin period objects, usually interpreted as mildly recycled systems, where the accretion has been halted by interactions with other stars. The distribution of orbital periods shows that GCs host more compact binaries than the Galactic field, as the result of energy exchanges with flying-by stars. Finally, the distribution of eccentricities shows that GCs host a significant number of eccentric binaries. According to the canonical scenario, the accretion stages lead to the formation of MSPs in almost perfectly circularized orbits. The trend observed in GCs suggests that dynamical interactions often perturb binaries, forcing them on eccentric orbits.

## 1.6.1 Dynamical Interactions

We will briefly review here three main dynamical interactions that are likely to occur in the central regions of GCs and able to produce exotic binaries such as LMXBs and consequently MSPs.

- **Tidal capture:** it occurs when an isolated NS, flying-by close to a main sequence star, menage to create a gravitational bond with it and thus a new binary system (e.g. Clark, 1975, see left panel of Figure 1.12) that can evolve through the scenario A depicted in
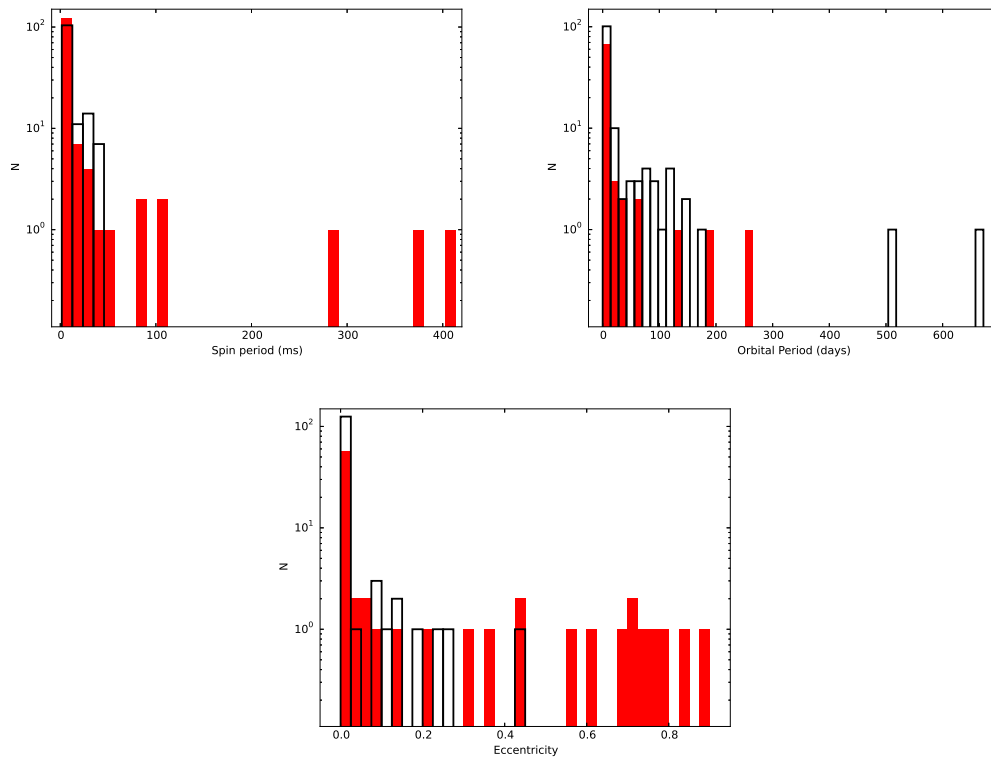
Figure 1.11: *Top left panel:* the red bars show the histogram of the spin periods of MSPs in GCs, while the empty black bars that of MSPs in the Galactic field (note that the three objects with spin periods larger than 200 ms are more likely young PSRs instead of recycled ones). *Top right panel:* same as before but for the distribution of orbital periods. *Bottom panel:* same as before but for the distribution of eccentricities.

Figure 1.7. Simulations by Ivanova et al. (2008) suggest that only a small fraction ($\sim 2\%$) of NSs is able to create a binary system in this way.

- **Direct collision:** it obviously occurs when a NS directly collide with another cluster star, eventually creating a new binary system. In a GC with 11 Gyr old stars, about $\sim 5\%$ of NSs are expected to form a binary system through this mechanism (Ivanova et al., 2008).

- **Exchange interaction:** it is an interaction between a star and a preexisting binary system, where the less massive component of the binary is kicked out (e.g. Hut, 1983). In the context of MSP evolution, this can happen in two different ways. In the first way, an isolated NS interacts with a binary system and, after the creation of an unstable triple system, the less massive companion of the triple is kicked out (see the right panel of Figure 1.12). The remaining binary will eventually go through the LMXB phase. In the second way, an isolated star interacts with a binary system containing a NS, possibly already recycled, and its companion star, most commonly a low-mass He WD. If the perturber is more massive
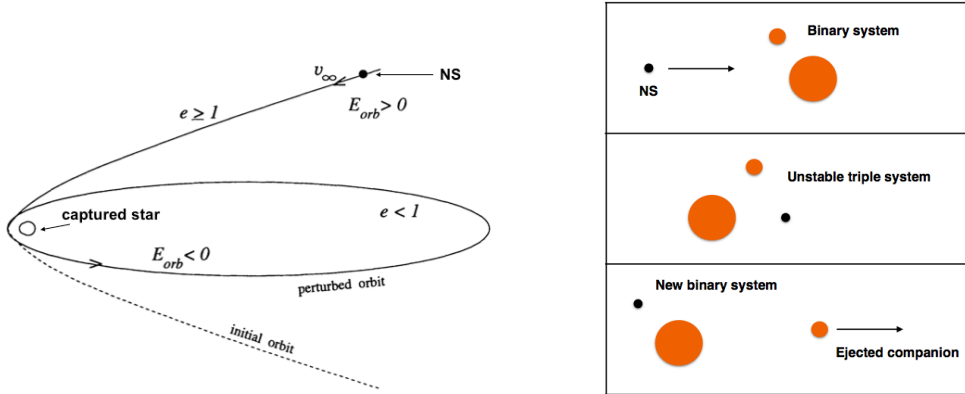
Figure 1.12: *Left panel:* A schematic representation of a tidal capture event. Taken from Mardling (1996). *Right panel:* Schematic representation of an exchange interactions between an isolated NS and a preexisting binary system.

than the current companion star, the latter is expelled and the NS will obtain a new companion star, thus starting, or re-starting, the recycling phase. Simulations by Ivanova et al. (2008) suggest that a large number of NSs (around $\sim 20\% - 25\%$) is able to create a binary system through this mechanism; this value can increase up to $\sim 40\% - 50\%$ in the very inner region of dense GCs.

Finally, there are other mechanisms, such as fly-byes (Hut, 1983), that can shrink or, at the contrary, force the binary systems on large eccentric orbits. Moreover, dynamical interactions between an isolated star and a preexisting binary system can also destroy the latter, without forming a new binary. This can explain the large fraction of isolated MSPs found in GCs.

An indicator of the rate of stellar interactions in the core of GCs is called "collisional parameter" or "stellar encounter rate" ($\Gamma$; Verbunt, Hut 1987) and can be expressed as:

$$(1.18) \qquad \Gamma \propto \int n_c\, n\, A\, v\, dV \propto \rho_0^{1.5} r_c^2$$

where $n$ and $n_c$ are the stellar density and the compact object density, respectively, $A$ is the cross-section of the encounter, $v$ is the relative velocity between the two interacting objects, $V$ is the GC volume, $\rho_0$ and $r_c$ are the GC central density and core radius, respectively. As can be seen in Figure 1.13, the number of MSPs in GCs, predicted by population synthesis models, clearly correlates with the stellar encounter rate.

There are some clusters (such as M15) which show a larger fraction of isolated MSPs or exotic systems (such as double NS binaries) than typical MSP binaries. In order to take into account these differences among GCs, Verbunt, Freire (2014) proposed a new indicator, quantifying the interaction rate per binary: $\gamma \propto \rho_0/\sigma$, where $\sigma$ is the velocity dispersion of stars in the cluster
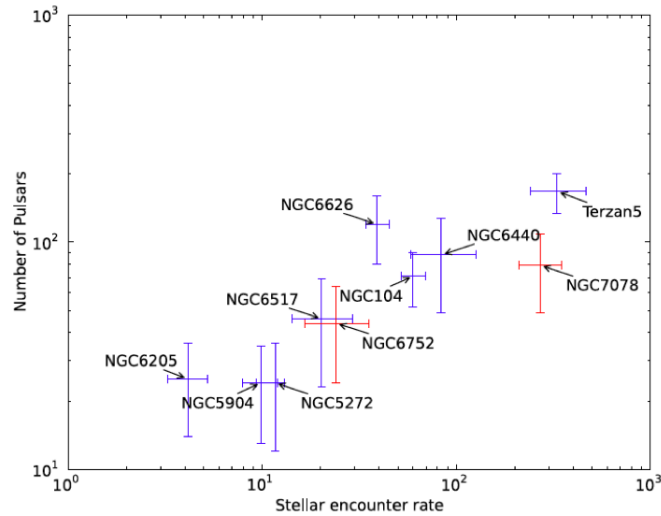
Figure 1.13: Number of MSPs expected to be hosted in GCs as a function of the stellar encounter rate. Taken from Bahramian et al. (2013).

core. In GCs with larger values of $\gamma$, a larger number of interactions between single stars and binary systems should occur. Therefore these GCs are expected to host a larger number of exotic systems, such as isolated MSPs, eccentric binary MSPs or mildly recycled MSPs. The Galactic GCs with the highest value of $\gamma$ are NGC 6652 and NGC 6624, while M3 and M13 have the lowest values.

## 1.7 Millisecond Pulsars in Globular Clusters: State of the Art

In the last decades, the study of MSPs in GCs at different wavelengths has provided a wealth of science (see Hessels et al., 2015, and references therein) spanning from fundamental physics to dynamics and stellar evolution. GCs host the most peculiar MSP systems, such as the fastest spinning one (Hessels et al., 2006), potentially the most massive NSs known (Freire et al., 2008a,b), at least one double NS system (Jacoby et al., 2006), a triple system composed of a MSP orbiting a WD and a planet, as well as various eccentric binaries and other non canonical systems. Before this thesis work, 146 MSPs were known in GCs. However, population synthesis show that the next generation of radio telescopes will be able to unveil from few hundreds to few thousands of new MSPs (e.g. Turk, Lorimer, 2013). This large population will hopefully also include unique systems such as MSP-MSP binaries or even MSP-black hole binaries, which are expected to formed in the extreme environments of GC cores through dynamical interactions.

Fundamental physics can be probed, for example, setting constraints on the equation of state of NS or by testing general relativity or alternative gravitation theories on small scales (Hessels

et al., 2006; Freire et al., 2008b; Demorest et al., 2010). The discovery of new very fast spinning MSPs, or even sub-MSP systems, will strongly constrain the maximum radius and hence the NS equation of state (Lattimer, Prakash, 2001; Hessels et al., 2006). Moreover, MSPs in GCs can in principle experience multiple recycling episodes if companion swappings occur. These should lead to the creation of even more fast spinning and also more massive NSs, thus also allowing to probe the maximum mass for such systems. Indeed, the mass of NSs is relatively easy to measure in GCs due to the presence of more eccentric systems with respect to the Galactic field. These are likely to show orbital relativistic effects such as the periastron precession (see Chapter 2.2.2) that allow precise mass measurements (e.g. Jacoby et al., 2006; Freire et al., 2008b).

The cumulative population of MSPs in a cluster can provide a wealth of information about the cluster structure, potential well, proper motion and also the dynamical status. This is feasible mainly because the spin period derivative of a MSP in a GC is not only due to its intrinsic spin-down rate, but also to its acceleration in the cluster potential field. Indeed, a PSR with intrinsic spin period $P_0$, moving with respect to the observer, is observed with a period:

$$(1.19) \qquad P = \left[ 1 + \left( \mathbf{V_p} - \mathbf{V_{bary}} \right) \cdot \frac{\mathbf{n}}{c} \right] P_0$$

where $\mathbf{V_p}$, $\mathbf{V_{bary}}$ and $\mathbf{n}$ are the PSR velocity, the velocity of the solar system barycenter and the unit vector along the line of sight, respectively. Following Phinney (1993) it can be shown that the derivatives of this equation give an equation for the spin period derivative expressed as the measured acceleration $a_{meas}$:

$$(1.20) \qquad \frac{a_{meas}}{c} = \left( \frac{\dot{P}}{P} \right)_{meas} = \left( \frac{\dot{P}}{P} \right)_{int} + \frac{a_{GC}}{c} + \frac{a_{add}}{c}$$

where $\left( \frac{\dot{P}}{P} \right)_{int}$ is the ratio between the intrinsic $\dot{P}$ and $P$, $a_{GC}$ is the acceleration due to the GC gravitational field and $a_{add}$ is any additional acceleration such as that due to the Galaxy potential field. Therefore, measuring the spin period derivative of a MSP population is a powerful tool to study the cluster potential in a very unique and direct way, possibly probing or excluding the presence of an intermediate-mass black hole in the center. For example, Prager et al. (2017) used the ensemble of MSPs in Terzan 5 to constrain the physical characteristics of this system, such as the structural parameters, the core density and the total mass, also excluding the presence of a central intermediate-mass black hole more massive than $\sim 10^4$ M$_\odot$. All their results are completely independent with respect to the optical derived quantities, though fully consistent.

Furthermore, measurements of an ensemble of MSP proper motions provide a direct and precise measurements of the GC motions in the sky. This can be used to constrain the orbits of clusters in the Galactic field, thus providing insight into their evolution. Precise and long-term timing of the MSPs in 47 Tucanae also revealed, for the very first time, the presence of an ionized intracluster medium (Freire et al., 2001b). The cumulative population can also be used to study the complex interplay between dynamics and stellar evolution, since binary NSs in GC cores are

believed to play a major role in delaying the core collapse phase of the system. Moreover, different clusters appear to host different kinds of MSP populations in terms of spin period distribution, location within the cluster, fraction of binaries versus isolated (Verbunt, Freire, 2014). All this is tightly linked to the cluster dynamical status and therefore MSP studies combined with that of other exotic systems, such as blue straggler stars (Ferraro et al., 2012), can provide major improvements in this field.

Evolutionary scenarios and accretion physics can be probed with multi-wavelength studies of these systems. In particular, the identification of the optical counterpart to binary systems is of utmost importance since it opens the possibility of evaluating the frequency and timescales of dynamical interactions in dense stellar systems, to explore the impact of dynamics on MSP evolutionary paths, and to investigate stellar evolution under extreme conditions (see, e.g., Ferraro et al., 2003b,c; Sabbi et al., 2003a,b; Mucciarelli et al., 2013; Ferraro et al., 2015a). Indeed the properties of MSP companion stars are extremely different from those of standard stars, due to the effects of the mass transfer phase and of the gravitational field, intense high energy emission and relativistic wind of the NS. In the case of WD companions, it is possible to estimate the masses and cooling ages of the systems through direct comparison of their properties with stellar evolutionary models (Edmonds et al., 2001; Ferraro et al., 2003a; Sigurdsson et al., 2003). Moreover, spectroscopic follow-ups allow to measure the radial velocities of the companion star, thus providing the mass ratio of the binary. This, together with the radio timing properties of the system, can lead to precise mass measurements of both the components of the binary (Ferraro et al., 2003c; Cocozza et al., 2006; Antoniadis et al., 2013). These measurements benefit from the known GC distance and optical extinction, thus reducing the uncertainties on the estimated quantities with respect to the case of MSPs in the Galactic field. Furthermore, the derived WD cooling ages are a more appropriate measurement of the system age with respect to the characteristic PSR ages derived from radio timing (see Section 1.2.2 and Tauris et al. 2012; Tauris 2012). The correct determination of MSP ages is an important tool for studying the spin evolution and constraining the physics of the recycling phases (see, e.g., van Kerkwijk et al. 2005 and the references therein).

Also X-ray counterparts allow to study the physics of the MSP intra-binary space and of the accretion physics. They also provide a way to put constraints on the NS radii (e.g. Bogdanov et al., 2005, 2011; Guillot et al., 2013). Interestingly, the *Fermi* $\gamma$-ray satellite revealed emission from a sample of GCs (Abdo et al., 2010; Zhang et al., 2016) that host (or are expected to host) a large population of MSPs.

Despite the importance of MSP optical counterparts, their identification in crowded stellar systems like GCs is extremely challenging. Only nine companions were identified in GCs before this thesis work, especially thanks to the high resolution performances of the *Hubble Space*
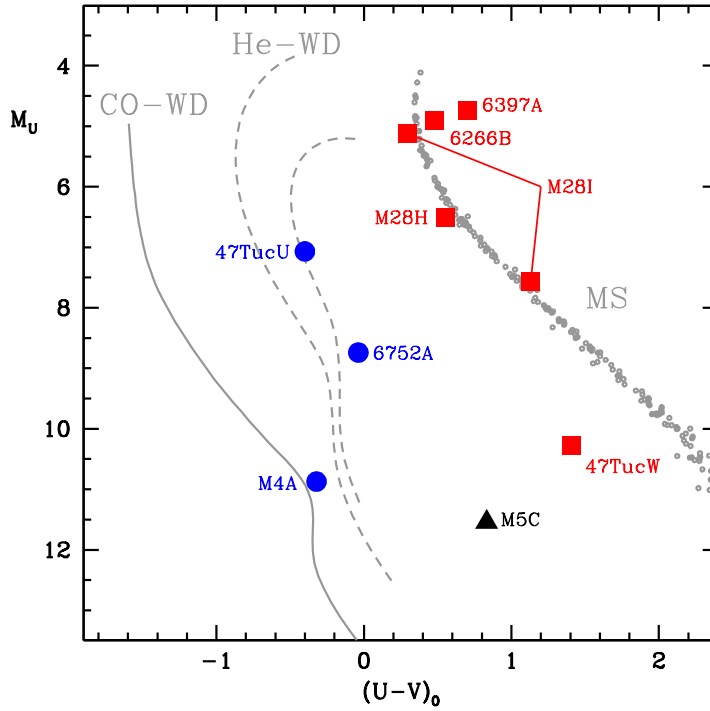
Figure 1.14: Position of the MSP optical counterparts in an absolute CMD. Blue dots mark the position of canonical MSPs, while red squares and black triangles the position of RBs and BWs, respectively.

*Telescope* cameras. We will briefly review their properties in the following, while the positions of the nine companion stars in an absolute color-magnitude diagram (CMD) are reported in Figure 1.14.

- **Canonical systems:** the companion to PSR J0024$-$7204U (COM-47TucU[6], Edmonds et al. 2001), to PSR J1740$-$5340A (COM-6752A, Ferraro et al. 2003a) and to PSR B1620$-$26 (COM-M4A, Sigurdsson et al. 2003) are He WD systems. Therefore they likely are the result of the canonical evolutionary scenario[7]. All of them are WD with low-masses around $0.15\,\mathrm{M_\odot} - 0.4\,\mathrm{M_\odot}$ and cooling ages in a range from 0.5 Gyr to 3 Gyr.

- **Redback systems:** five companions belong to the RB class. The companion to PSR J1740$-$5340A (COM-6397A, Ferraro et al. 2001b) is a bright and tidally distorted star located in the red side of the CMD at about the turn-off level. It has a mass of $0.2\,\mathrm{M_\odot} - 0.3\,\mathrm{M_\odot}$, and Mucciarelli et al. (2013) spectroscopically confirmed that it likely lost up to 80% of its original mass as a consequence of accretion and ablation due to the PSR wind.

---

[6]All the MSPs in GCs are usually named as the cluster name followed by a letter.

[7]Please note that M4A is a triple system with a Jupiter-mass third object. Thus it certainly experienced a deviation from the canonical scenario. This is, so far, the only planet known in a GC.

Similarly, the companions to PSR J1701−3006B and PSR J1824−2452H (COM-6266B and COM-M28H, Cocozza et al. 2008; Pallanca et al. 2010) are tidally distorted star located close to the cluster main sequence. The companion to PSR J0024−7204W (COM-47TucW, Edmonds et al. 2002) is a faint star and its light curve shows that it is subjected to a very strong heating by the PSR injected flux. Finally, the companion to the tMSP J1824−2452I (COM-M28I, Pallanca et al. 2013a) is another main sequence-like star if observed during the rotation powered state, while it becomes brighter and bluer during the accretion powered state. Also a strong $H_\alpha$ emission has been detected during its accretion powered state, which completely disappears during quiescence.

- **Black-Widow systems:** only the optical counterpart to the BW PSR J1518+0202C (COM-M5C, Pallanca et al. 2014) was identified before this thesis work. It is an extremely weak and variable star showing the signatures of a very strong heating of the stellar side facing the MSP. It is located in an anomalous region between the main sequence and the WD cooling sequence, where no stars in standard evolutionary stages are expected.

# SEARCHING, TIMING AND OPTICAL IDENTIFICATION OF MILLISECOND PULSARS IN GLOBULAR CLUSTERS

In this chapter we summarize the main methodologies used to study pulsars at radio and optical wavelengths. First of all, the main issues arising in classical pulsar searches are presented, along with the techniques routinely used to overcome them in order to discover these faint and exotic objects. Then we present the timing analysis technique and how it can be used to infer a wealth of physical properties of isolated and binary pulsars both. Finally, we show how to identify and characterize the optical counterparts to millisecond pulsars in globular clusters, by using photometric and spectroscopic techniques.

## 2.1 Searching for Pulsars

Pulsars (PSRs) are weak radio sources whose periodic signal is usually embedded in a sea of
noise and terrestrial interferences. These signals, on their way from the source to the observer,
interact with the interstellar medium through a number of physical processes such as dispersion,
scattering, scintillation and Faraday rotation. This, together with the PSR motion within a binary
system, make basically impossible the identification of new PSRs by simply analyzing the total
power registered by the radio telescope[1]. In the following, the main steps of the typical PSR
searches are described.

### 2.1.1 Dispersion and Dedispersion of the Signal

The first main problem to deal with when searching for PSRs is the dispersion of their signal: fre-
quency dependent time of arrivals of the PSR electromagnetic waves due to their travel through
a cold and ionized interstellar medium (see Figure 2.1). In order to compensate the intrinsic faint
emission of PSRs, observations covering large frequency bandwidth are needed, thus heavily
introducing such a dispersive effect that needs to be corrected, otherwise the signal would be
broadened and the signal to noise ratio (S/N) heavily reduced.

To understand the basic physics behind this phenomenon, consider that the group velocity
of the propagating wave, emitted by a PSR, is $v_g = c\mu$ where $\mu < 1$ is the frequency dependent
refracting index of the ionized interstellar medium. As a consequence, the PSR signal, while
traveling a distance $d$ from the source to Earth, experiences the following delay with respect of a
signal of infinite frequency:

$$(2.1) \qquad t = \left( \int_0^d \frac{dl}{v_g} \right) - \frac{d}{c} \equiv A \times \frac{DM}{f^2}$$

where $f$ is the wave (observing) frequency and the quantity DM is called "dispersion measure"
and it is defined as:

$$(2.2) \qquad DM = \int_0^d n_e dl$$

where $n_e$ is the electron density and $A$ is the "dispersion constant" $A \equiv \frac{e^2}{2\pi m_e c}$, where $e$ and $m_e$
are the electron charge and mass, respectively. It follows that the delay between two observing
frequencies is:

$$(2.3) \qquad \Delta t \simeq 4.15 \times 10^6 \, \text{ms} \, \times DM \times \left( f_1^{-2} - f_2^{-2} \right)$$

We will briefly show in the following the two main methods used to remove such an effect from
PSR data.

---

[1]Although the first PSRs were discovered in this way.
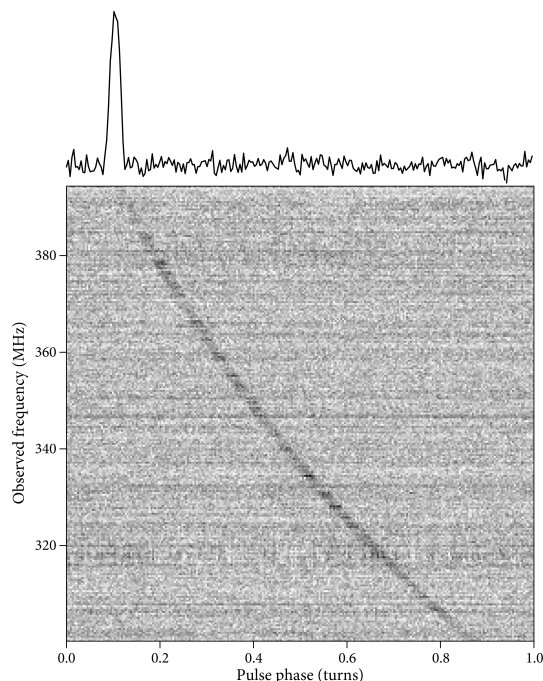
Figure 2.1: The effect of the dispersion of the PSR signal. The gray scale pattern show the uncorrected dispersed signal of PSR J1400+50, as a function of the observing frequency. The top panel report the corrected pulse profile. Figure credit: NRAO.

**Incoherent Dedispersion**

It is the simplest way to compensate the effect of the signal dispersion. It consists of splitting the observing frequency bandwidth into a large number of independent frequency channels and then applying to each one of them an appropriate delay measurable by equation (2.3), in which $f_1$ is a reference frequency channel (usually the central observing frequency) and $f_2$ the central frequency of channel to be corrected.

It is obvious that the main issue of incoherent dedispersion is the finite bandwidth of the single channels, that cannot be made arbitrary small,. Therefore each channel inherently retain a small dispersive delay. Such as dispersive delay across a single frequency channel strongly depends on the observing frequency. Therefore, broader channel bandwidths can be used at higher frequency observations.

**Coherent Dedispersion**

A much more efficient method, known as coherent dedispersion, allows to completely remove the dispersive effect on the signal by using the phase information of the incoming voltage $v(t)$ induced in the telescope by the incoming electromagnetic wave. Once this is measured, it is possible to recover the intrinsic complex voltage $v_{int}(t)$ as originated by the PSR (see Lorimer, Kramer, 2004, and references therein).

35

Briefly, this process is based on the fact that the modification of the electromagnetic wave by
the interstellar medium can be described as the result of a "phase" filter, or "transfer function $H$",
which can be easily analyzed in the Fourier domain. For a signal observed at a central frequency
$f_0$ and bandwidth $\Delta f$, the Fourier transforms $V(t)$ and $V_{int}(t)$ of $v(t)$ and $v_{int}(t)$, respectively, can
be expressed as:

(2.4) $$V(f_0 + f) = V_{int}(f_0 + f)H(f_0 + f)$$

These are non-zero only for $|f| < \Delta f/2$ and thus:

(2.5) $$v(t) = \int_{f_0 - \Delta f/2}^{f_0 + \Delta f/2} V(f)e^{i2\pi ft}df$$

(2.6) $$v_{int}(t) = \int_{f_0 - \Delta f/2}^{f_0 + \Delta f/2} V_{int}(f)e^{i2\pi ft}df$$

It can be shown that the transfer function $H$ can be written as:

(2.7) $$H(f_0 + f) = e^{-ik(f_0+f)d} = e^{+i\frac{2\pi A}{(f+f_0)f_0^2}DMf^2}$$

where $k$ is the wavenumber. By applying the inverse function of $H$ to the sampled voltage data,
the voltage as originally emitted by the PSR, and thus completely dedispersed, is recovered.

### 2.1.2 Standard Search Procedures

The standard search procedures start from the raw data that have to be, first of all, dedispersed
in a range of DMs in order to create a number of time series, one per DM value. The step interval
between different DM trials should be chosen as a tradeoff, being not too large, so that the PSR
signal at a true DM lying in the middle of two trials is not excessively broadened to be missed,
and being not too small, to avoid to waste computational time. To better quantify this, consider a
simple top-hat pulse of intrinsic width $W_{int}$, the observed width $W_{eff}$ at an incorrect DM value
that differs by $\Delta$DM from the true value is:

(2.8) $$W_{eff} = \sqrt{W_{int}^2 + (k_{DM} \times |\Delta DM| \times \Delta f/f^3)^2}$$

where $k_{DM}$ is a constant. It can be shown that the S/N is both a function of the PSR period and
observed width (see Section A1.22 of Lorimer, Kramer, 2004):

(2.9) $$S/N \propto \sqrt{\frac{P - W_{eff}}{W_{eff}}}$$

On the basis of S/N required for the analysis, an appropriate DM step interval has to be chosen.
This can be as large as few or tens of DM units for very long period PSRs, to few tenths for very
short period PSR, such as millisecond pulsars (MSPs) .

For very long integration time data, such as those needed to study MSPs in globular clusters (GCs), the effect of the rotation of the Earth around the Sun has to be taken into account by applying a barycentric correction. The standard approach to this aim is to refer the topocentric collected data to that of the solar system barycentre. To do this, the starting time of the observation has to be shifted appropriately to match the arrival time of the first sample at the solar system barycentre. Then, the arrival time of each following samples, has to be corrected taking into account the relative motion between the observer and the solar system barycentre.

Once the dedispersed and barycentered time series are obtained, they can be investigate to search for periodic signals. One of the most common routines used to do this is the Fourier transform of the time series and analysis of the resulting power spectrum. However, the continuous form of the Fourier transform cannot be applied, since the time series are a set of independently sampled data points. A discrete Fourier transform is then used and the resulting power spectrum is composed of bins with width equal to the inverse of the total integration time of the analyzed observation. To illustrate the effectiveness of Fourier transforms, in Figure 2.2 a sinusoidal signal is plotted both in a noisy time series and in its Fourier power spectrum. As can be seen, the signal is hopelessly confused within the noise in the former, while it appears as a strong peak in the Fourier space. In real life, however, PSRs are not perfectly sinusoidal signals. Indeed they can have very complex pulse profiles with different duty cycles. This means that the power spectrum powers will be distributed between the fundamental frequency and a significant number of harmonics. Since these contain a significant fraction of the PSR power, methods to perform incoherent harmonic summing have been successfully implemented (see, e.g., Ransom et al., 2002).
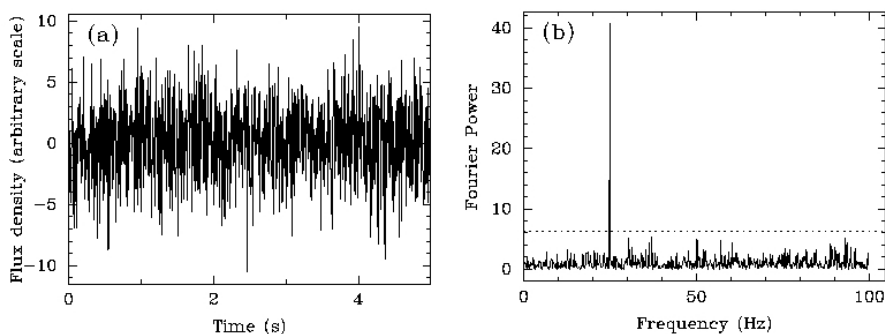


Taken from "Handbook of Pulsar Astronomy" by Lorimer & Kramer

Figure 2.2: *Panel a):* A noisy time series containing a purely sinusoidal 25 Hz signal. *Panel b):* The power spectrum of the Fourier transform of the same time series. The dashed horizontal line is the power threshold above which a peak is considered a PSR candidate instead of a noise fluctuation.

The following and final step is to select, in the power spectra obtained at different DMs, all the peaks above a chosen threshold. The resulting list of candidates will likely contain a number of false detections, radio frequency interferences (RFI) and, hopefully some new PSRs. The latter are expected to appear multiple times in the list, at different DMs, with larger S/N in the proximity of the PSR true DM. All the candidates can be folded, modulo the best period and DM known, starting from the raw data, in order to confirm or reject their PSR nature. This is a procedure in which, given all the known PSR ephemerides (the spin period, position and DM, at least), the corresponding rotational phase of each sample of the observation is calculated, in order to obtain, at the end, an integrated pulse profile, coherently summing all the pulse available in the observation. This represent an average emission of the neutron star (NS) as a function of the rotational phase. The folded data of a real PSR candidate is expected to present a signal across the whole bandwidth and possibly (but not necessarily) across the whole observation, with a peak at the true DM, period and period derivative.

**Pulsars in Binary Systems**

The method described in the previous section is not suitable to the identification of PSRs in binary systems, especially those with short period orbits (i.e. much shorter than the observation time). Indeed, the motion of the PSR in the binary system results in a Doppler shift of the spin frequency that spreads the signal over a number of adjacent spectral bins in the power spectra, thus significantly diluting the S/N.

Several algorithms have been built to compensate, at least partially, this problem. The most famous one is a time domain technique that allows to recover the PSR signal by resampling the time series to the rest frame of an inertial observer with respect to the PSR. Therefore, a standard periodicity search on this modified time series should be able to easily detect the PSR signal. This method is particularly efficient if the binary system orbital parameters are known, since the PSR velocity with respect to the observer as a function of time is known. However, in the most common blind searches, assuming a Keplerian model for such a velocity would require a search in a five-dimensional space and thus a prohibitive computational time. The simplest way to overcome this problem is to assume that, within the observations, the orbital acceleration of the PSR is constant and therefore its velocity scales linearly with the observing time. These are called "acceleration searches", and they are usually carried out on time series corrected assuming different values of orbital accelerations. The effectiveness of this method in recovering the PSR signal is shown in Figure 4.9. The main limitation of this method is that for long integration times the assumption of constant acceleration becomes very poor, as the PSR go through a large fraction of its orbit.

There are also a number of alternative methods, especially frequency-domain techniques. Among these, it is worth mentioning the so called "phase-modulation search technique" (Ransom et al., 2003). Having typical integration times of several hours, GCs observations usually sample
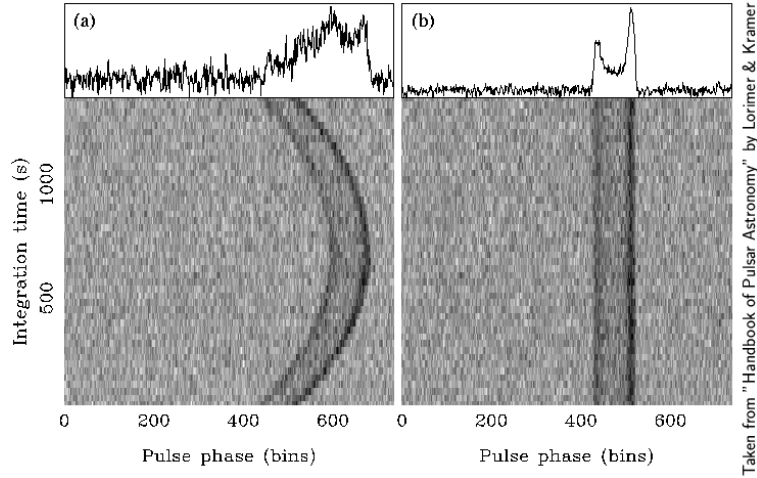
Figure 2.3: *Panel a):* Folded pulse profile of PSR B1913+16 without correction for the apparent changes of the spin period. *Panel b):* The same folded data, but assuming a constant acceleration to compensate the motion of the PSR in the binary.

many PSR orbital periods. The phase-modulation technique exploit the fact that the signal in a power spectrum covering several orbits has a characteristic shape imprinted by the constantly changing PSR spin frequency and it can be described as a family of Bessel functions forming sidebands around the true spin period of the PSR. Once this sidebands are localized, it is usually simple to recover the orbital period, semi-major axis and epoch of ascending node of the binary from sideband spacing, width and phases, respectively.

### 2.1.3  Flux Density Estimates

It can be demonstrated (see appendix A1.4 of Lorimer, Kramer 2004) that the S/N of a top-hat pulse of period $P$, width $W$ and peak amplitude $T_{peak}$ above a system noise temperature $T_{sys}$ can be written, starting from the radiometer equation (Dicke, 1946), as follows:

$$(2.10) \qquad S/N = \sqrt{n_p t_{obs} \Delta f} \left( \frac{T_{peak}}{T_{sys}} \right) \frac{\sqrt{W(P-W)}}{P}$$

where $t_{obs}$ is the total observing time, $\Delta f$ the observing bandwidth and $n_p = 1$ or $n_p = 2$ for single polarization observations and two orthogonal summed polarization observations, respectively. To express this value in terms of flux density, we know that the peak flux density of the pulsar is $S_{peak} = T_{peak}/G$, where $G$ is the telescope gain expressed in units of $\mathrm{Jy}^{-1}$. Since the mean flux density across the whole period is simply the peak flux density times the duty cycle ($W/P$), we get:

$$(2.11) \qquad S_{mean} = S_{peak} \left( \frac{W}{P} \right) = \frac{T_{peak} W}{GP}$$

39

Substituting in equation (2.10) the expression for $T_{peak}$ obtained in the latter formula, we obtain an equation that can be used to roughly measure the PSR flux density:

$$(2.12) \qquad S_{mean} = S/N \frac{T_{sys}}{G\sqrt{n_p t_{obs} \Delta f}} \sqrt{\frac{W}{P - W}}$$

In the context of PSR searches, this equation can be used to estimate the limiting detectable flux density of an observation, corresponding to a minimum signal to noise ratio (S/N$_{min}$):

$$(2.13) \qquad S_{min} = \beta (S/N)_{min} \frac{T_{sys}}{G\sqrt{n_p t_{obs} \Delta f}} \sqrt{\frac{W}{P - W}}$$

where $\beta \gtrsim 1$ is a correction factor introduced to account for system imperfections in the digitization of the signal.

## 2.2  Pulsar Timing

Once a new PSR is discovered, follow-up observations are usually obtained to monitor the pulse time of arrivals (TOAs), allowing to study the PSR physical properties, such as its spin, astrometric and orbital parameters.

The pulse TOA is defined as the arrival time of closest pulse at the mid-point of the observation. To obtain such a measure, being PSRs weak radio sources, it is necessary to fold the observation, thus adding together a significant number of pulses. The folded profile is then matched to a reference one, usually the highest S/N detection of the PSR or a noise-free template that can be obtained stacking together a proper amount of folded observations and then fitting the resulting pulse profile as a sum of Gaussian components. The TOA uncertainty ($\sigma_{TOA}$) can be defined as the ratio between the pulse width over its S/N. Using the radiometer equation, it can be shown that:

$$(2.14) \qquad \sigma_{TOA} \simeq \frac{W}{S/N} \propto \frac{S_{sys} P \delta^{2/3}}{S_{mean} \sqrt{t_{obs} \Delta f}}$$

where $S_{sys}$ is the system equivalent temperature (high sensitivity radio telescopes have low $S_{sys}$) and $\delta$ is the PSR duty cycle. Therefore, the best measurements are obtained observing short period, narrow pulse and (obviously) bright PSRs with sensitive and wide-band systems. The folding procedure, summing together a large amount of pulses, allows to reduce the TOA uncertainties. For MSPs, few minutes of observation allow to sum together few thousand pulses. This, together with the intrinsic stability of their signal, explains why MSPs provide better timing performances than classical PSRs.

Before starting the TOA analysis, it is necessary to transform all the measured topocentric TOAs into the solar barycentre system, which can be approximated as an inertial frame. This transformation also corrects for relativistic time delays due to the presence of masses in the solar

system. Moreover, this procedure allows to combine TOAs obtained at different times in different observatories. All the TOAs are also corrected for a pulse arrival at infinite high frequency, in order to remove any dispersive effect from the data.

### 2.2.1 Isolated Pulsars

To study the properties of PSRs, i.e. to study changes in the pulse arrival times as a function of time, it is necessary to describe the PSR rotations in a reference frame co-moving with the spinning object. The most common way to do it is to use a Taylor expansion of the PSR spin frequency $v$:

$$(2.15) \qquad v(t) = v_0 + \dot{v}_0(t - t_0) + \frac{1}{2}\ddot{v}_0(t - t_0)^2 + \dots$$

where $t_0$ is a reference epoch and $v_0$ the spin period at $t = t_0$. Alternatively, the same equation can be written in terms of number of pulses received (or expected) from a reference time $t_0$:

$$(2.16) \qquad N = N_0 + v_0(t - t_0) + \frac{1}{2}\dot{v}_0(t - t_0)^2 + \frac{1}{6}\ddot{v}_0(t - t_0)^3 + \dots$$

The timing procedure consists of a least square fitting between the measured TOAs and a multi parametric model that is expected to be able to unambiguously account for every single rotation of the PSR between different observations. Basically, the procedure tries to match the measured arrival times to the number of pulses, minimizing the following expression:

$$(2.17) \qquad \chi^2 = \sum_i \left( \frac{N(t_i) - n_i}{\sigma_i} \right)^2$$

where $n_i$ is the integer number of pulses nearest to $N(t_i)$ and $\sigma_i$ the TOA uncertainty in units of pulse turns. At the beginning of the procedure, when only few TOAs, covering a time baseline of few days, are usually available, only the spin period is fitted. When longer TOA time baseline are available, also the spin frequency derivatives and the astrometric position can be fitted. The latter is obtained by measuring the annual variation of TOAs due to the Earth orbit around the Sun. Incomplete or incorrect timing models causes systematic trends in the post-fit residuals, while they are expected to be Gaussianly distributed around zero for a good quality fit. The uncertainties on the fitted parameters decreases with follow up observations, thus with longer time baselines and also with observations obtained at different frequencies, particularly useful to better estimate the DM.

### 2.2.2 Binary Pulsars

In case of binary systems, the orbit of the PSR around the center of mass results in periodical modulation of the pulse TOAs. These are a consequence of the variation of the observed spin period due to the Doppler effect as the PSR moves through its orbit with different velocities

along the observer line of sight. For non relativistic systems, Kepler's law can be used to fully describe the orbital properties of these systems. Only five parameters need to be fitted in the timing solution, in order to refer the TOAs to the binary barycentre: the orbital period ($P_b$), the projected semi-major axis ($x \equiv a_p \sin(i)/c$, where a is the semi-major axis and i the orbital inclination angle), the orbital eccentricity ($e$), the longitude of the periastron ($\omega$) and the epoch of periastron passage ($T_0$). These parameters fully describe the orbital properties of the system and they can be also used to constrain the secondary mass through the mass function, that depends on the orbital period and projected semi-major axis:

$$(2.18) \qquad f(m_p, m_c) = \frac{(m_c \sin(i))^3}{(m_p + m_c)^2} = \frac{4\pi}{G} \frac{(a_p \sin(i))^3}{P_b^2} = \frac{4\pi^2}{T_\odot} \frac{x^3}{P_b^2}$$

where $m_p$ and $m_c$ are the PSR and companion mass, respectively, and $T_\odot = (GM_\odot/c^3) \approx 4.92\,\mu s$. Assuming a standard NS mass of $1.4\,M_\odot$ and an orbital inclination of $90°$, a lower limit on the companion mass can be obtained.

In the case of a relativistic binary system, the Keplerian description is no more able to fully reproduce the pulse TOAs and so a number of relativistic effects, due to the strong gravitational field and high orbital velocities, have to be included in the timing fit. These are usually parametrized through the so-called "post-Keplerian" parameters that for point masses with negligible spin contribution are only a function of the masses of the two orbiting bodies and of the standard Keplerian parameters. Therefore, measuring two post-Keplerian parameters allows to determine the masses of both the PSR and companion star in the frame of a given theory such as general relativity or possibly alternative gravitation theories. The measurement of a third parameter allows consistency checks of the assumed theory, and so, typically, validation of the general relativity theory. In general relativity, the relativistic orbit of a binary can be described through five main post-Keplerian parameters (see Lorimer, Kramer, 2004, and references therein):

$$(2.19) \qquad \dot{\omega} = 3T_\odot^{2/3} \left(\frac{P_b}{2\pi}\right)^{-5/3} \frac{(m_p + m_c)^{2/3}}{1 - e^2}$$

that describes the advance of periastron in units of rad s$^{-1}$, easily measurable for eccentric orbits. A second parameter is the so-called "gamma parameter", that expresses, in units of seconds, the modification of arrival times due both to the gravitational redshift induced by the companion star and time dilation as the PSR moves at different speeds in an elliptical orbit:

$$(2.20) \qquad \gamma = T_\odot^{2/3} \left(\frac{P_b}{2\pi}\right)^{1/3} e \frac{m_c(m_p + 2m_c)}{(m_p + m_c)^{4/3}}$$

Two other important parameters are the "range" and "shape" of the Shapiro delay:

$$(2.21) \qquad r = T_\odot m_c$$

42

(2.22)
$$s = \sin(i) = T_{\odot}^{-1/3} \left( \frac{P_b}{2\pi} \right)^{-2/3} x \frac{(m_p + m_c)^{2/3}}{m_c}$$

which is a delay caused by the gravitational field of the companion star and measurable only for nearly edge-on orbits. Finally, the last parameter is the derivative of the orbital period due to the emission of gravitational waves:

(2.23)
$$\dot{P}_b = -\frac{192\pi}{5} T_{\odot}^{5/3} \left( \frac{P_b}{2\pi} \right)^{-5/3} f(e) \frac{m_p m_c}{(m_p + m_c)^{1/3}}$$

where $f(e)$ is a simple function of the eccentricity.

Orbital properties of binary PSRs, both relativistic and non, can show periodical or secular changes due to different effects, such as emission of gravitational waves, mass loss, tidal dissipation or interaction with the companion stars. In the case of binaries in GCs, these changes can be the result of a changing Doppler effect due to a change in the distance between the solar system barycentre and the PSR, as the latter orbit in the GC potential field. In particular, this effect contaminates the observed values of the orbital period derivative, which by consequence are not a direct measurement of the intrinsic variation of the orbit. The cluster acceleration affects $\dot{P}_b$ the same way it affects $\dot{P}$ (Section 1.7). Thus measuring both the derivatives can help to disentangle the intrinsic values from those induced by the cluster.

## 2.3 Identification of Optical Counterparts in Globular Clusters

In the case of a binary system, the optical counterpart can be identified and it provides a complementary approach to study the properties of these systems from the secondary star point of view. Indeed, as already explained in Chapter 1.7, the optical emission is dominated by the companion star while that due to the NS emission, both thermal and non thermal, is totally negligible.

The analysis of the optical counterparts is articulated in two main step. The first one is the photometry of stellar system of the GC in order to identify the counterpart in a position coincident with that of the radio PSR, and then analyze its color-magnitude diagram (CMD) position and possible stellar variability. The second step is the spectroscopic follow-up of the counterpart, useful to mass measurements and to study the companion star chemical composition.

### 2.3.1 Photometry of the Companion Stars

Being NSs the most massive stars in GCs, they are usually located in their very central regions as a consequence of dynamical friction effects. Therefore, in order to properly resolve the extreme crowding conditions of these regions, high angular resolution observations are required. Most of the high resolution images used in this thesis have been obtained through the Wide Field Camera 3 (WFC3) and the Advanced Camera for Survey (ACS), both mounted on the *Hubble Space Telescope* (HST). Both the detectors provide pixel scales of the order of 0.04"/pixel and a

field of view (FOV) ranging from $160'' \times 160''$ for the UVIS channel of the WFC3 to $202'' \times 202''$ for the Wide Field Camera of the ACS. Their performances allow to resolve the crowded stellar population of GC core regions. Indeed, the typical full width half maximum of point sources in these instruments is of about $0.06'' - 0.08''$.

Multi-epoch and multi-filter observations are usually required in order to perform a secure identification and complete characterization of the companion stars. In fact, these are necessary in order to create CMDs, color-color diagrams and properly sampled light curves.

In the following we describe the typical procedure used to perform the photometric analysis of GC data (see, e.g. Dalessandro et al., 2008a,b). First of all, it is necessary to model the point-spread function (PSF) of each image of the data-set. This can be done by using a sample of $\sim 200$ bright but not saturated stars as reference objects. The PSF structure is determined using an iterative procedure and the final model is chosen on the basis of a $\chi^2$ test. The best fit model is usually provided by a Moffat function (Moffat, 1969). The next step is to perform a deep source detection analysis, usually setting a $\sim 3\sigma$ to $\sim 5\sigma$ detection limit, where $\sigma$ is the standard deviation of the background counts. Once a list of stellar objects is obtained, a PSF-fitting can be performed for each star of each image in order to measure their apparent magnitudes. Classical aperture photometry techniques are not recommended here due to the extreme crowding conditions of GC central regions. The main advantage of using the PSF-fitting method is that, if a proper PSF model has been derived, it is possible to measure the magnitudes of each star avoiding the contamination from the surrounding, possibly brighter, stars and accurately measuring the background level in order to assign a proper photometric uncertainty to the measurements.

In the resulting catalog of stars obtained after the PSF-fitting, we usually choose to include only stars that have been detected at least in half the images of each photometric filter. Then, for each star, the magnitudes estimated in different images are homogenized, and their weighted mean and standard deviation are finally adopted as the star mean magnitude and its related photometric error (see Ferraro et al., 1991, 1992). However, in order to perform variability studies, for each source we also keep the homogenized magnitudes measured in each frame in all the available filters.

The catalogs of stars obtained following this procedure contain instrumental magnitudes. Their calibration can be performed by using the following simple equation (Holtzman et al., 1995):

$$(2.24) \qquad m_{cal} = m_{instr} + 2.5\log(t_{exp}) + ZP + AC$$

where $m_{cal}$ and $m_{instr}$ are the calibrated and instrumental magnitudes, $t_{exp}$ is the exposure time of a given observation, $ZP$ is the zero point needed to report the magnitude to a particular photometric system (such as VEGAMAG for HST observations; Sirianni et al. 2005) and $AC$ is the aperture correction that quantifies the stellar flux lost during the PSF-fitting procedure due to the truncation of the PSF wings (unavoidable for computational reasons). Alternatively, if a catalog of photometric standards is available, the calibration can be easily performed by

cross-correlations of the catalogs.

The first necessary condition for a star to be considered as a possible optical counterpart is to be located in a position compatible with that of the MSP, determined with high precision ($\lesssim 0.1"$) through the radio timing. Therefore, before starting the analysis of the candidates, it is mandatory to obtain a high-accuracy astrometric solution for the stars in the cluster. This is usually done by cross-correlating the instrumental positions of stars with the absolute ones ($\alpha$ and $\delta$) reported in the most updated catalogs of astrometric standard stars (such as 2MASS, UCAC4; Cutri et al. 2003; Zacharias et al. 2013).

**CMD Position**

An anomalous position of a candidate star in the CMD is a valid indicator that it could be the MSP companion star. Indeed, since these stars have been going through to an anomalous evolution and could be subjected to perturbations due to the NS emission and gravitational field, their position in the CMD is not usually expected to be compatible with that of the classical stars of the cluster. From the analysis of the CMD position it is possible to infer the degenerate or non-degenerate nature of the companion star (see Figure 2.4). In fact, a typical He white dwarf (WD) companion will be located along the known WD cooling sequences, while non-degenerate objects will be usually more closely located to the main sequence. Moreover, comparing the position of the companion star with that predicted by stellar evolutionary models, it is possible to estimate its mass, radius, age and bolometric luminosity. These results are quite solid for the case of He WD companions, while in the case of non-degenerate companions, the position in the CMD could be heavily faked due to a perturbed, Roche Lobe filling companion. Measuring the mass in such a way usually lead to overestimated values (e.g. Pallanca et al., 2010; Mucciarelli et al., 2013).

**Light Curve Variability**

The strongest confirmation on the companion nature of the candidate counterpart is given by stellar variability with a periodicity compatible with that of the binary orbital period. Indeed, the interaction between the two objects likely results in an observable stellar flux variability, especially in the case of high inclination angle orbital planes.

The analysis of the companion star light curve is an useful tool to study the physical properties of the companion and of the intra-binary system, i.e. how the companion star and the MSP closely interacts and how this alters the properties and evolution of the secondary star, otherwise comparable to that of the other stars in the cluster.

In the following chapters we will adopt the formalism according to which the reference time used to fold the optical measurements is the PSR ascending node. Therefore orbital phases equal to zero and 0.5 correspond to the PSR ascending and descending node, respectively, while
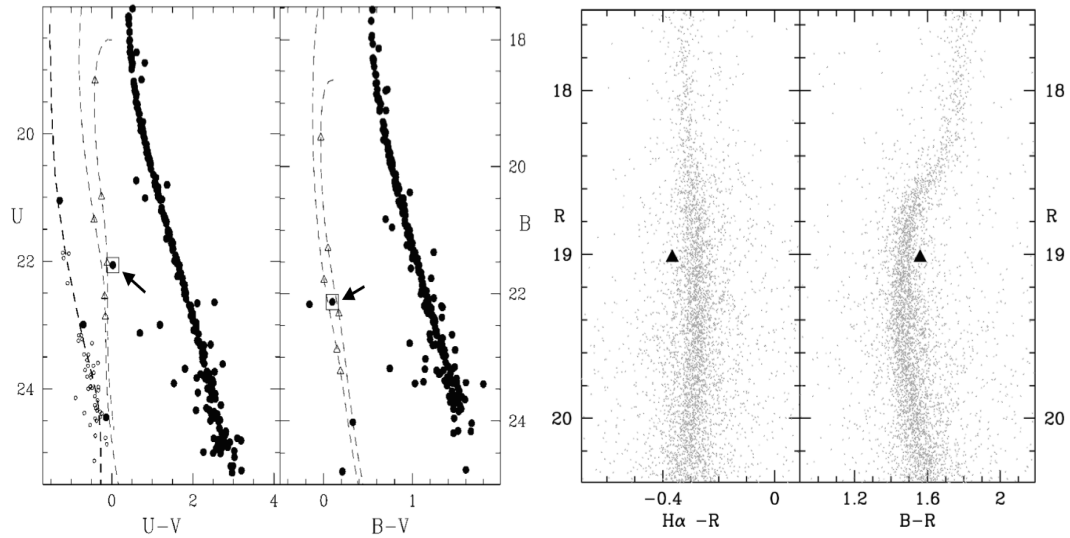
Figure 2.4: *Left panel:* CMD position of the He WD companion to PSR J1911−5958A in NGC 6752 (Ferraro et al., 2003a). *Right panel:* CMD position of the companion star to the redback system PSR J1701−3006B in NGC 6266 (Cocozza et al., 2008).

orbital phases equal to 0.25 and 0.75 correspond to the PSR superior and inferior conjunction, respectively.

The typical light curve of MSP companions can be classified in two main categories. The first one includes light curves with a single minimum and a single maximum structure, usually in correspondence of the PSR superior and inferior conjunctions. This structure is usually interpreted as the result of the heating of the companion side exposed to the PSR injected flux. Indeed, during the PSR inferior conjunction, the stellar side exposed to the PSR is observed, while it is at least partially hidden by the back side of the star during the PSR superior conjunction. The luminosity difference between the minimum and the maximum is a function of the physics of irradiation, properties of the companion star, as well as the orbital inclination angle at which the binary is seen. An example of this curve is reported on the left panel of Figure 2.5.

The second category includes those light curves that show two maxima and two minima, the formers in correspondence of the PSR ascending nodes and the latter in correspondence of the two conjunctions. Thus the companion appears brighter when its lateral sides are observed, while it appears fainter when the back side and the side facing the PSR are observed. This light curve structure is interpreted as the result of the tidal distortion of the companion star that is filling its Roche Lobe and therefore its surface is drop-like structured (Figure 2.6). Tidal distortions make surface gravity to change in different points of the stellar surface, reaching minimum values in the region facing the PSR and on the opposite side. This results in a stellar variability since the emitted flux ($F$) is proportional to the stellar surface temperature as $F \propto T^4$ and to the surface gravity as $F \propto g$, and thus $T \propto g^{1/4}$ (von Zeipel, 1924). The maximum values of the
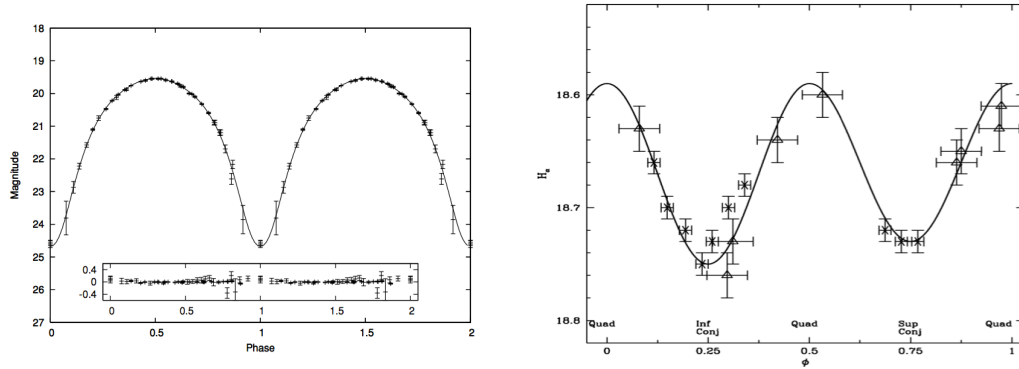
Figure 2.5: *Left panel:* PSR 1957+20 light curve of the companion star from Reynolds et al. (2007) as an example of single minimum and single maximum structured light curves (note that here the authors used as reference time the PSR superior conjunction instead of the PSR ascending node). *Right panel:* Light curve of PSR J1701-3006B from Cocozza et al. (2008) as an example of double minima and double maxima curves.
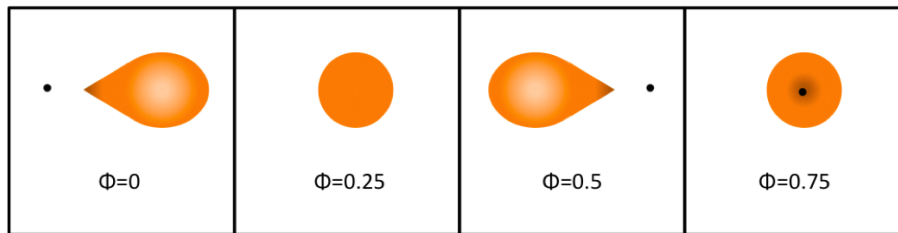


Figure 2.6: Schematic representation of the effects of tidal distortion on MSP companion stars. The system is seen perfectly edge-on. The black dot corresponds to the MSP, while the companion is the orange drop-like structure. Brighter colors correspond to higher temperatures. Credit: Pallanca (2014).

surface gravity, and thus of the temperature, are located at the stellar lateral side, visible at the orbital nodes, while the minimum values are located at the front and back ends of the drop-like structure, and thus during the conjunctions. Asymmetric minima can be the result of the different surface gravities between the stellar front and back side, as well as heating of the stellar side facing the MSP. An example of this light curve is reported in the right panel of Figure 2.5.

### 2.3.2 Spectroscopy of the Companion Stars

We will briefly describe here those studies that can be performed with spectroscopic observations of the companion stars. We will not enter in the details of the procedures, since they are beyond the goal of this chapter and thesis.

Following the discovery and the photometric analysis of the companion star, a spectroscopic follow-up can be performed if the star is bright enough to provide high quality spectra. Such
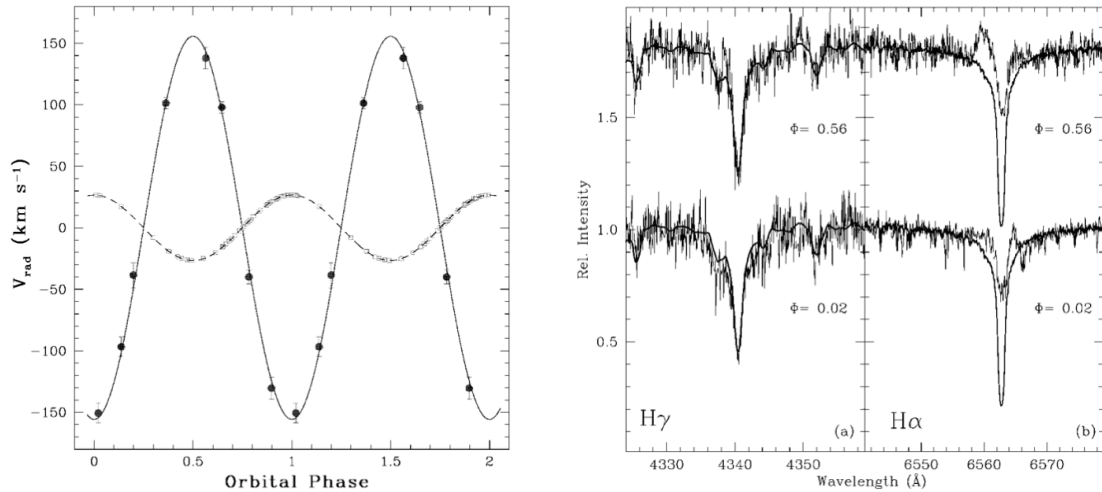
Figure 2.7: *Left panel:* Radial velocity curve of the companion to PSR J1740-5340A (black points) and of the PSR itself (open squares). Taken from Ferraro et al. (2003c). *Right Panel:* Optical spectra of the companion star to PSR J1740−5340A (Sabbi et al., 2003b) at two different orbital phases and for two different Balmer spectral lines. The solid black line is a reference spectrum for a classical sub-giant star of the cluster.

a follow-up is useful to study both the kinematic and chemistry of the system. The kinematic analysis is aimed at measuring the radial velocities of the companion star during the orbit. This can be done measuring the Doppler shifts of the spectral lines with respect to their rest position at different orbital phases. The radial velocity curve will have the same periodicity of the orbit and an average velocity corresponding to the line of sight velocity of the binary moving within the cluster (see left panel of Figure 2.7). This, together with the radial velocity curve of the MSP, obtained through radio timing, allows to measure the mass ratio between the two components of the binary system. The ratio can be used together with other mass estimates, such as the total mass, the mass function, and eventual inclination angle estimates (e.g. from the light curve analysis) to precisely constrain the mass of the two objects.

The chemical analysis is instead aimed at measuring the chemical properties of the stellar surface (e.g. Sabbi et al., 2003a,b). Of particular interest are the Balmer series line, since the presence of emission, instead of absorption, or of absorption with phase-dependent structures, allow to study the presence of ionized material in the intra-binary and surrounding space (see right panel of Figure 2.7). If the companion star is a WD, the comparison of the observed spectra with simulated ones allows to infer the physical properties of the WD (such as temperature, surface gravity, radius and mass). Moreover, since these stars have been subjected to the removal of the external envelope as a consequence of the accretion and possibly of subsequent ablation, the observed chemical abundances give us a direct view on the regions where the stellar chemical composition has been modified by thermonuclear reactions, thus shedding light on the original

48

properties of the star (Mucciarelli et al., 2013).

CHAPTER

3

## DISCOVERY OF THREE NEW MILLISECOND PULSARS IN TERZAN 5

We report on the discovery of three new millisecond pulsars (namely J1748−2446aj, J1748−2446ak and J1748−2446al) in the inner regions of the dense stellar system Terzan 5. These pulsars have been discovered thanks to a method, alternative to the classical search routines, that exploited the large set of archival observations of Terzan 5 acquired with the Green Bank Telescope over the last 5 years (from 2010 to 2015). This technique allowed the analysis of stacked power spectra obtained by combining ∼ 215 hours of observation. J1748−2446aj has a spin period of ∼ 2.96 ms, J1748−2446ak of ∼ 1.89 ms (thus it is the fourth fastest pulsar in the cluster) and J1748−2446al of ∼ 5.95 ms. All the three millisecond pulsars are isolated and currently we have timing solutions only for J1748−2446aj and J1748−2446ak. For these two systems, we evaluated the contribution to the measured spin-down rate of the acceleration due to the cluster potential field, thus constraining the intrinsic spin-down rates, which are in agreement with those typically measured for millisecond pulsars in globular clusters. Our results increase to 37 the number of pulsars known in Terzan 5, which now hosts ∼ 25% of the entire pulsar population identified, so far, in globular clusters.

## 3.1 Introduction

To date, the exotic millisecond pulsar (MSP) zoo in globular clusters (GCs) comprehend 146 pulsars (PSRs) in 28 GCs[1]. However, population synthesis simulations clearly showed that a very large population of several thousand MSPs is still to be unveiled (Bagchi et al., 2011; Chennamangalam et al., 2013; Turk, Lorimer, 2013; Hessels et al., 2015). The discovery of several GCs emitting also in the $\gamma$-ray corroborates this results, since such an emission can be exclusively due to a population of MSPs (Abdo et al., 2010; Zhang et al., 2016).

The number of MSPs identified in GCs per year decreased abruptly after 2011, thus showing the limit in performance and sensitivity reached by the current generation of radio telescopes. However, for more than one decade, GCs have been routinely observed at radio wavelength in order to obtain long-term timing solutions of the identified MPSs. This resulted in the production of a large archive of tens of observations of the same region of the sky. The work presented here is aimed at showing the large possibilities of finding new PSRs by exploiting these huge archival data sets. At odds with traditional PSR searches, which are based on the analysis of a single and long time sequence of data (see Chapter 2.1), we present here a method to search for PSRs by incoherently stacking the power spectra obtained from all the available observations. A similar procedure has been already successfully implemented in M15 by Anderson (1993), in Terzan 5 by Sulman et al. (2005), leading to the discovery of three isolated MSPs (namely J1748−2446af, J1748−2446ag and J1748−2446ah), and in 47 Tucanae by Pan et al. (2016). All these PSRs are isolated. Indeed, due to the Doppler shifts of the spin frequency induced by the PSR motion in binary systems, this method is only efficient to discover faint isolated PSRs or long period binary PSRs, the latter being unlikely to survive in GCs.

Among the Galactic GCs, Terzan 5 turned out to be the most amazing MSP factory. In fact, 34 MSPs have been identified so far in this system (Ransom et al., 2005; Hessels et al., 2006; Prager et al., 2017, Ransom et al. 2017, in preparation), which is about ∼ 23% of the total number of MSPs identified in GCs. Terzan 5 is, indeed, one of the most intriguing stellar system in the Galaxy. Ferraro et al. (2009, 2016) found out that this system is probably not a genuine GC, but more likely the pristine remnant of a building block of the Galactic bulge, which was originally much more massive than today (Lanzoni et al., 2010).

Here we present the identification of three new MSPs in Terzan 5. In Section 3.2 we present the dataset and the stacking procedures that led us to the discovery of the new MSPs. In Section 3.3 we describe the main properties of these new systems and their timing solutions. Finally, in Section 3.4 we constrain their acceleration and some of their physical parameters.

---

[1]see http://www.naic.edu/~pfreire/GCpsr.html

## 3.2 Observations and Data Analysis

### 3.2.1 Dataset and initial data reduction

The work presented here has been performed by using 33 archival observations of Terzan 5 obtained with the 100-m Robert C. Byrd Green Bank Telescope (GBT) from August 2010 to October 2015. Observations were acquired at 1.5 GHz and 2.0 GHz using 800 MHz of bandwidth, although radio frequency interference (RFI) excision reduced the effective bandwidth to ∼ 600 MHz. Only one observation was obtained at 820 MHz using 200 MHz of bandwidth. Observation lengths vary from a minimum of 1.5 hours to 7.5 hours, the latter typical for the majority of the observations. The total observation length, resulting from the stack of all these observations, is of about 9 days (∼ 215 hours).

The data recorded by GUPPI were Full Stokes with 10.24 $\mu$s sampling and 512 channels, each coherently dedispersed in hardware to a dispersion measure (DM) of 238 pc cm$^{-3}$, which is close to the cluster average. The total intensity (i.e. sum of two orthogonal polarizations) was extracted from those data and downsampled to 40.96 $\mu$s resolution for incoherent dedispersion into 23 DM trials.

The data have been processed using the PRESTO software suite (Ransom et al., 2002). We obtained 22 time series per observation ranging from a DM of 233 pc cm$^{-3}$ to 244 pc cm$^{-3}$ and spaced by 0.5 pc cm$^{-3}$, plus an additional time series at a control DM of 100 pc cm$^{-3}$. The time series have been transformed to the barycenter of the solar system using TEMPO. For each sample of the time series of each observation, we subtracted the mean of all the channels (i.e. we subtracted the DM=0 pc cm$^{-3}$ time series) and excised some interference by removing samples with values higher than $4\sigma$, where $\sigma$ is the standard deviation of all the sample values. Since we aim at stacking together the power spectra of observations of different lengths, we manually added samples with null values to the time series of shorter length, thus obtaining time series of length equal to that of the longest one. We then applied a fast Fourier transform to all the time series and squared the complex amplitudes to obtain the power spectra. Finally, in the power spectra, we ignored all the spectral bins expected to contain the powers of all the known Terzan 5 PSRs and their harmonics (also accounting for the shifts due to the binary PSRs orbital motions). We also excised the most relevant RFI.

### 3.2.2 Stacking search procedures

First of all, we normalized all the available power spectra dividing the spectral powers by the local median value. Then, we summed the 33 individual daily power spectra into a stacked power spectrum for each of the 22 DM trials and the control DM. These final stacked power spectra are nearly chi-squared distributed with 66 degrees of freedom. In all these stacked spectra, we performed an harmonic sum, by summing to each power bin the powers of the corresponding
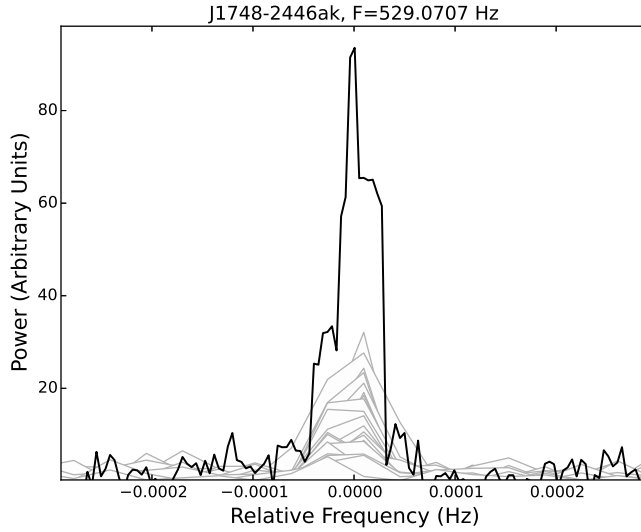
Figure 3.1: Power spectrum around the region of the newly discovered PSR J1748−2446ak (Ter5ak). We plotted in black the stacked and harmonic summed power spectrum obtained from ∼ 215 hours of archival observations, while in shaded gray we plotted the power spectra obtained from the single daily observations. The power in the stacked spectrum is spread over more bins than for single observations due to the effect of the harmonic sum.

harmonic, from the second up to the eighth. This has been done to further enhance the spectral powers of the still unidentified PSRs. At the end of this, we had 22 stacked power spectra, plus the one at the control DM. In order further remove periodic interference that can be still persistent in high DM spectra, we subtracted from each stacked power spectrum the control stacked spectrum obtained at DM=100 pc cm$^{-3}$. In this way, a large fraction of RFI, present in both the control and the science power spectra, are removed, leaving the signal of the still undiscovered PSRs virtually unaffected.

In order to illustrate the effectiveness of the method, in Figure 3.1 we compare the stacked power spectrum for one of the newly discovered MSPs, with that obtained from a single observation where this MSP has a high signal to noise ratio (S/N). It can be clearly seen how the stacking procedure greatly enhances the spectral powers of such a faint object.

The next step is to select, in the stacked power spectra, the periodic signals that likely originate from a real PSR instead of from RFI. To do this, we selected in the power spectra all the peaks above 4.5$\sigma$ ($\sigma$ is the standard deviation of the spectral powers) and saved them into a candidate file. We ended up with 22 candidates files, one per DM, each one containing ∼ 13000 candidate. Therefore the total number of candidates is about $3 \times 10^5$. We then applied a KD-tree algorithm to perform a selection of all these candidates. In fact, in the DM-frequency phase space, PSR candidates are expected to be closely segregated around their DM and spin frequency. On the other hand, RFI can appear in a large range of DMs, also with slightly different spin frequencies.
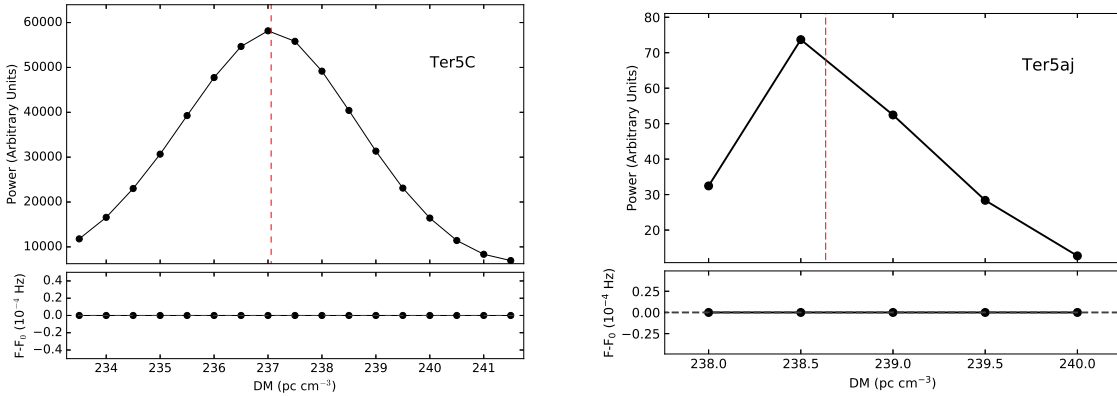
Figure 3.2: *Left Panel:* Spectral powers of a candidate PSR, corresponding to J1748−2446C (Ter5C), obtained from the stacked power spectra. The powers are plotted as a function of the DM as obtained from the KD-tree algorithm (see text). The red dashed vertical line is the MSP true DM as derived from its timing solution. A the bottom of the top panel the frequency difference across the different DMs in which the candidate has been found are plotted. In this case, the candidate has the same frequency in all the DMs, as expected from a real PSR. *Right Panel:* same as in the left panel, but for the newly discovered PSR Ter5aj.

We used the KD-tree routine included in the scipy package[2]. Briefly, we built a 2D tree in a DM-frequency space. Then, for each candidate, we searched for the 1000 closest neighbors and selected only those with a spin frequency compatible (within a tolerance of $10^{-5}$ Hz) with that of the candidate. Since the PSR signal is expected to be observed at contiguous DM values with an almost Gaussian distribution of powers around the true DM value, we selected as good candidates only those whose closest neighbors are found at contiguous DMs and with a maximum in the spectral power vs DM space. As an example, we show in Figure 3.2 the output of the KD-tree procedure for the case of the known PSR J1748−2446C (Ter5C). As can be seen, the algorithm found, for a candidate corresponding to Ter5C, neighbors at contiguous DMs, with a peak in the spectral powers very close to the MSP's true DM value. Moreover, the spin frequency does not show any variation at different DMs, as expected from a real PSR. Applying this procedure to our candidates, we discarded ∼ 97% of them and ended up with only ∼ 100 possible PSR candidates. These have been individually analyzed, folding the single observations at the candidate frequency and DM corresponding to that of the maximum spectral power, allowing also a search in spin period, spin period derivative and DM in order to maximize the S/N.

---

[2]https://docs.scipy.org/doc/scipy-0.18.1/reference/generated/scipy.spatial.KDTree.htmlscipy.spatial.KDTree

## 3.3 Results

The method described in the previous section allowed us to discover three previously unknown MSPs in Terzan 5: J1748−2446aj, J1748−2446ak and J1748−2446al (hereafter, Ter5aj, Ter5ak and Ter5al, respectively). We plot in Figure 3.3 the average pulse profiles and the signals as a function of time for these three new MSPs in the brightest individual days. Moreover, we have been able to blindly re-detect all the other isolated MSPs known in the cluster[3].

The stacking technique described in this work is of particular effectiveness in a high DM system like Terzan 5. Indeed, for typical 1.4 GHz observations, the high DM and very small scintillation bandwidth allow us to average, in the stacked power spectra, over many scintles, making negligible any effect due to diffractive scintillation. The only variability appreciable in the different terms of the power spectra sum is due to refractive scintillation, which can affect the flux densities of PSRs by typically up to a factor of ∼ 2. On the other hand, in a low DM cluster such as, for example, 47 Tucanae, diffractive scintillation can change the measured flux densities by more than an order of magnitude. Therefore few of the power spectrum sums will have high values, while most of them will have much lower values, thus diluting the S/N of the final sum.

### 3.3.1 Ter5aj

Ter5aj or J1748−2446aj has been discovered with a maximum spectral power at DM = 238.50 pc cm$^{-3}$ (see Figure 3.2). Folding the single observations, we have been able to clearly identify it and confirm its PSR nature in all the 33 GUPPI observations. As can be seen from the left panel of Figure 3.3 (see also the top panel of Figure 3.6), Ter5aj presents a double peaked pulse shape, where the two peaks are separated by ∼ 0.3 in phase. We extracted the pulse times of arrival (TOAs) with the get_TOAs routine within PRESTO, using a double Gaussian template, created by fitting the pulses obtained in the observations where this object has the highest S/N (see left panel of Figure 3.3). We phase connected all the ∼ 6 years of data using standard procedures with TEMPO[4]. The timing solution is tabulated in Table 3.1, the post-fit timing residuals are reported in the top panel of Figure 3.4 and the averaged pulse profile, obtained by summing all the daily detections, is reported in the top panel of Figure 3.6.

Ter5aj is an isolated MSP with a spin period of 2.96 ms and a DM = 238.63 pc cm$^{-3}$, very close to the cluster mean value. It is located 10.4" north from the cluster gravitational center (Lanzoni et al. 2010, see Figure 4.3). Its spin period derivative is partially contaminated by the effect of the MSP motion in the cluster potential field. We will analyze this in more detail in Section 3.4.

---

[3] To do this and to obtain the top panel of Figure 3.2, we re run the whole procedure without excising the signal of the known PSRs.

[4] http://tempo.sourceforge.net
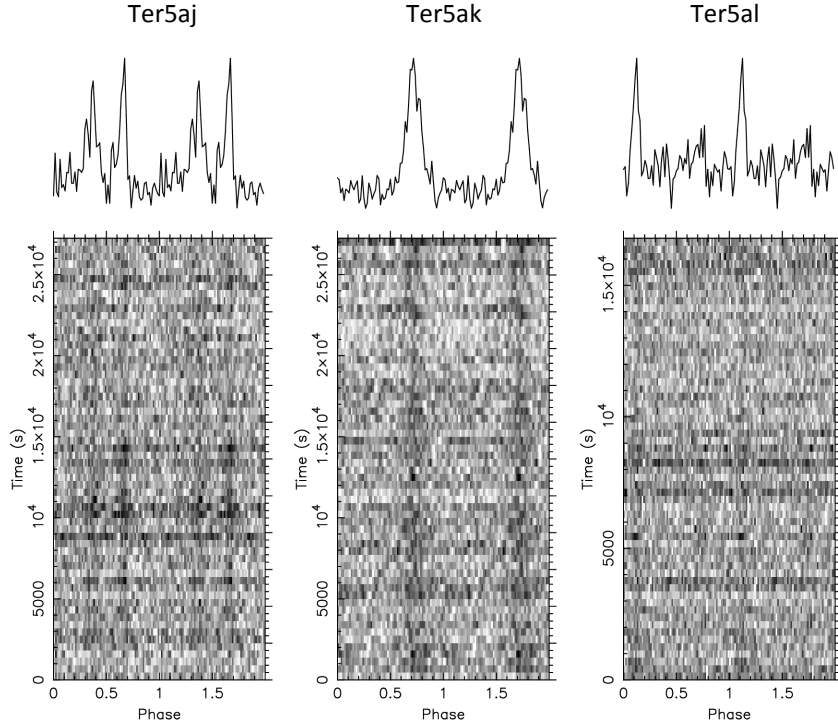
Figure 3.3: *Top panels:* Averaged pulse profiles of the best detections of Ter5aj (on the left), Ter5ak (in the middle) and Ter5al (on the right). *Bottom panel:* Intensity of the signal (gray scale) as a function of the rotational phase and time for each MSP.

We roughly estimated the PSR mean flux density using again the radiometer equation on daily detections. The values so obtained have been calibrated by comparison with those obtained applying the same method to other three isolated MSPs (namely Ter5R, Ter5S and Ter5T), for which measurements made referencing a flux calibrator are available (Ransom et al. 2017, in preparation). The average values of both the L-band and S-band flux densities are reported in Table 3.1. The typical flux density of this MSP is of the order of that measured for the other faint isolated MSPs of this cluster (Ransom et al. 2017, in preparation).

### 3.3.2  Ter5ak

Ter5ak or J1748−2446ak has been discovered with a maximum stacked spectral power at DM = 236.50 pc cm$^{-3}$. The PSR nature of this candidate has been confirmed by folding the single observations, where it turned out to be visible in almost all of them. We managed to obtain a full timing solution for this object  using similar methods described for Ter5aj, except that we obtained the initial timing solution using the TEMPO based phase-connection routine available at `https://github.com/pfreire163/Dracula` (Freire, Ridolfi, 2018). The timing solution is tabulated in Table 3.1, the post-fit residuals are reported in the bottom panel of Figure 3.4 and

Table 3.1: Timing parameters for the new Terzan 5 MSPs. Numbers in parentheses are the $1\sigma$ uncertainties in the last digits quoted; the time units are TDB and the adopted terrestrial time standard is UTC(NIST).

| Pulsar | Ter5aj | Ter5ak |
|---|---|---|
| Timing Parameters | | |
| Right ascension, $\alpha$ (J2000) ........................... | 17:48:05.0119(2) | 17:48:03.6860(2) |
| Declination, $\delta$ (J2000) .............................. | $-24$:46:34.85(7) | $-24$:46:37.83(8) |
| Spin frequency, $F$ (Hz) ............................. | 337.96234149929(4) | 529.07066473956(4) |
| Spin frequency derivative, $\dot{F}$ ($10^{-14}$ Hz s$^{-1}$) ....... | $-1.61313(7)$ | $-2.4771(2)$ |
| Spin frequency second derivative, $\ddot{F}$ ($10^{-25}$ Hz s$^{-2}$) | $-1.8(4)$ | - |
| Dispersion measure, DM (cm$^{-3}$ pc) ................. | 238.633(6) | 236.705(5) |
| MJD range ........................................ | 55423-57573 | 55423-57573 |
| Epoch (MJD) ...................................... | 56498 | 56498 |
| Data span (yr) .................................... | 5.9 | 5.9 |
| Number of TOAs ................................... | 42 | 31 |
| Residuals RMS ($\mu$s) ................................ | 12.51 | 17.03 |
| Reduced $\chi^2$ value ................................... | 1.00 | 1.04 |
| Solar system ephemeris model ..................... | DE436 | DE436 |
| EFAC ............................................. | 1.14 | 1.15 |
| Derived Parameters | | |
| Angular offset from cluster centre, $\theta_{\perp}$ (") ........... | 10.4 | 17.4 |
| Spin period, $P$ (ms) ................................ | 2.9589095505841(3) | 1.8901066845055(1) |
| Spin period derivative, $\dot{P}$ ($10^{-19}$) ................. | 1.41232(6) | 0.88495(6) |
| Spin period second derivative, $\ddot{P}$ ($10^{-30}$ s$^{-1}$) ....... | 1.6(3) | - |
| Intrinsic spin period derivative, $\dot{P}_{int}$ ($10^{-19}$) ....... | $< 4.9$ | $< 2.1$ |
| Characteristic age, $\tau_c$ (Myr) ....................... | $> 98$ | $> 142$ |
| Surface magnetic field, $B_0$ ($10^8$ G) ................. | $< 12.0$ | $< 6.4$ |
| Spin-down luminosity, $L_{SD}$ ($10^{35}$ erg s$^{-1}$) ........ | $< 7.3$ | $< 12.4$ |
| Flux density at 1.5 GHz, $S_{1.5}$ ($\mu$Jy) ............... | 34 | 30 |
| Flux density at 2.0 GHz, $S_{2.0}$ ($\mu$Jy) ............... | 18 | 16 |
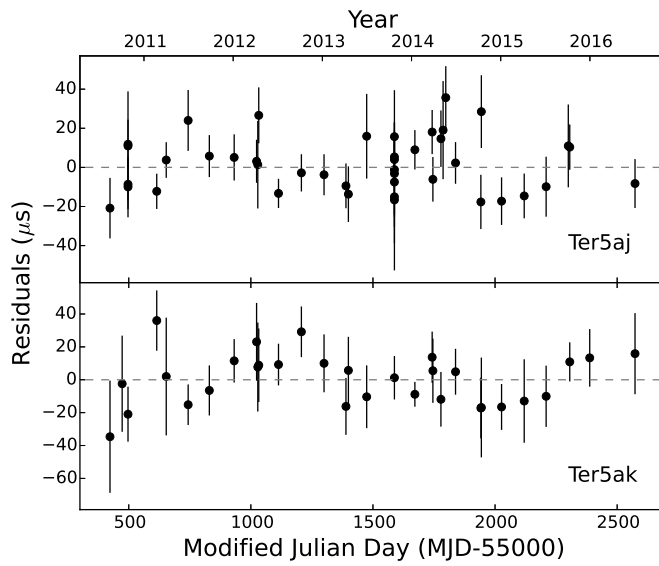
Figure 3.4: Timing residuals for Ter5aj (top panel) and Ter5ak (bottom panel).
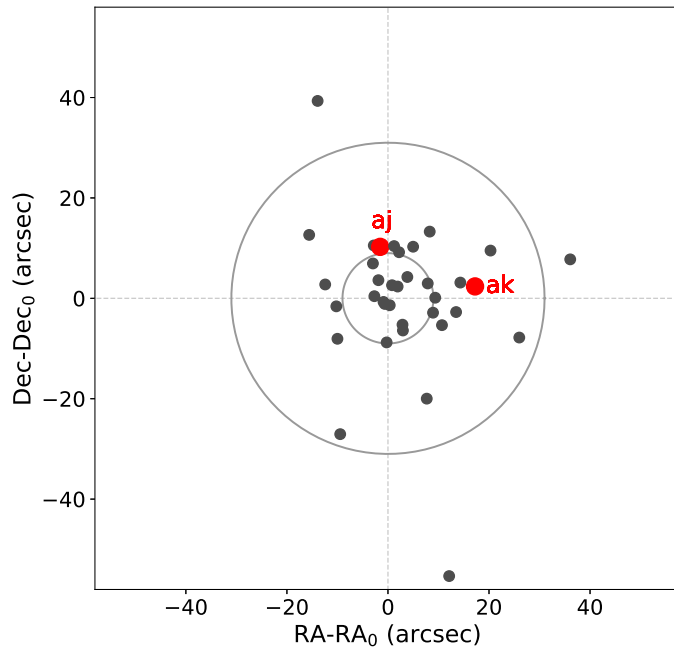


Figure 3.5: Positions of Ter5aj and Ter5ak with respect to the cluster gravitational center and to the other MSPs in the cluster. The inner and outer circles are the cluster core and half mass radius, respectively (Lanzoni et al., 2010).

the averaged pulse profile in the middle panel of Figure 3.6.

Ter5ak is also an isolated MSP and it has a spin period of ~ 1.89 ms, hence it is the fourth fastest MSP in Terzan 5 and the fifth fastest among all the GC PSRs. Its DM of 236.707 pc cm$^{-3}$ is well within the range covered by the other PSRs in the cluster. Its position with respect to the other cluster MSPs is reported in Figure 4.3, where it can be seen that it is located at about 17.4" east from the cluster center. As for Ter5aj, its spin period first derivative is clearly contaminated by its motion in the cluster potential field (see Section 3.4). The average flux density is also in this case of the order of that of the faintest isolated MSPs of this cluster.

### 3.3.3  Ter5al

Ter5al is the last MSP identified in our analysis, with a spectral power peaked at DM = 236.50 pc cm$^{-3}$. We have been able to reveal this object in only ~ 20 observations, being under the detection limit in all the others. In the right panel of Figure 3.3, we report the detection plot of the observation where Ter5al has the highest S/N. To date we have not been able to obtain a timing solution for this system, likely because of the insufficient number of good detections. In the ~ 20 detections we found no evidence of acceleration, thus it is likely another isolated system. Ter5al has a spin period of ~ 5.95 ms. We determined its DM by measuring the pulse TOAs in different sub-bands of the two brightest L-band observations and we found DM = 236.48(3) pc cm$^{-3}$.

The averaged pulse profile is reported in the bottom panel of Figure 3.6. This MSP turns out to be extremely faint. Indeed its average flux density is of only ~ 8 $\mu$Jy in L-band and ~ 6 $\mu$Jy in S-band, making this PSR the faintest in the cluster and also explaining the small number of good detections.

## 3.4  Accelerations and physical parameters

In this section we derive some constraints on the accelerations and on the main physical parameters of Ter5aj and Ter5ak, the two new MSPs for which we have been able to obtain a timing solution.

For the case of MSPs in GCs, the measured spin period derivative ($\dot{P}_{meas}$), derived through timing, does not represent a direct measurement of the MSP intrinsic spin-down, since it is the combination of different contributions (see, e.g., Phinney, 1993). Indeed, any motion of a PSR with respect to the observer produces a change of the observed spin period. In the case of GCs, the MSP motion in the cluster potential field induces a change that can be large enough to match or even exceed the value due to the intrinsic spin-down. Following Phinney (1993), $\dot{P}_{meas}$ can be written as follows:

$$(3.1) \qquad \left(\frac{\dot{P}}{P}\right)_{meas} = \left(\frac{\dot{P}}{P}\right)_{int} + \frac{a_{z,GC}}{c} + \frac{a_g}{c} + \frac{a_s}{c}$$
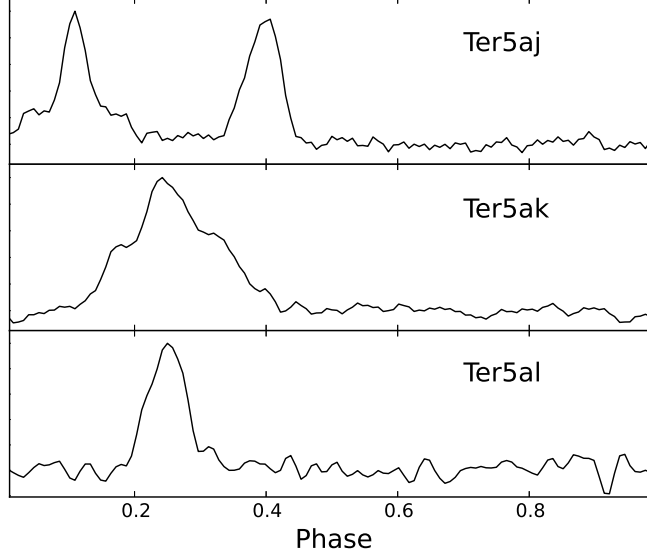
Figure 3.6: Averaged pulse profile of Ter5aj (top panel), Ter5ak (middle panel) and Ter5al (bottom panel), obtained by coherently summing all the GUPPI detections of the MSPs.

where $(\dot{P}/P)_{int}$ is the ratio between the intrinsic spin-down and the PSR spin period, $a_c$ is the line of sight acceleration due to the GC potential field, $a_g$ is the acceleration due to the Galactic potential, $a_s$ is an apparent centrifugal acceleration (the so-called Shklovskii effect; Shklovskii, 1970) and $c$ is the speed of light. The two latter terms are expected to be negligible with respect to the former two, and following Prager et al. (2017, and references within) we know that $a_g \approx 5.1 \times 10^{-10}$ m s$^{-2}$ and $a_s \sim 4.2 \times 10^{-12}$ m s$^{-2}$. According to Freire (2005) and Prager et al. (2017), the acceleration along our line of sight ($z$) due to the cluster potential ($a_{z,GC}$) can be written as:

$$(3.2) \qquad a_{z,GC}(z,x) = -3.5 \times 10^{-7} \left( \frac{\rho_0}{10^6 \, \mathrm{M_\odot \, pc^{-3}}} \right) \left( \frac{z}{0.2 \, \mathrm{pc}} \right) \left( \sinh^{-1}(x) - \frac{x}{\sqrt{1+x^2}} \right) x^{-3} \ \mathrm{m \, s^{-2}}$$

where $\rho_0$ is the cluster core density and $x \equiv r/r_c^{NS}$, where $r_c^{NS}$ is the cluster core radius of the neutron star population and $r = \sqrt{r_\perp^2 + z^2}$ is distance of the PSR from the cluster center. In the latter formula, $r_\perp = D\theta_\perp$ is the PSR projected distance from the cluster center, where D is the distance of the cluster from the Sun and $\theta_\perp$ the PSR angular offset from the cluster center.

Prager et al. (2017) used the ensemble of Terzan 5 MSPs, including Ter5aj and Ter5ak, to derive the cluster physical properties. They found $\rho_0 = 1.58 \pm 0.13 \times 10^6$ M$_\odot$ pc$^{-3}$ and $r_c^{NS} = 0.16 \pm 0.01$ pc. Given the angular offsets of Ter5aj and Ter5ak from the cluster center (see Table 3.1) and the cluster distance of 5.9 kpc (Lanzoni et al., 2010), we measured the possible line of sight accelerations of these two MSPs for different values of the line of sight distance $z$. We found that the maximum allowed accelerations are $\pm 3.4 \times 10^{-8}$ m s$^{-2}$ and $\pm 2.0 \times 10^{-8}$ m s$^{-2}$ for

Ter5aj and Ter5ak, respectively. We used these values to constrain, starting from Equation 3.1, the MSP intrinsic spin-down rates and, consequently, the characteristic ages, surface magnetic fields and spin-down luminosities. All these values are tabulated in Table 3.1 and, for both the MSPs, are in agreement with those typically expected for old and recycled MSPs.

## LONG-TERM TIMING OF THE MILLISECOND PULSARS IN THE GLOBULAR CLUSTER M28

Here we present the update of the timing solutions of 9 of the 12 millisecond pulsars in the globular cluster M28. The long-term timing solutions, covering a time span of about 10 years, allowed us to precisely measure the positions, spin and orbital parameters of these systems. Indeed, for most of the them we obtained accurate measurements of both the second spin period derivative and the orbital period derivative. Several relativistic effects have been observed for the case of M28C and M28D, allowing mass measurements that suggest that M28C companion star is a classical He white dwarf, while that of M28D could be either a massive He white dwarf or a low-mass C-O white dwarf. Moreover, the measurements of the pulsar proper motions allowed to constrain the cluster absolute proper motion and hence its orbit in the Galaxy gravitational field. It turns out that M28 spends a large fraction of its life orbiting within the Galactic bulge, despite its current location outside of it. Finally, the spin period derivatives, together with the orbital period derivatives of binary systems, have been used to constrain the pulsar accelerations in the cluster gravitational field and consequently their intrinsic spin-down rate. It turned out that a mass distribution based on a classical King model is able to account for the measured pulsar accelerations.

Part of the results presented here will be adapted and published by "Stairs et al. 2018, in preparation".

## 4.1 Introduction

M28 (NGC 6626) is a Galactic globular cluster (GC) with an intermediate central density around $10^5 \, \mathrm{M_\odot \, pc^{-3}}$ (see Section 4.6) and a relatively high metallicity ([Fe/H= $-1.32$], Harris 1996, 2010 edition) for a stellar system orbiting outside the Galactic bulge. It is located at 5.5 kpc from the Sun in the direction of the Galactic center and it is characterized by a core radius $r_c = 10.5 \pm 0.3''$, a half-mass radius $r_{hm} = 120 \pm 20''$ and a concentration parameter $c = 2.01 \pm 0.07$ (Miocchi et al., 2013).

It is the first GC where a millisecond pulsar (MSP) was discovered (Lyne et al., 1987) and it is currently known to be the third cluster in terms of MSP abundance after Terzan 5 and 47 Tucanae. Indeed 12 MSPs have been discovered, so far, in this system (Stairs et al., 2006; Bogdanov et al., 2011). Furthermore, a total number of 46 X-ray sources have been also identified within the cluster core radius (Becker et al., 2003), thus further probing that the environment of this cluster is particularly suitable for creating exotic binaries.

Among the 12 MSPs detected in this cluster, 4 are isolated (namely M28A, M28B, M28E and M28F) while the others are binaries. M28A is a very young and energetic pulsar (PSR), whose pulsation has been firmly identified also in the X-ray and $\gamma$-rays (Johnson et al., 2013). Two of the eight binaries, namely M28C and M28D, have highly eccentric orbits, and the latter is also a slowly rotating PSR located on a very long and unusual orbit of $\sim 1$ month. M28H is a redback (RB) system while M28I is the first discovered member of the transitional MSP family (Papitto et al., 2013). M28G, J and L are likely non eclipsing black-widow (BW) systems and finally M28K is the only canonical MSP. The optical counterparts of M28H and M28I have been identified by Pallanca et al. (2010) and Pallanca et al. (2013a), respectively. Finally, 7 of them have been identified by Chandra at X-ray wavelengths (Bogdanov et al., 2011).

Since the discovery of its PSRs, M28 has been routinely observed with the 100-m Green Bank Telescope (GBT) in order to obtain long-term timing solutions for all these systems. Observations acquired from 2006 to 2010 provided the initial timing solutions, including precise positions, spin and orbital parameters for almost all the systems, including a first measurement of the rate of periastron advance of M28C (Stairs et al., 2006). Here we report on the long-term timing solutions obtained extending the time span with 5 additional years of observations obtained with GUPPI. All the PSRs but M28A, M28H and M28I will be analyzed here. A detailed study of M28A has already been presented by Johnson et al. (2013), while the case of M28H and M28I will be presented by Stairs et al. 2018, in preparation.

## 4.2 Observations and Data Analysis

The update of the timing solutions has been performed through a series of observations obtained with the GBT from October 2010 to November 2015. Observations were acquired mostly at 1.5

GHz and 2.0 GHz using 800 MHz of bandwidth, while only a single observation has been acquired at 820 MHz using 200 MHz of bandwidth. Observation lengths vary from ∼ 1.5 hours up to ∼ 7.5 hours.

The data recorded by GUPPI were Full Stokes with 10.24 $\mu$s sampling and 512 channels, each coherently dedispersed in hardware to a dispersion measure (DM) of 121 pc cm$^{-3}$, close to the cluster average value. All the data have been folded, modulo the best known PSR ephemerides till 2010, using the `fold_psrfits`[1] program, which allows to fold the data acquired in search mode, obtaining a folded archive for each PSR. We removed the sub-integrations and channels showing intense RFI to maximize the pulse signal-to-noise ratio (S/N).

Measurements of the pulse time of arrivals (TOAs) have been obtained through the `pat` task inside the `PSRCHIVE`[2] suite of softwares. We created a high S/N pulse template for each PSR, aligning and stacking all the available folded data using the `PulsePortraiture` code (Pennucci et al., 2014), specifically written for high-precision PSR timing of folded wideband data. The pulse "portraits" so obtained have been fitted with a proper number of Gaussian functions in order to obtain a noise-free template, suitable to be used for TOA measurements. These templates are presented in Figure 4.1. The number of TOAs extracted per daily observation varies from one for isolated and the very long period systems (i.e. M28B, M28D, M28E and M28F), to 15 for the very compact binaries (i.e. M28G and M28L). The resulting TOAs have been analyzed with `TEMPO`, starting from the best ephemerides previously obtained with observations till early 2010. We used the Jet Propulsion Laboratory DE 436 Solar system ephemeris to account for the effect of the motion of the telescope relative to the barycentre of the Solar System. A JUMP segment between the new and old set of TOAs has been included wherever needed. The timing residuals are plotted in Figure 4.2, the timing solutions for the isolated PSRs are tabulated at the end of the chapter in Table 4.1, while that of binary systems are in Table 4.3, 4.2 and 4.4. As can be seen from Figure 4.2, all the timing solutions are able to nicely reproduce the data, with no observed trends in the residuals as a function of time.

The positions of all the PSRs with respect to the cluster center are reported in Figure 4.3, where we also included the position of M28A (Johnson et al., 2013), M28H (Pallanca et al., 2010) and M28I (Pallanca et al., 2013a). As expected, the vast majority of them are located within or nearby the cluster core radius. Indeed, being neutron stars (NSs) the most massive stars in the cluster, they are subjected to a strong mass segregation. The only exception is M28F, located at 168" from the center, largely outside the cluster half-mass radius (see Section 4.3 and the right panel of Figure 4.3).

---

[1] https://github.com/demorest/psrfits_utils/blob/master/fold_psrfits.c
[2] http://psrchive.sourceforge.net
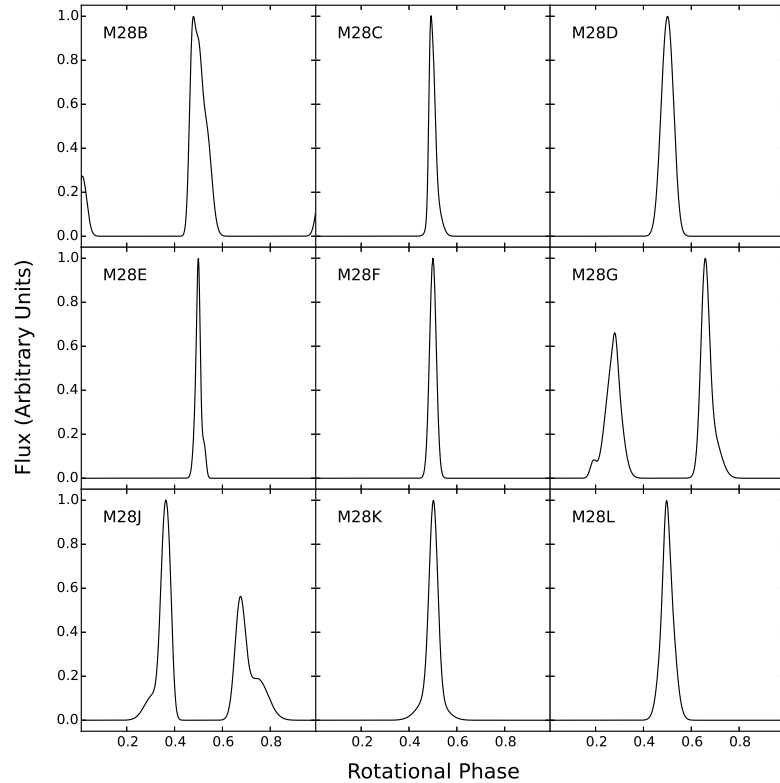
Figure 4.1: Pulse templates used to extract TOAs from the folded data. They have been obtained by aligning and stacking all the available observations and then fitting the resulting summed profiles with multi-Gaussian functions.

## 4.3   Isolated Millisecond Pulsars

We have obtained precise timing solutions of the three isolated MSPs (M28B, M28E and M28F) by fitting the observed TOAs for the first and second spin frequency derivatives, as well as the proper motion along both $\alpha$ and $\delta$. As discussed in Chapter 1.7, the spin frequency first derivative is contaminated by the acceleration of the PSR in the GC mean field, while the second derivative is mainly due to the derivative of this acceleration and possibly to the effect of nearby perturber stars. This will be discussed in Section 4.6.

For the case of M28E and M28F we have obtained very precise TOA measurements with uncertainties of the order of few $\mu$s. The timing fit resulted in tiny residual RMS but with small unfitted long period trends, not accountable by higher spin frequency derivatives and only partially corrected by fitting for the DM first derivative. Therefore, to improve these timing solutions, we measured the DM values at different epochs using the DMX parameter (see, e.g.,

66
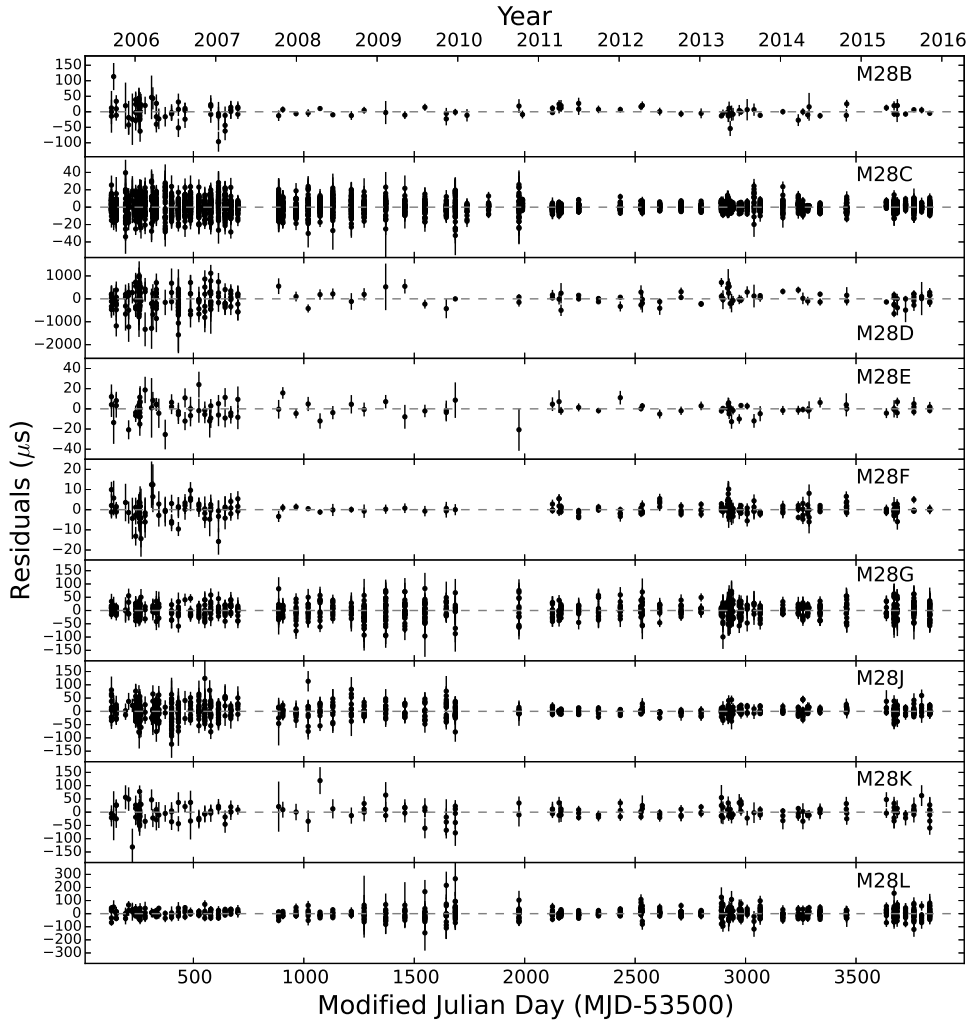
Figure 4.2: Timing residuals as a function of time for all the analyzed PSRs.

The NANOGrav Collaboration et al., 2015, for more details), determining a single constant DM value each 500 days. The best fit DMX values are plotted in Figure 4.4 where it can be seen a DM evolution across the ten year data span. This is likely the result of a change of the line of sight electron column density due to the relative motion of the Earth, the PSR and the interstellar medium.

Figure 4.3 clearly shows that M28F, unlike the other systems, is not located in the cluster inner regions, but far away in the outskirts, beyond the half-mass radius. Such a phenomenon is not commonly expected in GCs due to the effect of mass segregation and only few notorious similar cases are known: J1911−5958A in NGC 6752 (D'Amico et al., 2002), B2127−11C in M15 (Anderson et al., 1990) and J0024−7201X in 47 Tucanae (Freire et al., 2017). Three scenarios can
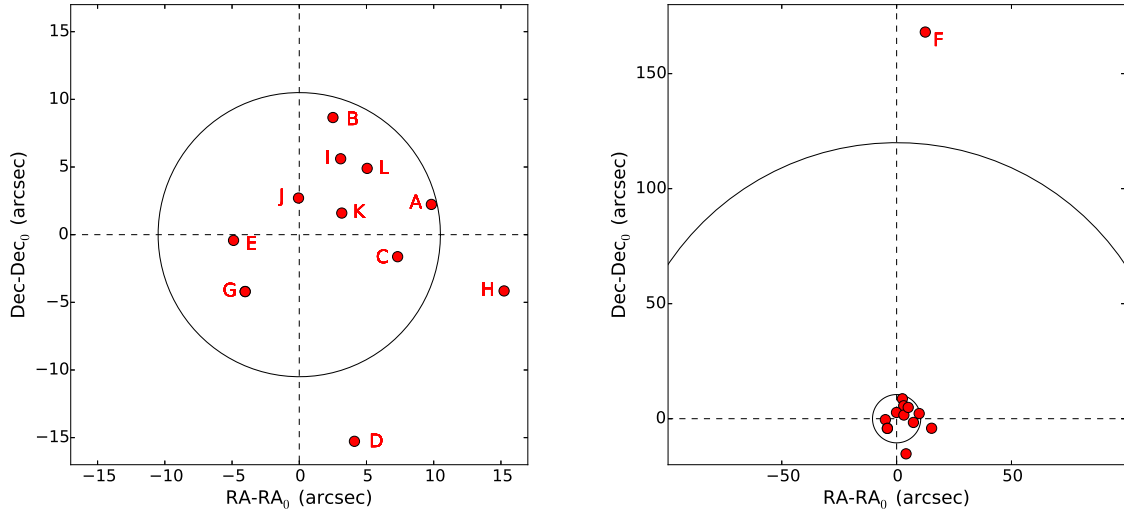
Figure 4.3: *Left Panel:* Positions of all the inner MSPs in M28 with respect to the cluster center. The solid circle represents the cluster core radius. *Right Panel:* same as in the left panel but with a larger field of view to show the position of the outsider M28F. The concentric inner and outer circles are the cluster core and half-mass radius, respectively. The cluster center and structural parameters are from Miocchi et al. (2013).
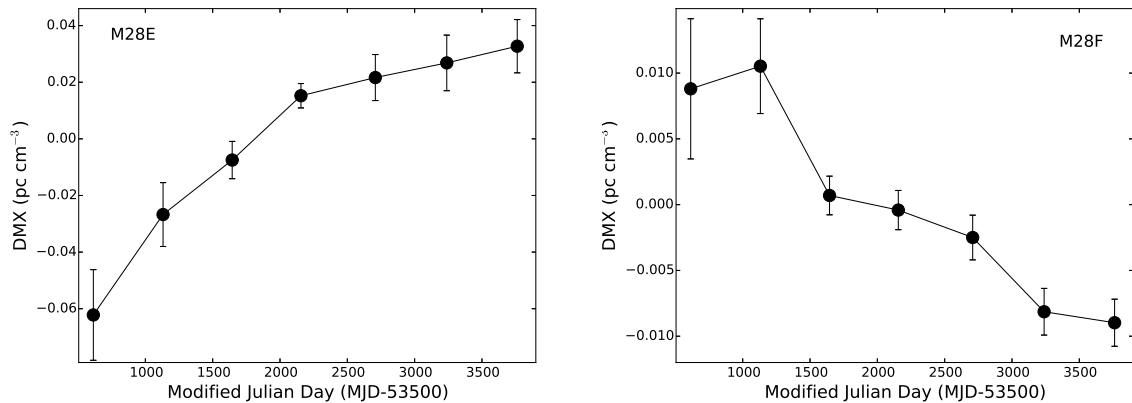


Figure 4.4: *Left Panel:* DMX values as a function of time for M28E. *Right Panel:* Same as in the left panel, but for M28F.

be invoked to explain such an anomalous position: *a)* M28F does not belong to the cluster but it is simply a Galactic field PSR in the foreground; *b)* M28F is indeed born in the cluster outskirts; *c)* M28F has been kicked out from the cluster center to the outskirts through a dynamical interaction with a massive star or binary. Hypothesis *a)* can be immediately ruled out since the proper motion of this system is precisely measured and compatible with that of all the other PSRs, thus confirming that M28F is located within the cluster. Hypothesis *b)* implies that M28F is incredibly stable against the dynamical friction that is expected to sink such a massive object toward the cluster center in a timescale of ~ 1 Gyr. Moreover, M28F is an isolated MSP, thus implying that it likely lost its companion star during a dynamical interaction with another star or binary, which is unlikely to occur in GC outskirts. Another possibility, already suggested by Colpi et al. (2002) for the MSP in NGC 6752, is the formation of this system through accretion-induced collapse (Freire, Tauris, 2014). It is not clear however if this process can unbound the PSR and the companion star. Moreover, it would not explain the stability of this system against dynamical friction.

In the hypothesis *c)* M28F is born from a binary in the cluster center and then ejected to the outskirts through an interaction with a star or a binary. Scattering or exchange interactions with very massive stars or binaries (such as massive white dwarfs (WDs), NSs, blue stragglers or even black holes) are likely responsible to such an ejection. The physics of this interaction can be very complex and detailed simulations are required in order to understand which mechanism is responsible for the MSP ejection. However, this hypothesis is the most likely explanation to the offset position of M28F. Indeed, dynamical encounters in the dense cluster central regions are expected to occur on very short timescale of $10^2 - 10^3$ yr (e.g., Hut et al., 1991) and so the possibility that M28F experienced such an interaction is not negligible. Unfortunately, the proper motion measurement here obtained reflects the motion of the cluster as a whole. It is still not precise enough to probe the motion of the PSR with respect to the cluster center. Such a measurement would give tighter constraints to understand which mechanism ejected M28F to the cluster outskirts.

## 4.4 Binary Millisecond Pulsars

### 4.4.1 The eccentric binaries M28C and M28D

M28C is a binary MSP located in a 8 day orbit with a high eccentricity around 0.85. It is therefore the most eccentric binary of the cluster. The high S/N of its detections and its large eccentricity allowed a precise measurement of all its orbital parameters, including the rate of periastron advance. However, the timing precision is still not enough to obtain a precise and independent measurement of a second post-Keplerian parameter, such as the $\gamma$ parameter (see Section 2.2.2), especially because of a strong covariance between this parameter and the projected semi-major axis. Therefore, we fitted the observed TOAs adopting the DDGR orbital model (Taylor, Weisberg,
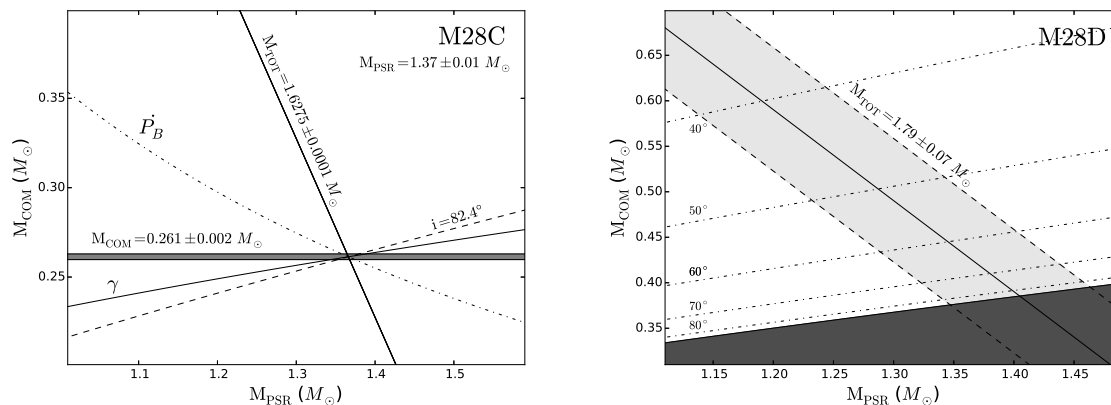
Figure 4.5: *Left Panel:* M28C companion mass as a function of the PSR mass. The black solid
diagonal line and the gray horizontal stripe are the measured values of total mass and com-
panion mass, respectively. Dashed lines are the corresponding post-Keplerian parameters (see
Chapter 2.2.2) obtained through the DDGR model. *Right Panel:* Same but for M28D. The solid
line and gray stripe surrounded by dashed lines mark the combinations of masses allowed by
the measurement of the rate of periastron advance. The black shaded region marks the region of
the diagram forbidden by the PSR mass function, while the dash-dotted lines are the curves for
constant inclination angles as predicted by the PSR mass function.

1989), a relativistic model in which general relativity is assumed to be correct and hence the free
parameters to be fitted are, in principle, only the masses of the two components of the binary
system. In TEMPO this can be achieved by fitting for the binary total mass and the companion mass
simultaneously. The resulting best fit also provides the whole set of post-Keplerian parameters
associated with the two measured masses. The best fit solution is presented in Table 4.2. We
have found that the PSR mass is $1.37 \pm 0.01 \, M_\odot$ and the companion mass is $0.261 \pm 0.002 \, M_\odot$,
thus suggesting that the latter is a classical He WD star, in a system observed at a high orbital
inclination angle of 82°. In Figure 4.5 we plot the companion mass as a function of the PSR mass
as predicted from all the post-Keplerian parameters obtained in the timing solution. Future
observations will expand the data time span and improve TOA precision, thus allowing the use
of a theory independent model to independently fit each post-Keplerian parameter. In the timing
solution, we also fitted for the XPBDOT parameter, which quantifies the orbital period derivative
excluding the pure general relativity effect. This has be done to account for the effect of the
motion of the PSR in the GC gravitational field. Indeed, the orbital period derivative is affected
by the GC mean field in the same way as the first spin period derivative (see equation 1.20 and
Section 4.9).

M28D is a slowly spinning and thus mildly recycled MSP located in a long orbit binary with
an orbital period of about 30 days and a large eccentricity of about 0.78. The combination of large

orbital period, eccentricity and slow spin period suggests that the binary has been perturbed in the past by a dynamical encounter with another star or binary. It is also quite a young system (see Section 4.6 and Table 4.3) and therefore such an interaction likely happened relatively recently. Being a slowly spinning PSR, the measured TOAs suffer larger uncertainties compared to those of the other PSRs. This is why the final timing solution shows large post-fit residual RMS, about one order of magnitude larger than those of the other analyzed systems. Nonetheless, we have been able to obtain a significative measurement of the rate of the periastron advance, and an initial measurement of the spin period second derivative and the orbital period derivative. However, no significant measurement of its proper motion has been obtained. The companion mass as a function of the PSR mass is plotted in Figure 4.5. The rate of periastron advance corresponds to a binary total mass of $1.79 \pm 0.07 \, M_\odot$. This, combined with the PSR mass function, which returns the companion mass as a function of the inclination angle assuming a typical PSR mass of $1.35 \, M_\odot$, constrains the companion mass to be larger than $0.37 \, M_\odot$ and the PSR mass to be smaller than $1.46 \, M_\odot$. Moreover, assuming that the PSR does not have a mass smaller than $1.2 \, M_\odot$, the companion mass is constrained to be smaller than $0.66 \, M_\odot$. Therefore we conclude that the companion star could be either a massive He WD, a low-mass C-O WD or even a main sequence star.

### 4.4.2 M28G, J, K and L

M28G, J and L are three non eclipsing, compact binaries, most likely of the BW family. Spider MSPs are characterized by unpredictable and stochastic changes over time of their orbital parameters. However, as pointed out by Freire et al. (2017), BWs timing behavior comes in two flavors: some of them show such unpredictable orbital changes, while others show stable orbital properties that can be usually described by a single orbital period derivative, despite the large time baseline considered in the timing analysis. The latter case could be ascribable both to intrinsic properties of the system or to an insufficient timing precision. In case of a BW with stochastic orbital variability, the BTX model can be used to describe the orbital evolution using a Taylor expansion of the binary orbital frequency. It is however important to note that such a model is purely phenomenological and valid only for the time span covered by the observations. Therefore it has no predictive power in describing the general orbital evolution of the system.

The BTX model has been used to describe the orbital properties of the non eclipsing system M28G. Its timing solution is reported in Table 4.4. Three orbital frequency derivatives were needed to fully remove the observed trends in the post-fit residuals. In Figure 4.6 we plot the post-fit residuals as a function of the orbital phase. As can be seen, although being a non-eclipsing system, several TOAs are delayed at orbital phases corresponding at the PSR superior conjunction, suggesting the presence of ionized material just like in the case of classical spider MSPs. This means that M28G is likely a common BW, probably observed at an intermediate inclination angle. It could behave as a classical eclipsing BW at lower frequency observations. All
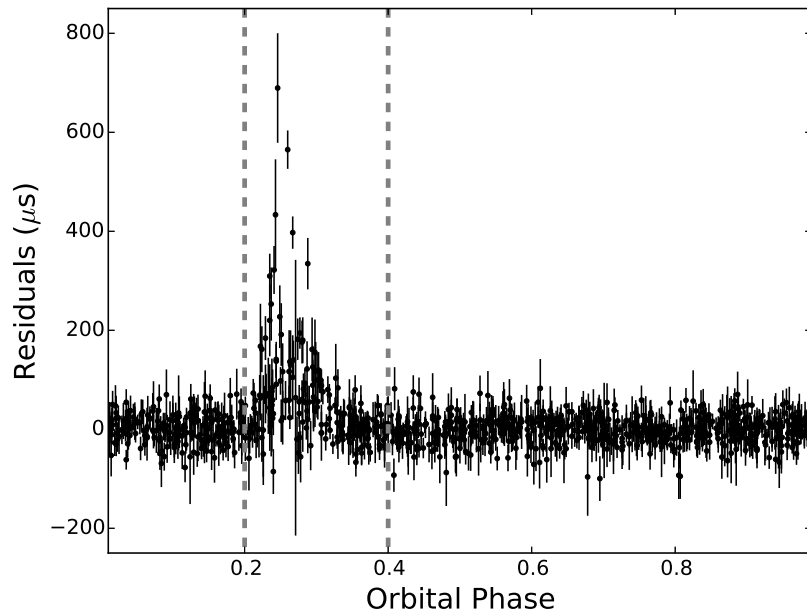
Figure 4.6: Post-fit residuals of M28G as a function of the orbital phase. The two dashed vertical lines enclose the TOAs that have been excluded from the timing solution.

the TOAs between orbital phase 0.2 and 0.4 have been excluded in the final timing solution.

On the other hand, M28J and M28L appear to belong to the secondary BW class, with stable orbits that have been nicely described through a single orbital period derivative. The latter is most likely dominated by the effect of the acceleration in the GC gravitational field. Indeed the $\dot{P}_b/P_b$ values are very similar to those predicted from the measured $\dot{P}/P$ values, corrected for an indicative intrinsic $\dot{P}$ evaluated assuming a typical surface magnetic field of $10^8$ G.

Finally, M28K is a canonical MSP with a $\sim 4$ day, slightly eccentric ($e \sim 0.0015$) orbit and likely a WD companion. The timing precision was sufficient to obtain a measurement of the orbital period derivative and a first, poorly significant detection of the rate of the periastron advance. The measured value implies a total mass that is still compatible with zero within $2\sigma$. Such a measurement will improve in the future extending the data span covered by the observations.

## 4.5   Proper Motions

We measured the proper motion of all the MSPs but M28D. These values are, in first approximation, a measurement of the cluster proper motion as a whole, while it is orbiting in the Galactic field. The measured proper motions are reported in Figure 4.7. All these values can

be used to estimate the absolute proper motion of M28 in the plane of the sky. Due to the very different uncertainties of the measured proper motion values, we evaluated the absolute motion as the weighted mean of the motions along $\alpha$ and $\delta$. We also included the proper motion of M28A reported by Johnson et al. (2013) but we chose to exclude that of M28B due to its very large uncertainty. The result is $\mu_\alpha = -0.11 \pm 0.04$ mas yr$^{-1}$ and $\mu_\delta = -9 \pm 2$ mas yr$^{-1}$ (see Figure 4.7). This result is approximatively consistent with that obtained through optical studies by Casetti-Dinescu et al. (2013). Our results benefit from a smaller uncertainty along $\alpha$, but suffer from a slightly larger uncertainty along $\delta$.

The GC absolute motion, combined with its radial velocity $v_r = 17 \pm 1$ km s$^{-1}$ (Harris, 1996, 2010 edition) can be used to determine the 3D space velocity of the cluster in a Cartesian Galactocentric rest frame. Using the formalism described in Johnson, Soderblom (1987), assuming the Local Standard of Rest velocity equal to 256 km s$^{-1}$ (Reid et al., 2009) and using the value of the Sun velocity with respect to it from Schönrich et al. (2010), we obtained $(v_x, v_y, v_z) = (45.8 \pm 0.6, 55 \pm 6, -95 \pm 4)$ km s$^{-1}$.
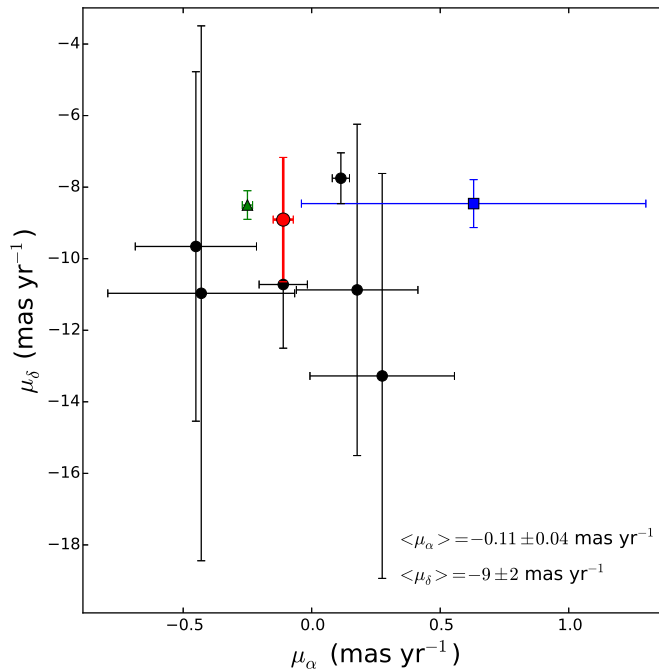


Figure 4.7: PSR proper motions measured in this work. The green triangle is the proper motion of M28A taken from Johnson et al. (2013). The red dot is the GC absolute proper motion obtained through a weighted mean, while the blue square is the value derived through optical measurements by Casetti-Dinescu et al. (2013).

Following Cadelano et al. (2017a, see also Appendix A), we then used the 3D velocity of the cluster and its current Galactocentric position $(x, y, z) = (5.4, 0.7, -0.5)$ kpc to reconstruct its orbit in the axisymmetric Galactic potential by Allen, Santillan (1991), which has been extensively used to study the kinematics of Galactic stellar systems (e.g. Ortolani et al., 2011; Massari et al., 2015). The orbit was time-integrated backwards, starting from the current conditions and using a second-order leapfrog integrator (Hockney, Eastwood, 1988) with a small time step of ∼ 100 kyr. Since the adopted Galactic potential is static, we choose to back-integrate the orbit only for 3 Gyr, since longer backward integrations become uncertain due to their dependence on the Galactic potential variations as a function of time. This numerical integration required about $3 \times 10^4$ steps. The errors on the conservation of the energy and the Z-component of the angular momentum never exceeded one part over one hundred and one thousand, respectively. We generated a set of 100 clusters starting from the phase-space initial conditions normally distributed within the uncertainties. For all of these clusters, we repeated the backward time integration. Figure A.9 shows the resulting cluster orbits in the equatorial and meridional Galactocentric plane. It can be seen that the cluster is moving on an eccentric orbit around the Galactic center. Despite its current position, outside the bulge, the cluster crosses it several times during its orbit. Indeed, assuming that the bulge is a spheroid of about 4 kpc of diameter, M28 orbited within the bulge for about 50% of the total simulation time. This should be taken into account when studying the dynamical evolution of this cluster, since such an orbit between the halo and bulge could be responsible of a huge mass-loss during the cluster lifetime, which would imply that M28 was born with an initial mass significantly larger than its current value. However, the chemical properties of its stellar population are quite different from those well known of bulge GCs (Villanova et al., 2017), suggesting that M28 was born outside of it.

## 4.6 Spin and Orbital Period Derivatives

In Chapter 1.7 we showed that the cumulative population of MSPs in a GC can help us probe the cluster dynamics. Indeed, the measured values of the spin period derivatives and orbital period derivatives are not a direct measurement of the PSR intrinsic properties since they are contaminated by their acceleration in the cluster gravitational field. As already discussed in Chapter 1.7 and 3.4, the ratio of the measured spin period derivative ($\dot{P}$) over the spin period ($P$) is the result of a combination of different terms:

$$(4.1) \qquad \left(\frac{\dot{P}}{P}\right)_{meas} = \left(\frac{\dot{P}}{P}\right)_{int} + \frac{a_{z,GC}}{c} + \frac{a_g}{c} + \frac{a_s}{c}$$

where $a_{z,GC}$ is the line of sight acceleration due to the GC mean field, $a_g$ an acceleration due to the Galaxy potential field and $a_s$ an apparent centrifugal acceleration (Shklovskii, 1970). The latter term is $a_s = \mu^2 d$, where $\mu$ is the composite cluster proper motion and $d$ its distance. The cluster proper motion, discussed in Section A.3, is $\mu \approx -9$ mas yr$^{-1}$. At the distance of M28, we
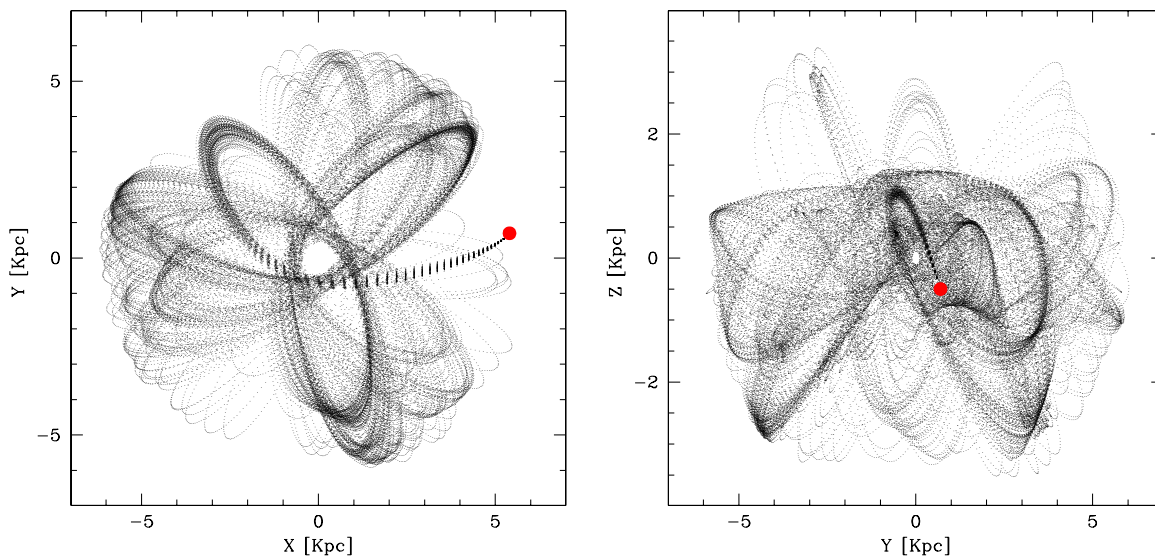
Figure 4.8: *Left Panel:*: simulated positions occupied by M28 during the last 3 Gyr along its orbit in the equatorial Galactic plane. Each point represents the position of 1 (out of 100) cluster in snapshots of the numerical integration. The red dot points the current cluster position. *Right Panel:* same as in the left panel, but for the orbit in the meridional Galactic plane.

find that $a_s/c \approx 1.1 \times 10^{-18}$ s$^{-1}$. The contribution $a_g$, due to the Galaxy field, can be evaluated following the prescriptions in Phinney (1992). At the position and distance of the cluster, using the Reid et al. (2014a) model of the Galactic rotation, we find that $a_g \approx a_s$. As expected, both the terms are smaller than the observed accelerations. The effects due to stars orbiting nearby the PSRs produce a negligible contribution to the spin period first derivative, while it can become significant for higher order derivatives. Given all this, and considering that $\dot{P}_{int}$ is unknown but positive, we can estimate an upper limit on the line of sight acceleration:

$$(4.2) \qquad \frac{a_{z,GC}}{c} \leq \left(\frac{\dot{P}}{P}\right)_{meas} - \frac{a_g}{c} - \frac{a_s}{c}$$

On the other hand, for the case of binary PSRs, for which a measurement of the orbital period derivative ($\dot{P}_b$) is available, we can evaluate the line of sight acceleration following a different approach. Indeed, $\dot{P}_b$ is affected by the acceleration in the GC in the same way as $\dot{P}$:

$$(4.3) \qquad \left(\frac{\dot{P}_b}{P_b}\right)_{meas} = \left(\frac{\dot{P}_b}{P_b}\right)_{int} + \frac{a_{z,GC}}{c} + \frac{a_g}{c} + \frac{a_s}{c}$$

Considering that the intrinsic orbital period derivative $\dot{P}_{b,int}$ is usually expected to be negligible (see, e.g., Freire et al., 2017), subtracting equation 4.3 from equation 4.1 we find:

$$(4.4) \qquad \dot{P}_{int} = \dot{P}_{meas} - \frac{\dot{P}_b}{P_b}P$$

75

Therefore, the measurement of both the spin and orbital period derivatives allows to measure the intrinsic spin-down rates and so to obtain a measurement of the line of sight acceleration due to the GC field through equation 4.1. This has been done for M28C, M28D, M28J, M28K and M28L. Their line of sight accelerations, intrinsic spin period derivatives and the corresponding surface magnetic fields, characteristic ages and spin-down luminosities are reported in the timing tables. Note that we excluded M28G since its orbital properties show stochastic changes that could result in unreliable acceleration values. We obtained upper limits following equation 4.2 for the isolated systems M28B, M28E, M28F and also for the binary M28G. Their line of sight acceleration values are reported in the timing tables.

We can now compare the derived acceleration values with those predicted by a GC analytical model. Following Freire (2005), we used a cluster model based on the King (1966) mass distribution. In this model, the acceleration of a star along the line of sight $z$ at different distances from the cluster center is (see also Prager et al. 2017):

$$(4.5) \qquad a_{z,GC}(z,x) = -3.5 \times 10^{-7} \left( \frac{\rho_0}{10^6 \, M_\odot \, pc^{-3}} \right) \left( \frac{z}{0.2 \, pc} \right) \left( \sinh^{-1}(x) - \frac{x}{\sqrt{1+x^2}} \right) x^{-3} \, m \, s^{-2}$$

where $\rho_0$ is the GC central mass density and $x \equiv r/r_c$. In the latter term $r = \sqrt{r_\perp^2 + z^2}$, where $r_\perp$ is the projected distance from the cluster center. The central mass density has been evaluated following Spitzer (1987) as $\rho_0 = 9\sigma_z^2(0)/(4\pi G r_c^2)$, where $\sigma_z(0)$ is the cluster central stellar velocity dispersion along the line of sight. Setting $\sigma_z(0) = 12 \pm 1 \, km \, s^{-1}$ (Ferraro et al. 2018, in preparation), we find that $\rho_0 = 3.1 \pm 0.6 \times 10^5 \, M_\odot \, pc^{-3}$. For each value of $r_\perp$, we recorded the maximum values of $a_{z,GC}$ as a function of $z$. The resulting curves of maximum accelerations at different projected distances from the cluster center are reported in Figure 4.9 together with the PSR measurements and upper limits obtained before. As can be seen, this analytical King model with this central velocity dispersion is able to account for the measured accelerations of all the PSRs, including also the innermost ones.

Starting from these maximum analytical values, we can evaluate upper limits on the intrinsic spin period derivatives for the isolated PSRs and M28G. In doing this, we just assumed that the line of sight acceleration of each of these PSRs is smaller than the maximum value at the corresponding $r_\perp$. In this way we obtained also lower limits to the characteristic ages and upper limits to the surface magnetic fields and spin-down luminosities, while for all the other binaries these values have been already evaluated from the derived intrinsic spin-down rates. All the PSR intrinsic properties are reported in the timing tables and they are generally compatible with those typically found for MSPs in GCs. However, the isolated and off-centered PSR M28F has a characteristic age of ~ 4 Gyr, thus appearing older than the other systems. On the other hand, the mildly recycled binary M28D appears to be quite a young object, having a characteristic age of only ~ 20 Myr. Interestingly, the characteristic age of the binary M28C is clearly not representative of the PSR true age, since its value of ~ 26 Gyr is much larger than the Hubble time. This is however not surprising since the characteristic age is a poor estimator of the PSR
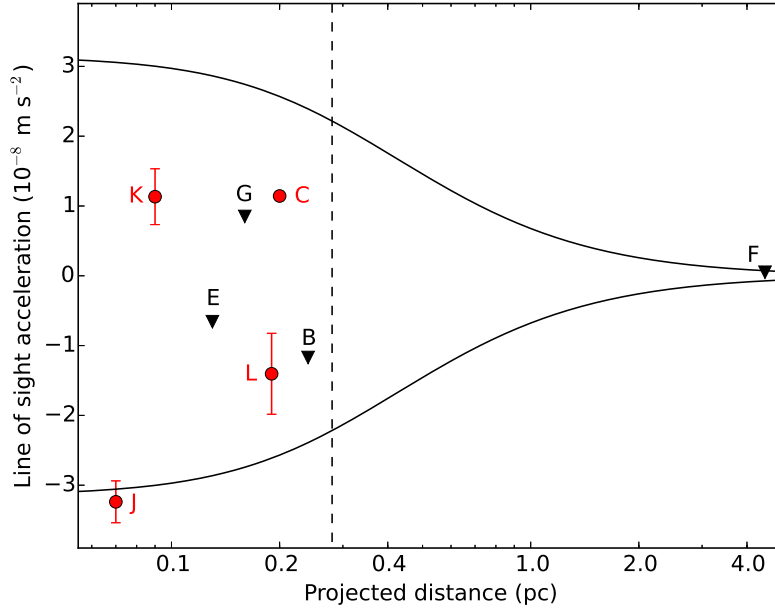
Figure 4.9: Line of sight accelerations of the PSRs in M28. The black triangles are the upper limits for the isolated systems and M28G. The red points are the values derived from the orbital period derivatives of the binary systems. The black curves are the maximum accelerations predicted by an analytical King model representative of the GC. The dashed vertical line is the cluster core radius. M28D is not plotted due to very large error bars, though is compatible with the analytical predictions within $2\sigma$.

true age and, as we showed in Chapter 1.2.2, it is based on the assumption that the PSR breaking index is $n = 3$ and that $P_0/P << 1$, where $P_0$ is the MSP birth spin period. If the latter condition is not satisfied, the characteristic age can be much higher than the PSR true age. This is the most likely explanation to the anomalous age derived for this system. The identification of the WD companion in the optical bands would provide an independent estimate of the age of the binary, thus allowing to infer a more reliable PSR age and also an estimate of its birth spin period.

The second spin period derivative is, like the first one, not representative of an intrinsic PSR property but is due, again, to the GC gravitational field. According to Phinney (1992), the derivative of the line of sight acceleration is the main contributor to this observed value, usually called line of sight "jerk":

$$\frac{\dot{a}_z}{c} = \left(\frac{\dot{f}}{f}\right)^2 - \frac{\ddot{f}}{f}$$

(4.6)

The second contributor to the second spin period derivative is the gravitational effect of possible stars orbiting nearby the PSR and anomalous jerk values could indeed suggest that the PSR is

perturbed by a nearby, possibly bounded, object (see, e.g., the case of J0024−7204H in Freire
et al. 2017). The line of sight jerk values for the systems in M28 are reported in the timing tables.
We can compare these values with analytical predictions. According to Freire et al. (2017), the
maximum values of the derivative of the line of sight acceleration as a function of the projected
distance from the cluster center can be written as:

$$(4.7) \qquad \dot{a}_{z,GC,max}(x_\perp) = 4\pi G\rho_0 \left( \frac{x_\perp}{\sqrt{1+x_\perp^2}} - \sinh^{-1}(x_\perp) \right) x_\perp^{-3} v_{z,max}$$

where $x_\perp \equiv r_\perp/r_c$, and $v_{z,max}$ the maximum velocity of PSRs with respect to the cluster center.
Since PSRs can travel within the cluster with velocities up to twice the central velocity dispersion
(e.g. Freire et al., 2017), we conservatively set $v_{z,max} = 2\sigma_z(0)$. The maximum acceleration deriva-
tive as a function of the projected distance from the cluster center is plotted in Figure 4.10, where
it can be compared with the measured line of sight jerks. As can be seen, most of the PSRs have
jerk values within that predicted by the analytical model. However, it is interesting to note that
M28J, M28E and, to a lesser extent, M28F, show values not fully compatible with the expected
ones. This could suggest that their motion within the cluster is perturbed by nearby stars. Future
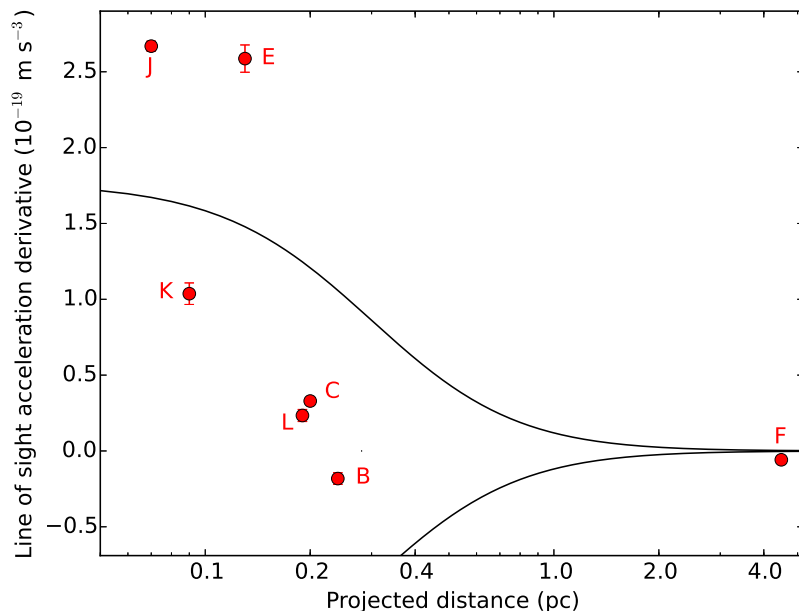


Figure 4.10: Line of sight derivative of the acceleration or "jerks" of the PSRs in M28. The black
curves are the maximum values predicted by a GC analytical model, assuming a maximum
velocity of PSRs with respect to the cluster center twice the central stellar velocity dispersion.
M28D is not plotted due to very large error bars, although its jerk value is compatible with the
analytical predictions within $2\sigma$.

observations will allow to confirm this and possibly infer if such nearby objects are also bounded to the PSRs.

Table 4.1: Timing solutions for the three isolated MSPs in M28 analyzed in this work, as obtained from the fit of the TOAs with TEMPO. In this and in all the following tables, numbers in parenthesis are the $1\sigma$ uncertainty on the last quoted digit; the time units are TDB and the adopted terrestrial time standard is UTC(NIST).

| Pulsar | M28B | M28E | M28F |
|---|---|---|---|
| *Timing Parameters* | | | |
| Right Ascension, $\alpha$ (J2000) ....................... | 18:24:32.5459(1) | 18:24:33.08918(6) | 18:24:31.81276(3) |
| Declination, $\delta$ (J2000) ........................... | −24:52:04.41(3) | −24:52:13.49(2) | −24:49:24.994(7) |
| Proper Motion in $\alpha$, $\mu_\alpha$ (mas yr$^{-1}$) ............... | 0.05(0.50) | −0.4(2) | −0.11(9) |
| Proper Motion in $\delta$, $\mu_\delta$ (mas yr$^{-1}$) ............... | −20(10) | −10(5) | −11(2) |
| Spin Frequency, $F$ (Hz) .......................... | 152.749522067833(6) | 184.53132298064(4) | 407.97094956581(2) |
| $1^{st}$ Spin Frequency Derivative, $\dot{F}$ ($10^{-15}$ Hz s$^{-1}$) | 5.63117(6) | 3.6480(1) | −1.5764(1) |
| $2^{nd}$ Spin Frequency Derivative, $\ddot{F}$ ($10^{-27}$ Hz s$^{-2}$) | 9(2) | −159(6) | 8(2) |
| Reference Epoch (MJD) .......................... | 55481 | 55480 | 54900 |
| MJD Range (MJD) .............................. | 53629-57334 | 53629-57334 | 53629-57334 |
| Dispersion Measure, DM (pc cm$^{-3}$) .............. | 119.323(2) | 119.63(2) | 123.598(7) |
| Number of TOAs ................................. | 132 | 112 | 252 |
| Residuals RMS ($\mu$s) ............................. | 14.45 | 4.64 | 2.11 |
| *Derived Parameters* | | | |
| Angular Offset from Center, $\theta_\perp$ (arcsec) .......... | 9.01 | 4.91 | 168.54 |
| Projected Distance from Center, $r_\perp$ (pc) .......... | 0.24 | 0.13 | 4.49 |
| Spin Period, $P$ (ms) .............................. | 6.5466653280651(3) | 5.419134181923(1) | 2.4511549193987(1) |
| $1^{st}$ Spin Period Derivative, $\dot{P}$ ($10^{-19}$) ............. | −2.41345(3) | −1.07133(4) | 9.4715(7) |
| $2^{nd}$ Spin Period Derivative, $\ddot{P}$ ($10^{-31}$ s$^{-1}$) ....... | −4.0(8) | 4.7(2) | −5(1) |
| Accel. from GC Field along $z$, $a_{z,GC}$ ($10^{-8}$ m s$^{-2}$) | <2.4 | <2.9 | <0.073 |
| Intrinsic Spin Period Derivative, $\dot{P}_{int}$ ($10^{-19}$) .... | <2.7 | <4.0 | <0.10 |
| Characteristic Age, $\tau_c$ (Gyr) ...................... | >0.39 | >0.21 | >3.9 |
| Surface Magnetic Field, $B$ ($10^8$ G) ............... | <13 | <15 | <1.6 |
| Spin-Down Luminosity, $L_{SD}$ ($10^{34}$ erg s$^{-1}$) ...... | < 3.7 | <9.9 | <2.7 |
| Line of Sight Jerk, $\dot{a}_{z,GC}$ ($10^{-20}$ m s$^{-3}$) ......... | -1.8(4) | 25.9(9) | −0.6(2) |

Table 4.2: Timing solution for M28C.

| Pulsar | M28C |
|---|---|
| **Timing Parameters** | |
| Right Ascension, $\alpha$ (J2000) ........................ | 18:24:32.19244(1) |
| Declination, $\delta$ (J2000) ........................... | $-24$:52:14.699(3) |
| Proper Motion in $\alpha$, $\mu_\alpha$ (mas yr$^{-1}$) ............... | 0.11(3) |
| Proper Motion in $\delta$, $\mu_\delta$ (mas yr$^{-1}$) ............... | $-7.6(7)$ |
| Spin Frequency, $F$ (Hz) .......................... | 240.483823754283(3) |
| $1^{st}$ Spin Frequency Derivative, $\dot{F}$ ($10^{-15}$ Hz s$^{-1}$) | $-9.84111(3)$ |
| $2^{nd}$ Spin Frequency Derivative, $\ddot{F}$ ($10^{-27}$ Hz s$^{-2}$) | $-26.4(4)$ |
| Reference Epoch (MJD) ........................... | 54834 |
| MJD Range (MJD) ............................... | 52335-57334 |
| Dispersion Measure, DM (pc cm$^{-3}$) ............... | 120.5465(3) |
| Number of TOAs ................................. | 3459 |
| Residuals RMS ($\mu$s) ............................. | 4.81 |
| **Binary Parameters** | |
| Binary Model ..................................... | DDGR |
| Projected Semi-major Axis, $x_p$ (lt-s) .............. | 7.36161(3) |
| Orbital Eccentricity, $e$ ........................... | 0.84704331(6) |
| Longitude of Periastron, $\omega$ (deg) ................. | 137.6350(2) |
| Epoch of Passage at Periastron, $T_0$ (MJD) ........ | 53756.59374599(8) |
| Orbital Period, $P_b$ (days) ........................ | 8.0778064373(7) |
| Rate of Periastron Advance, $\dot{\omega}$ (deg/yr) .......... | 0.0299614 |
| Gamma Parameter, $\gamma$ (s) ......................... | 0.003039517 |
| Orbital Period Derivative, $\dot{P}_b$ ($10^{-12}$) ........... | $-0.0573768$ |
| $\dot{P}_b$ minus GR prediction, $\dot{P}_{Xb}$ ($10^{-12}$) ........... | 28.1(4) |
| Sine of Inclination Angle ........................ | 0.991278 |
| Total Mass, $M_{TOT}$ (M$_\odot$) ........................ | 1.6274(1) |
| Companion Mass, $M_{COM}$ (M$_\odot$) .................. | 0.261(2) |
| **Derived Parameters** | |
| Angular Offset from Center, $\theta_\perp$ (arcsec) ......... | 7.49 |
| Projected Distance from Center, $r_\perp$ (pc) ......... | 0.20 |
| Spin Period, $P$ (ms) .............................. | 4.15828384790555(4) |
| $1^{st}$ Spin Period Derivative, $\dot{P}$ ($10^{-19}$) ............. | 1.701658(5) |
| $2^{nd}$ Spin Period Derivative, $\ddot{P}$ ($10^{-31}$ s$^{-1}$) ....... | 4.57(6) |
| Accel. from GC Field along $z$, $a_{z,GC}$ ($10^{-8}$ m s$^{-1}$) | 1.14(2) |
| Intrinsic Spin Period Derivative, $\dot{P}_{int}$ ($10^{-19}$) .... | 0.0251(4) |
| Characteristic Age, $\tau_c$ (Gyr) ...................... | 26.3(8) |
| Surface Magnetic Field, $B$ ($10^8$ G) ............... | 1.03(2) |
| Spin-Down Luminosity, $L_{SD}$ ($10^{34}$ erg s$^{-1}$) ...... | 0.138(2) |
| Line of Sight Jerk, $\dot{a}_{z,GC}$ ($10^{-20}$ m s$^{-3}$) ......... | 3.29(5) |

Table 4.3: Timing solutions for four binary MSPs analyzed in this work.

| Pulsar | M28D | M28J | M28K | M28L |
|---|---|---|---|---|
| **Timing Parameters** | | | | |
| Right Ascension, $\alpha$ (J2000) ..................... | 18:24:32.428(1) | 18:24:32.73412(6) | 18:24:32.4977(2) | 18:24:32.35887(8) |
| Declination, $\delta$ (J2000) .......................... | $-$24:52:28.3(4) | $-$24:52:10.36(2) | $-$24:52:11.47(4) | $-$24:52:08.17(2) |
| Proper Motion in $\alpha$, $\mu_\alpha$ (mas yr$^{-1}$) .............. | $-$ | 0.2(2) | 1.2(7) | $-$0.4(4) |
| Proper Motion in $\delta$, $\mu_\delta$ (mas yr$^{-1}$) ............... | $-$ | $-$11(5) | $-$23(14) | $-$11(7) |
| Spin Frequency, $F$ (Hz) ......................... | 12.52576561970(2) | 247.5437518346(2) | 224.16236824852(3) | 243.89603346899(2) |
| $1^{st}$ Spin Frequency Derivative, $\dot{F}$ ($10^{-15}$ Hz s$^{-1}$) | $-$15.4077(2) | 4.6586(1) | $-$11.5035(2) | 10.55091(9) |
| $2^{nd}$ Spin Frequency Derivative, $\ddot{F}$ ($10^{-27}$ Hz s$^{-2}$) | 10(3) | $-$220(3) | $-$77(5) | $-$19(3) |
| Reference Epoch (MJD) .......................... | 54915 | 55481 | 55481 | 55481 |
| MJD Range (MJD) ............................... | 52497-57334 | 53629-57334 | 53629-57334 | 53629-57334 |
| Dispersion Measure, DM (pc cm$^{-3}$) .............. | 119.80(7) | 119.160(1) | 119.488(3) | 118.967(2) |
| Number of TOAs .................................. | 252 | 797 | 189 | 667 |
| Residuals RMS ($\mu$s) ............................... | 267.02 | 15.48 | 19.94 | 23.33 |
| **Binary Parameters** | | | | |
| Binary Model ..................................... | BT | BT | ELL1 | BT |
| Projected Semi-Major Axis, $x_p$ (lt-s) .............. | 24.8713(2) | 0.0250231(8) | 2.604992(3) | 0.056967(1) |
| Orbital Eccentricity, $e$ ........................... | 0.776335(4) | 0.0 | $-$ | 0.0 |
| Longitude of Periastron, $\omega$ (deg) ................. | 311.0919(5) | 0.0 | $-$ | 0.0 |
| Epoch of Passage at Periastron, $T_0$ (MJD) ........ | 53815.97137(2) | 54406.9315422(8) | $-$ | 54406.836027(1) |
| First Laplace-Lagrange Parameter, $\eta$ ............. | $-$ | $-$ | 9.74(3)$\times 10^{-4}$ | $-$ |
| Second Laplace-Lagrange Parameter, $\kappa$ .......... | $-$ | $-$ | 1.177(3)$\times 10^{-3}$ | $-$ |
| Epoch of Passage at Ascending Node, $T_{\rm asc}$ (MJD) | $-$ | $-$ | 54403.927081(1) | $-$ |
| Rate of Periastron Advance, $\dot{\omega}$ (deg/yr) .......... | 0.00249(6) | $-$ | 0.06(3) | $-$ |
| Orbital Period, $P_b$ (days) ........................ | 30.411529(1) | 0.0974313248(1) | 3.910348502(5) | 0.2257062382(4) |
| Orbital Period Derivative, $\dot{P}_b$ ($10^{-12}$ s s$^{-1}$) ...... | 1000(600) | $-$0.89(8) | 14(5) | $-$0.9(4) |
| **Derived Parameters** | | | | |
| Angular Offset from Center, $\theta_\perp$ (arcsec) ......... | 15.81 | 2.71 | 3.54 | 7.03 |
| Projected Distance from Center, $r_\perp$ (pc) ......... | 0.42 | 0.07 | 0.09 | 0.19 |
| Spin Period, $P$ (ms) ............................. | 79.8354392347(1) | 4.0396899238566(4) | 4.4610520838687(6) | 4.1001076802143(3) |
| First Spin Period Derivative, $\dot{P}$ ($10^{-19}$) .......... | 982.04(1) | $-$0.76024(7) | 2.28932(4) | $-$1.77370(2) |
| First Spin Second Derivative, $\ddot{P}$ ($10^{-31}$ s$^{-1}$) ...... | $-$600(200) | 36.0(4) | 15(1) | 3.2(5) |
| Accel. from GC Field along $z$, $a_{z,GC}$ ($10^{-8}$ m s$^{-1}$) | 11(7) | -3.2(3) | 1.1(4) | -1.4(6) |
| Intrinsic Spin period Derivative, $\dot{P}_{int}$ ($10^{-19}$) .... | 700(400) | 3.5(3) | 0.5(2) | 0.06(2) |
| Characteristic Age, $\tau_c$ (Gyr) ..................... | 0.02(1) | 0.18(2) | 1.4(5) | 11(5) |
| Surface Magnetic Field, $B$ ($10^8$ G) ............... | 700(400) | 12(1) | 5(2) | 1.6(6) |
| Spin-Down Luminosity, $L_{SD}$ ($10^{34}$ erg s$^{-1}$) ...... | 0.5(3) | 21(2) | 2.3(8) | 0.3(1) |
| Line of Sight Jerk, $\dot{a}_{z,GC}$ ($10^{-20}$ m s$^{-3}$) ......... | $-$23(7) | 26.7(3) | 10.4(7) | 2.3(4) |

Table 4.4: Timing solutions for M28G.

| Pulsar | M28G |
|---|---|
| **Timing Parameters** | |
| Right Ascension, $\alpha$ (J2000) ........................ | 18:24:33.0256(1) |
| Declination, $\delta$ (J2000) ........................... | $-24$:52:17.27(3) |
| Proper Motion in $\alpha$, $\mu_\alpha$ (mas yr$^{-1}$) ............... | 0.3(3) |
| Proper Motion in $\delta$, $\mu_\delta$ (mas yr$^{-1}$) ............... | $-13$(6) |
| Spin Frequency, $F$ (Hz) ........................... | 169.23168173616(1) |
| $1^{st}$ Spin Frequency Derivative, $\dot{F}$ ($10^{-15}$ Hz s$^{-1}$) , | $-5.16499$(7) |
| Reference Epoch (MJD) ........................... | 54407 |
| MJD Range (MJD) .............................. | 53629-57334 |
| Dispersion Measure, DM (pc cm$^{-3}$) .............. | 119.766(2) |
| Number of TOAs ................................. | 1072 |
| Residuals RMS ($\mu$s) ............................. | 21.82 |
| **Binary Parameters** | |
| Binary Model ..................................... | BTX |
| Projected Semi-Major Axis, $x_p$ (lt-s) .............. | 0.016485(1) |
| Orbital Eccentricity, $e$ ........................... | 0.0 |
| Longitude of Periastron, $\omega$ (deg) ................. | 0.0 |
| Epoch of Passage at Periastron, $T_0$ (MJD) ........ | 54406.965179(2) |
| Orbital Frequency, $f_b$ (s$^{-1}$) ...................... | 1.106680739(4)$\times10^{-4}$ |
| $1^{st}$ Orbital Freq. derivative, $f_b^{(1)}$ (s$^{-2}$) ........... | $-7$(1)$\times10^{-20}$ |
| $2^{nd}$ Orbital Freq. derivative, $f_b^{(2)}$ (s$^{-3}$) .......... | $-2.0$(4)$\times10^{-27}$ |
| $3^{rd}$ Orbital Freq. derivative, $f_b^{(3)}$ (s$^{-4}$) ........... | 3.5(4)$\times10^{-35}$ |
| **Derived Parameters** | |
| Angular Offset from Center, $\theta_\perp$ (arcsec) ......... | 5.81 |
| Projected Distance from Center, $r_\perp$ (pc) .......... | 0.16 |
| Spin Period, $P$ (ms) .............................. | 5.9090590469876(4) |
| First Spin Period Derivative, $\dot{P}$ ($10^{-19}$) .......... | 1.80346(3) |
| Accel. from GC Field along $z$, $a_{z,GC}$ ($10^{-8}$ m s$^{-1}$) | <2.8 |
| Intrinsic Spin Period Derivative, $\dot{P}_{int}$ ($10^{-19}$) .... | <7.1 |
| Characteristic Age, $\tau_c$ (Gyr) ...................... | >0.13 |
| Surface Magnetic Field, $B$ ($10^8$ G) ............... | <20.1 |
| Spin-Down Luminosity, $L_{SD}$ ($10^{34}$ erg s$^{-1}$) ....... | <13.6 |

# 5

## THE BLACK-WIDOW PSR J1953+1846A IN THE GLOBULAR CLUSTER M71

*Mainly based on Cadelano et al. 2015b, ApJ, 807:91*

T his chapter is devoted to the identification and characterization of the companion star to PSR J1953+1846A, a "black widow" binary millisecond pulsar in the globular cluster M71. By using the accurate position and orbital parameters obtained from radio timing, we identified the optical companion in ACS/Hubble Space Telescope images. It turns out to be a faint ($m_{F606W} \approx 26$, $m_{F814W} \approx 25$) and variable star located at only $\sim 0.06''$ from the pulsar timing position. The light curve shows a maximum at the pulsar inferior conjunction and a minimum at the pulsar superior conjunction, thus confirming the association with the system. The shape of the optical modulation suggests that the companion star is heated, likely by the pulsar wind. The comparison with the X-ray light curve possibly suggests the presence of an intra-binary shock due to the interaction between the pulsar wind and the material released by the companion. This is the second identification (after COM-M5C) of an optical companion to a black widow pulsar in a globular cluster. Interestingly, the two companions show a similar light curve and share the same position in the color magnitude diagram.

## 5.1 Introduction

PSR J1953+1846A (hereafter M71A) is the only millisecond pulsar (MSP) known so far in M71 (Hessels et al., 2007). M71 is a low density globular cluster (GC; $\log \rho_0 = 2.83$ in units of $L_\odot$ $pc^{-3}$; Harris, 1996, 2010 edition), in a disk-like orbit (Cadelano et al., 2017a), located at $\sim 4$ kpc from the Earth. It is one of the most metal-rich clusters among GCs outside the bulge (Harris, 1996) and its density profile shows an extended core ($r_c = 56.2"$; Cadelano et al., 2017a) and no signatures of core collapse. M71A was discovered in a targeted survey of all GCs visible with the 305-m Arecibo radio telescope (Hessels et al., 2007). It is located at $\alpha = 19^h53^m46.42^s$ ; $\delta = 18°47'04.84"$, at a projected distance of only 20" (0.53 core radii) from the cluster center, it has a spin period of $\sim 4.9$ ms and a low eccentricity orbit of $\sim 4.2$ hours. M71A is classified as a black-widow (BW). In fact, because of its very low-mass function ($f \approx 1.6 \cdot 10^{-5}$ $M_\odot$), the companion is expected to have a minimum mass of $\sim 0.032$ $M_\odot$. Moreover, as commonly found for BW systems, the radio signal shows eclipses for about 20% of the orbital period (at 1400 MHz observing frequency), likely due to stripped material from an evaporating companion. A Chandra X-ray observation of this cluster revealed a source in a position compatible with the PSR location and a luminosity of about $10^{31}$ erg $s^{-1}$ in the $0.3 - 8.0$ keV spectral range (Elsner et al., 2008). The light curve is consistent with a non-steady source and the photon index ($\Gamma = 1.89 \pm 0.32$) suggests magnetospheric radiation and/or an emission from intra-binary shocks. In the context of an optical study of the M71 X-ray sources, Huang et al. (2010) suggested as possible optical companion to M71A a star located at $\sim 0.1"$ from the radio PSR and lying along the red side of the cluster main sequence (MS), in a region commonly occupied by binary systems. Nonetheless, its absolute magnitude ($M_V \sim 8.5$) implies a mass of about $0.5$ $M_\odot$, inconsistent with radio-derived mass function (in fact such a large mass would be compatible only with a nearly face-on orbit, where no radio eclipses are expected). Hence, Huang et al. (2010) concluded that this object is unlikely to be the real companion, which could be still below the detection threshold or, alternatively, that M71A could be a hierarchical triple system.

## 5.2 Radio Timing

Timing observations were carried out with the 305-m William E. Gordon telescope at the Arecibo Observatory in Puerto Rico, between MJDs 52420 (2002 May 26) and 53542 (2005 June 21), with the initial discovery observations on MJD 52082 (2001 June 22) incorporated into the timing solution. The Gregorian L-band Wide receiver was used for the observations, sending dual-polarization data to the Wideband Arecibo Pulsar Processor (WAPP; see Dowd et al., 2000) autocorrelation spectrometers.

All the data were then folded modulo the best-known PSR ephemeris. A Gaussian profile was fit to the summed profile from several observations for use as a standard profile, and the FFTFIT algorithm (Taylor, 1992) was used to determine pulse times of arrival (TOAs). Time segments

Table 5.1.   Timing parameters for PSR J1953+1847 (M71A)[a]

| Parameter | Value |
|---|---|
| Measured Parameters | |
| Right ascension, $\alpha$ (J2000) .......................... | 19:53:46.41966(3) |
| Declination, $\delta$ (J2000) ............................. | +18:47:04.8472(7) |
| Spin frequency, $F$ (Hz) ............................. | 204.57006473073(3) |
| Spin frequency derivative, $\dot{F}$ ($10^{-15}$ Hz s$^{-1}$) ....... | $-2.0299(3)$ |
| Spin frequency second derivative, $\ddot{F}$ ($10^{-25}$ Hz s$^{-2}$) | 5.4(3) |
| Epoch (MJD) ...................................... | 52812.0 |
| Dispersion measure, DM (cm$^{-3}$pc) ................. | 117.3941(15) |
| DM derivative (cm$^{-3}$pc yr$^{-1}$) ...................... | $-0.0274(17)$ |
| Orbital period, $P_b$ (d) ............................. | 0.1767950297(2) |
| Projected semi-major axis, $x$ (s) .................... | 0.0782246(12) |
| Epoch of Ascending Node, $T_0$ (MJD) ............... | 52811.8761877(3) |
| | |
| Derived Parameters | |
| Spin period, $P$ (ms) ............................... | 4.8883007458412(6) |
| Spin period derivative, $\dot{P}$ ($10^{-20}$) ................... | 4.8506(8) |
| Spin period second derivative, $\ddot{P}$ ($10^{-29}$ s$^{-1}$) ....... | $-1.28(7)$ |
| Angular offset from cluster centre, $\theta_\perp$ ($'$) .......... | 0.33 |
| Intrinsic period derivative, $\dot{P}_{int}$ ($10^{-20}$) ........... | $4.3 < \dot{P}_{int} < 5.4$ |
| Characteristic age, $\tau_c$ (Gyr) ....................... | $1.4 < \tau_c < 1.8$ |
| Surface magnetic field, $B_0$ ($10^8$ G) ................ | $4.6 < B_0 < 5.2$ |
| Mass function $f$ (M$_\odot$) ............................. | 0.0000164427(8) |
| Minimum companion mass $m_c$ (M$_\odot$)[b]............. | 0.032 |

[a]Numbers in parentheses are the $1\sigma$ uncertainties in the last digits quoted.

[b]Computed assuming an orbital inclination angle of $90°$ and a pulsar mass of $1.4\,\mathrm{M}_\odot$.

corresponding to eclipses and to the times when M71 transited at Arecibo (during which the telescope could not track the cluster) were not considered in the timing analysis.

Timing analysis was performed with the TEMPO software package[1] using the DE421 Solar System ephemeris and the TT(BIPM) clock standard. The BT timing model of Blandford, Teukolsky (1976) was used, as the orbit has no significant eccentricity. The timing parameters are listed in Table 5.1 and residuals are presented in Figure 5.1. The root-mean-square postfit residual is $35\,\mu$s. The reduced-$\chi^2$ of the fit is 4.8; however, we list the parameter uncertainties as reported by TEMPO without scaling, as the epoch-to-epoch wander in the residuals is likely due to the interactions between the two stars (see Figure 5.2) rather than to any misestimation of the TOA uncertainties. The high-precision radio timing position is slightly offset ($0.06''$) from the position of the optical counterpart (see Section 6.2), but agrees within the much larger uncertainty ($0.2''$) of the latter. Following the reasoning in Freire et al. (2005), we find the maximum possible acceleration due to

---

[1]tempo.sourceforge.net
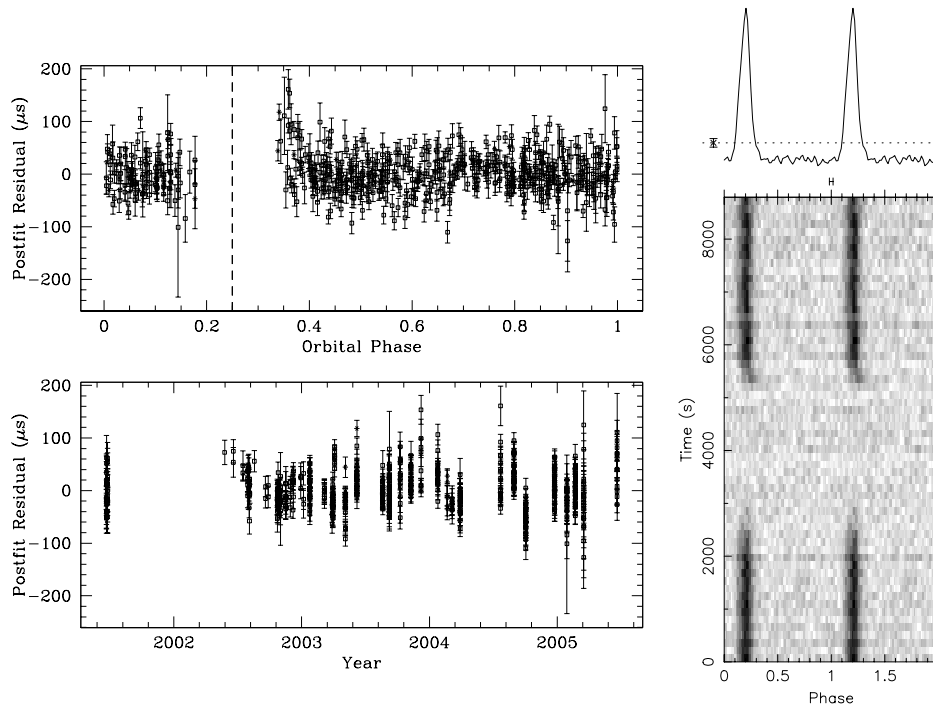
Figure 5.1: *Left panel:* Postfit timing residuals for M71A, as functions of orbital phase and date. The dashed line indicates orbital phase 0.25, the PSR superior conjunction. *Right panel:* An observation of M71A on MJD 52798 (2003 June 8). The abrupt disappearance of the PSR at the start of eclipse, as well as the slight dispersive delay on reappearance, are clearly visible. The cumulative pulse profile is plotted twice at the top of the figure.
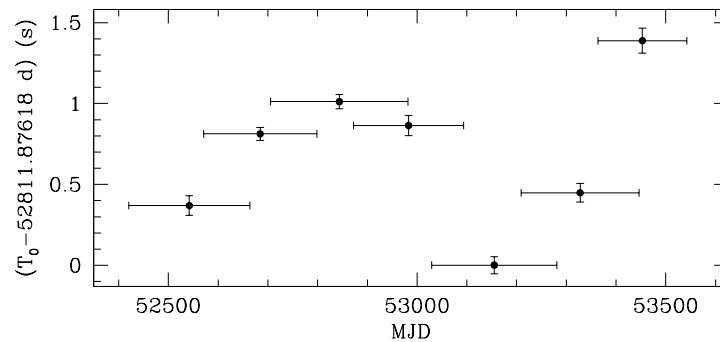


Figure 5.2: Variation of the time of passage through ascending node (orbital phase 0), computed for overlapping segments of data and holding all other timing parameters fixed at their nominal values.

the gravitational field of the cluster for this line of sight to be $\pm 3.2 \times 10^{-10} \, \mathrm{m\,s^{-2}}$. This implies that most of the observed pulse period derivative ($\dot{P}$) is intrinsic. Further corrections due to the differential acceleration in the Galaxy (e.g. Nice, Taylor, 1995; Reid et al., 2014b) are small. Given the small velocity dispersion in the core of the cluster (2.3 km s$^{-1}$; Harris, 1996), the velocity of the PSR relative to that of the cluster should be very small; therefore its proper motion should be very similar to the proper motion of the cluster ($\sim 3.5$ mas yr$^{-1}$; Cadelano et al., 2017a) as a whole, making the corresponding correction to $\dot{P}$ (Shklovskii, 1970) about half the size of that due to the Galactic acceleration. The timing data do not allow us to derive a reliable proper motion for the PSR. We use the range of allowed accelerations to constrain the intrinsic $\dot{P}$ as well as the characteristic age and surface magnetic field in Table 5.1.

The PSR is asymmetrically eclipsed between approximate orbital phases of 0.18 and 0.35, where orbital phase 0.25 represents superior conjunction. The eclipses begin fairly abruptly but when the signal returns, it at first suffers excess dispersive delay due to ionized material within the orbit (Figure 5.1). The mass loss from the companion star has a further manifestation in the variation of orbital parameters: Figure 5.2 shows the value of the time of ascending node passage for overlapping subsets of the data. The variation is comparable to that seen in other black widow eclipsing systems (e.g., Arzoumanian et al., 1994; Ng et al., 2014) and significantly less than what is typically present in the redback (RB) systems (e.g., Archibald et al., 2013a), which have much more massive, likely non-degenerate companion stars.

## 5.3 Optical Photometry of the Companion Star

### 5.3.1 Observations and data analysis

The identification of the companion to M71A has been performed through two datasets of high resolution images acquired with the Wide Field Camera (WFC) of the Advanced Camera for Surveys (ACS) mounted on the Hubble Space Telescope (HST). The primary dataset has been obtained on 2013 August 20 (GO12932, P.I.: Ferraro) and consists of a set of ten images in the F606W filter (with exposure times: $2 \times 459$ s; $3 \times 466$ s; $5 \times 500$ s) and nine images in the F814W filter ($5 \times 337$ s; $3 \times 357$ s; $1 \times 440$ s). We also analyzed an archival dataset, obtained on 2006 July 1 (GO1775, P.I.: Sarajedini) with the same instrument and same filters. It consists of four F606W images with an exposure time of 75 s and four F814W images with an exposure time of 80 s.

The standard photometric analysis has been performed on the "flc" images, which are corrected for flat field, bias, dark counts and charge transfer efficiency. These images have been further corrected for "Pixel-Area-Map"[2] with standard IRAF procedures. By using the `DAOPHOT II` `ALLSTAR` and `ALLFRAME` packages (Stetson, 1987), we performed an accurate photometric analysis of each image, following the procedure described in Chapter 2.3. The resulting catalog of stars

---

[2]For more details see the ACS Data Handbook.

contains instrumental magnitudes that have been calibrated to the VEGAMAG system cross-correlating with `CataXcorr` our catalog with that by Anderson et al. (2008), using the $\sim 7600$ stars in common. Since the WFC images suffer heavily from geometric distortion, we corrected the instrumental positions (x,y) by applying the equations reported by Meurer et al. (2003) and using the coefficients in Hack, Cox (2001). Then we transformed instrumental positions into the absolute astrometric system $(\alpha, \delta)$ using the stars in common with the Anderson et al. (2008) catalog. The resulting astrometric solution has an accuracy of $\sim 0.14''$ in $\alpha$ and of $\sim 0.13''$ in $\delta$, corresponding to a total position accuracy of $\sim 0.2''$.

### 5.3.2 The companion to M71A

The search for the companion star to M71A was performed by means of an accurate photometric analysis of all the detectable objects within a $5'' \times 5''$ wide region centered on the nominal position of the MSP. Figure 5.3 shows the zoomed $(0.5'' \times 0.5'')$ central part of that region. As can be seen, a relatively bright object is found to have a position compatible with the X-ray source (dashed circle) and the radio source (solid-line circle). This is the star proposed by Huang et al. (2010) to be the optical counterpart to M71A. However, a much fainter object, showing a strong variability, is visible in the figure. This is a quite promising object and it is located at $\alpha = 19^h 53^m 46.4062^s$ ; $\delta = 18°47'04.793''$, only $0.06''$ from the radio position and $0.13''$ from the X-ray source, thus in perfect positional coincidence within our positional uncertainty ($\sim 0.2''$). In the primary dataset, it has been detected in 9 (out of 10) images in the F606W filter, with a magnitude variation ranging from $m_{F606W} \approx 24.3$ to $m_{F606W} \approx 27$, while in the F814W filter has been detected in 6 images (out of 9) and the magnitude varies from $m_{F814W} \approx 23.4$ to $m_{F814W} \approx 24.9$. Unfortunately, the images in the archival dataset are too shallow to properly detect this faint object: in fact it turned out to be above the detection threshold in only one exposure in the F814W filter. For the four deep exposures of the primary dataset in which the star is not visible, we estimated an upper magnitude limit by simulating an artificial star of decreasing magnitude at the position of the candidate companion. The derived detection threshold turned out to be $m_{F606W} \sim 26.5$ and $m_{F814W} \sim 25.9$.

In order to reliably establish that the detected star is the binary companion to M71A, we built the light curve in both the available filters by folding the optical measurements with the orbital period and the ascending node time of the PSR (see Table 5.1). The results are shown in Figure 5.4, and in Table 5.2 we report the MJD of the images with their related orbital phases and magnitudes. As can be seen, the light curves show a sinusoidal modulation spanning at least three magnitudes and it is fully consistent with the orbital period of the binary system. This establishes the physical connection between the variable star and the MSP. Indeed the exposures in which the star is not detected nicely correspond to the light curve minima. The curves have a maximum at $\phi \approx 0.75$, corresponding to the PSR inferior conjunction (where we observe the
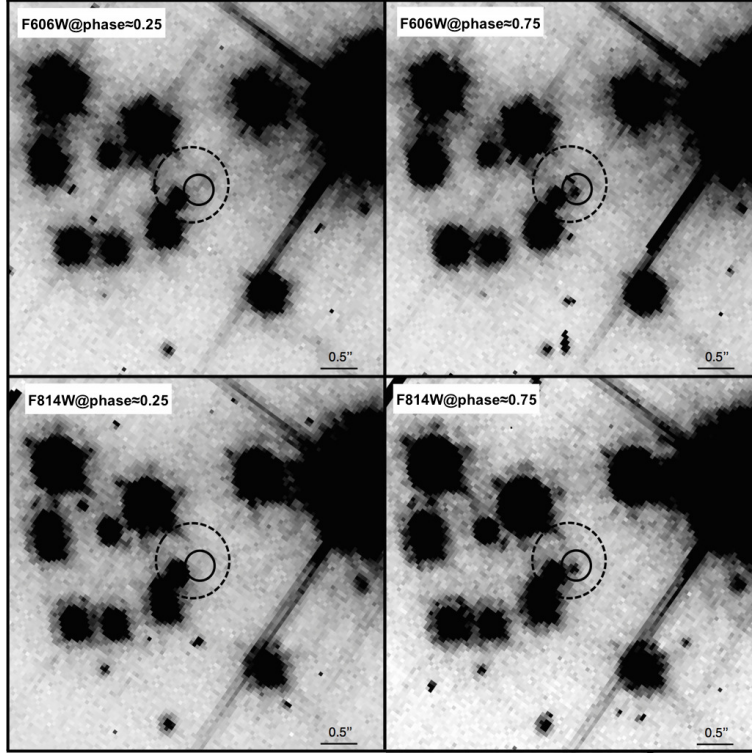
Figure 5.3: Primary dataset HST images of the 5" × 5" region around the nominal position of M71A. The filters and the orbital phases are labeled in each panel. The solid circle is centered on the radio position and it has a radius of 0.2" (which is larger than the formal uncertainty from PSR timing). The dashed circle is centered on the X-ray counterpart and it has a radius of 0.5". The relatively bright star on the left border of the solid circle is the candidate optical companion proposed by Huang et al. (2010). COM-M71A is clearly visible inside the solid circle in the right panels (corresponding to the inferior conjunction of the PSR, where the companion reaches maximum brightness), while in the left panels (at superior conjunction of the PSR) it is below the detection threshold.

companion side facing the PSR) and a minimum at $\phi \approx 0.25$, corresponding to the PSR superior conjunction (where we observe the back side of the companion). This behavior is indicative of a strong heating of the companion side exposed to the PSR emission and it is in good agreement with the observed optical properties of other similar objects (e.g. Stappers et al., 2001; Reynolds et al., 2007; Pallanca et al., 2012; Breton et al., 2013; Pallanca et al., 2014; Li et al., 2014). For the sake of comparison, in Figure 5.5 we plot the light curve (folded following the same procedure described above) of the possible companion suggested by Huang et al. (2010). As can be seen the star does not show any significant flux variation.

All these pieces of evidence suggest that the faint variable (which we name COM-M71A) is

the optical companion to the BW M71A. It is the tenth MSP optical companion and the second to a BW system in a GC. In the color-magnitude diagram (CMD), COM-M71A is located at faint magnitudes in a region between the MS and the white dwarf (WD) cooling sequences, where no normal GC stars are expected. This position is indicative of a non degenerate or semi-degenerate, low-mass and swollen star. Interestingly, the position of this object in the CMD is quite similar to that of COM-M5C, the only companion to a BW system known in GCs up to now and recently identified by Pallanca et al. (2014) in the GC M5.

## 5.4 Discussion

Since the available data do not uniformly sample the orbital phases of the system in either the F606W or the F814W filters (see upper and middle panels of Figure 5.4), in order to accurately
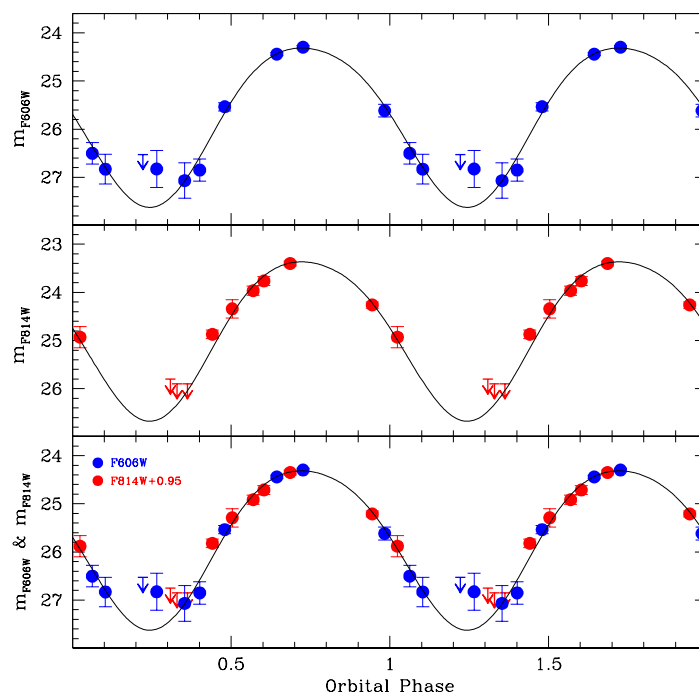


Figure 5.4: Light curves of COM-71A in the F606W and F814W filters separately (upper and middle panels) and for the combination of the two (bottom panel), obtained after a 0.95 mag shift of the F814W magnitudes. All curves are folded with the radio parameters and two periods are shown for clarity. Circles mark the observed points, arrows are the magnitude upper-limits for the images where the star is below the detection threshold. The black curve in each panel is the best analytical model obtained from the combined light curve and then adapted to each filter.

Table 5.2: Optical observations of COM-M71A

| $\phi$ | $t$ (MJD) | $m_{F606W}$ | $m_{F814W}$ |
|---|---|---|---|
| 0.02 | 56524.57602385 | – | $24.9 \pm 0.2$ |
| 0.06 | 56524.58290459 | $26.5 \pm 0.2$ | – |
| 0.10 | 56524.59012681 | $26.8 \pm 0.3$ | – |
| 0.22 | 56524.43431532 | $> 26.5$ | – |
| 0.26 | 56524.44193085 | $26.8 \pm 0.4$ | – |
| 0.31 | 56524.44960589 | – | $> 25.9$ |
| 0.33 | 56524.63013255 | – | $> 25.9$ |
| 0.35 | 56524.45750982 | $27.1 \pm 0.4$ | – |
| 0.36 | 56524.63586163 | – | $> 25.8$ |
| 0.40 | 56524.64270200 | $26.8 \pm 0.2$ | – |
| 0.44 | 56524.64977385 | – | $24.87 \pm 0.09$ |
| 0.48 | 56524.65661404 | $25.54 \pm 0.08$ | – |
| 0.50 | $53867.78512088^a$ | – | $24.3 \pm 0.2$ |
| 0.57 | 56524.49569959 | – | $23.97 \pm 0.09$ |
| 0.60 | 56524.50166033 | – | $23.76 \pm 0.09$ |
| 0.64 | 56524.50885348 | $24.44 \pm 0.03$ | – |
| 0.68 | 56524.51627848 | – | $23.40 \pm 0.05$ |
| 0.73 | 56524.52347163 | $24.30 \pm 0.03$ | – |
| 0.94 | 56524.56203070 | – | $24.26 \pm 0.06$ |
| 0.98 | 56524.56891144 | $25.6 \pm 0.1$ | – |

Note. — Orbital phases ($\phi$), corresponding MJD ($t$) of the observations and observed magnitudes or upper-limits in both filters.

$^a$ This is the only image of the archival dataset where the companion star is above the detection threshold.

determine the light curve of the companion star we combined the two datasets together, by applying a 0.95 mag shift to the F814W magnitudes (bottom panel of Figure 5.4). We then used the software GRATIS[3] and a $\chi^2$ criterion to determine the two harmonics best fit model[4] to the curve. This is shown as a solid line in the bottom panel of Figure 5.4. Finally, we verified that the same solution also provides a good fit to the light curves in each filter separately. Indeed, the reduced $\chi^2$ turned out to be 1.50 for the F606W filter, and 1.75 in F814W (see the solid curves in the upper and middle panels of Figure 5.4). This demonstrates that no significant modulation of the stellar color (temperature) along the orbit is measurable from the available dataset, and a much finer sampling of the light curve is needed to provide additional clues on this possibility. In Table 6.3 we report the maximum and minimum values for both the magnitude and the flux in each filter, evaluated from the best-fit model by following the procedure described in Bohlin (2012) for the ACS. The uncertainties are calculated by using the mean photometric errors for stars with similar magnitudes. The magnitude shift needed to superimpose the F814W light

[3]"Graphical Analyzer for TIme Series" is a software aimed at studying stellar variability phenomena. Developed by Paolo Montegriffo at INAF-Osservatorio Astronomico di Bologna.

[4]Note that a single harmonic model (i.e. a sinusoidal function) does not provide a good match of the observed light curve.
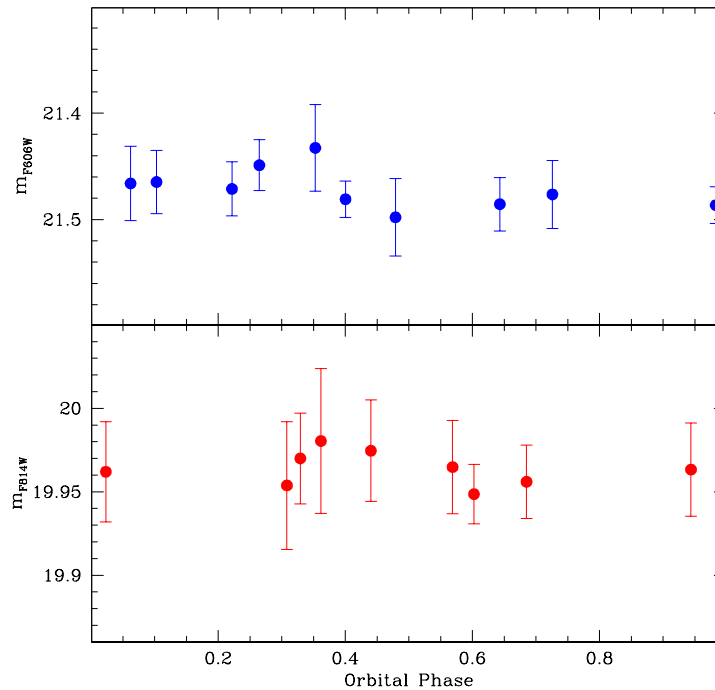
Figure 5.5: Light curves of the candidate companion proposed by Huang et al. (2010), folded with radio orbital parameters. The absence of any magnitude modulation as a function of the orbital phase is the definitive confirmation that this object is not connected to M71A.

curve to that in the F606W filter implies a color index of $0.95 \pm 0.12$ for the companion star. By adopting a $0.54 \, M_\odot$ WD cooling sequence from the BaSTI catalog[5] (Manzato et al., 2008; Salaris et al., 2010), this value can be converted into a temperature of $5100 \pm 800$ K, which is in good agreement with those evaluated for other BW systems (e.g. Stappers et al., 2001; Pallanca et al., 2012; Breton et al., 2013; Pallanca et al., 2014; Li et al., 2014).

In Figure 5.6 we show the CMD, with the shaded rectangle marking the region occupied by COM-M71A during the orbital period. The height of the rectangle corresponds to the maximum $m_{F606W}$ magnitude difference expected from the best-fit model shown in Figure 5.4, while the width corresponds to the photometric error at the minimum luminosity. As already mentioned, the star is located between the MS and the WD cooling sequence, and it spans a range of about three magnitudes. Of particular interest is the predicted star position during the PSR superior conjunction, where we expect to see the stellar side not exposed to the PSR flux (clearly this is exactly the case only for $i = 90°$). The CMD position of COM-M71A in this phase could be

---

[5]http://basti.oa-teramo.inaf.it

92

Table 5.3: Optical properties of COM-M71A

|  | F606W | F814W |
|---|---|---|
| $m_{bright}$ | $24.31 \pm 0.01$ | $23.37 \pm 0.02$ |
| $m_{faint}$ | $27.62 \pm 0.09$ | $26.7 \pm 0.1$ |
| $F_{bright}$ ($10^{-17}$ erg cm$^{-2}$ s$^{-1}$) | $126 \pm 1$ | $128 \pm 2$ |
| $F_{faint}$ ($10^{-17}$ erg cm$^{-2}$ s$^{-1}$) | $5.9 \pm 0.5$ | $6.1 \pm 0.6$ |
| $\Delta$F ($10^{-17}$ erg cm$^{-2}$ s$^{-1}$) | $120 \pm 50$ | $120 \pm 60$ |
| $L_{bright}$ ($10^{29}$erg s$^{-1}$) | $24.2 \pm 0.2$ | $24.5 \pm 0.4$ |
| $L_{faint}$ ($10^{29}$erg s$^{-1}$) | $1.15 \pm 0.09$ | $1.2 \pm 0.1$ |

Note. — Maximum and minimum luminosities of COM-M71A as derived from the model light curve.
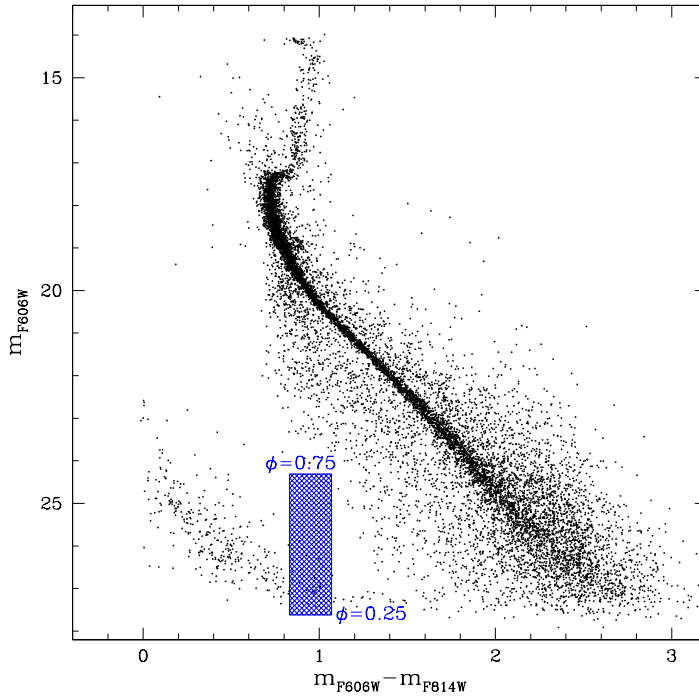


Figure 5.6: CMD of M71 with highlighted in blue the region occupied by COM-M71A during the whole orbital period, as predicted by the light curve model (see text, Figure 5.4 and Table 3).

compatible with the He WD cooling sequence, suggesting a semi-degenerate stellar structure. However, at these low luminosities, our analytical model is not appropriately constrained by data. Therefore, in order to confirm this possibility, further observations are needed. In principle, the companion mass can be constrained from the comparison of its CMD position and theoretical isochrones. However, in the case of strongly perturbed stars the mass inferred in this way can be overestimated, or suggestive of inclination angles too small to be consistent with the presence of

radio eclipses (see Ferraro et al., 2003a; Pallanca et al., 2010; Mucciarelli et al., 2013). In our case, not only the companion position in the CMD is clearly out of the canonical evolutionary sequences, but also its minimum luminosity is not properly constrained by the observations.

Assuming that the companion optical emission is mostly due to black-body radiation, the luminosity and temperature of this star would be consistent with an object of radius $R_{BB} \leq 0.02\,R_{\odot}$. However, the companions to BWs usually suffer from strong tidal distortion due to the interaction with the PSR, therefore they are swollen up and possibly they can even fill their Roche Lobes. Furthermore, the presence of radio eclipses suggests that the simple $R_{BB}$ is a gross underestimate of the true stellar radius. Indeed, the Roche Lobe (RL) radius is far more appropriate to describe the size of the companion (e.g. Stappers et al., 1996; Pallanca et al., 2012; Breton et al., 2013; Pallanca et al., 2014). According to Eggleton (1983), the Roche Lobe (RL) radius can be computed as:

$$(5.1) \qquad R_{RL} \simeq \frac{0.49 q^{\frac{2}{3}} a}{0.6 q^{\frac{2}{3}} + \ln\left(1 + q^{\frac{1}{3}}\right)},$$

where q is the ratio between the companion and the PSR masses and a is the orbital separation. Combining this relation with the PSR mass function, assuming a neutron star mass ranging from $1.2\,M_{\odot}$ to $2.5\,M_{\odot}$ (Özel et al., 2012) and an inclination angle ranging from $0°$ to $90°$, we find $0.22\,R_{\odot} < R_{RL} < 1.24\,R_{\odot}$.

Interestingly, the light curve shape presents a hint of asymmetric structure in both filters: the increase to the maximum seems to be smoother than the decrease to the minimum. Despite the low statistic, this behavior could be due to a slight asynchronous rotating companion, as in the case of PSR J2051−0827 (see Stappers et al., 2001). This could be the result of a tidal torque from the wind of a magnetically active star, which can result in a companion angular velocity that differs from the orbital angular velocity. Moreover, in this case the angular velocity could be subject to a variation with time due to a secular time dependence of the orbital period, due itself to a variation of the companion quadrupole moment (see e.g. Applegate, Shaham, 1994; Doroshenko et al., 2001; Lorimer, Kramer, 2004). However, in order to probe this intriguing possibility, an uniform sampling of the light curve from new observations is needed.

### 5.4.1 Reprocessing efficiency and Roche Lobe filling factor

Under the assumption that the optical magnitude modulation is mainly due to the heating of the companion surface by the PSR flux, we can compare the observed flux amplitude of the light curve with the expected one ($\Delta F_{exp}$) as a function of the inclination angle ($i$), by the following

relation (Pallanca et al., 2014):

$$\Delta F_{exp}(i) = \eta \frac{\dot{E}}{a^2} R^2_{COM}(i) \frac{\epsilon(i)}{4\pi d^2_{PSR}},$$
(5.2)

where $\eta$ is the reprocessing efficiency under the assumption of a PSR isotropic emission, $R_{COM}(i) = f R_{RL}(i)$ is the companion star radius, where $f$ is the volume-averaged Roche Lobe filling factor, $d_{PSR}$ is the MSP distance, assumed to be equal to the GC distance ($d_{PSR} = 4.0$ kpc; Harris, 1996) and $\epsilon(i)$ parametrizes the difference of the heated surface visible to the observer between maximum and minimum, as a function of the inclination angle. $\dot{E} = 4\pi I \frac{\dot{P}_{int}}{P^3}$ is the PSR spin-down luminosity where $I$ is the momentum of inertia. Using the the spin period and its intrinsic first derivative obtained from radio timing (see Table 1) and assuming $I = 10^{45}$ g cm$^2$, we found that $\dot{E} = 4.6 - 5.8 \times 10^{33}$ erg s$^{-1}$, typical values within the Galactic eclipsing MSP population. Setting $\Delta F_{exp} = \Delta F_{obs}$ in the F606W filter (see Table 3), we evaluated the reprocessing efficiency as a function of the inclination angle for different values of the RL filling factor. Results are shown in Figure 5.7. As can be seen, for high inclination angles and a RL filling companion, the reprocessing efficiency is $\sim 5\%$, while for filling factor $f = 0.8$ is $\sim 8\%$. A typical value of 15% (Breton et al., 2013) would be consistent with $f \sim 0.6$. Values of $f < 1$ would be plausible since some works showed that BW companions not always completely fill their RL (e.g. Callanan et al., 1995; Stappers et al., 1999; Breton et al., 2013). Similar results hold for the F814W filter.

It is worth noting that by using $R_{BB}$ instead of $R_{RL}$ for the stellar radius, the efficiency increases over 100% for almost every meaningful configuration. This can be admitted only if an anisotropic PSR emission is assumed. However, the presence of long radio eclipses and the behavior of similar objects is a strong indication that $R_{BB}$ heavily underestimates the stellar true radius.

### 5.4.2 A comparison between M71A and M5C

So far, the optical companion to PSR J1518+0204C (hereafter M5C) was the only BW companion known in a GC. M5C is a 2.48 ms PSR with an orbital period of $\sim 2.1$ hr located in the GC M5. Its radio timing and the optical photometry of the companion star (COM-M5C) is discussed in Pallanca et al. (2014). In section 3, we anticipated some interesting analogies between this star and COM-M71A. In order to further investigate similarities between these BW companions, we compared the optical properties of the two objects. Figure 5.8 shows their light curves, with the magnitudes reported to the absolute values. Indeed, despite the low sampling of the COM-M5C light curves, these two objects seem to have a quite similar optical behavior. As reference, we used COM-M71A analytical models (solid lines) for the COM-M5C, from which we inferred that a similar light curve structure could hold even for COM-M5C, being more appropriate than the simple sinusoid (dashed lines) used by Pallanca et al. (2014), given the sparse number of measurements that prevent them to build an accurate model. Figure 5.8 shows the position of
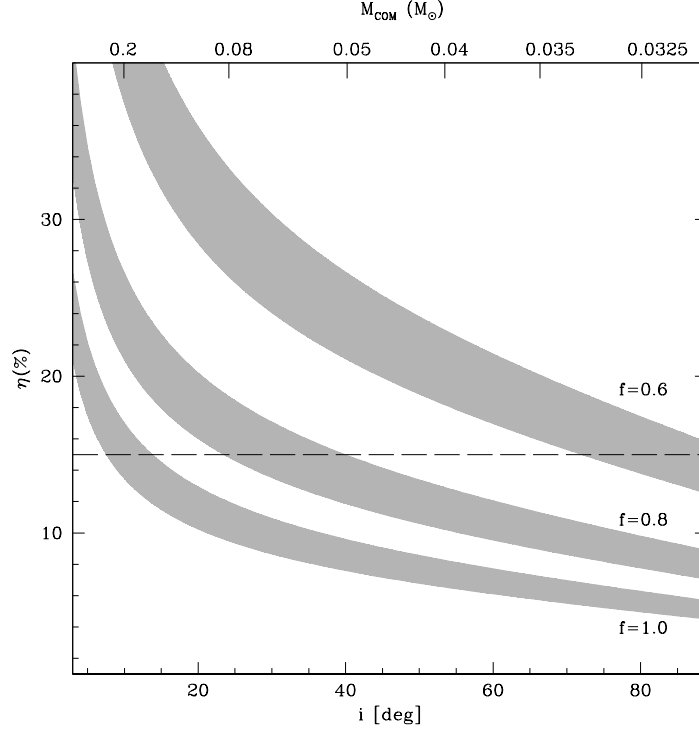
Figure 5.7: Reprocessing efficiency of the PSR emitted energy as a function of the inclination angle, assuming three different values of the RL filling factor and a PSR mass of $1.4\,M_\odot$. The thickness of each strip corresponds to the range of spin-down energies measured for this PSR (see text). The horizontal dashed line at $\eta = 15\%$ is a typical reprocessing efficiency reported in Breton et al. (2013). On the top axis, the companion masses for a PSR mass of $1.4\,M_\odot$ are reported.

the two objects in the CMD. Again, considering the uncertainties in COM-M5C magnitudes and colors, we found that they are located in the same region, suggesting a common evolutive path for these low-mass, possibly non degenerate, swollen and heated companions. Interestingly, in the CMD the two BW companions are located in a region completely different from that usually occupied by RBs (Pallanca, 2014). Of course, additional identifications of BW companions are needed to firmly characterize the evolution of these objects. In addition, using equation (5.2) for COM-M5C, setting the filling factor $f = 1$ and using the spin-down period from Pallanca et al. (2014) to evaluate the spin-down luminosity ($\dot{E} = 0.7 - 3 \times 10^{34}$ erg s$^{-1}$), we found a reprocessing efficiency $\eta \sim 5 - 20\%$, a value fully in agreement with what found for COM-M71A, thus further strengthening the analogies between these two systems.
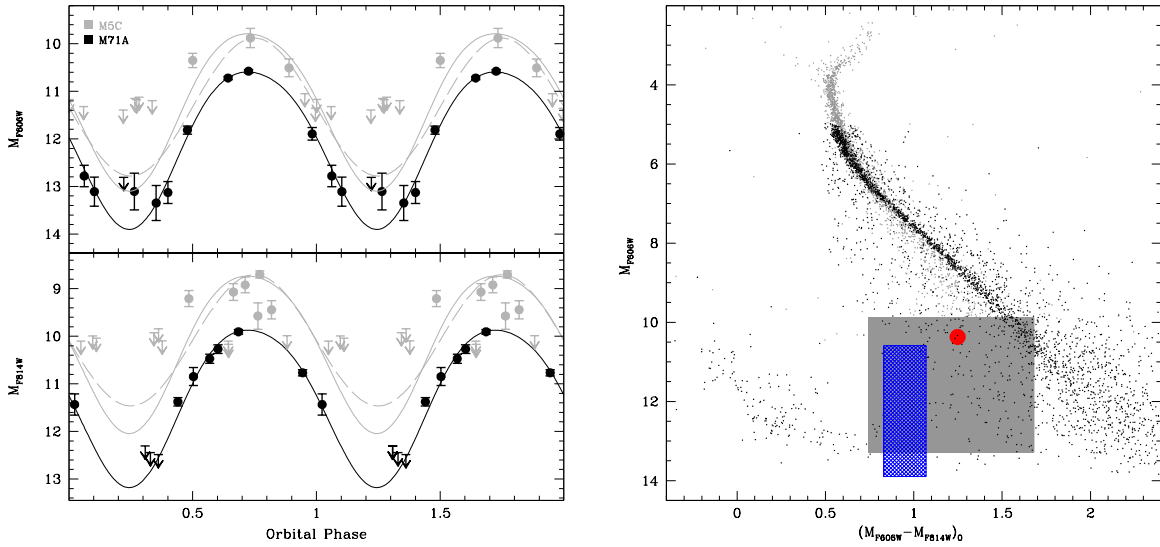
Figure 5.8: *Left panel:* Optical light curves of COM-M71A (this work; black points and lines) and COM-M5C (from Pallanca et al., 2014, gray points and dashed lines), with magnitudes reported to absolute values. The gray solid lines are COM-M71A model adapted to COM-M5C to reproduce the observed points. *Right panel:* CMD of M71 (black dots) and M5 (gray dots). The blue shaded region is the position of COM-M71A along the whole orbital phase, as derived from the light curve model (see Figure 5.6). The red point and the gray area are the indicative position of the COM-M5C (see Pallanca et al., 2014, for more details). Both the objects are located between the MS and the WD cooling sequence, suggesting common properties of these two BW companions.

### 5.4.3 Comparing X-ray and optical light curves

Usually, BWs with a high energy counterpart do not show any appreciable X-ray variability related to their orbital period (see, e.g., Bogdanov et al., 2006; Gentile et al., 2014, respectively for the BWs in the GC 47 Tucanae and in the Galactic field). However, this could be an observational bias, due to the lack of deep enough and systematic surveys of BWs in the X-rays. On the other hand, it is worth noting that several RB systems clearly show orbital X-ray modulation likely due to the presence of intra-binary shocks (Bogdanov et al., 2006, 2011, 2014). M71A is an exception, since it has been found to show periodic X-ray variability (Elsner et al., 2008). Very interestingly, the determination of COM-M71A optical light curve offers the opportunity to perform a comparison between the two. The most intriguing feature emerging from the comparison of the light curves (both folded with the binary system parameters) is that the phase spanned by the radio eclipses ($0.18 < \phi < 0.35$) does not correspond to the phase of the X-ray minimum ($0 < \phi < 0.2$), but it nicely lines up with the optical minimum ($\phi \approx 0.25$). Thus we found that the X-ray minimum precedes the optical PSR superior conjunction. A similar effect was

already observed for the RB 47TucW, a 2.35 ms binary MSP with an orbital period of $\sim 3.2$ hr and a companion mass of $\sim 0.15\,M_\odot$ (Camilo et al., 2000), whose optical light curves indicate the presence of a strong heating (Edmonds et al., 2002), as usually observed for BW systems. For this object Bogdanov et al. (2006) argue that the X-ray variability can be attributed to the presence of an intra-binary shock that is eclipsed by the companion star. The length of the X-ray eclipse suggests that this shock is located closer to the companion star than to the MSP. In particular this behavior could be due to a swept-back shocked region, produced by the interaction between the PSR wind and the stream of gas issuing from the inner Lagrange point L1, elongated perpendicular to the semi-major axis of the binary (see Bogdanov et al., 2005, for a detailed description). Despite the low X-ray statistics, this is likely to be the case also for M71A, where the intra-binary shock could be eclipsed just before the PSR superior conjunction. Even for a companion that is under-filling its Roche Lobe, this shocked region can be created thanks to the stellar wind which can result in mass outflow through L1 (Bogdanov et al., 2005).

As discussed in Bogdanov et al. (2005), the Accreting Millisecond X-ray Pulsar (AMXP) SAX J1808.4$-$3658, during quiescent states, shows several analogies with the RB 47TucW, in terms of both the X-ray spectrum and the optical variability. Based on the discussion above, these properties are also similar to those observed for M71A and, very interestingly, even the companion mass is comparable in these two cases: above $0.032\,M_\odot$ for COM-M71A, and $\sim 0.05\,M_\odot$ for the companion to SAX J1808.4$-$365 (Campana et al., 2004). This puts M71A in the middle of the riddle, supporting the possibility that AMXPs could be the bridge between RB and BW systems (Roberts et al., 2014). Clearly, multi-wavelength studies of these objects are urged to unveil connections between AMXPs and eclipsing MSPs, and between BWs and RBs. Indeed, several important new connections between AMXPs and RBs have been made in the last years, especially with the discoveries of systems transitioning from one state to the other (see Archibald et al., 2009; Papitto et al., 2013; Patruno et al., 2014; Bassa et al., 2014; Stappers et al., 2014).

# 6

# THE HE WHITE DWARFS ORBITING THE MILLISECOND PULSARS IN THE GLOBULAR CLUSTER 47 TUCANAE

I n this chapter we show how we used ultra-deep UV observations obtained with the Hubble Space Telescope to search for optical companions to the binary millisecond pulsars in the globular cluster 47 Tucanae. The analysis allowed us to identify four new counterparts (to 47TucQ, 47TucS, 47TucT and 47TucY) and confirmed those already known (to 47TucU and 47TucW). In the color-magnitude diagram, the detected companions are located in a region between the main sequence and the CO white dwarf cooling sequences, consistent with the cooling tracks of He white dwarfs of mass between 0.15 $M_\odot$ and 0.20 $M_\odot$. For each identified companion, mass, cooling age, temperature and pulsar mass (as a function of the inclination angle) have been derived and discussed. For 47TucU we also found that the past accretion history likely proceeded in a sub-Eddington rate. The companion to the redback 47TucW is confirmed to be a non degenerate star, with properties particularly similar to those observed for black-widow systems. Two stars have been identified within the 2$\sigma$ astrometric uncertainty from the radio positions of 47TucH and 47TucI, but the available data prevent us from firmly assessing whether they are the true companions of these two MSPs.

## 6.1   Introduction

47 Tucanae (also known as NGC 104) is one of the most studied globular cluster (GC) in the
Milky Way. It is located at a distance of about 4.7 kpc from the Sun, its stellar population has an
age of about 12 Gyrs (e.g. Brogaard et al., 2017), an intermediate metallicity among the Galaxy
GCs ([Fe/H] = −0.7; Brogaard et al., 2017) and its structural properties show no signature of
core-collapse. It also has an high interaction rate (Bahramian et al., 2013), which can explain
the largest population of X-ray sources (300 detected sources within the half-mass radius) ever
identified, so far, in a GC (Heinke et al., 2005). Moreover, radio observations revealed the 47
Tucanae hosts the largest population of millisecond pulsars (MSPs) after Terzan 5. Indeed, 25
radio MSPs have been discovered to date (Manchester et al., 1990, 1991; Robinson et al., 1995;
Camilo et al., 2000; Pan et al., 2016). All of them have spin periods shorter than 8 ms and
14 of them are located in binary systems[1]. The discovery and timing of these systems (Freire
et al., 2001a, 2003; Ridolfi et al., 2016; Freire et al., 2017) opened the possibility to study stellar
evolution and the cluster dynamics with unprecedented detail. Indeed it has been possible to
detect for the very first time the ionized interstellar medium within a GC (Freire et al., 2001b),
to measure the cluster proper motion as a whole with a better precision than that obtained from
optical studies and to put constrains on the possible presence of an intermediate-mass black hole
by measuring the pulsar (PSR) line of sight accelerations (Freire et al., 2017). All the PSRs with
a precise timing position have also an X-ray counterpart, whose emission is usually dominated by
the blackbody radiation of the extremely hot neutron star (NS) surfaces (Bogdanov et al., 2006).
The optical counterparts to the canonical MSP 47TucU and to the redback (RB) system 47TucW
have been already identified in the past (Edmonds et al., 2001, 2002).

In this chapter we describe the identification and the properties of four new MSP companions
in 47 Tucanae and we present the follow-up study of two previously known companions. In
Table 6.1 we report the main radio timing properties of the analyzed objects, which are useful in
the following discussions.

## 6.2   Optical Photometry of the Star Cluster

### 6.2.1   Observations and data analysis

The identification of the MSP companions has been performed through an ultra-deep, high
resolution, photometric dataset acquired under GO 12950 (P.I: Heinke) with the UVIS camera of
the Wide Field Camera 3 (WFC3) mounted on the Hubble Space Telescope (HST). The dataset
consists of 8 images in the F390W filter, with exposure times of $567 - 590$ s, and 24 images in the
LP F300X filter, with exposure times of $604 - 609$ s.

---

[1]Please visit `http://www.naic.edu/~pfreire/GCpsr.html`, for a complete list of the main radio timing proper-
ties of MSPs in GCs.

Table 6.1. Radio timing ephemeris of the analyzed MSPs

| MSP | $\alpha$ (h m s) | $\delta$ (° ′ ″) | Offset (′) | $P_b$ (d) | $f$ (M$_\odot$) | $M_{COM}^{min}$ (M$_\odot$)[a] | $\tau_c$ (Gyrs) |
|---|---|---|---|---|---|---|---|
| 47TucH | 00 24 6.7032(2) | -72 04 6.8067(6) | 0.77 | 2.36 | $1.927 \times 10^{-3}$ | 0.168 | > 1.9 |
| 47TucI | 00 24 7.9347(2) | -72 04 39.6815(7) | 0.28 | 0.23 | $1.155 \times 10^{-6}$ | 0.0132 | 0.6 |
| 47TucQ | 00 24 16.4909(1) | -72 04 25.1644(6) | 0.95 | 1.19 | $2.374 \times 10^{-3}$ | 0.181 | > 5.0 |
| 47TucS | 00 24 3.9794(1) | -72 04 42.3530(4) | 0.21 | 1.20 | $3.345 \times 10^{-4}$ | 0.091 | > 1.3 |
| 47TucT | 00 24 8.5491(5) | -72 04 38.932(3) | 0.32 | 1.13 | $2.030 \times 10^{-3}$ | 0.171 | > 0.43 |
| 47TucU | 00 24 9.8366(1) | -72 03 59.6882(4) | 0.94 | 0.43 | $8.532 \times 10^{-4}$ | 0.126 | 3.8 |
| 47TucW | 00 24 6.058(1) | -72 04 49.088(2) | 0.09 | 0.13 | $8.764 \times 10^{-4}$ | 0.123 | > 1.15 |
| 47TucY | 00 24 1.4026(1) | -72 04 41.8363(4) | 0.37 | 0.52 | $1.178 \times 10^{-3}$ | 0.141 | > 3.1 |

Note. — From left to right: MSP name, position, offset from the GC center, orbital period, mass function and characteristic age. Numbers in parentheses are uncertainties in the last digits quoted. Reference: Ridolfi et al. (2016); Freire et al. (2017).

[a]Computed assuming an orbital inclination angle of 90° and a PSR mass of 1.4 M$_\odot$.

The standard photometric analysis has been performed, following the prescription reported in Chapter 2.3, on the "flt" images, which are corrected for flat field, bias and dark counts[2]. These images have been further corrected for "Pixel-Area-Map"[3] with standard IRAF procedures. The photometric analysis of the images resulted in the creation of a catalog of the cluster sources detectable dataset images, with instrumental positions and magnitudes. The latter have been calibrated to the VEGAMAG system by using the zero points quoted in the WFC3 Data Handbook and by performing aperture corrections (see Chapter 2.3).

### 6.2.2 Astrometry

Since the WFC3 images suffer from geometric distortions, we corrected the instrumental positions ($x$,$y$) following Bellini et al. (2011). In order to transform the instrumental positions into the absolute astrometric system ($\alpha$,$\delta$), we used, first of all, the wide field catalog presented in Ferraro et al. (2004). Its astrometric solution has been improved by using `CataXcorr` to cross-correlate it with the UCAC4 astrometric standard catalog (Zacharias et al., 2013; ~ 4600 stars have been found in common between the two catalogs). The latter is based on the International Celestial Reference System, thus allowing a more appropriate comparison with the MSP positions derived from timing using solar system ephemerides (which are referenced to the same system). The newly astrometrized wide field catalog has then been used as a secondary reference frame to astrometrize the WFC3 data set, by means of ~ 22000 stars in common. The resulting $1\sigma$ astrometric uncertainty is 0.10″ and 0.11″ in $\alpha$ and $\delta$, respectively. Thus the final total astrometric

---

[2]"flc" images, corrected also for charge transfer efficiency, were not available at the time this work was performed.
[3]For more details see the WFC3 Data Handbook.

uncertainty is ~ 0.15''. Unfortunately, there are only few stars in common between the WFC3 and
the UCAC4 catalogs, since the latter does not cover the cluster central regions. This prevented
a direct cross-correlation between the two catalogs and thus we could not take into account
the stellar proper motions between the two observation epochs, which would have reduced the
astrometric uncertainty.

### 6.2.3   Identification of the MSP companions

First of all, in order to search for the companions to the MSPs in 47 Tucanae, we checked the
precision of our astrometric solution re-identifying the two companion stars already known in
the cluster (see Edmonds et al., 2001, 2002). To this aim, we performed a detailed analysis of
all the detectable objects within a $5'' \times 5''$ wide region centered on the nominal position of each
MSP. The companion to 47TucU (COM-47TucU; hereafter all the companions will be named as
COM-47Tuc followed by the letter of the respective MSP) and 47TucW have been re-identified in
stellar sources located at 0.06'' from the MSP nominal positions. Both the identifications turn
out to be largely within our astrometric uncertainty, thus confirming the accuracy of the adopted
astrometric solution. The finding charts of these two reference objects are shown in Figure 6.1.

Following the same procedure, we searched for the companions to all the other MSPs with a
known position (Ridolfi et al., 2016; Freire et al., 2017). Stars located within the $2\sigma$ uncertainty
from the PSR position have been considered as possibile counterparts. Four companions (to
47TucQ, 47TucS, 47TucT and 47TucY) have been identified on the basis of their positional
coincidence (all of them are located at a distance $\leq 0.06''$ from the nominal radio position) and of
their position in the color-magnitude diagram (CMD). Two faint stars have been detected also
within the $2\sigma$ uncertainty circle from 47TucI and 47TucH. However, their distances (0.15'' and
0.24'' respectively) from the PSR radio positions are significantly larger than in all the other
cases, thus casting doubts about these objects being the true optical counterparts (see more
discussion in Section 6.3.2). The finding charts of all these objects are shown in Figure 6.1 and
their main photometric properties are reported in Table 6.2. Their location in the cluster CMD is
shown in Figure 6.2, where only the stars with a sharpness parameter[4] $|sh| \leq 0.05$ are plotted.
As can be seen, with the exception of the candidate companion to 47TucI, all the newly identified
counterparts are located in the region where He white dwarfs (WDs) are expected, although the
candidate companion to 47TucH could be compatible also with the CO WD cooling sequence (see
Section 6.3.2). Since the radio timing properties suggest that these systems are the product of
the canonical recycling scenario, their location along the He WD cooling sequences guarantees
their connection with the MSPs. Note in fact that the probability of a chance coincidence with
another He WD is extremely low (P $\approx$ 0.1%)[5], since these objects can only be the product of the

---

[4]The sharpness parameter is a DAOPHOT II output that quantifies the stellar-like structure of each object fitted
with the PSF model. See the User Manual for more details.

[5]The chance coincidence probability has been evaluated predicting the number He WD expected within a radius
equal to the $2\sigma$ astrometric uncertainty. We derived the He WD density by direct counting of the all objects located
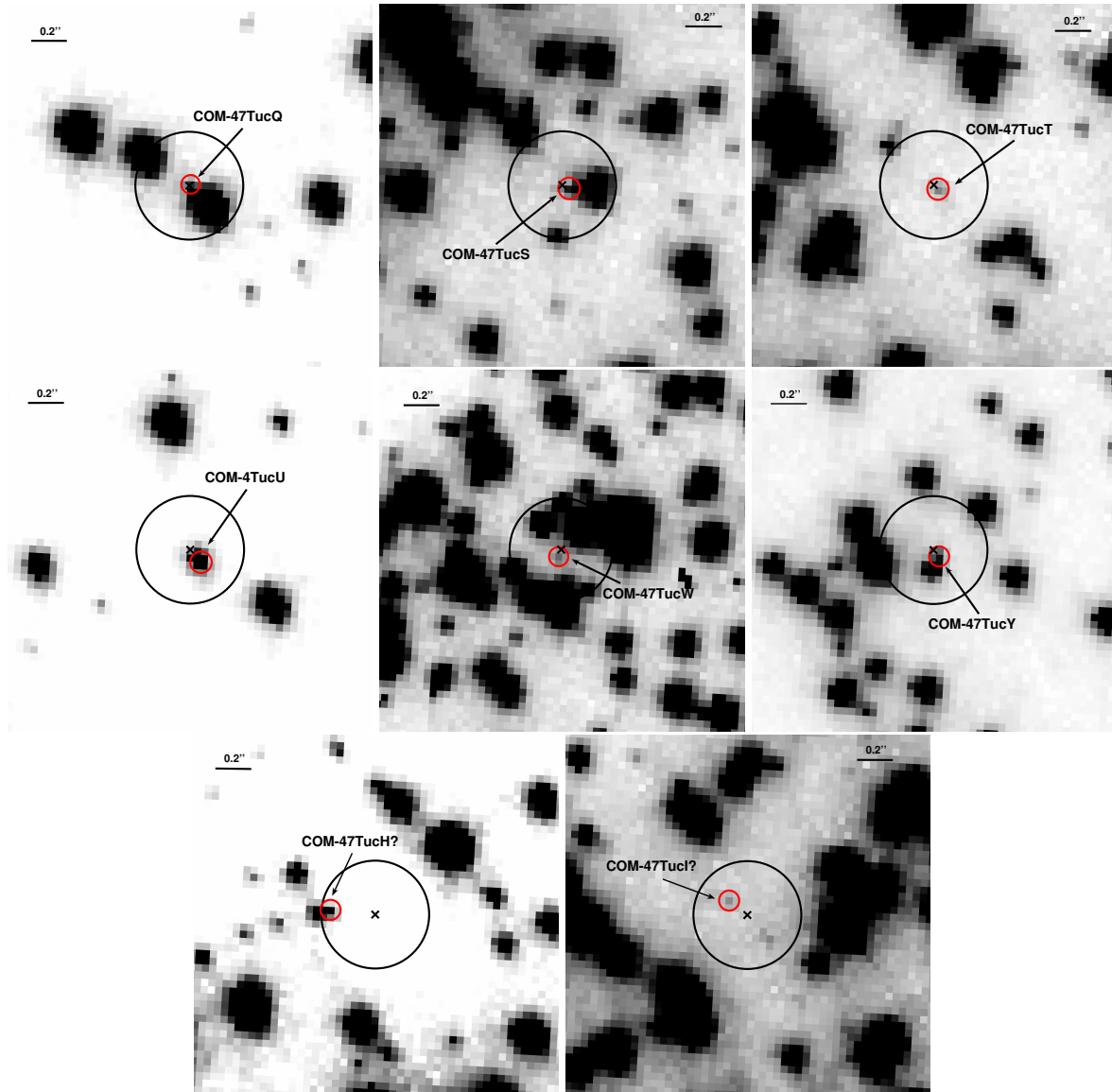
Figure 6.1: HST images of the 2" × 2" region around the nominal position of the seven MSPs analyzed in this chapter. North is up and east is left. All the charts are obtained from a combinations of the available F300X images, with the exception of that of 47TucW that is from an image where the companion star is at its maximum luminosity. The black circles are centered on the radio PSR nominal position in the optical astrometric system and their radii are equal to our 2σ astrometric uncertainty (0.30"). The red circles mark the identified MSP companions.

Figure 6.2: UV CMD of the GC 47 Tucanae. Only stars with sharpness parameter $|sh| \leq 0.05$ are plotted. The blue solid squares mark the companions to the canonical MSPs. The possible counterparts to 47TucH and 47TucI are plotted as an open square and circle respectively. Since COM-47Tuc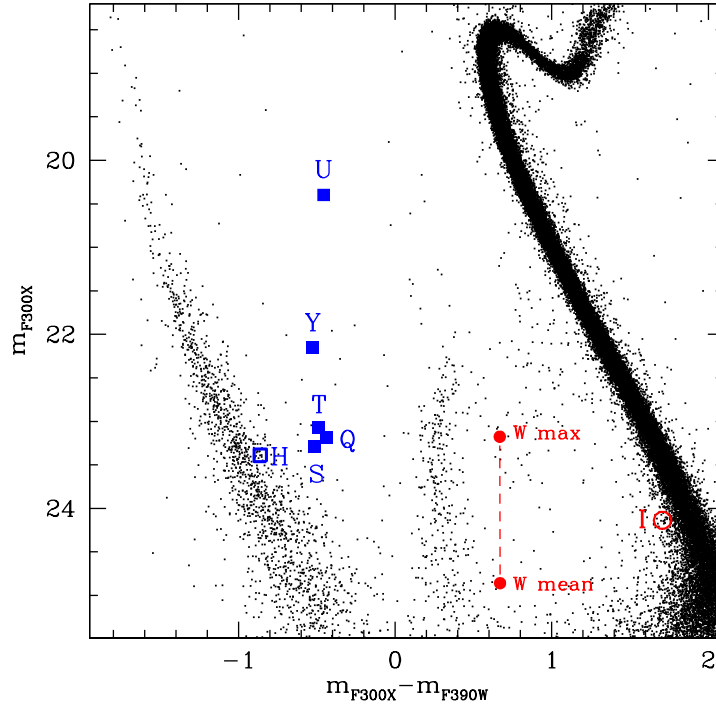W is a strongly variable object, we report its position at the maximum and mean luminosities, as derived by the best-fit models (see Section 6.3.4 and Figure 6.6).

late stage of the evolution of exotic objects like, for example, MSPs and cataclysmic variables. The candidate companion to 47TucI is instead a main sequence-like object, and its properties will be briefly discussed in Section 6.3.2. As concerns the previously known companions, COM-47TucU is also located along the He WD sequence, while the RB COM-47TucW is located in an anomalous region between the main sequence and the WD cooling sequence (see Section 6.3.4).

With the exception of the COM-47TucW, no significant variability related to the orbital period has been detected. For 47TucU, 47TucY and 47TucW (see Section 6.3.4) the observations sample a significant fraction of the orbital period. Instead, for the other systems (with orbital periods longer than 1 day) the coverage is too poor to allow any appropriate variability analysis. However, a strong magnitude modulation, as the one observed for non degenerate companions (see e.g. Stappers et al., 1999; Edmonds et al., 2002; Reynolds et al., 2007; Pallanca et al., 2010; Romani,

---

among the cooling tracks (see Section 6.3.1 and Figure 6.3) and dividing this number by the size of the WFC3 field of view. Please note that even including all the stars of the catalog with sharpness $|sh| > 0.05$, the chance probability remains $\lesssim 0.5\%$.

Table 6.2. Optical properties of the companion stars

| Name | $\alpha$ (h m s) | $\delta$ (° ′ ″) | dist (″) | $m_{F300X}$ | $m_{F390W}$ |
|------|------|------|------|------|------|
| COM-47TucQ | 00 24 16.489 | -72 04 25.209 | 0.04 | $23.19 \pm 0.02$ | $23.63 \pm 0.05$ |
| COM-47TucS | 00 24 3.977 | -72 04 42.385 | 0.03 | $23.29 \pm 0.02$ | $23.80 \pm 0.05$ |
| COM-47TucT | 00 24 8.549 | -72 04 38.965 | 0.04 | $23.07 \pm 0.02$ | $23.56 \pm 0.03$ |
| COM-47TucU | 00 24 9.835 | -72 03 59.746 | 0.06 | $20.40 \pm 0.01$ | $20.85 \pm 0.03$ |
| COM-47TucW | 00 24 6.063 | -72 04 49.133 | 0.06 | $24.28^{a}$ | $23.62^{a}$ |
| COM-47TucY | 00 24 1.401 | -72 04 41.875 | 0.04 | $22.16 \pm 0.02$ | $22.69 \pm 0.04$ |
| COM-47TucH? | 00 24 6.755 | -72 04 6.781 | 0.24 | $23.39 \pm 0.02$ | $24.25 \pm 0.05$ |
| COM-47TucI? | 00 24 7.953 | -72 04 39.559 | 0.15 | $24.14 \pm 0.04$ | $22.43 \pm 0.03$ |

Note. — From left to right: MSP companion name, position, distance from the radio MSP nominal position, F300X and F390W magnitudes and the relatives uncertainties.

[a]The values for COM-47TucW correspond to the mean magnitudes of the best-fit models (see Figure 6.6).

Shaw, 2011; Pallanca et al., 2014; Cadelano et al., 2015b), is not expected and usually not observed for degenerate objects, since the flux enhancement due to re-heating of the companion star by the PSR emitted energy is negligible.

## 6.3 Discussion

### 6.3.1 The physical properties of the He WD companions

In order to constrain the main properties of the He WD companions, we have compared the position of each candidate in the CMD with a set of He WD cooling tracks computed by Althaus et al. (2013). These models span a mass range from $0.15\,M_\odot$ to $0.43\,M_\odot$, spaced at about $0.005\,M_\odot$ for masses between $0.15\,M_\odot$ to $0.19\,M_\odot$ and up to $0.07\,M_\odot$ for larger masses. We transformed the theoretical luminosities and temperatures into the absolute F300X and F390W magnitudes, by applying the bolometric corrections kindly provided by P. Bergeron (see Holberg, Bergeron, 2006; Bergeron et al., 2011). Then, the model absolute magnitudes have been transformed into the apparent ones by using the distance modulus $(m-M)_0 = 13.32 \pm 0.10$ (Ferraro et al., 1999)[6]. and the color excess $E(B-V) = 0.04 \pm 0.02$ (Ferraro et al., 1999; Zoccali et al., 2001; Salaris et al., 2007) and extinction coefficients $A_{F300X}/A_V = 1.77309$, $A_{F390W}/A_V = 1.42879$ (Cardelli et al., 1989; O'Donnell, 1994). Figure 6.3 shows the zoomed portion of the CMD in the WD region with a sample of cooling tracks for different masses overplotted. As can be seen, the range in mass of the models is large enough to properly sample the portion of the CMD where all the companions

---

[6] Many literature works reported on different values of 47 Tucanae distance modulus (see, e.g. Woodley et al., 2012, and references therein). However, all these possibile values have only a minimal influence on our derived companion properties (e.g. the derived companion masses would vary of less than ∼ 7% for all the companion stars)
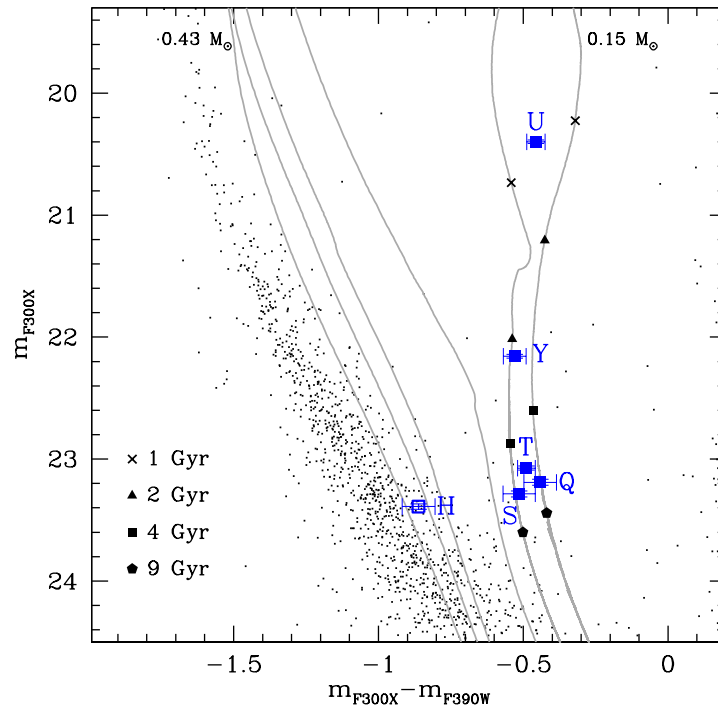
Figure 6.3: Same as in Figure 6.2, but zoomed into the WD region. The continuous curves are
reference He WD cooling tracks for stars of 0.15 $M_\odot$, 0.17 $M_\odot$, 0.20 $M_\odot$, 0.32 $M_\odot$, 0.36 $M_\odot$ and
0.43 $M_\odot$ (from right lo left). For the two rightmost tracks, points at 1,2,4 and 9 Gyrs have been
marked with different symbols. The photometric errors of the companion stars are also drawn.

are located. Therefore we used this set of models to derive the combinations of parameters (mass,
cooling age and temperature) that simultaneously satisfy the observed photometric magnitudes
in both the filters, also taking into account the uncertainties on the companion magnitudes,
distance modulus and reddening. The best values have been evaluated with a simple $\chi^2$ statistic.
In doing this, linear interpolations (for different masses but equal ages) among the tracks have
been performed in order to have a tighter mass sampling. We assumed that each companion is
located at the distance of 47 Tucanae[7] and it is affected by the same extinction[8]. Figure 6.4 shows,
for each system, the combination of cooling age (left panel), temperature (central panel) and
PSR mass (right panel) appropriate for the derived value of the companion mass. In particular,
in each plot the right panel shows the results obtained for different values of the inclination
angle and interesting constraints on each system can be drawn. For instance, by setting the
inclination angle to 90°, the maximum PSR mass allowed from the inferred companion mass can

---

[7]Even though Freire et al. (2001b) measured distance offsets between the cluster MSPs, such differences are very
small and can be neglected for our goals.

[8] The effects of differential reddening are negligible for our goals (see Milone et al., 2012b,a).
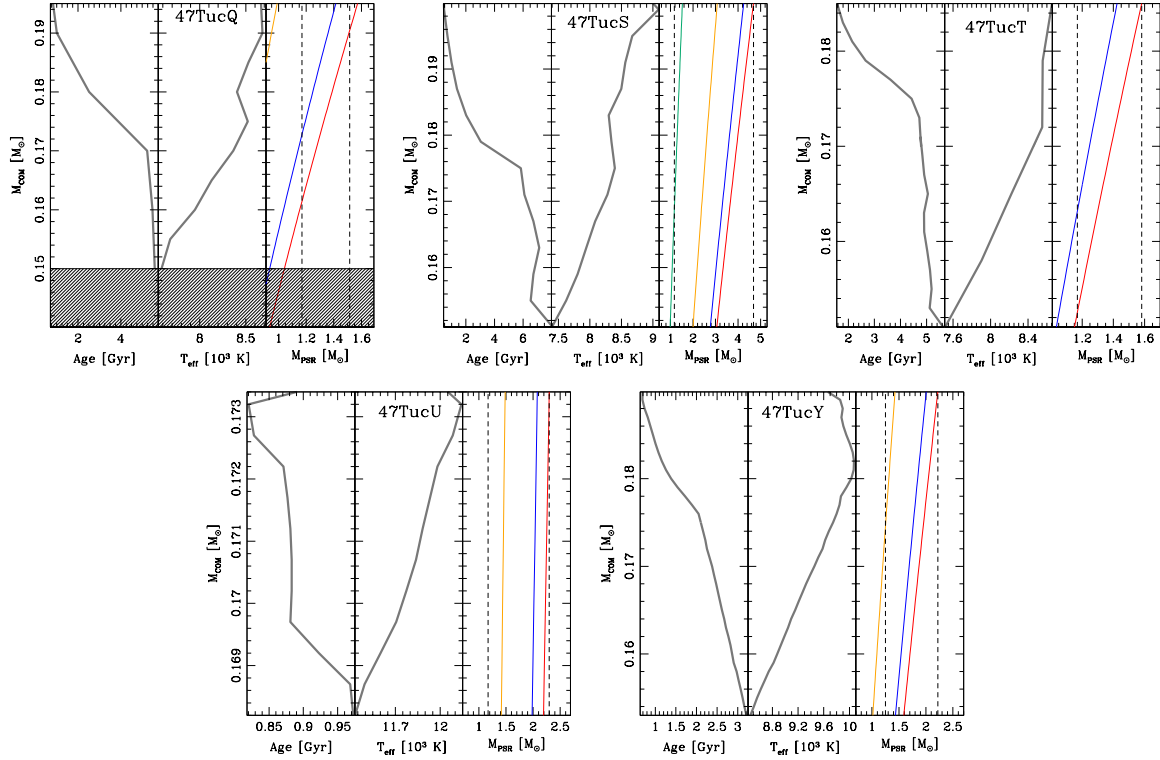
Figure 6.4: Physical properties of 47TucQ, 47TucS, 47TucT, 47TucU and 47TucY (see labels), as derived from the comparison between the photometric characteristics of each companion and the WD cooling track models. In each plot, the gray lines drawn in the left and central panels show the allowed combinations between companion mass and cooling age or temperature (see text). In the case of COM-47TucQ the shaded area marka the region not allowed by the theoretical cooling tracks. In the rightmost panel of each plot, the solid curves represent the combination of values allowed by the PSR mass function for different inclination angles ($i = 90°$ in red, $i = 70°$ in blue, $i = 50°$ in orange, and $i = 30°$ in green). The blue dashed lines correspond to the assumed minimum NS mass ($\sim 1.17\,\mathrm{M_\odot}$; Janssen et al., 2008) and the largest NS mass value obtained for $i = 90°$.

be evaluated. Conversely, by assuming the minimum PSR mass equal to $1.17\,\mathrm{M_\odot}$ (the lowest mass ever measured for a NS; Janssen et al., 2008), a conservative lower limit to the inclination angle can be derived. All these results are also summarized in Table 6.3[9]. Note that we are not analyzing here the cases of 47TucH and 47TucI, which we will discuss in Section 6.3.2.

As can be seen, all the companions have masses between $\sim 0.15\,\mathrm{M_\odot}$ and $\sim 0.2\,\mathrm{M_\odot}$. The derived ranges of ages are in agreement with the lower limits to the PSR characteristic ages reported in

---

[9]The reader should be aware that the WD parameters should not be assumed at face value as perfectly correct but as estimations, since they are model dependent and could also suffer from some hardly quantifiable uncertainty linked to the bolometric corrections.

Table 6.3.  Derived properties of the five MSPs with He WD companions

| Parameter | 47TucQ | 47TucS | 47TucT | 47TucU | 47TucY |
|---|---|---|---|---|---|
| $M_{COM}$ (M$_\odot$) | $0.150 - 0.195$ | $0.150 - 0.200$ | $0.150 - 0.185$ | $0.168 - 0.173$ | $0.150 - 0.190$ |
| Age (Gyr) | $0.7 - 5.5$ | $0.4 - 8.1$ | $1.6 - 6.0$ | $0.82 - 0.93$ | $0.6 - 3.2$ |
| $T$ ($10^3$ K) | $7.5 - 8.7$ | $7.4 - 9.1$ | $7.5 - 8.6$ | $11.4 - 12.1$ | $8.4 - 10.1$ |
| $L$ ($10^{-3}$ L$_\odot$) | $8.6 - 9.7$ | $7.8 - 9.1$ | $9.4 - 10.5$ | $141 - 165$ | $22.5 - 23.5$ |
| $M_{PSR}$ (M$_\odot$) | $< 1.57$ | $< 4.69$ | $< 1.58$ | $< 2.30$ | $< 2.22$ |
| $i$ (°) | $> 58$ | $> 26$ | $> 57$ | $> 42$ | $> 45$ |

Note. — From top to bottom: companion mass, age, temperature, luminosity, PSR mass and incli-
nation angle.
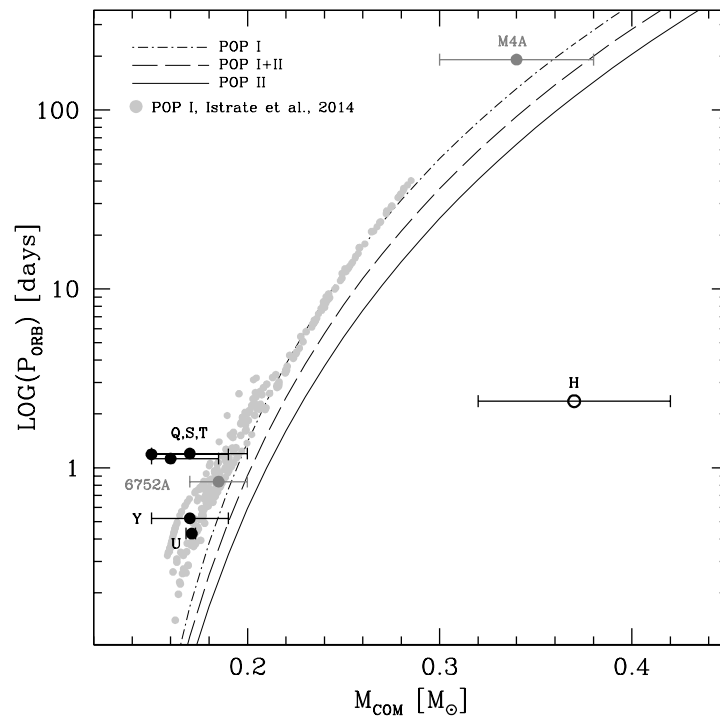


Figure 6.5: MSP orbital periods plotted as a function of the best-fit companion masses, for each
identified object, plus the ones detected in NGC 6752 and M4 (dark gray points; see Ferraro
et al., 2003a; Sigurdsson et al., 2003). The three curves correspond to the theoretical predictions
of Tauris, Savonije (1999) for three different stellar population progenitors, as reported in the
top-left legend. The light gray points correspond to the theoretical results obtained by Istrate
et al. (2014).

Table 5.2. The only exception is COM-47TucU, which is discussed below. In principle the mass of COM-47TucQ could be smaller than our best-fit value ($0.15 \, M_\odot$), since not theoretical tracks for masses below this value are available. However, already a $0.15 \, M_\odot$ companion would imply an extremely low value of the PSR mass ($\lesssim 1 \, M_\odot$). This puzzling result could be partially explained with the difficulty of accurately determine the color of the optical counterpart, because of the presence of a very close bright object (see Figure 6.1).

Our results rule out a massive NS in the case of 47TucQ and 47TucT, while the possibility of a $\sim 2 \, M_\odot$ NS remains opened in the cases of 47TucS, 47TucU and 47TucY. However, Figure 6.4 shows that the PSR mass can be significantly reduced by assuming an intermediate-low inclination angle of the orbital plane. In any case these systems are worthy of future, especially spectroscopical, investigations.

We also compared our results with the theoretical predictions on the behavior of the orbital period as a function of the companion mass discussed in Tauris, Savonije (1999). Such a model has been already empirically verified by Corongiu et al. (2012) and Bassa et al. (2006). As shown in Figure 6.5, where we also added the two He WD companions identified in NGC 6752 and M4 (see Ferraro et al., 2003a; Sigurdsson et al., 2003), our results are in reasonable agreement with the model. The analytical prediction seems to slightly overestimate the companion mass or to underestimate the system orbital period. However, this model is valid for binary systems with $0.18 \, M_\odot < M_{WD} < 0.45 \, M_\odot$, thus only marginally representative of our sample, where most of the companions appear to be less massive than $0.18 \, M_\odot$. More updated models (from Istrate et al. 2014; gray points in Figure 6.5) are in better agreement, although they are the results of simulations of donor stars with metallicity Z = 0.02, larger than that of 47 Tucanae (i.e. Z = 0.008, Lapenna et al., 2015).

The brightness of COM-47TucU allowed us to put tighter constraints to the system parameters with respect to the other objects. Both its mass and temperature are in excellent agreement with those reported in Edmonds et al. (2001), while our derived age ($\approx 0.9 \, \mathrm{Gyr}$) turns out to be 0.3 Gyr larger than their estimate. Such a discrepancy could be due to the different theoretical models used. However, as already noticed by Edmonds et al. (2001), the cooling age is significantly lower than the characteristic age of 3.8 Gyr (see Table 6.1). This discrepancy should not alarm, since the PSR characteristic ages are based on many assumptions and large deviations from the companion cooling ages are commonly observed (see e.g. Lorimer, Kramer, 2004; Tauris et al., 2012; Tauris, 2012). Using the WD age together with the intrinsic spin period derivative $\dot{P} = 2.7 \pm 0.5 \times 10^{-20}$ (Freire et al., 2017) and the actual spin period $P \approx 4.343 \, \mathrm{ms}$, we evaluated a MSP birth spin period (the so-called equilibrium spin period) of $P_0 \approx 3.576 \, \mathrm{ms}$. This value, combined with the surface magnetic field $B \approx 3.145 \times 10^8 \, \mathrm{G}$ and assuming a NS with a radius of 10 km and a canonical mass of $1.4 \, M_\odot$, can be used to infer the typical accretion rate that reaccelerated the NS during the low-mass X-ray binary phase. By using equation (8) of Van den Heuvel (2009), we find that the system past accretion history likely proceeded at a sub-Eddington rate ($\dot{M}/\dot{M}_{EDD} \sim 0.02$),

as expected from the typical evolution of close binary systems with light donor stars (Tauris, Savonije, 1999; Istrate et al., 2014). Although the mass accretion rate strongly depends on the NS radius, the general result does not change assuming different radii or even different NS masses.

### 6.3.2  Possible candidate companion stars

As can be seen from Figures 6.2, 6.3 and 6.5, the possible companion to 47TucH appears to have properties quite different from those observed for the other companions, first of all its much larger distance from the MSP nominal position (0.24"), which corresponds to almost twice our astrometric uncertainty. Moreover, following the procedure adopted in the previous section, we derived for this object a mass of $0.37 \pm 0.05$ M$_\odot$. This value, combined with the binary system total mass of 1.66 M$_\odot$ (Freire et al., 2003), would imply a PSR mass of $\sim 1.29$ M$_\odot$, a value slightly lower than expected for a recycled PSR, although still acceptable within the uncertainties. Its position in the CMD is compatible also with the CO WD cooling sequence, which would increase the probability of a chance coincidence to $\sim 2 - 3\%$. Furthermore, at odds with the others objects, this candidate counterpart occupies an anomalous region in the orbital period companion mass plane shown in Figure 6.5. Although this anomaly could be real (since 47TucH has a large eccentricity, probably due to some kind of dynamical interaction), all these pieces of evidence suggest that the observed object is probably an isolated WD and the true companion star is still under the detection threshold (see Section 6.3.3).

A possible candidate companion to MSP 47TucI has been also detected (see Figure 6.1 for the finding chart). This is a binary system with a short orbital period ($\sim 0.23$ days) and a very small eccentricity. From the PSR mass function, the companion is expected to be a very low-mass star ($M_{COM} \sim 0.015$ M$_\odot$). The absence of radio eclipses, probably due to a low inclination angle, prevents its characterization as a black-widow (BW) system. At 0.15" from the PSR position, we identified a star located at the faint-end of the cluster main sequence (see Figure 6.2 and Table 6.2). If we assume that the companion is a bloated star seen in a binary system with a low inclination angle, such a CMD position could be reasonable. However, the lack of any significant variability related to the orbital period prevents us from firmly associating this candidate to the MSP. In fact, the orbital period coverage of the F390W images is too poor, while the signal to noise ratio of the F300X data allows us to only infer that, in case of photometric variability, the maximum variation amplitude must be smaller than $\sim 0.8$ mag. We therefore conclude that it is more likely that the real companion star is still under the detection threshold. Indeed, the probability of a chance coincidence with a main sequence star is non negligible ($\sim 45 - 50\%$). We finally note that another object lies within the astrometric uncertainty circle, but its association with the MSP can be excluded, since it is a common CO WD, with properties incompatible with the MSP timing ephemeris.

### 6.3.3 Non detections

No interesting counterparts have been identified for all the other known binary MSPs. These non-detections are likely due to companion stars still under the detection threshold (as in the case, e.g., of 47TucE and the BW 47TucJ), or to the severe crowding conditions of the area surrounding the MSP positions (as in the case of the BWs 47TucO and 47TucR). No search could be performed for 47TucX since its position is outside the field of view.

Considering that the companion to 47TucJ should be a non-degenerate object, its non-detection in UV passbands cannot be used to get useful information on its properties. Instead, the counterpart to 47TucE is expected to be He WD, which remains undetected down to our limiting magnitudes ($\sim 25$ in the F300X filter and $\sim 25.5$ in the F390W filter). Hence, taking into account that the cooling age of a $\sim 0.17\,M_\odot$ WD at these detection thresholds is larger than the cluster age ($\sim 10 - 11$ Gyr; Gratton et al., 2003; Hansen et al., 2013), it is unlikely that this star has a mass similar to that estimated for the other companions. It is more probable that it is more massive than $0.2\,M_\odot$ (corresponding to a faster cooling) and its cooling age is larger than 1 Gyr. The same should apply also to the case of 47TucH if its true companion is still under our detection limits (as suggested above). Interestingly, according to the theoretical relation of Tauris, Savonije (1999) and the orbital periods of 47TucE and 47TucH ($\sim 2.3$ and $\sim 2.4$ days, respectively), the companions to both these MPSs are indeed expected to have masses $\gtrsim 0.2\,M_\odot$.

### 6.3.4 The companion to the RB 47TucW

47TucW is the only RB in 47 Tucanae with an available timing solution. It is a binary MSP with a spin period of 2.35 ms, an orbital period of $\sim 3.2$ hr and a companion mass of $\sim 0.15\,M_\odot$. The first optical identification of this system was presented in Edmonds et al. (2002), who suggested that the companion is a perturbed and non degenerate star with a light curve structure indicating a strong heating by the PSR flux. In Figure 6.6 we show, for both the filters, the light curves we obtained by folding our photometric measurements with the most updated radio timing ephemeris (Freire et al., 2017). The zero orbital phase has been set at the PSR ascending node time[10]. As can be seen, in agreement with previous works (Edmonds et al., 2002; Bogdanov et al., 2005), the light curves present a single maximum-minimum structure, likely due to the heating by the PSR flux. Unfortunately, the star has been measured above the detection threshold only near its maximum luminosity. Nonetheless, modeling[11] the sinusoidal light curve, we found that, in both the filters, the companion spans $\sim 3.5$ magnitudes between the maximum and the derived minimum, in agreement with previous observations. The best fit-model is shown as a solid curve in Figure 6.6. Interestingly, the light curve structure is more similar to the ones observed for BWs than for RBs companions, which usually, but not always, show a double minimum-maximum structure due

---

[10]Please note that we are using a different formalism with respect to Edmonds et al. (2002).

[11]We used the "Graphical Analyzer for TIme Series", a software aimed at studying stellar variability phenomena, developed by Paolo Montegriffo at INAF-Osservatorio Astronomico di Bologna.
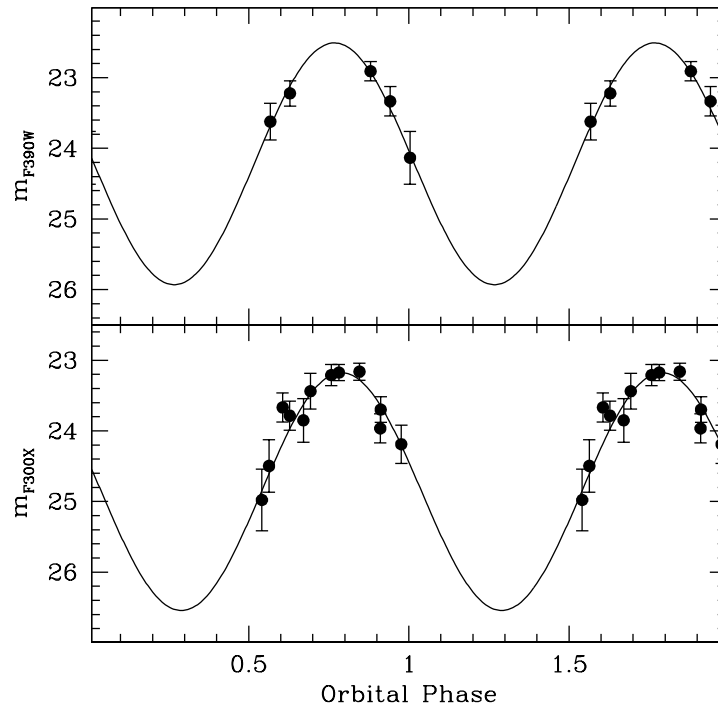
Figure 6.6: Light curves of COM-47TucW in the F390W (upper panel) and F300X (lower panel). The two curves are folded with the radio parameters and two periods are shown for clarity. The black curve in each panel is the best analytical model obtained independently for each filter.

to tidal deformation (see e.g. Ferraro et al., 2003a; Cocozza et al., 2008; Pallanca et al., 2010; Li et al., 2014). The CMD position of the companion during the maximum and at a mean phase (as derived by the adopted model) is shown in Figure 6.2. The system is located between the main sequence and the WD cooling sequence, where no normal stars are expected and thus suggesting a perturbed and strongly heated companion star. Again, at odds with other RB systems, this lies in a region more similar to that occupied by the two BW companions identified so far in GCs (Pallanca, 2014, Cadelano et al., 2015). The X-ray counterpart to 47TucW shows a variability which is likely due to an intra-binary shock between the PSR wind and the matter lost by the companion (Bogdanov et al., 2005). Interestingly, as discussed by Bogdanov et al. (2006), the minimum of the X-ray light curve is displaced with respect to the optical one. Such a behavior has been also noticed for the BW M71A (Cadelano et al., 2015b), thus further strengthening the connection of this MSP with BW systems. All this allows us to speculate that a scenario where 47TucW will evolve into a canonical MSP with a He WD companion (as in the case of MSP-A in NGC 6397; see Burderi et al., 2002) is somewhat unlikely, opening the possibility to an evolution toward the BW stages. Indeed such an evolutionary path has been already suggested by the simulations of Benvenuto et al. (2014). The identification of new RB companions will shed light

on this possibility.

# 7

# The Optical Counterpart to the Accreting Millisecond X-ray Pulsar SAX J1748.9-2021 in the Globular Cluster NGC 6440

*Mainly based on Cadelano et al. 2017b, ApJ, 844:53C*

W e used a combination of deep optical and Hα images of the Galactic globular cluster NGC 6440, acquired with the Hubble Space Telescope, to identify the optical counterpart to the accreting millisecond X-ray pulsar SAX J1748.9-2021 during quiescence. A strong Hα emission has been detected from a main sequence star (hereafter COM-SAX J1748.9-2021) located at only 0.15" from the nominal position of the X-ray source. The position of the star also agrees with the optical counterpart found by Verbunt et al. (2000) during an outburst. We propose this star as the most likely optical counterpart to the binary system. By direct comparison with isochrones, we estimated that COM-SAX J1748.9-2021 has a mass of $0.70\,\mathrm{M_\odot} - 0.83\,\mathrm{M_\odot}$, a radius of $0.88 \pm 0.02\,\mathrm{R_\odot}$ and a superficial temperature of $5250 \pm 80$ K. These parameters combined with the orbital characteristics of the binary suggest that the system is observed at a very low inclination angle ($\sim 8° - 14°$) and that the star is filling or even overflowing its Roche-Lobe. This, together with the equivalent width of the Hα emission ($\sim 20$ Å), suggest on-going mass transfer. The possible presence of such an on-going mass transfer during a quiescence state also suggests that the radio pulsar is not active yet and thus this system, despite its similarity with the class of redback millisecond pulsars, is not a transitional millisecond pulsar.

## 7.1 Introduction

As we described in Chapter 1.5.3, Accreting Millisecond X-ray Pulsars (AMXPs) are a sub-group
of transient low-mass X-ray binaries that show, during outbursts, X-ray pulsations from a rapidly
rotating neutron star. During these outbursts, the matter lost from the companion star via
Roche-Lobe overflow is channeled down from a truncated accretion disk onto the neutron star
magnetic poles, producing X-ray pulsations at frequencies $\nu \geq 100$ Hz (see Patruno, Watts, 2012,
and references therein). Two of these systems are located in the globular cluster (GC) NGC 6440,
the only cluster, together with NGC 2808 and M28, known to host AMXPs. NGC 6440 is located
in the Galactic bulge, above the Galactic plane, at 8.5 kpc from the Sun (Valenti et al., 2007). It
is a metal-rich system ([Fe/H] $\sim -0.5$, Origlia et al. 1997, 2008b) affected by a quite large and
differential extinction, with a mean color-excess $E(B-V) = 1.15$ (Valenti et al., 2004). The cluster
also hosts six (classic) radio millisecond pulsars (MSPs) (Freire et al., 2008a).

SAX J1748.9-2021 was discovered with the *Beppo*SAX/WFC satellite in 1998 as a part of a
program aimed at monitoring the X-ray activity around the Galactic center (In't Zand et al.,
1999). Since its discovery, it has experienced four outbursts, approximately one each five years:
in 2001 (In't Zand et al., 2001), 2005 (Markwardt, Swank, 2005), 2010 (Patruno et al., 2010) and
finally in 2015 (Bozzo et al., 2015). The X-ray pulsar (PSR) has been observed pulsating at a
spinning frequency of $\sim 442$ Hz and these pulsations have been used to obtain a phase-coherent
timing solution (Gavriil et al., 2007; Altamirano et al., 2008; Patruno et al., 2009; Sanna et al.,
2016) which revealed that SAX J1748.9-2021 is a binary system with an orbital period of $\sim 8.76$
hours, a projected semi-major axis of $\sim 0.4$ light-seconds and a companion mass of at least $0.1\,M_\odot$.
Altamirano et al. (2008) suggested that the companion star is more likely a $0.85\,M_\odot - 1.1\,M_\odot$ star,
i.e. a bright main sequence or a slightly evolved star, thus implying a binary system seen at a low
orbital inclination angle. Verbunt et al. (2000) identified the optical counterpart during the 1998
outburst as a blue star with $B \simeq 22.7$. This outburst counterpart was identified through images
obtained with a ground-based telescope and during nonoptimal seeing conditions.

The spin and orbital properties of SAX J1748.9-2021 are similar to those observed in the
emerging class of "transitional millisecond pulsars" (tMSPs, see Chapter 1.5.3): binary systems
that alternate between stages of classical rotation-powered emission, where radio emission is
detected as in a common eclipsing MSPs of the redback (RB) class, and stages of accretion-powered
emission where the radio emission is off and X-ray pulsations are detected like in AMXPs. The
similarity between SAX J1748.9-2021 and the class of tMSPs suggests that this system might be
a tMSP whose radio PSR emission during quiescence has not been revealed yet. In fact, no radio
pulsed emission has been detected from this object, in spite of the radio searches devoted to this
aim (see Patruno et al., 2009). The identification of the optical counterpart during quiescence can
provide crucial information to understand the properties and the nature of the binary system.

## 7.2 Observations and Data Reduction

This work is based on two different datasets of images obtained with the *Hubble Space Telescope* (HST) using the UVIS camera of the Wide Field Camera 3 (WFC3). The first dataset (GO12517, P.I.: Ferraro) has been obtained on July 2012 and it consists of 27 images in the F606W filter with an exposure time of 392 s each and 27 images in the F814W filter with an exposure time of 348 s each. The second dataset (GO13410, P.I.: Pallanca) has been acquired during three different epochs: October 2013, May 2014 and September 2014. Each epoch consists of 5 images in the F606W filter and exposure time of 382 s, 5 images in the F814W filter and exposure time of 222 s and 10 images in the F656N filter and exposure time of 934 s.

We used the images processed, flat-fielded and bias subtracted ("flt" images[1]) by the standard HST pipeline. The photometric analysis has been performed using standard procedures, after correcting the images for "Pixel-Area-Map"[2] and following the prescription described in Chapter 2.3. The resulting instrumental catalog, containing instrumental magnitudes, has been calibrated on the VEGAMAG system using the WFC3 zeropoints publicly available at `http://www.stsci.edu/hst/wfc3/phot_zp_lbn` (Ryan et al., 2016).

The instrumental positions have been corrected for geometric distortions by applying the equations reported in Bellini et al. (2011). In order to transform the instrumental positions to the absolute coordinate system $(\alpha, \delta)$, we used the Pan-STARRS1 catalog of stars (Flewelling et al., 2016) reported, by means of $\sim 120$ in common, to the UCAC4 astrometric standard catalog (Zacharias et al., 2013). Then, this catalog has been used as reference frame to astrometrize the HST dataset, by means of 1200 stars in common. The resulting $1\sigma$ astrometric uncertainty is $\sim 0.15"$ both in $\alpha$ and $\delta$, thus providing a total uncertainty of about $0.21"$.

NGC 6440 is affected by a substantial differential reddening. In order to estimate the extinction variation within the observed field of view, we adopted a method similar to that already applied to other clusters (see Massari et al. 2012). The detailed procedure and the reddening map will be published in a forthcoming paper (Pallanca et al. 2018, in preparation). Here we just briefly describe the procedure. We first selected a sample of reference stars with small photometric errors and values of the sharpness parameter ("well-fitted" stars), located along the cluster evolutionary sequences in the color-magnitude diagram (CMD). These stars have been used to built a "reference" mean ridge line. Then, for each star a mean ridge line has been constructed by using the fifty "well-fitted" stars spatially located close to it. Finally, the shift $\delta E(B-V)$ needed to register this ridge line to the "reference" mean ridge line is computed. The derived extinction map shows absorption clouds with a patchy structure, and extinction variations as large as $\delta(B-V) = 1.0$ mag have been measured. The map has been used to build the differential reddening-corrected CMD used in the following analysis.

---

[1]"flc" images, corrected also for charge transfer efficiency, were not available at the time this work was performed.
[2]For more details see the WFC3 Data Handbook.

## 7.3 Results

In order to search for the optical counterpart to SAX J1748.9-2021, we analyzed all the objects
located within a $3\sigma$ radius ($\sim 2''$) from the X-ray position reported by Pooley et al. (2002), where $\sigma$
is the combined X-ray ($\sim 0.6''$) and optical ($\sim 0.21''$) astrometric uncertainty. The finding charts
of the region around the X-ray nominal position are shown, for all the filters, in Figure 7.1.
We emphasize that in all the epochs sampled by the observations discussed in this thesis,
SAX J1748.9-2021 was in a quiescence state. Thus we did not expect to find a bright star like that
reported in Verbunt et al. (2000). From the analysis of the $H\alpha$ images, we found a quite promising
candidate. In the right panel of Figure 7.2, we show the $(m_{F814W} - m_{F656N}, m_{F606W} - m_{F814W})$
color-color diagram of the entire cluster of stars (small grey dots), with all the stars detected in
the region around the X-ray source position highlighted as large black dots. This diagram has
been found to be particularly powerful in pinpointing $H\alpha$ emitters (Beccari et al., 2014, e.g.). All
the stars detected in the X-ray source region appear to be standard stars, with the only exception
of one object (the red dot) that shows a quite anomalous $H\alpha$ color $(m_{F814W} - m_{F656N}) \sim 1.7$, thus
indicating a strong $H\alpha$ excess (see Section 7.4). This object occupies instead a standard position in
the optical CMD (left panel of Figure 7.2), being located along the cluster main sequence, about $\sim 2$
magnitudes below the turn-off. Interestingly enough, this object is located at $\alpha = 17^h 48^m 52.161^s$
and $\delta = -20°21'32.406''$, at only $\sim 0.15''$ from the nominal position of the X-ray source and it is the
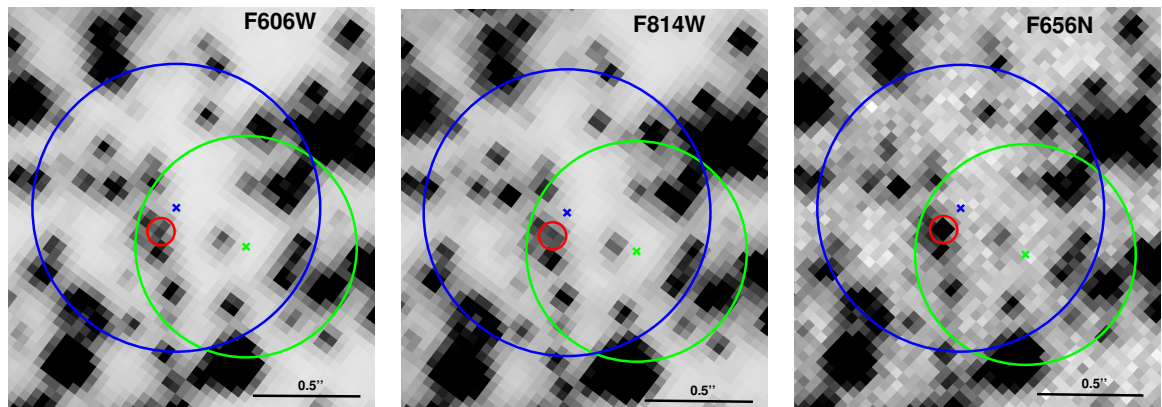


Figure 7.1: Finding charts of the counterpart to COM-SAX J1748.9-2021 (north is up and east is
left). The left, central and right panels are combined images from the F606W, F814W and F656N
expositions, respectively. In all the panels, the blue cross indicates the X-ray nominal position,
while the blue circle, centered on the blue cross, has a radius equal to the combined X-ray and
optical astrometric uncertainty. The green cross is centered on the outburst counterpart reported
by Verbunt et al. (2000) and the circle has a radius equal to their astrometric uncertainty. The
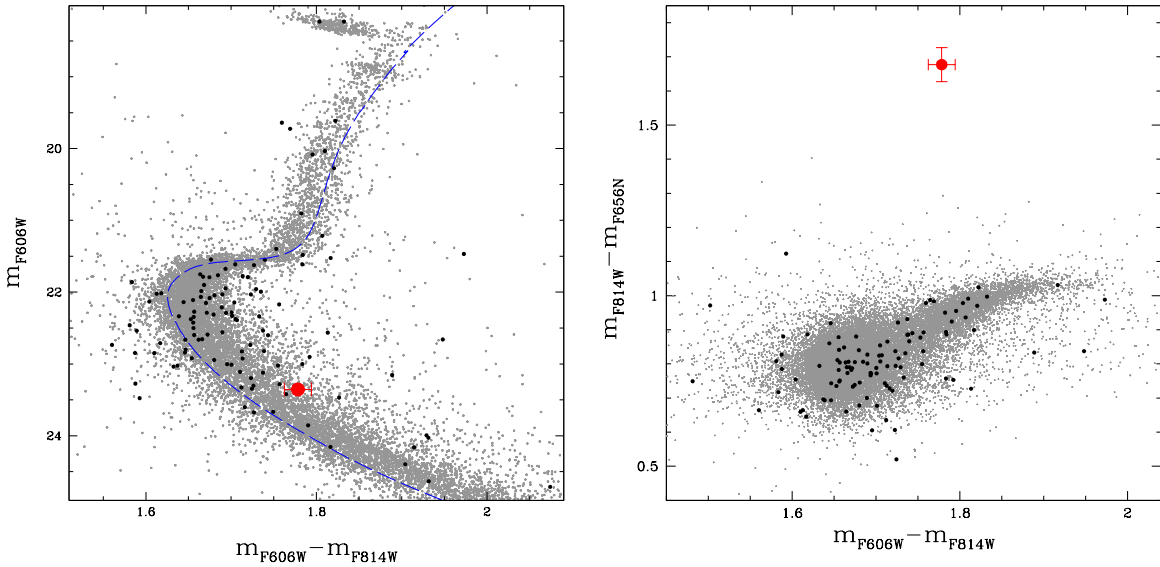solid red circle marks the candidate optical counterpart.

Figure 7.2: *Left Panel:* $(m_{F606W}, m_{F606W} - m_{F814W})$ differential reddening corrected CMD of NGC 6440. The stars within 2" from the nominal position of the X-ray source are shown as big black dots. Cluster stars detected in the WFC3 field of view are plotted in grey. The dashed blue curve is the best fit isochrone (see Section 8.3) and the red point is the mean position of COM-SAX J1748.9-2021 in the four epochs. *Right Panel:* $(m_{F814W} - m_{F656N}, m_{F606W} - m_{F656N})$ cluster color-color diagram. The symbols are as in the upper panel.

closest star to the X-ray position. Its location is also consistent with that of the burst counterpart proposed by Verbunt et al. (2000): in fact, the distance between our and their counterpart is $\sim 0.35"$, smaller than the quoted uncertainty of the latter ($\sim 0.5"$).

Therefore, from both the positional agreement and the presence of $H\alpha$ emission we can conclude that this object is likely the companion star to the neutron star in the binary system SAX J1748.9-2021 observed during quiescence (hereafter COM-SAX J1748.9-2021 ). Figure 7.3 shows the measured magnitudes of COM-SAX J1748.9-2021 in different filters at the four epochs available. As it can be seen, no significant variation is detected across the different epochs. The mean magnitudes in each photometric band are: $m_{F606W} = 23.35 \pm 0.01$, $m_{F814W} = 21.58 \pm 0.01$ and $m_{F656N} = 21.68 \pm 0.05$. From the bottom panel of Figure 7.3 we can conclude that in the three epochs for which $H\alpha$ observations are available, a persistent $H\alpha$ emission was present. Thus, these observations indicate an ongoing mass transfer activity from the companion toward the neutron star when the AMXP is in a quiescence state. This is in line with what commonly observed in different classes of interactive binaries (e.g. low-mass X-ray binaries, cataclysmic variables) that are experiencing accretion phenomena also during quiescence (e.g. Ferraro et al., 2000; Torres et al., 2008; Beccari et al., 2014; Torres et al., 2014).
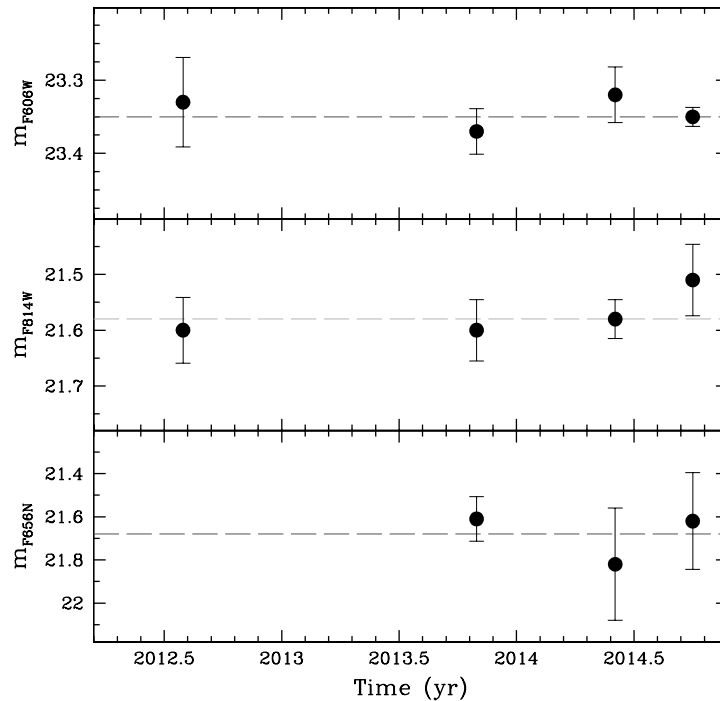
Figure 7.3: Magnitude of COM-SAX J1748.9-2021 in the three different filters measured at the epochs at which observations are available. The mean magnitudes are indicated with the dashed horizontal lines. No significant luminosity variations in all the photometric bands across the different epochs can be detected.

The physical properties of COM-SAX J1748.9-2021 can be derived from the comparison of its position in the optical CMD with appropriate isochrone models. We used the isochrone set from the Dartmouth Stellar Evolution Database (Dotter et al., 2008), for a 12 Gyr-old cluster (Origlia et al., 2008a) with reddening, distance modulus and metallicity as reported in Section 7.1. The isochrone (reported as a blue dashed curve in the left panel of Figure 7.2) nicely reproduces the cluster evolutionary sequences. By projecting the magnitude and color of COM-SAX J1748.9-2021 onto the isochrone, we found a stellar mass $M = 0.73 \pm 0.01 \, M_\odot$, an effective temperature of $T_e = 5250 \pm 80$ K and a bolometric luminosity of $0.53 \pm 0.01 \, L_\odot$, the latter two corresponding to a radius of $R = 0.88 \pm 0.02 \, R_\odot$ (see the discussion in Section 7.4). From the isochrone we can also infer that the expected $B$ magnitude of the object in quiescence should be $B \simeq 25.7$. This value is 3 mag fainter than that measured by Verbunt et al. (2000) during the 1998 outburst. Such a large variation is similar to what observed between the outburst and the quiescence states of other AMXPs (see e.g. Patruno, Watts, 2012, and references therein) and, more generally, of transient low-mass X-ray binaries (e.g. Ferraro et al., 2015b). Since different isochrone models can lead to slightly different results, we re-made the computations by using isochrones from the *BaSTI*
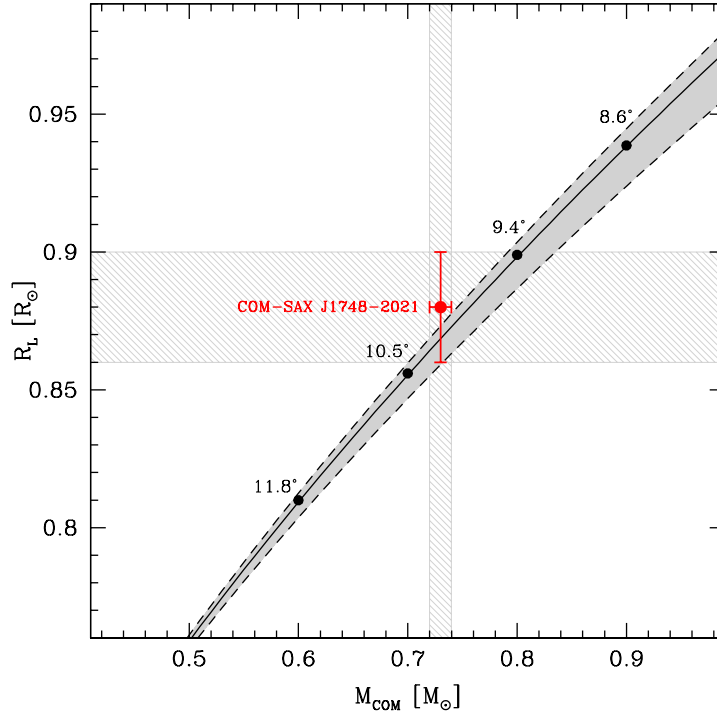
Figure 7.4: Roche Lobe radius as function of the COM-SAX J1748.9-2021 mass. The solid line represents the analytic prediction for a PSR mass of $1.4 \, M_\odot$, while the shaded gray area surrounded by the dashed curves correspond to the predictions for a PSR mass ranging from $1.2 \, M_\odot$ to $2.4 \, M_\odot$. The labelled black dots indicate the inclination angle of the binary system as predicted by its mass function. The red circle and gray striped area mark the derived COM-SAX J1748.9-2021 radius and mass.

database (Pietrinferni et al., 2004) and isochrones from the Padova Stellar Evolution Database (Girardi et al., 2000), finding similar results.

It is worth mentioning that NGC 6440 hosts another AMXP: NGC6440X-2 (Altamirano et al., 2010). This is an ultracompact system with an orbital period of only $\sim 0.96$ hours and a X-ray PSR pulsating at $\sim 206$ Hz. From the binary system mass function, the companion mass is expected to be $\geq 0.007 \, M_\odot$. Despite a careful search for the optical counterpart to this system in the available set of images, we did not find any reasonable candidate. Likely, the optical counterpart of this AMXP is still under the detection threshold, given the extremely low-mass expected for this companion star. We can therefore provide only lower limits in luminosity for this system: $m_{F606W} > 25.0$, $m_{F814W} > 23.5$ and $m_{F656N} > 23.0$.

## 7.4  Discussion

We can now compare the radius of COM-SAX J1748.9-2021 obtained in Section 8.3 with the
expected dimension of the Roche-Lobe (RL) radius. The latter quantity can be estimated according
to the following relation (Eggleton, 1983):

$$R_L = \frac{0.24 M_{PSR}^{1/3} q^{2/3} (1+q)^{1/3} P_{b,hr}^{2/3}}{0.6 q^{2/3} + \log(1 + q^{1/3})}$$

where q is the ratio between the companion and the PSR mass and $P_{b,hr}$ is the orbital period in
hours. In Figure 7.4 (solid line) we plot the RL radius, computed by assuming a PSR mass in the
range $1.2\,M_\odot - 2.4\,M_\odot$, as a function of the companion mass. The position of COM-SAX J1748.9-
2021 in this diagram (large filled dot) indicates that it is at least completely filling its RL and
possibly even overflowing it. Indeed, the RL radius corresponding to the estimated mass of COM-
SAX J1748.9-2021 is $0.86\,R_\odot - 0.87\,R_\odot$, implying a filling factor of $0.99 - 1.05$. The derived filling
factor is in agreement with what expected from such a system, where the presence of on-going
mass transfer implies that the companion star is most likely in a RL overflow state. However, it is
worth noticing that the mass derived for COM-SAX J1748.9-2021 from standard stellar isochrones
can be biased. In fact, the companion star could have suffered a strong mass loss if it is the same
object that has recycled, via mass transfer, the neutron star. Such an effect is not accounted
for by the stellar evolutionary models used to create isochrones, thus introducing a bias in the
derivation of the companion physical properties (see the notorious cases of PSR J1740$-$5340A
and PSR J1824$-$2452H: Ferraro et al., 2001b; Pallanca et al., 2010; Mucciarelli et al., 2013). On
the other hand, we can assume the derived photospheric radius more reliable, since it exclusively
depends on the companion luminosity and temperature. Setting this measured radius equal to
the RL radius, we found that the companion star is filling its Roche-Lobe in the mass range of
$0.70\,M_\odot - 0.83\,M_\odot$. However, the possible presence of heating of the companion star due to the
neutron star emitted flux could affect the observed luminosity and temperature of the companion
star, introducing an additional bias, which is difficult to quantify. Nevertheless, the position of
COM-SAX J1748.9-2021, compatible with the cluster main sequence, suggests that this effect
might not be very relevant for this system, at odds with what observed for strongly heated
companion stars (see, e.g., Edmonds et al., 2002; Pallanca et al., 2014; Cadelano et al., 2015b).
We can therefore conclude that the observed properties of COM-SAX J1748.9-2021 are likely
compatible with that of a binary system where the secondary star has a mass of $0.70\,M_\odot - 0.83\,M_\odot$
and it is filling and possibly overflowing its RL, whose radius is $0.88 \pm 0.02\,R_\odot$. These quantities
can be used to constrain the inclination angle of the system. Using the orbital solution reported
by Patruno et al. (2009) and Sanna et al. (2016), we found that, for a PSR mass in the range
$1.2\,M_\odot - 2.4\,M_\odot$, the binary inclination angle should be very low, between $8°$ and $14°$. Interestingly,
a low orbital inclination angle was independently suggested by the absence of dips and eclipses
in the X-ray light curve (e.g. Sanna et al., 2016) and by the expected properties of the companion
star discussed by Altamirano et al. (2008).

The evidence of $H\alpha$ emission previously discussed and shown in Figure 7.2 can be used to estimate the equivalent width (EW) of the emission line of main sequence stars. In doing this, we followed the method reported by De Marchi et al. (2010) and already used in previous papers (Pallanca et al., 2013a; Beccari et al., 2014). Briefly, the excess in the de-reddened $H\alpha$ $(m_{F606W} - m_{F656N})_0$ can be expressed in terms of the equivalent width of the $H\alpha$ emission by using equation (4) in De Marchi et al. (2010): $EW = RW \times [1 - 10^{(-0.4 \times \Delta H\alpha)}]$, where :

- $RW$ is the "rectangular width" of the adopted $H\alpha$ filter, its definition being similar to that of equivalent width used to measure the intensity of an emission/absorption line. According to Table 4 in De Marchi et al. (2010), $RW = 17.48$Å for the HST-WFC3 $H\alpha$ filter we adopted here.

- $\Delta H\alpha$ is the difference in the de-reddened $H\alpha$ color $(m_{F606W} - m_{F656N})_0$ between COM-SAX J1748.9-2021 and the value expected from a star with the same optical color $(m_{F606W} - m_{F814W})_0$ but showing no $H\alpha$ emission.

On the basis of this relation, different curves at increasing $H\alpha$ EW can be computed and they are plotted in Figure 7.5. When main sequence stars are plotted in this diagram, the vast majority of them are located around the "no $H\alpha$ emission" curve (solid curve), as expected by canonical cluster stars. COM-SAX J1748.9-2021 is instead located significantly above this line, showing a mean systematic excess of $\Delta H\alpha = 0.80 \pm 0.07$ in all the sampled epochs. As it can be seen from Figure 7.5 such an excess corresponds to an EW of the $H\alpha$ emission of $19 \pm 1$ Å. Such a value is too large to be attributed to chromospheric activity (Beccari et al., 2014). It is instead a typical value for system with a low mass accretion rate. In fact it turns out to be in agreement with the $H\alpha$ EWs measured in the majority of quiescent low mass X-ray binaries with a neutron star accretor ($EW = 20$ Å $- 50$ Å, see Heinke et al., 2014, and references therein). The evidence of such a low-level accretion rate in this system was already suggested by the X-ray studies of Bahramian et al. (2015), performed two years after and one year before a burst. The value of $\Delta H\alpha$ just measured can be used to directly estimate the $H\alpha$ luminosity due to the accretion processes $L(H\alpha)$, by using the photometric zeropoints and the values of the inverse sensitivity (PHOTFLAM parameter) publicly available for all the WFC3 filters (see `http://www.stsci.edu/hst/wfc3/phot_zp_lbn`). At the cluster distance, we found $L(H\alpha) = 1.27 \pm 0.08 \times 10^{-4}$ L$_\odot$. This value, together with the COM-SAX J1748.9-2021 mass and radius quoted in Section 8.3, can be inserted in equation (7) of De Marchi et al. (2010) to estimate the mean mass transfer rate of the binary system, that turns out to be $\dot{m} \sim 3 \times 10^{-10}$ M$_\odot$ yr$^{-1}$. Note, however, that the derived value of $\dot{m}$ must be taken with extreme caution, since the De Marchi et al. (2010) method has been calibrated for accretion processes in pre main sequence stars, hence its applicability to the different cases (as low-mass X-ray binaries) could be risky.

Sanna et al. (2016) measured for this binary system a large orbital period derivative of $1.1 \times 10^{-10}$. This large value is interpreted as the result of a non conservative mass transfer
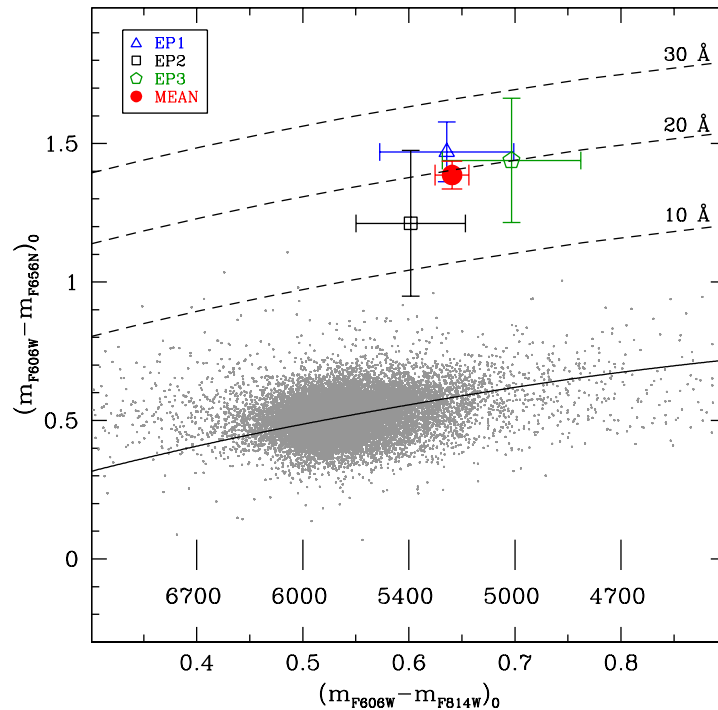
Figure 7.5: Reddening corrected $(m_{F606W} - m_{F814W})_0$ vs $(m_{F606W} - m_{F656N})_0$ color-color diagram of NGC 6440. The solid line marks the region occupied by main sequence stars with no $H\alpha$ emission, while the dashed ones show, respectively, the regions where stars with $H\alpha$ emission and an EW of 10Å, 20Å and 30Å are located. The colored points are the positions of COM-SAX J1748.9-2021 in the different epochs, as reported in the legend. Effective temperatures (in Kelvin) related to the corresponding colors are also marked.

driven by the emission of gravitational waves. In this model, the large orbital period derivative implies a large time-averaged mass transfer rate ($\sim 10^{-8}\,M_\odot\,yr^{-1}$) that can be explained by a companion star with a low-mass of $\sim 0.12\,M_\odot$, where only the 3% of its lost mass is accreted by the neutron star (see their Figure 9). Our findings are not in agreement with such a scenario, since the companion mass is significantly more massive. If we assume that the large orbital period derivative is indeed the result of a strong mass transfer, our and their results could be reconciled by assuming that the fraction of lost mass that is accreted by the neutron star is even smaller than 3%. However, in the previous paragraph we roughly estimated that the mass transfer rate during quiescence is $\dot{m} \sim 3 \times 10^{-10}\,M_\odot\,yr^{-1}$. This value, although extremely uncertain, is $\sim 100$ times smaller than their predicted value. This could suggest that the mass transfer rate, estimated by Sanna et al. (2016) on the basis of the orbital period derivative, is overestimated. More generally, the disagreement between our and Sanna et al. (2016) results could suggests that the large orbital period derivative is due to a different effect such as, for example, a variable

quadrupole moment of the companion star (Applegate, 1992; Applegate, Shaham, 1994; Hartman et al., 2008; Patruno et al., 2012), a phenomenon commonly invoked to explain the time evolution of the orbits of black-widows, RBs and tMSPs (Applegate, Shaham, 1994; Archibald et al., 2013b; Pallanca et al., 2014; Pletsch, Clark, 2015). The similarity of SAX J1748.9-2021 to the RB class might corroborate this hypothesis, although other alternatives exist (see for example Patruno et al., 2017, for a discussion).

Since the analyzed dataset samples almost homogeneously the entire orbital period of the system, an additional aspect that we can investigate is the possible presence of light modulations. Indeed, sinusoidal variations due to irradiation processes or ellipsoidal deformation of the star, are expected to be observed in these systems (see e.g. Homer et al., 2001; D'Avanzo et al., 2009), although the amplitude of the modulation strongly depends on the system inclination angle. In order to determine the amplitude of the light curve expected from the system, we constructed a very basic model of SAX J1748.9-2021 by using the software NIGHTFALL[3]. We simulated a set of light curve models (in the F606W and F814W filters)[4] with a point-like primary star of $1.4\,M_\odot$ and a RL filling companion star with masses in the range of $0.1\,M_\odot - 1\,M_\odot$ (compatible with both the binary mass function and the cluster stellar population)[5]. We found that amplitudes $\lesssim 0.01$ mags are expected for an inclination angle of $\sim 10°$, corresponding to the derived companion mass ($\sim 0.7\,M_\odot$). Since the typical photometric uncertainty on the single measurements is $\sim 0.08$ mags, such a small magnitude modulation cannot be detected with our dataset. Magnitude modulations comparable to or larger than our typical photometric uncertainty are expected only for $i \geq 30°$, corresponding to companion masses $\leq 0.2\,M_\odot$ (see an example in Figure 7.6), which have been excluded by our analysis. This seems to further support the conclusion that the system is seen at a small inclination angle. However, this is a very basic model and the addition of processes like irradiation from the primary star, truncated disk, etc.. can modify the light curve shape. Hence, deeper observations are needed before drawing solid conclusions about the optical variability of the system.

The spin and orbital properties of SAX J1748.9-2021 are quite similar to those generally observed in RB systems. This, combined with the periodical occurrence of outbursts, might suggest that this system is a tMSP whose radio pulsed emission has not been revealed yet (see Section 7.1). However, here we presented some observational evidence suggesting an ongoing mass transfer during the quiescence state. This is not expected in the radio PSR state of tMSPs (see e.g. Archibald et al., 2009; Pallanca et al., 2013a) and suggests that in the case of

---

[3]This software is publicly available at http://www.hs.uni-hamburg.de/DE/Ins/Per/Wichmann/Nightfall.html.

[4]Note that since the software does not allow to evaluate light curves for the specific WFC3 photometric filters, we used the V and I Johnson filter to simulate respectively the F606W and F814W light curves.

[5]The binary system mass function predicts, for a system with very low inclination angles ($i < 5°$), companion masses larger than $2\,M_\odot$, incompatible with the old population of stars in GCs.
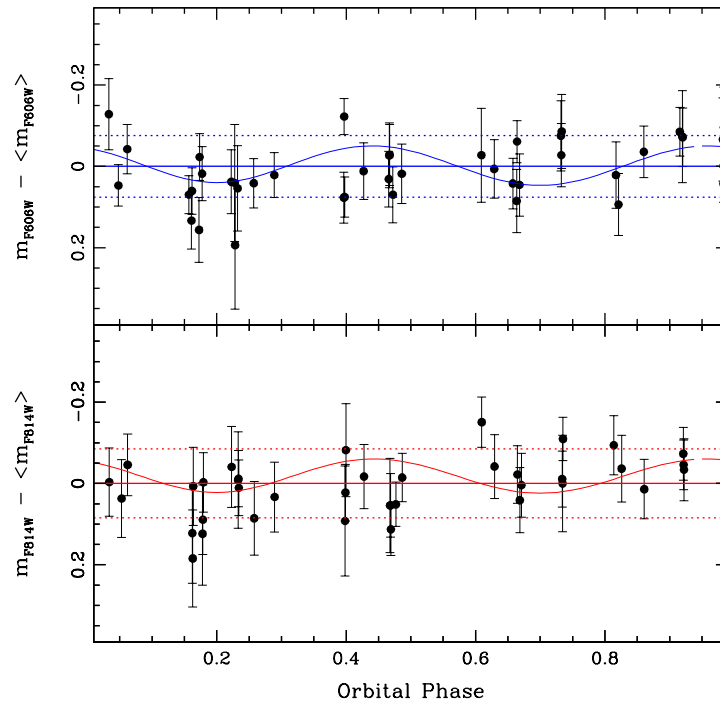
Figure 7.6: Light curve of COM-SAX J1748.9-2021 (black circles and error bars) obtained by folding the F606W measurements (top panel) and F814W measurements (bottom panel) with the binary system orbital parameters. The solid and dashed horizontal lines are respectively the mean and the standard deviations of the measurements. No evidence of variability associated to the orbital period is visible with the photometric errors on the single exposures. For illustrative purposes, we also show the simulated light curves obtained with NIGHTFALL (blue and red curves) for an orbital inclination of 30°, which is, however, excluded by our analysis.

SAX J1748.9-2021 the radio emission mechanism is not active and thus that the system is not a tMSP. The $H\alpha$ emission detected in SAX J1748.9-2021 clearly indicates that this system behaves as a typical low-mass X-ray binaries in quiescence, with mass transfer currently on-going and a possible residual accretion disk still present around the neutron star. This shows that not all accreting neutron stars with main sequence companions and orbital parameters similar to RB behave as tMSPs.

# 8

## THE OPTICAL IDENTIFICATION OF THE X-RAY BURSTER EXO 1745-248 IN TERZAN 5

*Mainly based on Ferraro et al. 2015b, ApJ, 807L:1F*

W e report on the optical identification of the neutron star burster EXO 1745-248 in Terzan 5. The identification was performed by exploiting HST/ACS images acquired in Director's Discretionary Time shortly after (approximately 1 month) the Swift detection of the X-ray burst. The comparison between these images and previous archival data revealed the presence of a star that currently brightened by ∼ 3 magnitudes, consistent with expectations during an X-ray outburst. The centroid of this object well agrees with the position, in the archival images, of a star located in the Turn-Off/Sub Giant Branch region of Terzan 5. This supports the scenario that the companion should has recently filled its Roche Lobe. Such a system represents the pre-natal stage of a millisecond pulsar, an evolutionary phase during which heavy mass accretion on the compact object occurs, thus producing X-ray outbursts and re-accelerating the neutron star.

## 8.1   Introduction

As discussed in Chapter 1, low-mass X-ray binaries (LMXBs) and radio millisecond pulsars (MSPs) are thought to be, respectively, the starting and the ending stages of a common evolutionary path, where a neutron star accretes matter (and angular momentum) from a companion (e.g., Alpar et al., 1982; Bhattacharya, van den Heuvel, 1991). The early phases of this evolutionary path are characterized by active mass accretion accompanied by intense X-ray emission (larger than $\sim 10^{35}$ erg s$^{-1}$). These systems are observed as LMXBs characterized by a few outburst in the X-ray due to accretion disk instabilities. These objects are usually called "X-ray transients" (White et al., 1984) and are commonly found both in globular clusters and in the Galactic field.

X-ray transient outbursts are easily and promptly detectable in the X-ray energy bands thanks to the constant sky monitoring of X-ray satellites such as INTEGRAL and Swift. Indeed, on March 13, 2015, Swift/BAT observations detected an X-ray burst in Terzan 5 (Altamirano et al., 2015). The Swift/XRT observations promptly following the Swift/BAT detection localized the transient source at RA(J2000)= 267.0207 deg, DEC(J2000)= −24.779 deg, with a 90% uncertainty of 3.5″ (Bahramian et al., 2015). The measured spectrum turned out to be consistent with a relatively hard photon index of $1.0 \pm 0.2$ and a hydrogen column density $N_H = (4 \pm 0.8) \times 10^{22}$ cm$^{-2}$. The latter is larger than the typical value measured in Terzan 5 (Bahramian et al., 2014) and well in agreement with the hydrogen column density of the previously known transient EXO 1745-248 (Kuulkers et al., 2003). Indeed, the subsequent position refinement by Linares et al. (2015) centered the system around EXO 1745-248 with a 2.2″ error circle. These data therefore strongly suggest that the new Swift/BAT outburst coincides with EXO 1745-248, an X-ray neutron star transient that already showed outbursts in 2000 and 2011 (Degenaar, Wijnands, 2012). Such an identification has been also confirmed by radio VLA observations (Tremou et al., 2015), which locate the source position within 0.4″ of the published coordinates of EXO 1745-248 obtained from *Chandra* data (source CX3 in Heinke et al., 2006). The most recent Swift/XRT observations indicate that the source is probably on the way to transit to a soft state (Yan et al., 2015).

Such an intriguing object is not uncommon in Terzan 5. In fact, as already discussed in Chapter 1 and 3, this stellar system is known to harbor several X-ray sources (see, e.g., Heinke et al., 2006) and to be the most efficient furnace of MSPs in the Milky Way (Ransom et al., 2005; Cadelano et al., 2018). Ferraro et al. (2009) recently demonstrated that, at odds with what is commonly thought, Terzan 5 is not a globular cluster, but a system hosting stellar populations characterized by significantly different iron abundances, spanning a total metallicity range of 1 dex (see also Origlia et al., 2011, 2013; Massari et al., 2014) and a very large collision rate (Lanzoni et al., 2010), the largest among all Galactic globular clusters (see also Verbunt, Hut, 1987), which can explain the production of the large population of MSPs and low-mass X-ray binaries (LMXBs) now observed in the system.

Since the X-ray outburst detected by SWIFT is expected to also produce a significant enhancement of the optical luminosity (see Shahbaz, Kuulkers, 1998; Charles, Coe, 2006; Testa et al., 2012; Pallanca et al., 2013a), we successfully applied for HST Director Discretionary Time to urgently survey the central region of Terzan 5 and thus provide new insights into this still unexplored phase of the LMXB-to-MSP path. Here we report on the identification of the optical counterpart to EXO 1745-248 obtained from the analysis of these images.

## 8.2 Observations and Data Reduction

To search for the expected optical emission from EXO 1745-248 during its X-ray bursting phase, we submitted a HST Director Discretionary Time proposal (GO 14061, PI: Ferraro) asking for two orbits with the Advanced Camera for survey (ACS/WFC). The observations have been promptly performed on April 20, 2015, about one month into the X-ray outburst (continuing at time of writing). The dataset (hereafter Epoch 3, EP3) consists of $5 \times 398$ s images in F606W, $5 \times 371$ s images in F814W, and one short exposure per filter (50 s and 10 s, respectively; these latter have not been used in the present work).

Previous optical images of Terzan 5 acquired with the same instrument in the same filters were already present in the HST Archive: GO 12933 (PI: Ferraro) performed on August 18th, 2013 (hereafter EP2), and GO 9799 (PI: Rich) performed on September 9th, 2003 (hereafter EP1). We already used these data to construct the deepest optical color-magnitude diagram (CMD) of Terzan 5 (see Ferraro et al., 2009; Lanzoni et al., 2010; Massari et al., 2012).

For the present study, all the datasets have been homogeneously analyzed, following the prescription reported in Chapter 2.3 on the (flc) images corrected for Charge Transfer Efficiency. For each image we modeled a point spread function (PSF) by using 150-200 bright and nearly isolated stars. Afterwards, we performed source detection in each image imposing a 3-$\sigma$ threshold over the background level. By using all the sources detected and PSF fitted in at least 1 out of 2 images in EP1, and 3 out of 10 images in EP2 and EP3, we then created a catalog for every epoch. In spite of including sources detected in only one filter, such an approach allowed us to avoid losing very faint (but possibly real) objects, while safely discarding spurious detections, as cosmic rays and detector artifacts. The obtained master lists (one for every epoch) have been then used to identify the stellar sources in each single frame and the PSF model has been applied to derive the final magnitudes. As a final step, to build the EP2 and EP3 catalogs we considered all the stars with magnitude measured in both filters in at least 3 out of 5 images, while the EP1 catalog obviously consists of the objects detected in both the available images. For each star, the magnitudes estimated in different images of the same filter have been homogenized (see Ferraro et al., 1992) and their weighted mean and standard deviation have been finally adopted as the star magnitude and photometric error. The magnitude calibration to the VEGAMAG system has been performed by using the catalog by Massari et al. (2012) as reference.

To precisely determine the star coordinates, we first applied the equations reported by Meurer et al. (2003) and corrected the instrumental positions for the known geometric distortions affecting the ACS images. Through cross-correlation with the catalog of Massari et al. (2012), which had been placed onto the 2MASS system, we then obtained the absolute coordinates for each star, with a final astrometric accuracy of $\sim 0.2''$ in both right ascension and declination.
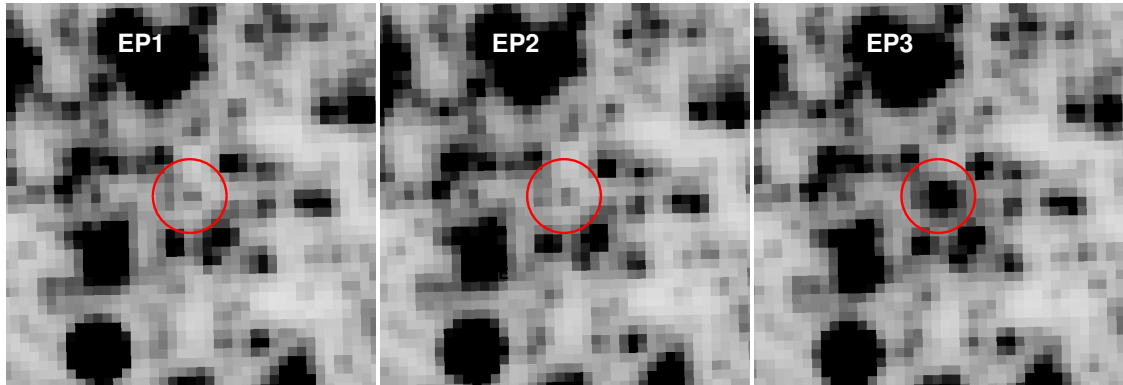


Figure 8.1: HST/ACS drz combined images of the $2'' \times 2''$ region around EXO 1745-248, in the F814W filter, for the three epochs (EP1, EP2, EP3, from left to right, respectively). The source (highlighted with a red circle) is visible as a faint star during the quiescence epochs EP1 and EP2, while it is observed in an outburst stage during EP3. North is up, east is to the left.

## 8.3 Results

The photometric analysis of our dataset in a region around the position of EXO 1745-248 immediately revealed, in EP3, the presence of a bright star that was not visible in EP1 and EP2 images (see Figure 8.1). The comparison of the three epochs unequivocally identifies the bright object (hereafter COM-EXO 1745-248) as the optical counterpart to EXO 1745-248. The absolute position of the optical source is $\alpha = 17^h 48^m 05.23^s$, $\delta = -24^o 46' 47.6''$. This is consistent at 1-$\sigma$ with the VLA position quoted by Tremou et al. (2015, see the red and the green circles in Figure 8.2). Instead, the star previously suggested as the possible optical counterpart to this X-ray transient (Heinke et al., 2003) is located $\sim 0.7''$ to the west (cyan square in the figure).

After the astrometric transformations, the centroid position of the bright object in EP3 is within 0.05 pixels from the centroid of a fainter star clearly detected in EP1 and EP2 (see Figure 8.3). This could be the optical counterpart caught in quiescence. The probability that the true counterpart is a fainter, non detected star aligned (within 0.05 pixels) along the line of sight is very low ($P \sim 0.4\%$).[1] In addition, the brightness profile of this star does not show any significant deviation from symmetry, thus supporting the hypothesis that it is a single object. Hence, the

---

[1]To estimate the probability of a chance superposition with a star fainter than the proposed counterpart, the number of stars down to 5 magnitudes below the Turn Off level at the same distance ($\sim 5''$) from the cluster center is
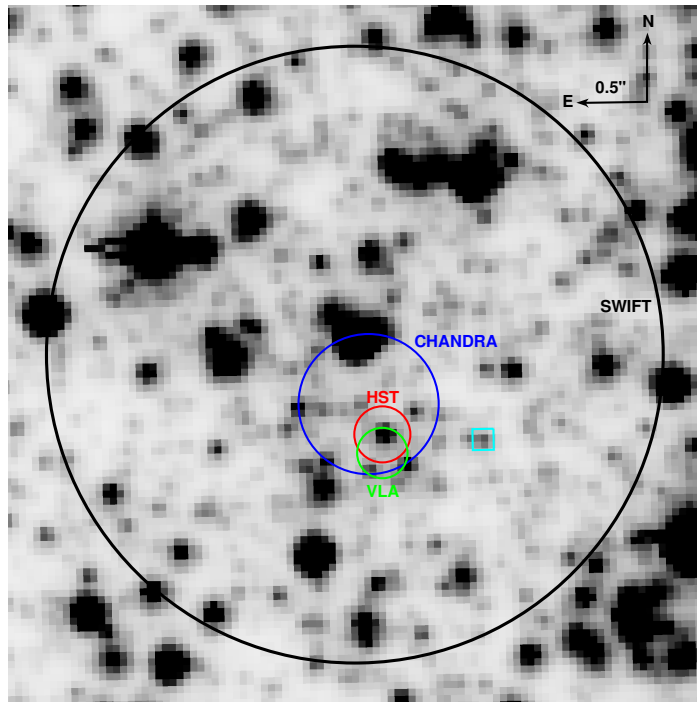
Figure 8.2: F814W-band drz combined image of the 5" × 5" region around EXO 1745-248 in the EP3 exposure. The source positions and uncertainties obtained from the various observational campaigns are marked: the Swift/XRT 2.2" radius error circle is shown in black, the Chandra error circle in blue, the VLA measure in green, and the HST optical determination in red. The cyan square marks the star previously proposed (Heinke et al., 2003) as the possible optical counterpart to EXO 1745-248.

most natural conclusion is that identified star is indeed the counterpart in quiescence. The identified object passed from observed magnitudes $m_{F606W} = 24.74$ and $m_{F814W} = 21.74$ during quiescence (EP1 and EP2)[2], to $m_{F606W} = 21.77$ and $m_{F814W} = 18.88$ in the outburst state (EP3), thus experiencing a brightening of 3 magnitudes (corresponding to a factor 16 in luminosity). Because of its location in the inner Galactic bulge, Terzan 5 is affected by a large extinction, with an average color excess $E(B-V) = 2.38$ (Valenti et al., 2007), showing strong variations, up to $\delta E(B-V) = 0.67$ mag, within the ACS field of view (Massari et al., 2012). We therefore applied the high-resolution differential reddening map obtained by Massari et al. (2012) to correct the observed magnitudes (in the following, the notation $\tilde{m}$ indicates magnitudes corrected for differential reddening). Figure 8.3 shows the position of COM-EXO 1745-248 in the differential

---

needed. Since no data-set available for Terzan 5 reaches such a faint magnitude limit, we adopted as reference the luminosity function of 47 Tucanae derived from deep HST observations (Sarajedini et al., 2007). Star counts have been normalized to the number of Terzan 5 stars counted between the Turn Off level and two magnitudes above, in a ring of 2" width, centered at 5" from the center.

[2]The magnitudes of the star in the EP1 ($m_{F606W} = 24.7\pm0.1$; $m_{F814W} = 21.6\pm0.1$) and EP2 ($m_{F606W} = 24.74\pm0.04$; $m_{F814W} = 21.7\pm0.1$) quiescent stages are fully consistent within the errors.
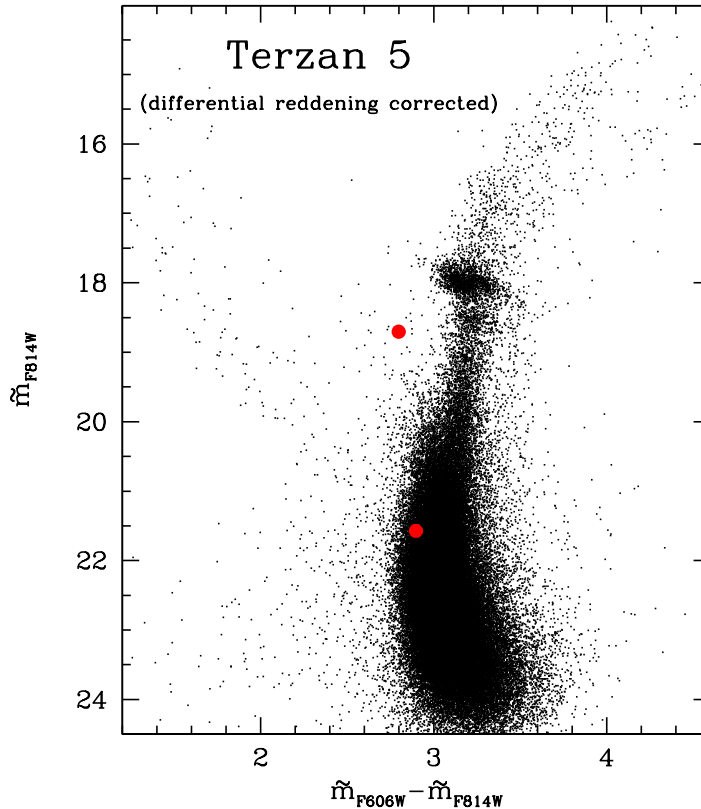
Figure 8.3: ($m_{F814W}$, $m_{F606W} - m_{F814W}$) CMD of Terzan 5 corrected for differential reddening
(according to Massari et al., 2012). The position of the optical counterpart to EXO 1745-248, in
the outburst and in quiescence states, is marked with large red circles.

reddening corrected CMD during the two states. We found $\widetilde{m}_{F606W} = 24.47$ and $\widetilde{m}_{F814W} = 21.57$
during EP1 and EP2, while $\widetilde{m}_{F606W} = 21.50$ and $\widetilde{m}_{F814W} = 18.70$ in EP3, corresponding to a small
(0.1 mag) color variation, which is however within the errors. No variability has been detected
over the period of ~ 50 min covered by each HST orbit in EP3 and EP2. It is worth mentioning
that EP3 data were acquired on April 20, 2015, almost simultaneously to the X-ray observations
(Yan et al., 2015) suggesting that the system is transiting from a hard to a soft state.

An estimate of the orbital period of the system can be obtained by following (Shahbaz, Ku-
ulkers, 1998), who reporte a relation between the orbital period and the $V$-band luminosity
variation. Since we observe $\Delta V \sim 3$ mag in the case of EXO 1745-248, the orbital period turns out
to be $P \sim 1.3$ days. On the other hand, for LMXBs van Paradijs, McClintock (1994) proposed an
empirical relation between the absolute $V$ magnitude in outburst and the parameter $\Sigma$, which
depends on the ratio between the X-ray and the Eddington luminosities ($L_X/L_{Edd}$) and the orbital
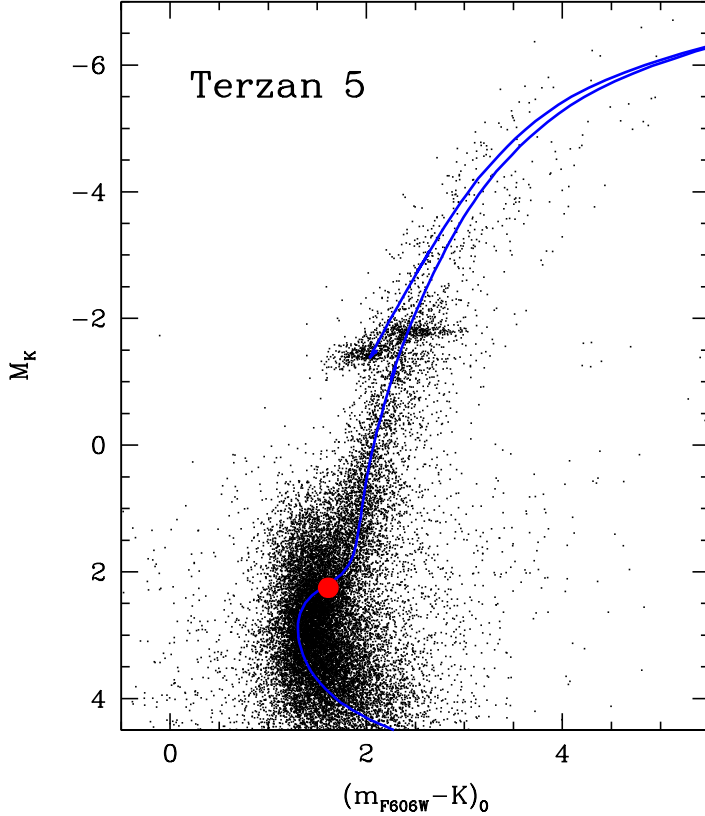
Figure 8.4: Absolute ($M_K$, $m_{F606W} - K)_0$ CMD of Terzan 5 obtained from a combination of HST/ACS and ESO/MAD observations. The position of COM-EXO 1745-248 in the quiescent state is marked with the large red circle. The blue line corresponds to a 12 Gyr isochrone with [Fe/H]$= -0.3$ (from Girardi et al., 2010), well reproducing the main metal poor sub-population of Terzan 5.

period. By assuming $L_X/L_{Edd} \sim 0.5$ (Yan et al., 2015) and $M_V = 1.37$ (in Johnson $V$ magnitude) for EXO 1745-248, we obtain $P \sim 0.1$ days. From these estimates, the orbital period of the system is likely to be between 1.3 and 0.1 days.

In order to more deeply investigate the nature of COM-EXO 1745-248 in the quiescence state under the assumption that the disk contribution to the observed magnitude is negligible, we identified the star in the K-band adaptive optics images obtained with ESO/MAD, used by Ferraro et al. (2009) to discover the two main multi-iron populations hidden in this system. We have first corrected the combined ($K, m_{F606W} - K$) CMD for differential reddening. Then we transformed it into the absolute plane by assuming the average color excess quoted above, and the distance modulus $(m - M)_0 = 13.87$ corresponding to a distance of 5.9 kpc (Valenti et al., 2007).

The result is shown in Figure 8.4, where the position of COM-EXO 1745-248 in the quiescent
state is marked. A more detailed characterization of the nature of COM-EXO 1745-248 is strongly
hampered by the complexity of the stellar populations harbored in Terzan5. The comparison with
a 12 Gyr old isochrone (Girardi et al., 2010) well reproducing the main metal-poor sub-population
of Terzan 5, at [Fe/H]= $-0.3$ dex[3] suggests that COM-EXO 1745-248 could be a sub-giant branch
star. On the other hand the metal-rich sub-population could be significantly (a few Gyr) younger
than the main metal poor component (see Ferraro et al., 2009). Thus, if COM-EXO 1745-248
belongs to the metal-rich component, it would be located below the sub-giant branch, in a position
where companions to redback MSPs have been found (see, e.g., the case of COM-6397A in Ferraro
et al., 2001b). Since no spectroscopic information on the metallicity of this star is available, both
possibilities are equivalently valid. While in the case of redbacks any prediction on the stellar
parameters based on the observed photometric properties can be difficult (see the case of COM-
6397A), this is possible for a sub-giant branch star belonging to the metal poor population. In
this case, the following stellar parameters are obtained: mass $M = 0.9\,M_\odot$, effective temperature
$T_{eff} = 5440$ K, surface gravity $\log g = 3.9$, and luminosity $\log L/L_\odot = 0.35$. The corresponding
stellar radius therefore is $R \sim 1.7\,R_\odot$. Hence, by assuming that the star has completely filled its
Roche-Lobe and adopting a canonical value for the neutron star mass ($\sim 1.4\,M_\odot$), we derive an
orbital separation $a \approx 5.2\,R_\odot$ and a period $P_{orb} \sim 0.9$ d for the binary system, fully in agreement
with the range estimated above. We estimate that the radial velocity variations of such a binary
system should have an amplitude of $\sim 170\,\sin i$ km s$^{-1}$ ($i$ being the system inclination angle),
which could be detectable through a dedicated spectroscopic follow-up.

---

[3]As discussed in Massari et al. (2014), this population consists of $\sim 62\%$ of the total, while a super-solar component
at [Fe/H]= $+0.3$ dex accounts for $\sim 29\%$, and an even metal poorer component, at [Fe/H]= $-0.8$ dex, recently detected
by Origlia et al. (2013), corresponds to $\sim 5\%$ of the total. The CMD plotted in Fig. 8.4 nicely shows two distinct red
clumps at $M_K = -1.5$ and $M_K = -1.81$, corresponding to the two major sub-populations first discovered in the system
by Ferraro et al. (2009).

In this thesis work we presented the results obtained from the analysis of multi-wavelength observations of millisecond pulsars (MSPs) in different Galactic globular clusters (GCs). Observations obtained at radio, optical and near-UV wavelengths have been exploited to search for, timing and identify the optical counterparts to these exotic systems. In this chapter we summarize the main results obtained and discuss future perspectives.

### Radio Observations

In the first part of the thesis (Chapter 3 and Chapter 4), we presented the analysis of radio observations obtained with the 100-m Robert Bird Green Bank Telescope.

In Chapter 3 we discussed how to use archival observations to search for new pulsars (PSRs) and we applied this method to the case of the stellar system Terzan 5. Instead of using classical search routines based on the analysis of single observations, we developed an alternative method which combines multiple observations. In this method, stacked power spectra at different dispersion measures (DMs) are created by summing the spectral powers obtained in the single observations. In order to remove radio frequency interference (RFI), a control DM spectrum has been subtracted from all the stacked power spectra. All the candidates selected in these "corrected" stacked power spectra have been processed with a KD-Tree algorithm, in order to select those that are likely PSR candidates and discard those that are more likely persistent RFI.

The application of the method to Terzan 5 led us to discover three new MSPs in this stellar system. For two of them, we have been able to obtain a phase connected timing solution that confirmed their association with the GC, having a DM close to the cluster mean value and being located within $\sim 17''$ ($\sim 1.9$ core radii) from the cluster gravitational center. These discoveries bring the total number of known MSPs in this system to 37, which corresponds to $\sim 25\%$ of the entire PSR population identified so far in GCs.

Indeed Terzan 5 turns out to be the most efficient factory of MSPs in the Milky Way and the large number of X-ray sources (see, e.g., Heinke et al., 2006) and X-ray bursters (see the recent case of EXO 1745−248, Altamirano et al. 2015; Ferraro et al. 2015a) suggests that this furnace is currently very active. Ferraro et al. (2009) first pointed out that, at odds with what is commonly thought, Terzan 5 probably is not a genuine GC, but a much more complex stellar

system, since it hosts different stellar populations characterized by significantly different iron abundances (see also Origlia et al., 2011, 2013; Massari et al., 2014). Recently Ferraro et al. (2016) measured the ages of the two main sub-populations, (finding 12 and 4.5 Gyr for the sub-solar and super-solar metallicity component, respectively), thus identifying Terzan 5 as a site of multiple bursts of star formation in the Galactic bulge. Indeed, the measured chemical patterns and the large age difference between the two main sub-populations could be naturally explained in a self-enrichment scenario where Terzan 5 was originally much more massive ($\sim 10^8$ M$_\odot$) than today ($\sim 10^6$ M$_\odot$; Lanzoni et al., 2010), and therefore able to retain the iron-enriched gas ejected by violent supernova explosions from which the second generation of stars formed. In particular, the chemical patterns measured in Terzan 5 require a large number of type II supernovae. In turns, these should have also produced a large population of neutron stars (NSs), mostly retained into the deep potential well of the massive *proto*-Terzan 5 and likely forming binary systems through tidal capture interactions. This, together with its large collision rate (the largest among all Galactic GCs; Lanzoni et al. 2010) could have highly promoted PSR recycling processes, which can naturally explain the large population of MSPs and other stellar exotica now observed in the system.

Population synthesis models predict that Terzan 5 could host from few hundreds up to one thousand MSPs (e.g., Bagchi et al., 2011), making this system a top priority target for future deep radio searches with the new generation of radio telescopes, which is expected to plausibly double to triple the current MSP population (Hessels et al., 2015). The relative simplicity and effectiveness of the method here proposed can be applied to observations obtained with the new generation of instruments. Together with the classical routine searches on single observations, it could be a complementary method to discover extremely faint PSRs by using the large amount of GC data that the new generation of radio telescopes (such as "MeerKAT") is going to produce.

While the new generation of radio telescope is still under development, this method can be applied to the currently available archival data of other clusters. Indeed, being quite a powerful tool to search for very faint PSRs, it opens the possibility to identify a significant number of still unknown objects by simply using the large amount of observations that have been devoted to GCs in the past decades. Special attention should be reserved to those clusters expected to harbor a rich population of exotic systems like isolated and very long period binaries, typical of dynamically evolved cluster such as NGC 6752, NGC 6624 and NGC 6522. Furthermore, this method can be improved by implementing techniques such as the "phase-modulation search" (see 2.1.2). This would make this method sensitive also to MSPs in very compact binaries.

In Chapter 4 we presented the long-term timing solutions of 9 PSRs in M28, the third richest cluster in terms of MSP abundance. The updated timing solutions now cover about 10 years of observations and provide precise spin, astrometric and orbital parameters for all the analyzed PSRs. Among the isolated systems, it is of particular interest the case of M28F,

located at 168" from the cluster center, largely beyond the half-mass radius. Such a position is uncommon and unexpected, since mass segregation is expected to make massive objects like NSs sink toward the cluster center in a short timescale ($\sim$ 1 Gyr). The proper motion of this PSR confirms its membership to the cluster. Therefore its position is likely the result of a scattering event with a massive object or a binary in the cluster center that kicked out the NS. Future observations, improving the timing precision and the data time span, will allow to measure the PSR motion with respect to the cluster center, disentangling it from the contribution due to the cluster absolute proper motion. Such a value, compared to that of the other systems, will help to constrain the mechanism of the scattering event. Among the binary MSPs, we obtained precise mass measurements for the components of the eccentric binary M28C: by using a relativistic orbital model, which assumes that general relativity is correct, we evaluated the PSR mass to be $1.37 \pm 0.01 \, M_\odot$, a typical average NS mass value, and the companion mass to be $0.261 \pm 0.002 \, M_\odot$, a typical value for a classical He white dwarf (WD). Future observations will allow to independently measure the post-Keplerian parameters for this system, thus opening the possibility to perform general relativity tests. For the case of the mildly recycled binary M28D we measured the rate of periastron advance, from which we inferred that the PSR mass is smaller than $1.46 \, M_\odot$ and the companion mass is in the range $0.37 \, M_\odot - 0.66 \, M_\odot$. Therefore the latter could be either a high-mass He WD, a low-mass C-O WD or even a main sequence star. To disentangle among these different possibilities, optical observations can be used to directly identify the companion star. Given the properties of this exotic system, which is young and only mildly recycled, the identification of the companion star is of particular interest and would help to constrain its formation scenario and what kind of dynamical interaction was involved in its creation. Unfortunately, no counterpart has been discovered in the publicly available optical archives, therefore further observations are needed.

We also constrained the orbit of the GC within the Galaxy by measuring the individual proper motions of each PSR. At a first approximation, these reflect the cluster motion as a whole and thus their mean value is a good measurement of the cluster absolute proper motion. Back-integrating the cluster orbit during the last 3 Gyr, it turned out that M28 is currently orbiting outside the Galactic bulge but it spent a large fraction of its life within it. In any case, its stellar population properties suggest that M28 was born outside the bulge, although Bica et al. (2016) included it as a genuine bulge GC.

Finally, by using the spin and orbital period derivatives, we constrained the MSP line of sight accelerations induced by the GC potential field. We found that the values can be reproduced by a classical King model with a central velocity dispersion in agreement with that obtained from spectroscopic studies. No anomalous accelerations have been measured, not even for the innermost PSRs. We can likely conclude that there is no need of an additional population of massive dark remnant in the center (or even an intermediate-mass black hole) to explain the PSR accelerations. Similar results have been obtained also for other MSP rich clusters, such

as Terzan 5, 47 Tucanae and NGC 6624 (Prager et al., 2017; Freire et al., 2017; Gieles et al., 2017). The second spin period derivatives have been used to constrain the line of sight "jerks" and these values have compared with the analytical predictions. Interestingly, the jerk values of M28E and M28J are larger than expected from the simple first derivative of the GC line of sight acceleration. This suggests that these objects could be perturbed by nearby stars. Future observations, extending the time span and improving the precision of the timing solutions, will open the possibility to confirm this and possibly understand if these suspected nearby orbiting objects are gravitationally bound to the PSRs.

## Optical Observations

The second part of the thesis was focused on the identification and characterization of optical counterparts to MSPs at different evolutionary stages. Six new companion have been identified.

In Chapter 5 we presented the identification of the companion to the black-widow (BW) PSR J1953+1846A (M71A) in the GC M71. Taking advantage of the precise measure of the PSR position from the radio timing analysis, we have used a set of high resolution ACS/HST images to search for its companion star in the optical bands. We identified a faint and strongly variable star (COM-M71A), showing a modulation of at least three magnitudes in both the filters used (F606W and F814W). In the color-magnitude diagram (CMD), COM-M71A lies in the region between the cluster main sequence and the WD cooling sequences, thus suggesting that it is a low-mass, non-degenerate or at least semi-degenerate star, with a temperature of about 5100 K. Unfortunately, because of its faintness, it was detectable only in 16 out of 27 images, mostly during the PSR inferior conjunction. The light curve shows a sinusoidal shape with a period fully consistent with that of the binary MSP. The maximum, during the PSR inferior conjunction, and the minimum, during the PSR superior conjunction, suggest a strong heating of the companion star side exposed to the PSR flux. Such a behavior is comparable with that observed for similar objects in the Galactic field. By modeling the light curve, we showed that the companion reprocessing efficiency of the PSR energy is ~ 5% for a Roche-Lobe filling companion, while a typical value of 15% is found by assuming a filling factor of 0.6. The comparison between the optical and X-ray light curves suggests the possible presence of an intra-binary shock, similar to that observed for the redback (RB) 47TucW. A X-ray and optical follow-up will highlight the presence of this shock and, possibly, will allow to characterize its property and structure. Unfortunately, the star is too faint to allow a spectroscopic follow-up with the available instruments. However, an optimized photometric follow-up would provide the opportunity to better constrain the system properties, and by using, for example, phase-resolved observations with a narrow $H\alpha$ filter we could constrain the presence of ionized material, possibly related to the intra-binary shock. COM-M71A is, so far, the second BW companion identified in a GC, after COM-M5C in M5 (Pallanca et al., 2014). Interestingly, both the light curve shape and the position in the CMD are

quite similar in the two systems. This suggests that probably the two objects underwent a similar evolutionary path. Even though the statistic is by far too limited to draw any solid conclusion, at the moment no significant differences between BWs in GCs and those in the Galactic field are observed, both in the radio and in the optical band. This, together with the increasing number of eclipsing MSPs identified in the Galactic field (e.g. Breton et al., 2013; Li et al., 2014, Sanpa-arsa et al. 2018, in preparation), confirms that no dynamical interactions are strictly needed for forming these systems, at odds with what usually believed in the past (e.g. King et al., 2003).

In Chapter 6 we showed that, thanks to ultra-deep, high resolution near-UV WFC3/HST observations, we identified the companions to four binary MSPs in 47 Tucanae (47TucQ, 47TucS, 47TucT and 47TucY) and confirmed the two already known objects (COM-47TucU and COM-47TucW). The optical counterparts have coordinates compatible, within the errors, with the PSR nominal positions. In the CMD, all the objects are located along the He WD cooling sequences, as expected from the MSP canonical evolutionary scenario. The only exception is the companion to the RB system 47TucW, which is located in an anomalous region between the main sequence and the WD cooling sequences, suggesting that it is a low-mass main sequence star highly perturbed and heated by the PSR flux. We compared the observed CMD positions of the detected He WD companions with a set of cooling tracks and derived the companion main properties (as masses, cooling ages, temperatures) and also some constraints on the PSR masses. All the companion stars have masses between $\sim 0.15\,\mathrm{M_\odot}$ and $\sim 0.20\,\mathrm{M_\odot}$, and all the derived cooling ages are smaller than the cluster stellar population age ($\sim 10-11$ Gyr). The orbital periods vs companion masses are in fair agreement with the evolutionary models of Tauris, Savonije (1999) and Istrate et al. (2014). By combining the cooling age with the PSR spin down rate we found that the accretion history of 47TucU likely proceeded at a sub-Eddington rate.

In Chapter 7 we presented the optical identification and characterization of the AMXP SAX J1748.9-2021 during quiescence. We identified a possible counterpart (COM-SAX J1748.9-2021) in a star located at only $\sim 0.15''$ from the X-ray nominal position. This star, although being located along the cluster main sequence, shows an excess in the F656N filter, thus implying the presence of $H\alpha$ emission. We discussed the physical properties of the companion star and showed that it has a mass of $0.70\,\mathrm{M_\odot}-0.83\,\mathrm{M_\odot}$, an effective temperature of 5250 K and it is filling, or even overflowing, its Roche-Lobe radius of $0.88\pm0.02\,\mathrm{R_\odot}$. This mass, combined with the binary system mass function and assuming a canonical range of NS masses, implies that the binary system is observed at a very low inclination angle ($\sim 8°-14°$). This can also explain the absence of any significant magnitude variability and also the absence of dips and eclipses in the X-ray light curve. The EW of the $H\alpha$ emission has been evaluated to be of about $20\,\text{Å}$, which corresponds to a mean mass transfer rate during quiescence of $\sim 10^{-10}\,\mathrm{M_\odot\,yr^{-1}}$. The possibility of on-going mass transfer and residual accretion disk around the NS during quiescence implies that the radio

139

PSR is not reactivated yet. Hence SAX J1748.9-2021 is probably not a tMSP and its behavior during quiescence is comparable with that commonly observed in classical quiescent low-mass X-ray binaries, even though its orbital and spin parameters are very similar to those observed for RBs. This directly implies that not all the RB-like AMXP with main sequence companions are tMSPs. For some reasons, the PSR in SAX J1748.9-2021 is not able to turn-on the radio emission during the quiescence state, at odds with what happens for tMSPs. The reasons behind this are still obscure. Intriguingly, it is worth noticing that COM-SAX J1748.9-2021 has a mass larger than that measured for the companion stars of RBs and tMSPs ($0.2\,M_\odot - 0.4\,M_\odot$, see, e.g., Breton et al., 2013; Mucciarelli et al., 2013; Bellm et al., 2016). Therefore the companion mass could be one of the ingredients to understand why this RB-like AMXP is not behaving like a tMSP.

In Chapter 8 we presented the identification of the optical counterpart to the NS transient EXO 1745-248 in Terzan 5. This has been performed by exploiting a data-set of high resolution images obtained during three different epochs. During the third epoch, this object is detected in an outburst state and shows a brightening of $\sim 3$ magnitudes. In the quiescence state it is a sub-giant branch star, i.e., an object that is experiencing its first envelope expansion, while evolving toward the red giant branch stage. The analysis of this source revealed that the companion star has a mass of about $0.9\,M_\odot$ and effective temperature of about 5500 K, while the binary orbital period has been constrained to be in the range 0.1- 1.3 days. Very interestingly, the X-ray emission of EXO 1745-248 during quiescence was found to be highly variable both on short and long time-scales (Degenaar, Wijnands, 2012), and Linares et al. (2014) recently underlined that these properties are similar to those observed for the tMSP J1824$-$2452I (Papitto et al., 2013). This evidence suggests that EXO 1745-248 could be another system belonging the rare class of objects caught shortly before the formation of a radio MSP, possibly in a stage preceding the swinging phase in which tMSPs are observed.

Summarizing, in this thesis work we have identified six new optical counterparts to MSPs in GCs. This corresponds to have increased the total sample of such objects by 40%, reaching the number of 15. Moreover we have identified the optical counterpart to a X-ray burster in Terzan 5. It is now possible to clarify the evolutionary mechanism of MSPs, identifying different possible paths. Figure 8.5 reports the CMD position of all the companions known after this thesis work (see Figure 1.14 for the state of the art before this thesis). The first inspection of this updated plot clearly reveals that different typologies of companion stars correspond to different typologies of MSPs. In other words, the classification of the companion stars alone appear to be sufficient to classify the binary MSPs. Even not accounting for the radio properties of the MSPs, the positions of the companions in an absolute CMD allow a clear classification of the typology of each binary. Indeed, as can be seen, canonical MSPs have exclusively low-mass He WD companion stars, the vast majority with masses $\lesssim 0.2\,M_\odot$. Only one system, M4A, has a companion with a slightly
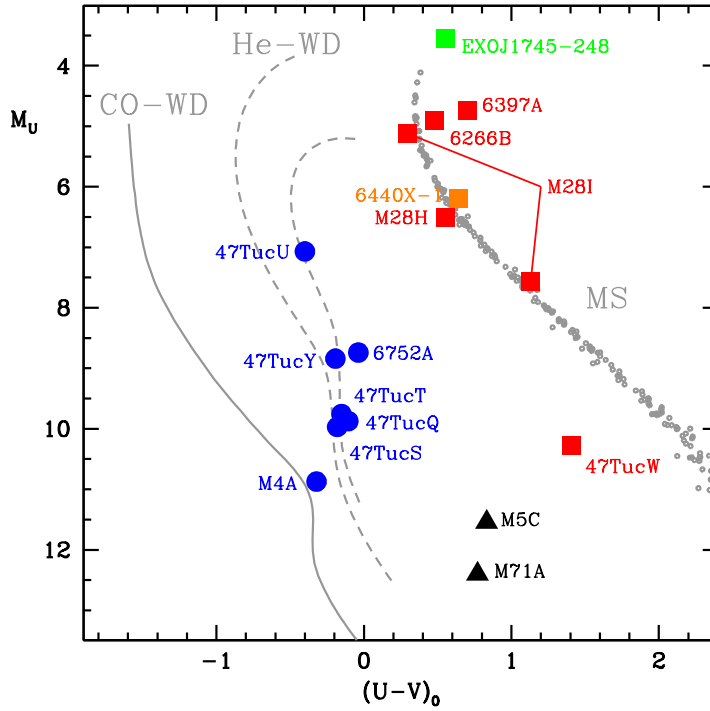
Figure 8.5: Position of the MSP optical counterparts in an absolute CMD. This plot is the same as in Figure 1.14 but includes all the companion stars identified in this thesis work. Blue dots mark the position of canonical MSPs, while red squares and black triangles the position of RBs and BWs, respectively. The AMXP SAX J1748.9−2021 is in orange and labelled as 6440X-1 for clarity, while the companion to EXO J1745−248 is marked with a green square.

larger mass of $0.35\,\mathrm{M_\odot}$. However, being a triple system, its evolution is somewhat different than that expected for canonical systems. As shown in Figure 6.5, this mass range is exactly what expected from binary evolution models (Tauris, Savonije, 1999; Istrate et al., 2014). This suggests that the cluster environment does not significantly affect the evolution of canonical MSPs. While it is well known and assessed that the cluster environment is able to create a large number of new MSPs, their general properties appear to remain unaltered during the typical timescale of their formation and evolution ($\sim$ 1 Gyr). Signatures of environmental effects can be found in those systems with eccentric orbits, mildly recycled PSRs or very long orbital periods, which have been, so far, almost exclusively found in the densest GCs (Verbunt, Freire, 2014). Unfortunately, no optical counterpart to these "perturbed" systems has been identified so far, and therefore it has been impossible to compare the properties of their companion stars with those of standard canonical low-mass He WDs.

At odds with canonical MSP companions, both the spider MSP companions (COM-M71A and COM-47TucW) are, as expected, non degenerate objects. The companions to RB systems are all

141

closely located along the cluster main sequence. The vast majority of them are packed in the upper main sequence, few magnitudes below the turn-off point. While this could be a selection effect, it is interesting to note that the only exception is the companion to 47TucW, located on the blue side of the main sequence, in a low-luminosity region ~ 7 magnitudes below the turn-off. BW systems have, on the other hand, very peculiar companion stars located in a very low-luminosity region, between the main sequence and the WD cooling sequence. This is a region where no standard evolving stars are expected, thus confirming the high degree of perturbation that these systems suffer during their evolution.

Aside from the position in the CMD, another key difference between canonical and spider MSP companions is the presence of flux variability, usually showing a periodicity compatible with the orbital period of the binary. This is usually not observed and not expected in canonical MSPs, since the PSR flux intercepted by their degenerate (thus very compact) companions is negligible (but see the case discussed in Edmonds et al. 2001). Instead, the flux variability of spider MSPs comes in two flavors: RB systems show mildly variable light curves, with typical magnitude differences of few tenths and with a double minimum and double maximum structure that is due to the tidal distortions of the companion star caused by the NS (Ferraro et al., 2001b; Cocozza et al., 2006; Pallanca et al., 2010; Breton et al., 2013; Li et al., 2014). Heating effects are sometimes observed but do not dominate the light curve shapes. On the other hand, all the BW systems and some RB systems (such as 47TucW, Edmonds et al. 2002) present light curves with strong variability, usually reaching magnitude differences larger than 3, and with a single minimum and a single maximum structure, which is the result of the heating of the stellar side exposed to the PSR injected flux (Pallanca et al., 2012, 2014; Li et al., 2014; Cadelano et al., 2015b). This effect dominates the light curves, while other effects, such as tidal distortions and spin asynchronicity of the companion stars, are secondary.

The scenario explained above confirms that the efficiency of the irradiation of the companion star by the PSR injected flux is a key ingredient to understand the evolution and the differences among RBs and BWs, as already pointed out by theoretical works (e.g. Chen et al., 2013; Benvenuto et al., 2014). In spite of the new discoveries, however, the formation and evolution of these systems is still difficult to underline. Benvenuto et al. (2014) proposed that RBs represent somehow an early stage of MSP evolution: some of them evolve toward the canonical MSP stage, where the companion star forms a He degenerate nucleus and loses its remaining thin envelope (see also Burderi et al., 2002); others evolve toward the stage of BWs, where the companion star is no able to form (or only partially forms) a He degenerate nucleus and a strong evaporation due to the primary injected flux leads to the creation of a very low-mass companion with a mass of few hundredths of solar masses. However, ad odds with these results, Chen et al. (2013) stated that the evolution of canonical, RB and BW systems is independent. According to their results, RBs do not evolve neither into canonical MSPs, nor in BWs. From an observational point of view, starting from the results obtained by the identification of these objects in GCs and in the Galactic field (e.g.

Reynolds et al., 2007; Kaplan et al., 2012; Pallanca et al., 2012; Bellm et al., 2013; Breton et al., 2013; Li et al., 2014), we can see that the majority of RB companions are not subject to strong heating. Therefore their evolution toward the BW stage would appear unlikely. Their evolution toward the He WD stage still cannot be probed, especially because of the lack of identifications of objects in an intermediate stage between the two. However, it is interesting to note that there are some RB systems, both in the Galactic field and in GCs, such as 47TucW, whose companion light curves are dominated by the strong irradiation due to the PSR flux, as commonly observed for all the BW companions. Moreover, as can be seen from Figure 8.5, in the CMD, 47TucW is located on the blue side of the main sequence, in a region close to that occupied by the two BW systems. This suggests that RB systems whose companions are subject to strong heating and thus ablation can indeed evolve to the BW stage, and 47TucW would be therefore a prototype of a RB evolving into a BW. As concerns the final destiny of BWs, it is possible that the progressive evaporation of the companion star could in the end lead to its total destruction, thus creating an isolated MSP. However, the evaporation time-scale appear to be too large to account for the observed number of isolated MSPs (e.g. Chen et al., 2013), and since the latter are mostly found in dense GCs, it is reasonable to think that their companion stars have been unbound through a dynamical interaction with another star or a binary in the cluster. However, the total disruption of the BW companions can still explain the small number of isolated MSPs in the Galactic field.

The CMD position of the companion to the AMXP SAX J1748.9-2021 is compatible with that of RBs, and it closely resembles that of COM-M28H. This is not surprising, since this system is a RB-like AMXP and therefore can be considered, within an evolutionary scenario, as the precursor of a RB system or also of a tMSP. This system will evolve toward the tMSP/RB stage as soon as the residual accretion halts and the PSR emission will be finally reactivated.

Finally, the CMD position of the NS burster EXO 1745−248 reveals that the companion is a sub-giant branch star. Therefore, we can speculate that EXO1745-248 is experiencing the very early phase of the mass accretion stage, when an expanding star (a sub giant branch object) is filling its Roche-Lobe and transferring material that eventually spins-up the NS. Indeed, the few outbursts in the X-ray occurring during this stage unambiguously indicate that heavy mass accretion on the NS is taking place. As time passes, the mass accretion rate will decrease and the system will enter in a later stage of the evolution, possibly characterized by a cyclic alternation between accretion and rotation-powered emission and finally by the re-activation of the re-accelerated NS.

## Future Developments

The study of MSPs in GCs will receive a major boost in the near future thanks to the performances of the new generation of telescopes. Radio observations with "MeerKAT" and then with the "Square Kilometer Array" (SKA) should be able to identify most of the expected MSPs, especially

those in nearby clusters and in those systems (such as Omega Centauri, M80, NGC 6388, etc...) expected to host rich populations of MSPs not revealed yet. The new discoveries will open the possibility to perform systematic studies of the different typologies of MSP populations in GC characterized by different structural and dynamical properties. This will improve our understanding of the cluster itself. New large sample of exotic binaries will be discovered and will be an important ground where to test fundamental physics. The number of identified companion stars will be easily enhanced thanks to the infrared capabilities of the "James Webb Space Telescope" (JWST), whose sensitivity and angular resolution will provide an unique view on the faintest companion stars, especially those in exotic systems like BWs and especially those in heavily obscured bulge GCs like Terzan 5, NGC 6440, NGC 6441, etc..., which are known or expected to host very rich populations of MSPs. Ground-based new facilities like the "European Extremely Large Telescope" (E-ELT) will complement the observation of these clusters in the optical bands, also providing the opportunity of perform spectroscopic studies that will give us new clues on the chemical properties of these objects, and thus on their evolutionary processes.

# A

# Proper Motions and Structural Parameters of the Galactic Globular Cluster M71

*Mainly based on Cadelano et al. 2017a, ApJ, 836:170*

I n this appendix we show how we have exploited the two ACS/HST datasets used to the analysis presented in Chapter 5 to additionally study the cluster kinematic. Since the two dataset are separated by a temporal baseline of ~ 7 years, we used them to determine the relative stellar proper motions (providing membership) and the absolute proper motion of the Galactic globular cluster M71. The absolute proper motion has been used to reconstruct the cluster orbit within a Galactic, three-component, axisymmetric potential. M71 turns out to be in a low latitude disk-like orbit inside the Galactic disk, further supporting the scenario in which it lost a significant fraction of its initial mass. Since large differential reddening is known to affect this system, we took advantage of near-infrared, ground-based observations to re-determine the cluster center and density profile from direct star counts. The new structural parameters turn out to be significantly different from the ones quoted in the literature. In particular, M71 has a core and a half-mass radii almost 50% larger than previously thought. Finally we estimate that the initial mass of M71 was likely one order of magnitude larger than its current value, thus helping to solve the discrepancy with the observed number of X-ray sources.

## A.1  Introduction

As discussed in Chapter 1, the high central densities of globular clusters provide the ideal ground to the formation of exotic objects like blue straggler stars, cataclysmic variables, low-mass X-ray binaries and millisecond pulsars (e.g. Ferraro et al., 1997, 2003d; Pooley et al., 2003; Ransom et al., 2005; Heinke et al., 2005). In this respect, remarkable is the case of M71, which is a low-density GC located at a distance of about 4 kpc from Earth. It has a quite high metallicity ([Fe/H]$= -0.73$), a color excess $E(B-V) = 0.25$ (Harris, 1996, 2010 edition) and a total mass of about $2 \times 10^4$ M$_\odot$ (Kimmig et al., 2015). X-ray observations revealed that it hosts a large population of X-ray sources, most likely consisting of stellar exotica. Surprisingly, as discussed in Elsner et al. (2008); Huang et al. (2010), the number of X-ray detections in M71 is significantly larger than what is expected from its present-day mass and its collisional parameter (which is a characteristic indicator of the frequency of dynamical interactions and thus of the number of stellar exotica in a GC; e.g. Bahramian et al., 2013). However, it is worth noticing that M71 is located at a low Galactic latitude ($l = 56.75°, b = -4.56°$), likely on a disk-like orbit (Geffert, Maintz, 2000). Hence, it could have have lost a substantial fraction of its initial mass, due to heavy interactions with the Galactic field and to shocks caused by encounters with molecular clouds and/or spiral arms. Moreover the structural parameters of this cluster have been estimated from shallow optical images (Peterson, Reed, 1987), and therefore need to be re-determined more accurately. Hence, the value of the collisional parameter, which directly depends on the cluster structural parameters (Verbunt, Hut, 1987), could be biased.

By taking advantage of two epoch of observations  obtained with the *Hubble Space Telescope* (HST) and wide-field near-infrared and optical datasets for M71, in this appendix we present the determination of: *(i)* the stellar proper motions (which allow us to distinguish cluster members from Galactic contaminants), *(ii)* the absolute PM of the system (from which we estimate its orbit within the Galaxy during the last 3 Gyr), and ($iii$) the cluster gravitational center and structural parameters.

In Section A.2 we describe the procedures adopted for the data reduction and analysis. Sections A.3 and A.4 are devoted to the determination of relative stellar proper motions (PMs), and of the cluster absolute PM and orbit, respectively. In Section A.5 we present the new determination of cluster gravity center, density profile and structural parameters from near-infrared data and we study how the latter change if optical observations are used instead. We also provide an estimate of the initial mass of the system. Finally, in Section A.6 we summarize the results and discusse the X-ray source abundance discrepancy in light of the new values of the cluster structural parameters and the initial mass estimate.

## A.2   Observations and Data Reduction

The work presented in this Appendix is based on two different datasets. Their characteristics and the adopted data reduction procedures are described in the following.

*High-Resolution Dataset* – This has been used to determine the stellar PMs. It consists of two sets of images acquired with the Wide Field Camera (WFC) of the Advanced Camera for Surveys (ACS) mounted on HST (see the left panel of Figure A.1 for a map of the fields of view - FOVs - covered by these observations). This camera provides a FOV of $202'' \times 202''$ with a pixel scale of $0.05''$ pixel$^{-1}$. The first epoch data have been collected under GO10775 (P.I.: Sarajedini) on 2006 July 1, and consist of a set of ten dithered images, five in the F606W filter (with exposure times: $1 \times 4$ s; $4 \times 75$ s) and five in the F814W filter ($1 \times 4$ s; $4 \times 80$ s). The second epoch is composed of proprietary data obtained under GO12932 (P.I.: Ferraro) on 2013, August 20. It consists of a set of ten deep images acquired through the F606W filter ($2 \times 459$ s; $3 \times 466$ s; $5 \times 500$ s) and nine images in the F814W filter ($5 \times 337$ s; $3 \times 357$ s; $1 \times 440$ s). The photometric analysis has been performed on the -flc images (which are corrected for flat field, bias, dark counts and charge transfer efficiency) following the procedures described in detail in Anderson, King (2006). Briefly, both the epochs have been analyzed with the publicly available program img2xym_WFC.09x10, which uses a pre-determined model of a spatially varying point spread function (PSF) plus a single time-dependent perturbation PSF (to account for focus changes or spacecraft breathing). The final output of this process are two catalogs (one for each epoch) with instrumental magnitudes and positions for all the sources above a given threshold. Star positions were corrected in each catalog for geometric distortion by adopting the solution provided by Anderson (2007). By using the stars in common with the public catalog of Sarajedini et al. (2007, see also Anderson et al., 2008), instrumental magnitudes have been calibrated on the VEGAMAG system and instrumental positions have been reported on the absolute right ascension and declination coordinate reference system ($\alpha$ and $\delta$, respectively). The final color-magnitude diagrams (CMDs) are shown in Figure A.2 for the two different epochs.

*Wide-field Dataset* – To determine the cluster gravitational center and structural parameters, we used ground-based near-infrared images (Prop ID: 11AD90; PI: Thanjavur) obtained with the wide field imagers WIRCam mounted at the Canada-France-Hawaii Telescope (CFHT). To study the effect of differential reddening, we also made use of optical wide-field images (Prop ID: 04AC03, 03AC16; PI: Clem) acquired with MegaCam at the same telescope. The WIRCam camera consists of a mosaic of four chips of $2040 \times 2040$ pixels each, with a pixel scale of $0.31''$ pixel$^{-1}$, providing a total FOV of $\sim 21.5' \times 21.5'$. We analyzed seven images obtained with the $J$ and $K_s$ filters, with exposure times of 5 s and 24 s, respectively. A dither pattern of few arcseconds was applied to fill the gaps among the detector chips. The MegaCam camera consists of a mosaic of 36 chips of $2048 \times 4612$ pixels each, with a pixel scale of $0.185''$ pixel$^{-1}$ providing a FOV of $\sim 1° \times 1°$. A total of 50 images have been acquired, both in the g' and in the r' bands, with exposure times of 250 s each. A dither pattern of few arcseconds was adopted for each pointing, thus allowing the
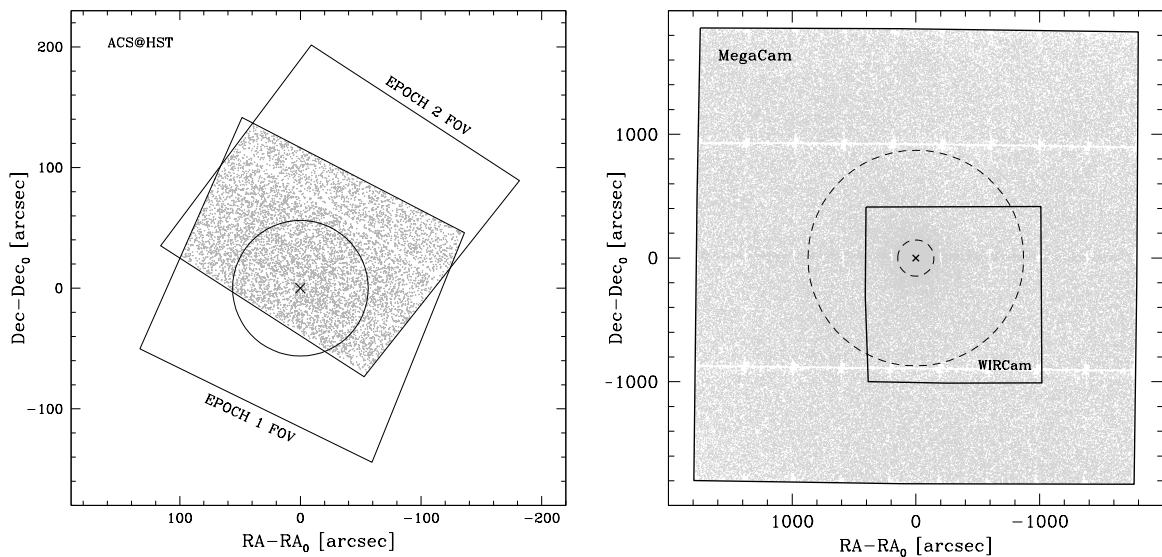
Figure A.1: *Left:* FOVs of the ACS first and second epoch datasets, centered on the newly estimated gravity center of M71 (black cross; see Section A.5.1). The grey dots highlight the stars in common are between the two datasets, which has been used to measure the stellar proper motions. The solid circle marks the core radius of the cluster as derived in this work ($r_c = 56.2''$; see Section A.5.2). *Right:* FOVs of the MegaCam and WIRCam datasets, centered on the cluster gravity center (black cross). The small and large dashed circles mark, respectivey, the half-mass and the tidal radii derived in this work.

filling of most of the interchip gaps, with the exception of the most prominent, horizontal ones. The right panel of Figure A.1 shows the map of the Wide-field dataset.

For both these sets of observations, the images were pre-processed (i.e. bias and flat-field corrected) by means of the Elixir pipeline developed by the CFHT team and the photometric analysis has been performed independently on each chip by following the procedures described in Chapter 2.3. The obtained star instrumental magnitudes have been reported to the SDSS photometric system[1] for the MegaCam catalog, and to the 2MASS system for the WIRCam catalog. Finally the instrumental positions have been reported to the absolute coordinate reference frame by using the stars in common with the 2MASS catalog[2]. The CMDs for these datasets are shown in Figure A.3 for stars located at less than 300" from the center.

As can be seen from both Fig. A.2 and Fig. A.3, the standard evolutionary sequences are well defined. However, they are also heavily contaminated by foreground objects, as expected from the location of M71 close to the Galactic disk.

---

[1] See http://www.cfht.hawaii.edu/Science/CFHTLS-DATA/megaprimecalibration.html#P2.

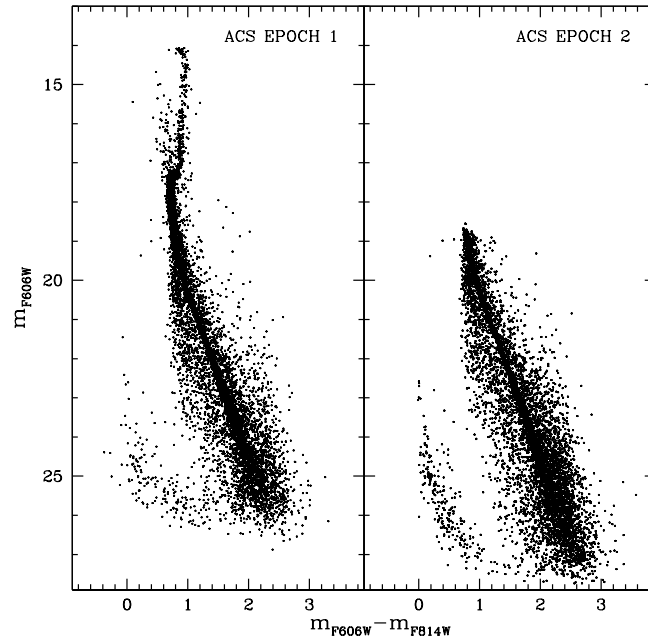[2] Publicly available at http://vizier.u-strasbg.fr

Figure A.2: Optical CMD of M71 obtained from the first and second epoch ACS datasets (left and right panels, respectively).
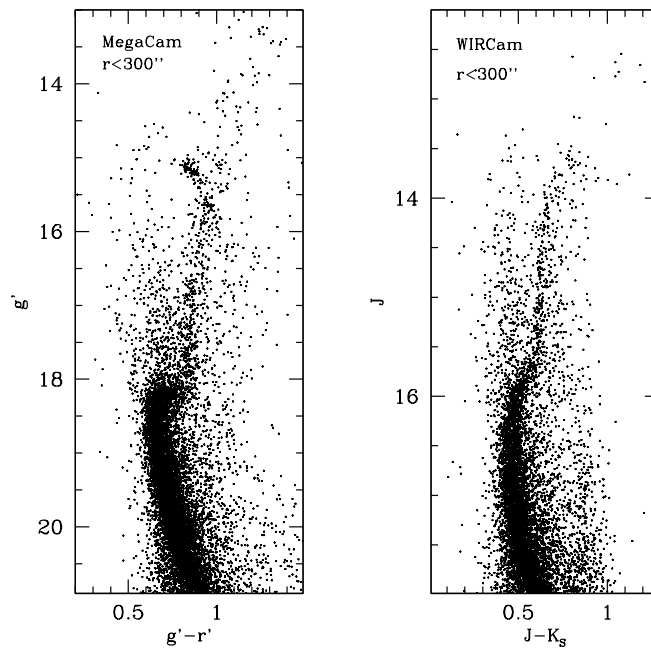


Figure A.3: Optical and near-infrared CMDs of M71, obtained from the MegaCam (left panel) and the WIRCam datasets (right panel), respectively. In both cases, only stars within 300" from the center are plotted.

## A.3   Relative Proper Motions

To study the PMs of M71, we used the high resolution datasets. These are separated by a temporal
baseline of 7.274 years and  because of their different orientation, pointing and magnitude
limit, the PM analysis could be performed only on the $\sim 5000$ stars in common, located in the
overlapping FOV (see Figure A.1) and having magnitudes $18 < m_{F814W} < 24$ (corresponding to
magnitudes $19 < m_{F606W} < 25$). We adopted the procedure described in Massari et al. (2013, see
also Dalessandro et al., 2013; Bellini et al., 2014; Massari et al., 2015).  Briefly, we used six
parameters linear transformations[3] to report the coordinates of the stars in each exposure to
the distortion-free reference catalog of Sarajedini et al. (2007). Since we are interested in the
stellar PMs relative to the cluster frame, these transformations have been determined by using a
sample of $\sim 6600$ stars that, in the reference catalog, are likely cluster members on the basis of
their CMD position (i.e. stars located along the main sequence). Moreover, the transformations
have been determined independently on each detector chip in order to maximize the accuracy. At
the end of the procedure, for each of the $\sim 5000$ stars we have up to ten position measurements
in the first epoch catalog and up to nineteen in the second epoch catalog. To determine the
relative PMs, we computed the mean X and Y positions of each star in each epoch, adopting a
$3\sigma$ clipping algorithm. The star PMs are thus the difference between the mean X,Y positions
evaluated in the two epochs, divided by $\Delta t = 7.274$ years. The resulting PMs are in units of
pixels years$^{-1}$. Since the master frame is already oriented according to the equatorial coordinate
system, the X-component of the PM corresponds to a projected PM along the (negative) RA and
the Y-component corresponds to a PM along the Dec. Therefore, we converted our PMs in units of
mas years$^{-1}$ by multiplying the previous values for the ACS pixel scale ($0.05'' \text{pixel}^{-1}$), and we
named $\mu_\alpha \cos(\delta)$ and $\mu_\delta$ the PMs along the RA and Dec directions, respectively. To maximize the
quality of our results, we built a final PM catalog by taking into account only stars for which
at least three position measurements are available in each epoch. At the end of the procedure
we counted 4938 stars with measured PMs. The errors in the position of the stars in each epoch
($\sigma_{1,2}^{\alpha,\delta}$) have been calculated as the standard deviation of the measured positions around the
mean value. Then the errors in each component of the PM have been assumed as the sum in
quadrature between the error in the first and second epoch: $\sigma_{PM}^{\alpha,\delta} = \sqrt{(\sigma_1^{\alpha,\delta})^2 + (\sigma_2^{\alpha,\delta})^2}/\Delta t$. The
errors as a function of the star magnitudes are shown in Figure A.4. For both the PM directions,
the typical uncertainty for stars with $m_{F814W} < 21$ is less of $\sim 0.07$ mas yr$^{-1}$, demonstrating the
good quality of our measurements. Following Bellini et al. (2014), we also verified that our PM
measurements are not affected by chromatic effects, i.e., there is no dependence of $\mu_\alpha \cos(\delta)$ and
$\mu_\delta$ on the (F606W-F814W) color. Finally, our PM measurements are not even affected by positional
effects, i.e., there is no dependence of the derived PMs on the instrumental (X,Y) positions.

In Figure A.5 we show the PM distribution in the vector points diagram (VPD). As can be
seen, the VPD is dominated by two prominent features: the clump in the center with zero relative

---

[3] To do this we applied six parameters linear transformations using `CataXcorr`.
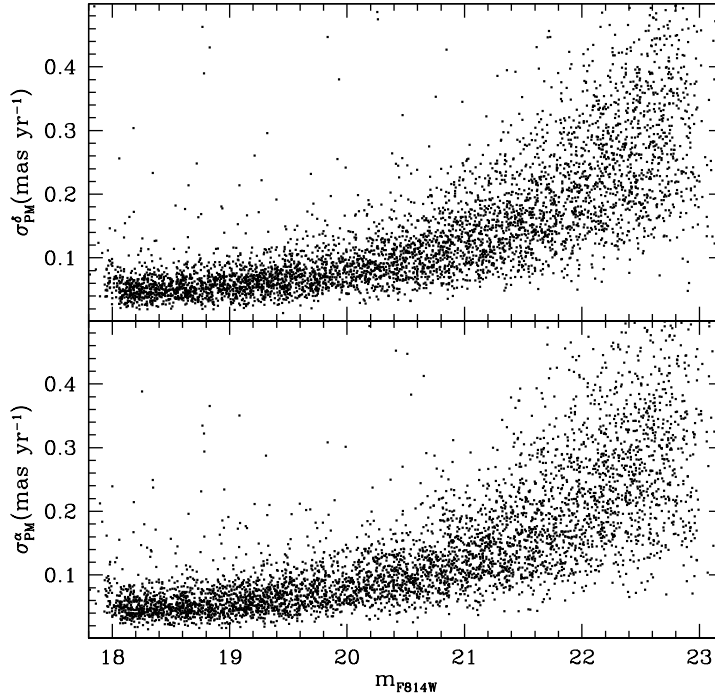
Figure A.4: Estimated uncertainties of the derived proper motions as a function of the $m_{F814W}$ magnitude of the measured stars. The upper and the lower panels show, respectively, the uncertainties in the $\alpha$ and in the $\delta$ directions. For stars with $m_{F814W} \lesssim 21$ the typical error is smaller than 0.07 mas yr$^{-1}$.

PM is, by definition, dominated by the cluster population, while the elongated sparse distribution of points extending beyond this clump is dominated by contaminating field stars, mostly from the Galactic disk. At first inspection of the VPD we can see that only $\lesssim 60\%$ of the $\sim 5000$ analyzed stars are likely cluster members. A high percentage of field contamination is indeed expected in the case of M71, since it has a quite low stellar density and is located in a crowded field at low Galactic latitudes. By selecting in the VPD the likely cluster members (i.e. the stars with relative PM around 0 both in $\alpha$ and in $\delta$) we find that the mean motion is 0.01 mas yr$^{-1}$ with a standard deviation of 0.1 mas yr$^{-1}$ both in $\alpha$ and in $\delta$, thus, as expected, consistent with zero.

The effect of decontaminating the CMD from field stars is shown in Figure A.6, where we have separated the objects with PM$\lesssim 0.6$ mas yr$^{-1}$ (likely cluster members), from those with larger PMs. The selection of stars in the VPD is shown, per bins of one magnitude, in the left-hand column of the figure, with the objects having PM$\lesssim 0.6$ mas yr$^{-1}$ encircled in red. The effect on the CMD is shown in the other three columns: from left to right, the observed CMD, the CMD of cluster members only, and the CMD of field stars. In the latter, it is well appreciable the main sequence of the Galactic field. Instead, the decontaminated CMD clearly shows a sharp and well
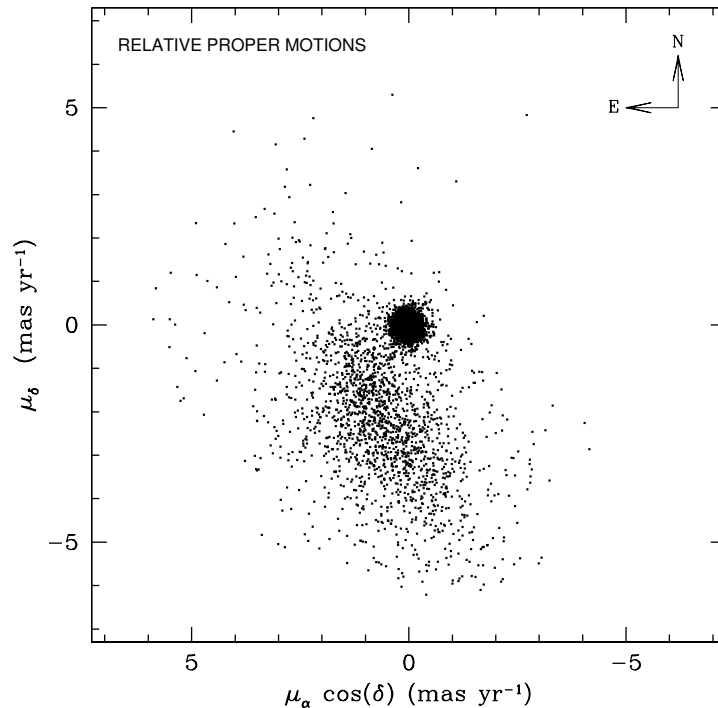
151

Figure A.5: VPD of the relative PMs. The clump in the (0,0) mas yr$^{-1}$ position is dominated by the cluster population. The elongated region beyond this clump is instead due to contaminating stars, mostly from the Galactic disk.

defined main sequence, also revealing the binary sequence. The few stars on the blue side of the main sequence could be cluster exotic objects, such as cataclysmic variables, X-ray binaries or millisecond pulsars (e.g. Ferraro et al., 2001a; Pallanca et al., 2010; Cohn et al., 2010; Cadelano et al., 2015b), where a main sequence companion star is heated by a compact object. Nonetheless, we cannot completely rule out the possibility that some of these stars are field objects with PMs compatible with those of the cluster members.

## A.4   Absolute Proper Motions

To transform the relative PMs into absolute ones, we used background galaxies as reference, since they have negligible PMs due to their large distances. This method has been successfully used in several previous works (e.g. Dinescu et al., 1999; Bellini et al., 2010; Massari et al., 2013). Unfortunately, the NASA Extragalactic Database report no sources in the FOV used for the PM estimate. Thus, we carefully inspected our images in order to search for diffuse galaxy-like objects. We found four galaxies with central point-like structure and relative high brightness, which allowed us to precisely determine their centroid position. Although many
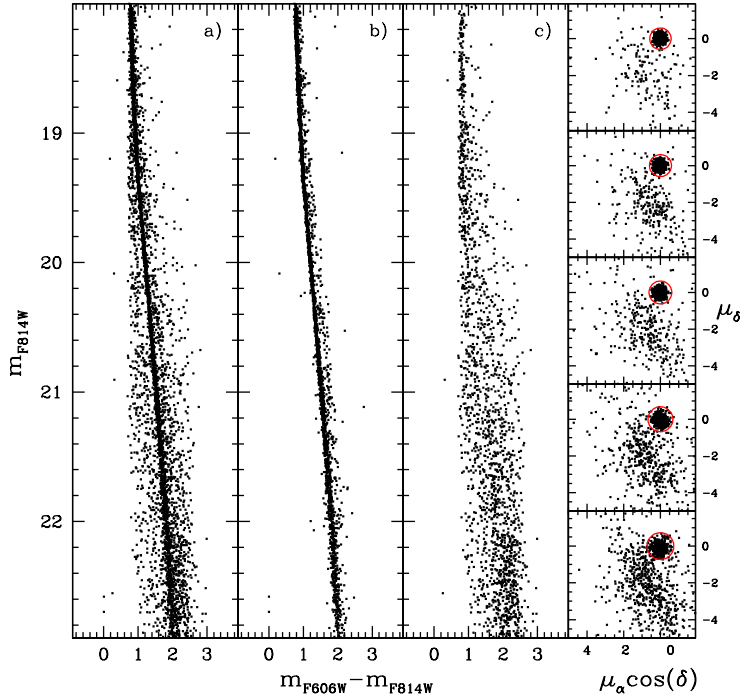
Figure A.6: *Panel a:* Optical CMD of all the stars in common between the two observation epochs. *Panel b:* Decontaminated CMD obtained by using only the likely cluster members selected from the VPDs shown in the rightmost column. As can be seen, a sharper and more delineated main sequence and the binary sequence are now appreciable. *Panel c:* CMD made of all the contaminating objects, selected from the VPDs as those with PMs not compatible with the that of the GC. The Galactic sequence can be appreciate from this plot. *Rightmost column:* VPDs of the measured stars divided in bins of magnitudes. The solid red circles contain all the objects selected as likely cluster members.

other galaxies are present in the FOV, they have no point-like structure or are too faint to allow the determination of a reasonable PM value. Moreover, as part of a project aimed at searching for optical counterparts to X-ray sources, we identified two promising active galactic nuclei (AGN) candidates. Two Chandra X-ray sources, named s05 and s41 in Elsner et al. (2008), have high energy and optical properties that can be attributed either to AGNs or to cataclysmic variables (see Huang et al., 2010, for more details). In order to distinguish between these two possibilities, we analyzed their PMs. We reported our relative PM reference frame to the absolute cluster PM ($\mu_\alpha \cos\delta, \mu_\delta = -3.0 \pm 1.4, -2.2 \pm 1.4$ mas yr$^{-1}$) previously determined by Geffert, Maintz (2000) and found that these two sources have an absolute PM significantly different from the cluster motion and compatible with zero. We therefore conclude that these two
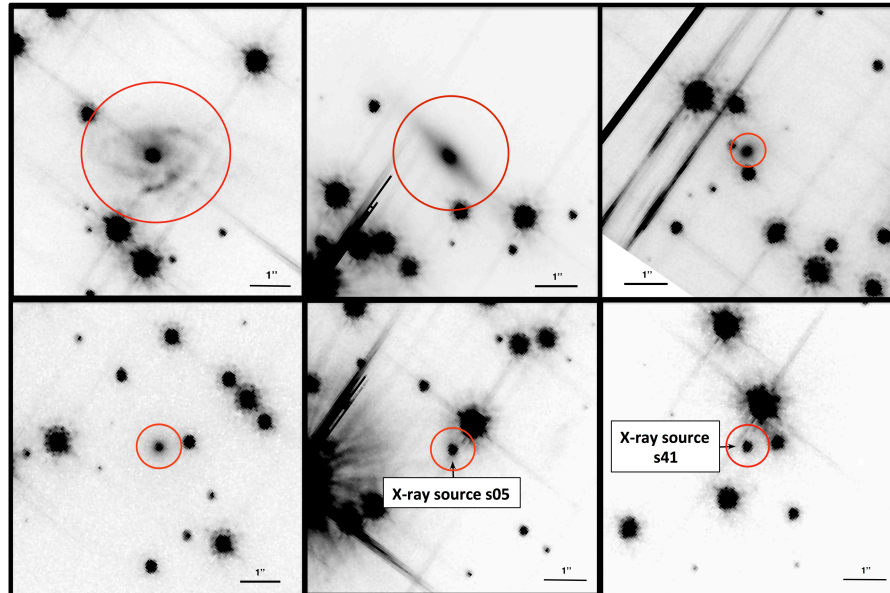
Figure A.7: Finding charts of the six selected extra-Galactic objects used to determine the absolute reference frame zero point. The charts are taken from an ACS image acquired in the F814W filter. The three upper panels and the bottom-left panel show the four galaxies found through the visual inspection of the images. The central and right bottom panels show the optical counterparts to the X-ray sources s05 and s41, classified as AGNs. The point-like structure of these sources allowed a precise determination of the centroid position and of their PM.

objects are likely background AGNs[4] and add them to the list of objects used to determine our reference absolute zero point. The six selected objects are located very close to each other in the VPD, as expected for extragalactic objects, and their finding charts are shown in Figure A.7. We defined the absolute zero point as the weighted mean of their relative PMs and assumed as error the uncertainty on the calculated mean. By anchoring this mean position to the $(0,0)$ mas yr$^{-1}$ value, we find that the absolute PM of M71 is:

(A.1)
$$(\mu_\alpha \cos\delta, \mu_\delta) = (-2.7 \pm 0.5, -2.2 \pm 0.4) \text{ mas yr}^{-1}.$$

This value is in good agreement with (but more accurate than) the previous determination (Geffert, Maintz, 2000), and it remains unchanged within the errors even if the two candidate AGNs are excluded from the analysis: in that case we get: $(\mu_\alpha \cos\delta, \mu_\delta) = (-2.4 \pm 0.6, -1.9 \pm 0.1)$ mas yr$^{-1}$, still in agreement with the previous results. The VPD in the absolute frame is plotted in Figure

---

[4]Of course, these sources could be foreground cataclysmic variables with PMs almost perfectly aligned with our line of sight, but this possibility seems to be quite unlikely.
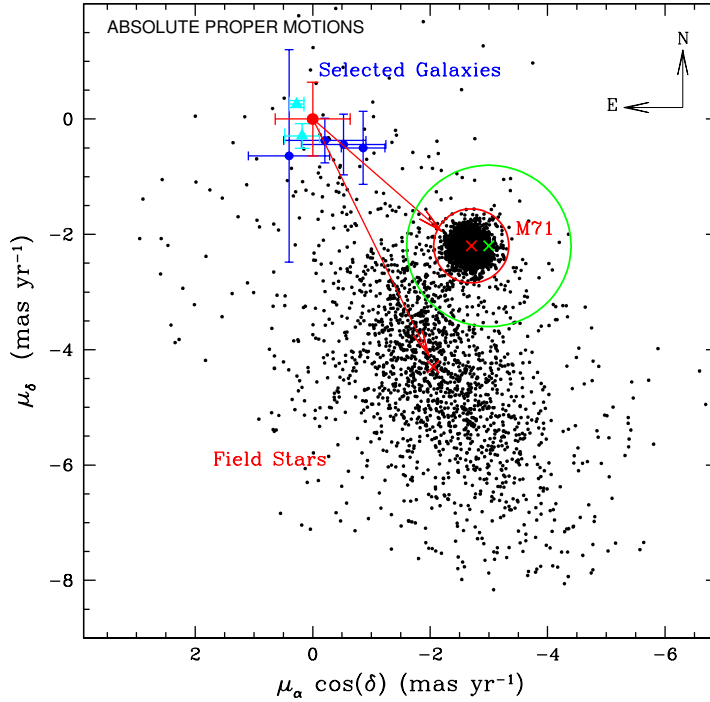
Figure A.8: VPD of absolute PMs. The extra-Galactic objects used to determine the absolute reference frame zero point are marked as blue dots (galaxies) and cyan triangles (AGNs), and their mean motion is marked a large red dot. The red arrows indicate the absolute PM vectors of M71 and of the Galactic field population. The absolute PM value of M71 estimated in this work is marked with a red cross and the red circle represents its $\sim 1\sigma$ confidence region. The values previously determined in the literature (Geffert, Maintz, 2000) are marked with a green cross and a green circle. The red cross centered on the elongated structure is centered on the field mean PM (see Section A.4).

A.8, with the red and green crosses and circles marking, respectively, the absolute PM and its uncertainty as determined in this study and as quoted in Geffert, Maintz (2000).

Since every absolute PM measurement is strictly dependent on the accuracy of the absolute reference frame, we need to verify the possible presence of systematic errors in its determination. One of the possible source of systematic errors is the rotation of the GC on the plane of the sky. Indeed, since we used only cluster stars to define the relative reference frame, if the GC is rotating, then our frame will be rotating too. This would introduce an artificial rotation to background and foreground objects around the cluster center. To quantify this possible effect we followed the procedure described in Massari et al. (2013). We selected a sample of field stars as those that in the VPD of Figure A.5 have relative PMs larger than 0.8 mas yr$^{-1}$. Then we decomposed their PM vectors into a radial and tangential component with respect to the cluster

center. If the GC is rotating, we would expect to find a clear dependence of the PM tangential component on the distance from the cluster center. Such a dependence is however excluded by our results, thus that the internal regions of M71 are not rotating, in agreement with the recent findings by Kimmig et al. (2015).

We also compared the field star motion to that expected from theoretical Galactic models in the analyzed FOV. To evaluate the field mean motion, we followed the procedure described in Anderson, van der Marel (2010). First, we excluded the stars within 0.8 mas yr$^{-1}$ from the cluster mean motion. Then we iteratively removed field stars in a symmetric position with respect to the GC exclusion region and evaluated the weighted mean motion by applying a $3\sigma$ algorithm. We found $(\mu_\alpha \cos\delta, \mu_\delta) = (-2.0 \pm 0.2, -4.3 \pm 0.2)$ mas yr$^{-1}$. We compared these values with those predicted for the same region of the sky in the Besançon Galactic model (Robin et al., 2003), simulating a sample of $\sim 2000$ artificial stars distant up to 15 kpc from the Galactic center, in a FOV centered on M71, covering a solid angle of $\sim 11'$, and having V magnitudes ranging 12 from to 25. The predicted field mean motion is $(\mu_\alpha \cos\delta, \mu_\delta) = (-2.4, -4.7)$ mas yr$^{-1}$, in good agreement with our results.

### A.4.1 The cluster orbit

The GC absolute PM, combined with the radial velocity $v_r = -23.1 \pm 0.3$ km s$^{-1}$ from Kimmig et al. (2015), can be used to determine 3D space velocity of the cluster in a Cartesian Galactocentric rest frame. Using the formalism described in Johnson, Soderblom (1987), assuming the Local Standard of Rest velocity equal to 256 km s$^{-1}$ (Reid et al., 2009) and using the value of the Sun velocity with respect to it from Schönrich et al. (2010), we obtained $(v_x, v_y, v_z) = (52 \pm 10, 204 \pm 6, 31 \pm 12)$ km s$^{-1}$, where the major source of uncertainty is the GC absolute PM error. We then used the 3D velocity of the cluster and its current Galactocentric position[5] $(x, y, z) = (-6.2 \pm 0.6, 3.4 \pm 0.3, -0.32 \pm 0.03)$ kpc, to reconstruct its orbit in the axisymmetric potential discussed in Allen, Santillan (1991), which has been extensively used to study the kinematics of Galactic stellar systems (e.g. Ortolani et al., 2011; Moreno et al., 2014; Massari et al., 2015). The orbit was time-integrated backwards, starting from the current conditions and using a second-order leapfrog integrator (e.g. Hockney, Eastwood, 1988) with a small time step of $\sim 100$ kyr. Since the adopted Galactic potential is static, we choose to back-integrate the orbit only for 3 Gyr, since longer backward integrations become uncertain due to their dependence on the Galactic potential variations as a function of time. This numerical integration required about 32000 steps and reproduced $\sim 20$ complete cluster orbits. The errors on the conservation of the energy and the Z-component of the angular momentum never exceeded one part over $10^9$ and $10^{16}$, respectively. We generated a set of 1000 clusters starting from the phase-space initial conditions normally distributed within the uncertainties. For all of these clusters we repeated

---

[5]We adopted the Galactic coordinates quoted in Harris (1996) and the convention in which the X axis points opposite to the Sun, i.e., the Sun position is $(-8.4, 0, 0)$, where the distance of the Sun from the Galactic center is from Reid et al. (2009).

the backward time integration. Figure A.9 shows the resulting cluster orbits in the equatorial and meridional Galactocentric plane. As can be seen, the cluster has a low-latitude disk-like orbit within the Galactic disk. Indeed in the equatorial plane it reaches a maximum distance of $\sim 8$ kpc from the Galactic center and a minimum distance of $\sim 5$ kpc. Thus, it orbits around the assumed spheroidal bulge, never crossing it. Moreover, it persists on a low-latitude orbit, with a typical height from the Galactic plane of about $\pm 0.4$ kpc, thus again confined within the disk. The estimated orbits indicate that, at least during the last 3 Gyr, M71 tightly interacted with the inner Galactic disk.  With respect to the large majority of Galactic GCs, which are on large orbits across the (low-density) halo, these interactions likely induced heavy mass-loss (Vesperini, Heggie, 1997) in M71, thus supporting the possibility that it lost a significant fraction of its initial mass, as already suggested by its flat mass function (De Marchi et al., 2007). Moreover, such a heavy mass-loss could finally explain why M71 harbors a large population of X-ray sources, in spite of its present low mass (Elsner et al., 2008).
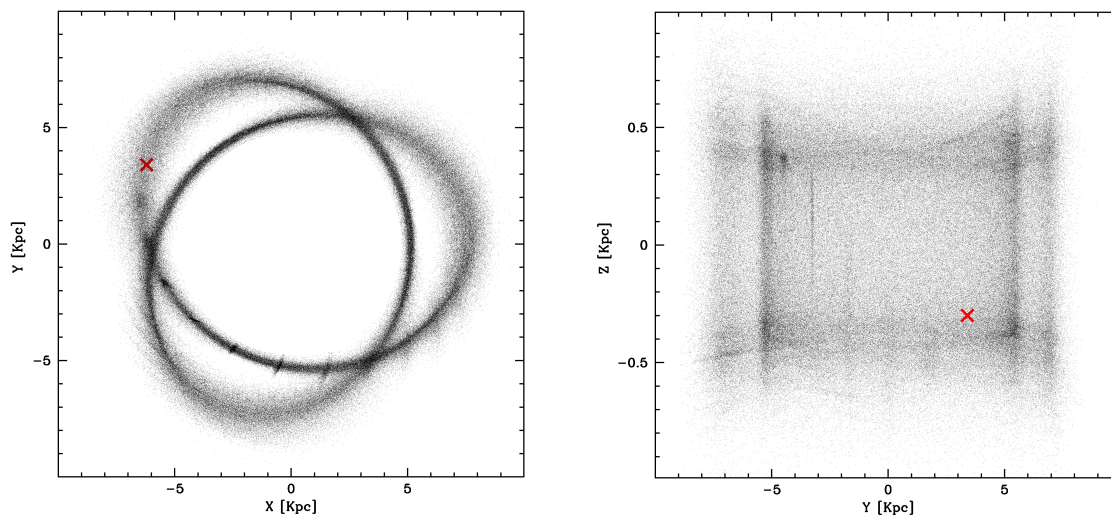


Figure A.9: *Left:* Simulated positions occupied by M71 during the last 3 Gyr along its orbit in the equatorial Galactic plane. Each point represents the position of one (out of 1000) cluster in one of the 32000 snapshots obtained during the numerical integration. The red cross marks che current cluster position. *Right:* Same as in the left panel, but for the orbit in the meridional Galactic plane.

## A.5   Gravitational Center, Structural Parameters and Initial Mass

In this section we present the determination of the gravitational center and of the new structural parameters of M71.

## A.5.1 Gravitational center

To avoid biases due to the strong differential reddening affecting the system (e.g. Schlegel et al., 1998), for the determination of the cluster center of gravity $C_{grav}$ we used the near-infrared WIRCam catalog, which has the same level of completeness of the ACS one in the magnitude range $14 < K_s < 16.8$. $C_{grav}$ has been determined following an iterative procedure that, starting from a first-guess center, selects a sample of stars within a circle of radius r and re-determine the center as the average of the star coordinates ($\alpha$ and $\delta$). The procedure stops when convergence is reached, i.e., when the newly-determined center coincides with the previous ones within an adopted tolerance limit (Lanzoni et al., 2010, see also Montegriffo et al. 1995; Lanzoni et al. 2007). For M71, which is a relative loose GC (Harris, 1996), we repeated the procedure eighteen times, using different values of $r$ and selecting stars in different magnitude ranges, chosen as a compromise between having high enough statistics and avoiding spurious effects due to incompleteness and saturation. In particular, the radius $r$ has been chosen in the range $140" - 160"$ with a step of $10"$, thus guaranteeing that it is always larger than the literature core radius $r_c = 37.8"$ (Harris, 1996). For each radius $r$, we have explored six magnitude ranges, from $K_s > 14$ (in order to exclude stars close to the saturation limit), down to $K_s = 16.3 - 16.8$, in steps of 0.1 magnitudes. As first-guess center we used that quoted by Goldsbury et al. (2010). The final value adopted as $C_{grav}$ is the mean of the different values of $\alpha$ and $\delta$ obtained in the eighteen explorations, and its uncertainty is their standard deviation. We found $\alpha = 19^h 53^m 46.106^s$ and $\delta = +18°46'43.38"$, with an uncertainty of about 1.7". The newly determined center of M71 is $\sim 5.7"$ west and $\sim 0.3."$ north from the one measured from optical ACS data by Goldsbury et al. (2010). Such a discrepancy is likely ascribable to an effect of differential reddening impacting the optical determination.

## A.5.2 Stellar density profile

Since the surface brightness profile can suffer from strong biases and fluctuations due to the presence of few bright stars (see, e.g., the case of M2 in Dalessandro et al., 2009), in order to re-evaluate the structural parameters of M71 we used direct star counts. The determination of the stellar density profile (number of stars per unit area, in a series of concentric annuli around $C_{grav}$) has been performed following the procedure fully described in Miocchi et al. (2013). Also in this case, in order to minimize the differential reddening effect we used the near-infrared WIRCam data, which covers distances out to $\sim 1000"$ from $C_{grav}$ in the south-west portion of the cluster (see the right panel Figure A.1). To build the density profile we considered 13 concentric annuli around $C_{grav}$, each one divided into four sub-sectors. We then counted the number of stars with $14 < K_s < 16.5$ in each sub-sector and divided it by the sub-sector area. The projected stellar density in each annulus is the mean of the values measured in each sub-sector and the uncertainty has been estimated from the variance among the sub-sectors. The stellar background has been estimated by averaging the outermost values, where the profile flattens, and it has been

subtracted to the observed distribution to obtain decontaminated density profiles. The result is shown in Figure A.10.

The cluster structural parameters has been derived by fitting the observed density profiles with a spherical, isotropic, single-mass King (1966) model.[6]. The single-mass approximation is justified by the fact that the magnitude range chosen to build the profile includes cluster stars with negligible mass differences. The best-fit model results in a cluster with a King dimensionless potential $W_0 = 5.55 \pm 0.35$, a core radius $r_c = 56.2^{+4.5}_{-4.0}$ arcsec, a half-mass radius $r_h = 146.2^{+11.5}_{-10.0}$ arcsec, a truncation radius $r_t = 871.8^{+247}_{-164}$ arcsec and, thus, a concentration parameter, defined as the logarithm of the truncation to the core radius, $c = \log(r_t/r_c) = 1.19$.

There is a significant difference between these parameters and those quoted in the Harris (1996) catalog, originally estimated by Peterson, Reed (1987) from a surface brightness profile

---

[6]These models can be generated and freely downloaded from the Cosmic-Lab web site: `http://www.cosmic-lab.eu/Cosmic-Lab/Products.html`. The fitting procedure is fully described in Miocchi et al. (2013)
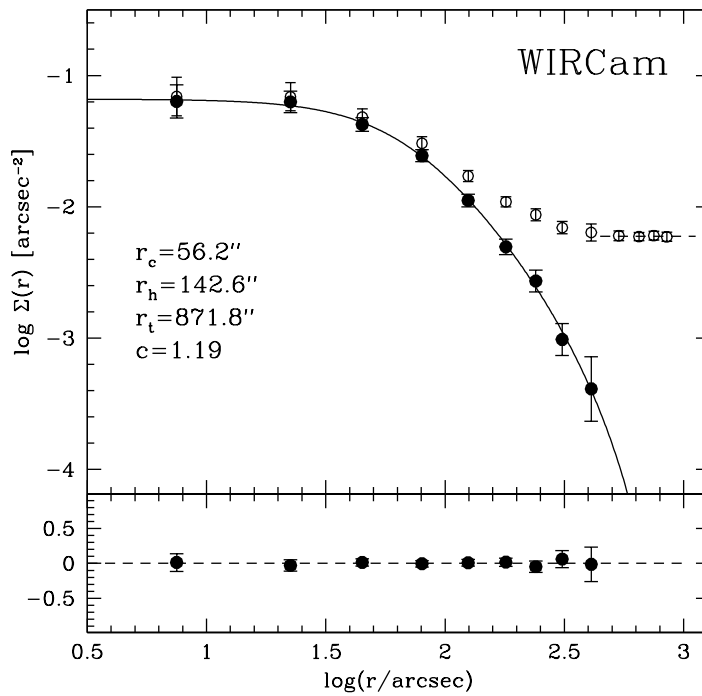


Figure A.10: Observed density profile of M71 obtained from the WIRCam near-infrared dataset (open circles). The dashed line marks the density value of the Galactic field background, obtained by averaging the four outermost points. The black filled circles are the density values obtained after background subtraction (see Section A.5.2). The best-fit King model (solid line) is overplotted to the observations and the residuals of the fit are reported in the bottom panel. The best-fit structural parameters are also labelled in the figure.

obtained from shallow optical images: $r_c = 37.8''$, $r_h = 100.2''$ and $r_t = 533.9''$ (the latter being derived from the quoted value of the concentration parameter: $c = 1.15$). To further investigate this discrepancy, we built the cluster surface brightness profile using a K-band 2MASS image, and we found that it is in agreement with the number density profile shown in Figure A.10, thus further reinforcing the reliability of the newly-determined parameters. On the other hand, if we take into account only the brightest pixels of the K-band image, we find a surface brightness profile consistent with the literature one. This implies that the structural parameters quoted in the literature (which are determined from the light of the most luminous giants only) are not representative of the overall cluster profile.

The availability of a very wide ($\sim 1° \times 1°$) sample at optical wavelengths (the MegaCam dataset) with an analogous level of completeness (comparable to the ACS one for $13 < g' < 19$) allowed us to investigate how the derivation of the cluster stellar number density profile from optical observations can be affected by the presence of large differential extinction. Figure A.11 compares the extinction map and the 2D density map of the $1500'' \times 1500''$ region of the sky centered on M71. The former is obtained from Schlegel et al. (1998) and shows that the color excess $E(B-V)$ varies from $\sim 0.24$ to $\sim 0.54$, with several "spots" and a clear gradient across the field. The density map in the right-hand panel shows the number of stars with $13 < g' < 19$,
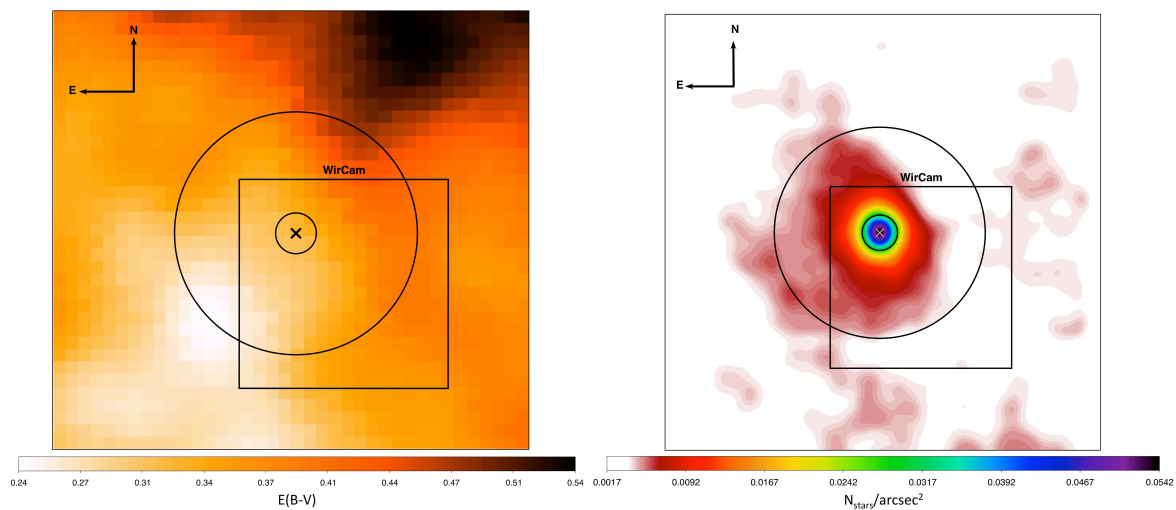


Figure A.11: *Left Panel:* Reddening map (from Schlegel et al., 1998) of the $1500'' \times 1500''$ region centered on M71. The small and large circles mark, respectively, the half-mass and truncation radii of the cluster. The square marks the FOV of the WIRCam dataset. The presence of severe differential reddening across the system, especially in the north-west sector, is apparent. *Right Panel:* 2D stellar density map in the same region of the left panel, obtained by counting all the stars with $13 < g' < 19$ in the optical (MegaCam) dataset. The comparison with the reddening map on the left makes the effect of extinction well visible: the significant decline in the stellar density observed in the external regions of the map (especially in the north-east sector) is clearly due to the presence of thick dust clouds.

per unit area, detected in the MegaCam sample. As expected, at large scales it reveals a direct correspondence with the extinction map: in particular, the stellar density manifestly drops in the north-west sector, where the color excess is the highest, while the opposite is true in the south-east part of the cluster. Obviously, this is expected to significantly impact the density profile obtained from star counts in the optical bands.

To quantitatively test this effect, we determined the cluster density profile by using the Mega-Cam (optical) data. The result is plotted in Figure A.12 and shows that, indeed, the structural parameters of the best-fit King model turn out to be very different from those obtained from the near-infrared (almost reddening-unaffected) dataset (compare with Fig. A.10). In particular, the concentration parameter is much larger ($c = 1.6$), as a consequence of a comparable core radius ($r_c = 58''$ *versus* $56.2''$), but a more than doubled truncation radius ($r_t = 2347.8''$ *versus* $871.8''$). Such a severe over-estimate of $r_t$ is due to the high extinction affecting the external portions of the MegaCam sample, where the Galactic field background is evaluated, and it clearly
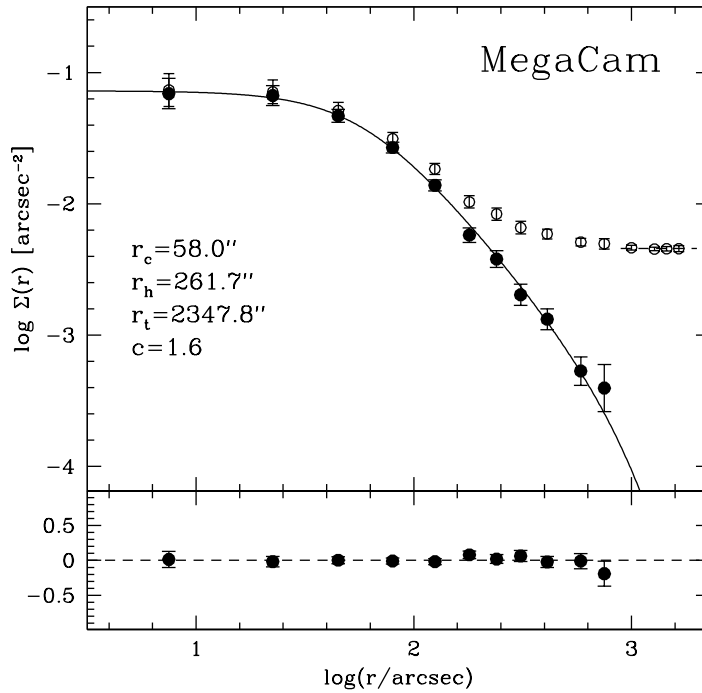


Figure A.12: Density profile of M71 obtained from the optical (MegaCam) dataset. The meaning of all symbols and lines is as in Fig. A.10. The best-fit King model parameters (especially the truncation radius and the concentration) are significantly different from those obtained from near-infrared observations, mainly because the Galactic background is underestimated at optical wavelengths, due to the large differential reddening affecting the external regions of the covered FOV (compare to Fig. A.11).

demonstrates how important is to take differential reddening under control for the determination of a cluster density profile.

### A.5.3 Cluster initial mass

In Sect. A.4.1 we have argued that M71 likely lost a significant fraction of its original mass, mostly due to environmental effects. In this section, we attempt to estimate the total cluster initial mass. Although many recipes can be used to this aim (e.g. Vesperini et al., 2013), we adopted the simple analytical approach described in Lamers et al. (2005); Lamers, Gieles (2006). It describes the way a cluster loses its mass due to the effects of both stellar and dynamical evolution (including processes such as interactions with the Galactic tidal field and shocks due to encounters with giant molecular clouds or spiral arms). Although this method has been developed specifically for open clusters, it can be used also in the case of M71, since its current mass ($M = 2.0^{+1.6}_{-0.9} \times 10^4\,\mathrm{M_\odot}$; from Kimmig et al., 2015) and orbit are consistent with those typical of open clusters (see also Dalessandro et al., 2015, for a similar implementation of this procedure). The initial mass $M_{ini}$ of the cluster can be expressed as follows:

$$(A.2) \qquad M_{ini} \simeq \left[ \left( \frac{M}{M_\odot} \right)^\gamma + \frac{\gamma t}{t_0} \right]^{\frac{1}{\gamma}} [1 - q_{ev}(t)]^{-1},$$

where $M$ is the cluster current mass, $t = 12 \pm 1$ Gyr is the cluster age (Di Cecco et al., 2015), $t_0$ is the dissolution time-scale parameter, $\gamma$ is a dimensionless index and $q_{ev}(t)$ is a function describing the mass-loss due to stellar evolution. The dissolution time-scale parameter is a constant describing the mass-loss process, which depends on the strength of the tidal field. Small values of $t_0$ are typically associated with encounters with molecular clouds and spiral arms, while larger values are used to describe the effect of the Galactic tidal field (see Lamers et al., 2005). Since M71 has an orbit and a structure quite similar to those of open clusters, we assumed $t_0$ in the same range of values ($2.3 < t_0 < 4.7$ Myr) constrained in Lamers et al. (2005). The parameter $\gamma$ depends on the cluster initial density distribution and is usually constrained by the value of the King dimensionless potential $W_0$. We adopted $\gamma = 0.62$, corresponding to $W_0 = 5$, a typical value for an averagely concentrated cluster. The function $q_{ev}(t)$, which describes the mass-loss process due to stellar evolution, can be approximated by the following analytical expression:

$$(A.3) \qquad \log q_{ev}(t) = (\log t - a)^b + c, \quad for \ t > 12.5 \text{ Myr},$$

where $a$, $b$ and $c$ are coefficients that depend on the cluster metallicity. The iron abundance ratio of M71 is [Fe/H]$=-0.73$ (Harris, 1996), which corresponds to $a = 7.03$, $b = 0.26$ and $c = -1.80$ (Lamers et al., 2005).

The resulting initial mass of the cluster is shown in Figure A.13 as a function of the explored range of values of $t_0$. It varies between 1.8 and $6.8 \times 10^5\,\mathrm{M_\odot}$, which are all values typical of the mass of Galactic halo GCs, and is one order of magnitude (or more) larger than the current mass.

Also considering the largest possible value of $t_0$ ($\sim 30$ Myr; see Lamers et al., 2005), we find that the cluster initial mass is at least twice its current value. Clearly, this estimate is based on a simplified approach and on parameters derived by the average behaviors of open clusters, and different assumptions may lead to different results. However, it is interesting to note that, while such a high mass loss would be unlikely for a halo GC, it can be reasonable for a system moving along an orbit confined within the disk (see Sect. A.4.1).
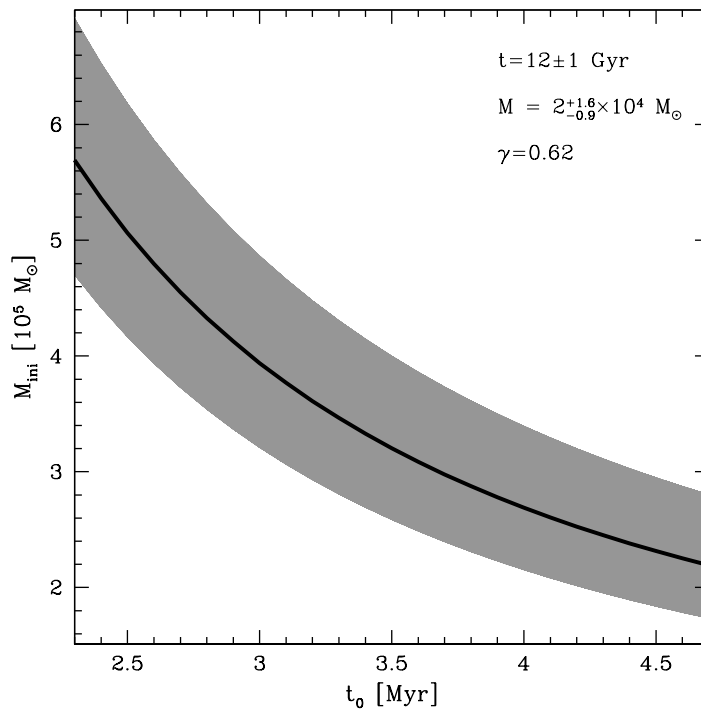


Figure A.13: Initial mass of M71 as a function of the dissolution time-scale parameter $t_0$, estimated as described in Sect. A.5.3. The black curve shows the values obtained by assuming a cluster current mass of $2 \times 10^4$ M$_\odot$ and an age of 12 Gyr. The gray shaded area includes all the values determined by considering the uncertainties in these quantities (see labels).

## A.6 Summary

By using two high-resolution ACS datasets separated by a temporal baseline of $\sim 7$ years, we determined the relative PMs of $\sim 5000$ individual stars in the direction of the low-mass GC M71, finding that only $\sim 60\%$ of them have PMs consistent with being members of the cluster. The identification of four galaxies and two AGNs within the sampled FOV, allowed us to also constrain the absolute PM of M71. This has been used to infer the orbit of the cluster within the Galactic potential well, which has been modeled by using a three-component axisymmetric analytic model.

It turned out that, at least during the last 3 Gyr, M71 has been in a disk-like orbit confined within the Galactic disk. It therefore seems reasonable to suppose that M71 suffered a number of dynamical processes (e.g., with the dense surrounding environment, the Milky Way spiral arms, various molecular clouds) that made it lose an amount of mass significantly larger than what expected for the majority of Galactic GCs, which are on halo-like orbits. We re-determined the gravitational center and density profile of M71 by using resolved star counts from a wide-field near-infrared catalog obtained with WIRCam at the CFHT. This allowed us to minimize the impact of the large and differential reddening affecting the system. With respect to the values quoted in the literature (which have been determined from optical data), we found the cluster centre to be located almost 6" to the west, a $\sim 50\%$ larger core and half-mass radii. Finally, we used a simplified analytical approach to take into account mass-loss processes due to stellar and dynamical evolution, and thus estimate the initial cluster mass, finding that the system likely was one order of magnitude more massive than its current value.

As discussed in Sect. A.1, M71 is known to harbor a rich population of X-ray sources (Elsner et al., 2008), in a number that exceeds the predictions based on the values of its mass and its collision parameter $\Gamma$ (Huang et al., 2010). Since this latter depends on the cluster central luminosity density and core radius ($\Gamma \propto \rho_0^{1.5} r_c^2$; Verbunt, Hut, 1987; Huang et al., 2010), we have re-evaluated it by using the newly determined structural parameters. By adopting the central surface brightness quoted in Harris (1996) and equation (4) in Djorgovski (1993), we found $\log \rho_0 = 2.60$ (in units of $L_\odot/pc^{-3}$). From this quantity and the value of $r_c$ here determined, the resulting value of $\Gamma$ is about half the one quoted in Huang et al. (2010), and the discrepancy in terms of the expected number of X-ray sources aggravates. Instead, the much larger initial mass here estimated for the system would be able to naturally account for the currently observed X-ray population, thus reinforcing the hypothesis that M71 lost a large fraction of stars during its orbit. An accurate investigation of the possible presence of tidal tails around the cluster would be important to confirm such a significant mass-loss from the system. However, this is currently hampered by the large differential reddening affecting this region of the sky, and a wide-field infrared observations are urged to shed light on this issue.

*Abdo A. A., Ackermann M., Ajello M., Baldini L., Ballet J., Barbiellini G., Bastieri D., Bellazzini R., Blandford R. D., Bloom E. D., Bonamente E., Borgland A. W., Bouvier A., Brandt T. J., Bregeon J., Brigida M., Bruel P., Buehler R., Buson S., Caliandro G. A., Cameron R. A., Caraveo P. A., Carrigan S., Casandjian J. M., Charles E., Chaty S., Chekhtman A., Cheung C. C., Chiang J., Ciprini S., Claus R., Cohen-Tanugi J., Conrad J., Decesar M. E., Dermer C. D., de Palma F., Digel S. W., Silva E. D. C. E., Drell P. S., Dubois R., Dumora D., Favuzzi C., Fortin P., Frailis M., Fukazawa Y., Fusco P., Gargano F., Gasparrini D., Gehrels N., Germani S., Giglietto N., Giordano F., Glanzman T., Godfrey G., Grenier I., Grondin M.-H., Grove J. E., Guillemot L., Guiriec S., Hadasch D., Harding A. K., Hays E., Jean P., Jóhannesson G., Johnson T. J., Johnson W. N., Kamae T., Katagiri H., Kataoka J., Kerr M., Knödlseder J., Kuss M., Lande J., Latronico L., Lee S.-H., Lemoine-Goumard M., Llena Garde M., Longo F., Loparco F., Lovellette M. N., Lubrano P., Makeev A., Mazziotta M. N., Michelson P. F., Mitthumsiri W., Mizuno T., Monte C., Monzani M. E., Morselli A., Moskalenko I. V., Murgia S., Naumann-Godo M., Nolan P. L., Norris J. P., Nuss E., Ohsugi T., Omodei N., Orlando E., Ormes J. F., Pancrazi B., Parent D., Pepe M., Pesce-Rollins M., Piron F., Porter T. A., Rainò S., Rando R., Reimer A., Reimer O., Reposeur T., Ripken J., Romani R. W., Roth M., Sadrozinski H. F.-W., Saz Parkinson P. M., Sgrò C., Siskind E. J., Smith D. A., Spinelli P., Strickman M. S., Suson D. J., Takahashi H., Takahashi T., Tanaka T., Thayer J. B., Thayer J. G., Tibaldo L., Torres D. F., Tosti G., Tramacere A., Uchiyama Y., Usher T. L., Vasileiou V., Venter C., Vilchez N., Vitale V., Waite A. P., Wang P., Webb N., Winer B. L., Yang Z., Ylinen T., Ziegler M., Fermi LAT Collaboration .*
A population of gamma-ray emitting globular clusters seen with the Fermi Large Area Telescope
// Astronomy & Astrophysics. XII 2010. 524. A75.


*Allen C., Santillan A.*
An improved model of the galactic mass distribution for orbit computations
// Rev. Mexicana Astron. Astrofis.. X 1991. 22. 255–263.


*Alpar M. A., Cheng A. F., Ruderman M. A., Shaham J.*
A new class of radio pulsars
// Nature. XII 1982. 300. 728–730.

*Altamirano D., Bahramian A., Sivakoff G., Middleton M., Knigge C., Gandhi P., Hynes R., Johnson C., Casella P., Motta S., Miller-Jones J., Neilsen J.*
Swift follow-up observations of the new outburst of the black hole candidate V4641 Sgr
// The Astronomer's Telegram. VIII 2015. 7874.

*Altamirano D., Casella P., Patruno A., Wijnands R., van der Klis M.*
Intermittent Millisecond X-Ray Pulsations from the Neutron Star X-Ray Transient SAX J1748.9-2021 in the Globular Cluster NGC 6440
// Astrophysical Journal Letters. II 2008. 674. L45.

*Altamirano D., Patruno A., Heinke C. O., Markwardt C., Strohmayer T. E., Linares M., Wijnands R., van der Klis M., Swank J. H.*
Discovery of a 205.89 Hz Accreting Millisecond X-ray Pulsar in the Globular Cluster NGC 6440
// Astrophysical Journal Letters. III 2010. 712. L58–L62.

*Althaus L. G., Miller Bertolami M. M., Córsico A. H.*
New evolutionary sequences for extremely low-mass white dwarfs. Homogeneous mass and age determinations and asteroseismic prospects
// Astronomy & Astrophysics. IX 2013. 557. A19.

*Anderson J.*
Variation of the Distortion Solution. VII 2007.

*Anderson J., King I. R.*
PSFs, Photometry, and Astronomy for the ACS/WFC. II 2006. 1.

*Anderson J., Sarajedini A., Bedin L. R., King I. R., Piotto G., Reid I. N., Siegel M., Majewski S. R., Paust N. E. Q., Aparicio A., Milone A. P., Chaboyer B., Rosenberg A.*
The Acs Survey of Globular Clusters. V. Generating a Comprehensive Star Catalog for each Cluster
// Astronomical Journal. VI 2008. 135. 2055–2073.

*Anderson J., van der Marel R. P.*
New Limits on an Intermediate-Mass Black Hole in Omega Centauri. I. Hubble Space Telescope Photometry and Proper Motions
// Astrophysical Journal. II 2010. 710. 1032–1062.

*Anderson S. B.*
A study of recycled pulsars in globular clusters. 1993.

*Anderson S. B., Gorham P. W., Kulkarni S. R., Prince T. A., Wolszczan A.*
Discovery of two radio pulsars in the globular cluster M15

// Nature. VII 1990. 346. 42–44.

*Antoniadis J., Freire P. C. C., Wex N., Tauris T. M., Lynch R. S., van Kerkwijk M. H., Kramer M., Bassa C., Dhillon V. S., Driebe T., Hessels J. W. T., Kaspi V. M., Kondratiev V. I., Langer N., Marsh T. R., McLaughlin M. A., Pennucci T. T., Ransom S. M., Stairs I. H., van Leeuwen J., Verbiest J. P. W., Whelan D. G.*
A Massive Pulsar in a Compact Relativistic Binary
// Science. IV 2013. 340. 448.

*Applegate J. H.*
A mechanism for orbital period modulation in close binaries
// Astrophysical Journal. II 1992. 385. 621–629.

*Applegate J. H., Shaham J.*
Orbital period variability in the eclipsing pulsar binary PSR B1957+20: Evidence for a tidally powered star
// Astrophysical Journal. XI 1994. 436. 312–318.

*Archibald A. M., Kaspi V. M., Hessels J. W. T., Stappers B., Janssen G., Lyne A.*
Long-Term Radio Timing Observations of the Transition Millisecond Pulsar PSR~J1023+0038
// ArXiv e-prints. XI 2013a.

*Archibald A. M., Kaspi V. M., Hessels J. W. T., Stappers B., Janssen G., Lyne A.*
Long-Term Radio Timing Observations of the Transition Millisecond Pulsar PSR~J1023+0038
// ArXiv e-prints. XI 2013b.

*Archibald A. M., Stairs I. H., Ransom S. M., Kaspi V. M., Kondratiev V. I., Lorimer D. R., McLaughlin M. A., Boyles J., Hessels J. W. T., Lynch R., van Leeuwen J., Roberts M. S. E., Jenet F., Champion D. J., Rosen R., Barlow B. N., Dunlap B. H., Remillard R. A.*
A Radio Pulsar/X-ray Binary Link
// Science. VI 2009. 324. 1411.

*Arzoumanian Z., Fruchter A. S., Taylor J. H.*
Orbital variability in the eclipsing pulsar binary PSR B1957+20
// Astrophysical Journal Letters. V 1994. 426. 85–88.

*Backer D. C., Kulkarni S. R., Heiles C., Davis M. M., Goss W. M.*
A millisecond pulsar
// Nature. XII 1982. 300. 615–618.

*Bagchi M., Lorimer D. R., Chennamangalam J.*
Luminosities of recycled radio pulsars in globular clusters
// Monthly Notices of the Royal Astronomical Society. XI 2011. 418. 477–489.

*Bahramian A., Heinke C. O., Degenaar N., Chomiuk L., Wijnands R., Strader J., Ho W. C. G., Pooley D.*
Limits on thermal variations in a dozen quiescent neutron stars over a decade
// Monthly Notices of the Royal Astronomical Society. X 2015. 452. 3475–3488.

*Bahramian A., Heinke C. O., Sivakoff G. R., Altamirano D., Wijnands R., Homan J., Linares M., Pooley D., Degenaar N., Gladstone J. C.*
Discovery of the Third Transient X-Ray Binary in the Galactic Globular Cluster Terzan 5
// Astrophysical Journal. I 2014. 780. 127.

*Bahramian A., Heinke C. O., Sivakoff G. R., Gladstone J. C.*
Stellar Encounter Rate in Galactic Globular Clusters
// Astrophysical Journal. IV 2013. 766. 136.

*Bassa C. G., Patruno A., Hessels J. W. T., Keane E. F., Monard B., Mahony E. K., Bogdanov S., Corbel S., Edwards P. G., Archibald A. M., Janssen G. H., Stappers B. W., Tendulkar S.*
A state change in the low-mass X-ray binary XSS J12270-4859
// Monthly Notices of the Royal Astronomical Society. VI 2014. 441. 1825–1830.

*Bassa C. G., van Kerkwijk M. H., Koester D., Verbunt F.*
The masses of PSR J1911-5958A and its white dwarf companion
// Astronomy & Astrophysics. IX 2006. 456. 295–304.

*Beccari G., De Marchi G., Panagia N., Pasquini L.*
Hα photometry of low-mass stars in 47 Tucanae: chromospheric activity and exotica
// Monthly Notices of the Royal Astronomical Society. I 2014. 437. 2621–2631.

*Becker W., Swartz D. A., Pavlov G. G., Elsner R. F., Grindlay J., Mignani R., Tennant A. F., Backer D., Pulone L., Testa V., Weisskopf M. C.*
Chandra X-Ray Observatory Observations of the Globular Cluster M28 and Its Millisecond Pulsar PSR B1821-24
// Astrophysical Journal. IX 2003. 594. 798–811.

*Bellini A., Anderson J., Bedin L. R.*
Astrometry and Photometry with HST WFC3. II. Improved Geometric-Distortion Corrections for 10 Filters of the UVIS Channel
// Astronomical Society of the Pacific, Publications. V 2011. 123. 622.

*Bellini A., Anderson J., van der Marel R. P., Watkins L. L., King I. R., Bianchini P., Chanamé J., Chandar R., Cool A. M., Ferraro F. R., Ford H., Massari D.*
Hubble Space Telescope Proper Motion (HSTPROMO) Catalogs of Galactic Globular Clusters. I. Sample Selection, Data Reduction, and NGC 7078 Results
// Astrophysical Journal. XII 2014. 797. 115.

*Bellini A., Bedin L. R., Pichardo B., Moreno E., Allen C., Piotto G., Anderson J.*
Absolute proper motion of the Galactic open cluster M 67
// Astronomy & Astrophysics. IV 2010. 513. A51.

*Bellm E., Djorgovski S. G., Drake A. J., Hessels J., Kulkarni S. R., Levitan D. B., Mahabal A. A., Phinney E. S., Ransom S. M., Roberts M., Prince T. A., Sesar B., Tang S.*
The Optical Counterpart of the Redback Pulsar J2129-0428
// American Astronomical Society Meeting Abstracts #221. 221. I 2013. 154.10.
(American Astronomical Society Meeting Abstracts).

*Bellm E. C., Kaplan D. L., Breton R. P., Phinney E. S., Bhalerao V. B., Camilo F., Dahal S., Djorgovski S. G., Drake A. J., Hessels J. W. T., Laher R. R., Levitan D. B., Lewis F., Mahabal A. A., Ofek E. O., Prince T. A., Ransom S. M., Roberts M. S. E., Russell D. M., Sesar B., Surace J. A., Tang S.*
Properties and Evolution of the Redback Millisecond Pulsar Binary PSR J2129-0429
// Astrophysical Journal. I 2016. 816. 74.

*Benvenuto O. G., De Vito M. A., Horvath J. E.*
Understanding the Evolution of Close Binary Systems with Radio Pulsars
// Astrophysical Journal Letters. V 2014. 786. L7.

*Bergeron P., Wesemael F., Dufour P., Beauchamp A., Hunter C., Saffer R. A., Gianninas A., Ruiz M. T., Limoges M.-M., Dufour P., Fontaine G., Liebert J.*
A Comprehensive Spectroscopic Analysis of DB White Dwarfs
// Astrophysical Journal. VIII 2011. 737. 28.

*Bhattacharya D., van den Heuvel E. P. J.*
Formation and evolution of binary and millisecond radio pulsars
// Physics Reports. 1991. 203. 1–124.

*Bica E., Ortolani S., Barbuy B.*
Globular Clusters in the Galactic Bulge
// . VI 2016. 33. e028.

*Bisnovatyi-Kogan G. S., Komberg B. V.*
Pulsars and close binary systems
// Soviet Astronomy. X 1974. 18. 217.

*Blandford R., Teukolsky S. A.*
Arrival-time analysis for a pulsar in a binary system.
// Astrophysical Journal. IV 1976. 205. 580–591.

169

*Bogdanov S., Grindlay J. E., Heinke C. O., Camilo F., Freire P. C. C., Becker W.*
Chandra X-Ray Observations of 19 Millisecond Pulsars in the Globular Cluster 47 Tucanae
// Astrophysical Journal. VIII 2006. 646. 1104–1115.

*Bogdanov S., Grindlay J. E., van den Berg M.*
An X-Ray Variable Millisecond Pulsar in the Globular Cluster 47 Tucanae: Closing the Link to Low-Mass X-Ray Binaries
// Astrophysical Journal. IX 2005. 630. 1029–1036.

*Bogdanov S., Patruno A., Archibald A. M., Bassa C., Hessels J. W. T., Janssen G. H., Stappers B. W.*
X-Ray Observations of XSS J12270-4859 in a New Low State: A Transformation to a Disk-free Rotation-powered Pulsar Binary
// Astrophysical Journal. VII 2014. 789. 40.

*Bogdanov S., van den Berg M., Servillat M., Heinke C. O., Grindlay J. E., Stairs I. H., Ransom S. M., Freire P. C. C., Bégin S., Becker W.*
Chandra X-ray Observations of 12 Millisecond Pulsars in the Globular Cluster M28
// Astrophysical Journal. IV 2011. 730. 81.

*Bohlin R. C.*
Flux Calibration of the ACS CCD Cameras IV. Absolute Fluxes. II 2012.  1.

*Bozzo E., Kuulkers E., Ferrigno C.*
Swift/XRT observations of the X-ray transient in NGC6440
// The Astronomer's Telegram. II 2015. 7106.

*Breton R. P., Kaspi V. M., Kramer M., McLaughlin M. A., Lyutikov M., Ransom S. M., Stairs I. H., Ferdman R. D., Camilo F., Possenti A.*
Relativistic Spin Precession in the Double Pulsar
// Science. VII 2008. 321. 104.

*Breton R. P., van Kerkwijk M. H., Roberts M. S. E., Hessels J. W. T., Camilo F., McLaughlin M. A., Ransom S. M., Ray P. S., Stairs I. H.*
Discovery of the Optical Counterparts to Four Energetic Fermi Millisecond Pulsars
// Astrophysical Journal. VI 2013. 769. 108.

*Brogaard K., VandenBerg D. A., Bedin L. R., Milone A. P., Thygesen A., Grundahl F.*
The age of 47 Tuc from self-consistent isochrone fits to colour-magnitude diagrams and the eclipsing member V69
// Monthly Notices of the Royal Astronomical Society. VI 2017. 468. 645–661.

*Burderi L., D'Antona F., Burgay M.*
PSR J1740-5340: Accretion Inhibited by Radio Ejection in a Binary Millisecond Pulsar in the Globular Cluster NGC 6397
// Astrophysical Journal. VII 2002. 574. 325–331.

*Burgay M., D'Amico N., Possenti A., Manchester R. N., Lyne A. G., Joshi B. C., McLaughlin M. A., Kramer M., Sarkissian J. M., Camilo F., Kalogera V., Kim C., Lorimer D. R.*
An increased estimate of the merger rate of double neutron stars from observations of a highly relativistic system
// Nature. XII 2003. 426. 531–533.

*Cadelano M., Dalessandro E., Ferraro F. R., Miocchi P., Lanzoni B., Pallanca C., Massari D.*
Proper Motions and Structural Parameters of the Galactic Globular Cluster M71
// Astrophysical Journal. II 2017a. 836. 170.

*Cadelano M., Pallanca C., Ferraro F. R., Dalessandro E., Lanzoni B., Patruno A.*
The Optical Counterpart to the Accreting Millisecond X-ray Pulsar SAX J1748.9-2021 in the Globular Cluster NGC 6440
// ArXiv e-prints. VI 2017b.

*Cadelano M., Pallanca C., Ferraro F. R., Salaris M., Dalessandro E., Lanzoni B., Freire P. C. C.*
Optical Identification of He White Dwarfs Orbiting Four Millisecond Pulsars in the Globular Cluster 47 Tucanae
// Astrophysical Journal. X 2015a. 812. 63.

*Cadelano M., Pallanca C., Ferraro F. R., Stairs I., Ransom S. M., Dalessandro E., Lanzoni B., Hessels J. W. T., Freire P. C. C.*
Radio Timing and Optical Photometry of the Black Widow System PSR J1953+1846A in the Globular Cluster M71
// Astrophysical Journal. VII 2015b. 807. 91.

*Cadelano M., Ransom S. M., Freire P. C. C., Ferraro F. R., Hessels J. W. T., Lanzoni B., Pallanca C., Stairs I. H.*
Discovery of three new millisecond pulsars in Terzan 5
// ArXiv e-prints. I 2018.

*Callanan P. J., van Paradijs J., Rengelink R.*
The orbital light curve of PSR 1957 + 20
// Astrophysical Journal. II 1995. 439. 928–932.

*Camilo F., Lorimer D. R., Freire P., Lyne A. G., Manchester R. N.*
Observations of 20 Millisecond Pulsars in 47 Tucanae at 20 Centimeters
// Astrophysical Journal. VI 2000. 535. 975–990.

*Campana S., D'Avanzo P., Casares J., Covino S., Israel G., Marconi G., Hynes R., Charles P., Stella L.*
Indirect Evidence of an Active Radio Pulsar in the Quiescent State of the Transient Millisecond Pulsar SAX J1808.4-3658
// Astrophysical Journal Letters. X 2004. 614. L49–L52.

*Cardelli J. A., Clayton G. C., Mathis J. S.*
The relationship between infrared, optical, and ultraviolet extinction
// Astrophysical Journal. X 1989. 345. 245–256.

*Casetti-Dinescu D. I., Girard T. M., Jílková L., van Altena W. F., Podestá F., López C. E.*
Space Velocities of Southern Globular Clusters. VII. NGC 6397, NGC 6626 (M28), and NGC 6656 (M22)
// Astronomical Journal. VIII 2013. 146. 33.

*Charles P. A., Coe M. J.*
Optical, ultraviolet and infrared observations of X-ray binaries
// Compact stellar X-ray sources. IV 2006. 215–265.

*Chen H.-L., Chen X., Tauris T. M., Han Z.*
Formation of Black Widows and Redbacks –Two Distinct Populations of Eclipsing Binary Millisecond Pulsars
// Astrophysical Journal. IX 2013. 775. 27.

*Chennamangalam J., Lorimer D. R., Mandel I., Bagchi M.*
Constraining the luminosity function parameters and population size of radio pulsars in globular clusters
// Monthly Notices of the Royal Astronomical Society. V 2013. 431. 874–881.

*Clark G. W.*
X-ray binaries in globular clusters
// Astrophysical Journal Letters. VIII 1975. 199. L143–L145.

*Cocozza G., Ferraro F. R., Possenti A., Beccari G., Lanzoni B., Ransom S., Rood R. T., D'Amico N.*
A Puzzling Millisecond Pulsar Companion in NGC 6266
// Astrophysical Journal Letters. VI 2008. 679. L105–L108.

*Cocozza G., Ferraro F. R., Possenti A., D'Amico N.*
The Puzzling Properties of the Helium White Dwarf Orbiting the Millisecond Pulsar PSR J1911-5958A in NGC 6752
// Astrophysical Journal Letters. IV 2006. 641. L129–L132.

*Cohn H. N., Lugger P. M., Couch S. M., Anderson J., Cool A. M., van den Berg M., Bogdanov S., Heinke C. O., Grindlay J. E.*
Identification of Faint Chandra X-ray Sources in the Core-collapsed Globular Cluster NGC 6397: Evidence for a Bimodal Cataclysmic Variable Population
// Astrophysical Journal. X 2010. 722. 20–32.

*Colpi M., Possenti A., Gualandris A.*
The Case of PSR J1911-5958A in the Outskirts of NGC 6752: Signature of a Black Hole Binary in the Cluster Core?
// Astrophysical Journal Letters. V 2002. 570. L85–L88.

*Corongiu A., Burgay M., Possenti A., Camilo F., D'Amico N., Lyne A. G., Manchester R. N., Sarkissian J. M., Bailes M., Johnston S., Kramer M., van Straten W.*
A Shapiro Delay Detection in the Binary System Hosting the Millisecond Pulsar PSR J1910-5959A
// Astrophysical Journal. XII 2012. 760. 100.

*Cutri R. M., Skrutskie M. F., van Dyk S., Beichman C. A., Carpenter J. M., Chester T., Cambresy L., Evans T., Fowler J., Gizis J., Howard E., Huchra J., Jarrett T., Kopan E. L., Kirkpatrick J. D., Light R. M., Marsh K. A., McCallon H., Schneider S., Stiening R., Sykes M., Weinberg M., Wheaton W. A., Wheelock S., Zacarias N.*
VizieR Online Data Catalog: 2MASS All-Sky Catalog of Point Sources (Cutri+ 2003)
// VizieR Online Data Catalog. VI 2003. 2246.

*D'Amico N., Possenti A., Fici L., Manchester R. N., Lyne A. G., Camilo F., Sarkissian J.*
Timing of Millisecond Pulsars in NGC 6752: Evidence for a High Mass-to-Light Ratio in the Cluster Core
// Astrophysical Journal Letters. V 2002. 570. L89–L92.

*D'Avanzo P., Campana S., Casares J., Covino S., Israel G. L., Stella L.*
The optical counterparts of accreting millisecond X-ray pulsars during quiescence
// Astronomy & Astrophysics. XII 2009. 508. 297–308.

*Dalessandro E., Beccari G., Lanzoni B., Ferraro F. R., Schiavon R., Rood R. T.*
Multiwavelength Photometry in the Globular Cluster M2
// The Astrophysical Journal Supplement Series. VI 2009. 182. 509–518.

*Dalessandro E., Ferraro F. R., Massari D., Lanzoni B., Miocchi P., Beccari G., Bellini A., Sills A., Sigurdsson S., Mucciarelli A., Lovisi L.*
Double Blue Straggler Sequences in Globular Clusters: The Case of NGC 362
// Astrophysical Journal. XII 2013. 778. 135.

*Dalessandro E., Lanzoni B., Ferraro F. R., Rood R. T., Milone A., Piotto G., Valenti E.*
Blue Straggler Stars in the Unusual Globular Cluster NGC 6388
// Astrophysical Journal. IV 2008a. 677. 1069–1079.

*Dalessandro E., Lanzoni B., Ferraro F. R., Vespe F., Bellazzini M., Rood R. T.*
Another Nonsegregated Blue Straggler Population in a Globular Cluster: the Case of NGC 2419
// Astrophysical Journal. VII 2008b. 681. 311–319.

*Dalessandro E., Miocchi P., Carraro G., Jílková L., Moitinho A.*
Evidence of tidal distortions and mass-loss from the old open cluster NGC 6791
// Monthly Notices of the Royal Astronomical Society. V 2015. 449. 1811–1818.

*De Marchi G., Panagia N., Romaniello M.*
Photometric Determination of the Mass Accretion Rates of Pre-main-sequence Stars. I. Method and Application to the SN 1987A Field
// Astrophysical Journal. V 2010. 715. 1–17.

*De Marchi G., Paresce F., Pulone L.*
Why Haven't Loose Globular Clusters Collapsed Yet?
// Astrophysical Journal Letters. II 2007. 656. L65–L68.

*De Martino D., Papitto A., Belloni T., Burgay M., De Ona Wilhelmi E., Li J., Pellizzoni A., Possenti A., Rea N., Torres D. F.*
Multiwavelength observations of the transitional millisecond pulsar binary XSS J12270-4859
// Monthly Notices of the Royal Astronomical Society. XII 2015. 454. 2190–2198.

*Degenaar N., Wijnands R.*
Strong X-ray variability in the quiescent state of the neutron star low-mass X-ray binary EXO 1745-248
// Monthly Notices of the Royal Astronomical Society. V 2012. 422. 581–589.

*Demorest P. B., Pennucci T., Ransom S. M., Roberts M. S. E., Hessels J. W. T.*
A two-solar-mass neutron star measured using Shapiro delay
// Nature. X 2010. 467. 1081–1083.

*Di Cecco A., Bono G., Prada Moroni P. G., Tognelli E., Allard F., Stetson P. B., Buonanno R., Ferraro I., Iannicola G., Monelli M., Nonino M., Pulone L.*
On the Absolute Age of the Metal-rich Globular M71 (NGC 6838). I. Optical Photometry
// Astronomical Journal. VIII 2015. 150. 51.

*Dib R., Kaspi V. M.*
16 yr of RXTE Monitoring of Five Anomalous X-Ray Pulsars

// Astrophysical Journal. III 2014. 784. 37.

*Dicke R. H.*
The Measurement of Thermal Radiation at Microwave Frequencies
// Review of Scientific Instruments. 1946. 17, 7. 268–275.

*Dinescu D. I., van Altena W. F., Girard T. M., López C. E.*
Space Velocities of Southern Globular Clusters. II. New Results for 10 Clusters
// Astronomical Journal. I 1999. 117. 277–285.

*Djorgovski S.*
Physical Parameters of Galactic Globular Clusters
// Structure and Dynamics of Globular Clusters. 50. I 1993. 373.
(Astronomical Society of the Pacific Conference Series).

*Doroshenko O., Löhmer O., Kramer M., Jessner A., Wielebinski R., Lyne A. G., Lange C.*
Orbital variability of the PSR J2051-0827 binary system
// Astronomy & Astrophysics. XI 2001. 379. 579–587.

*Dotter A., Chaboyer B., Jevremović D., Kostov V., Baron E., Ferguson J. W.*
The Dartmouth Stellar Evolution Database
// The Astrophysical Journal Supplement Series. IX 2008. 178. 89–101.

*Dowd A., Sisk W., Hagen J.*
WAPP — Wideband Arecibo Pulsar Processor
// IAU Colloq. 177: Pulsar Astronomy - 2000 and Beyond. 202. 2000. 275–276.
(Astronomical Society of the Pacific Conference Series).

*Edmonds P. D., Gilliland R. L., Camilo F., Heinke C. O., Grindlay J. E.*
A Millisecond Pulsar Optical Counterpart with Large-Amplitude Variability in the Globular Cluster 47 Tucanae
// Astrophysical Journal. XI 2002. 579. 741–751.

*Edmonds P. D., Gilliland R. L., Heinke C. O., Grindlay J. E., Camilo F.*
Optical Detection of a Variable Millisecond Pulsar Companion in 47 Tucanae
// Astrophysical Journal Letters. VIII 2001. 557. L57–L60.

*Eggleton P. P.*
Approximations to the radii of Roche lobes
// Astrophysical Journal. V 1983. 268. 368.

*Elsner R. F., Heinke C. O., Cohn H. N., Lugger P. M., Maxwell J. E., Stairs I. H., Ransom S. M., Hessels J. W. T., Becker W., Huang R. H. H., Edmonds P. D., Grindlay J. E., Bogdanov S., Ghosh K., Weisskopf M. C.*

Chandra X-Ray Observatory Observations of the Globular Cluster M71
// Astrophysical Journal. XI 2008. 687. 1019–1034.

*Ferraro F. R., Beccari G., Rood R. T., Bellazzini M., Sills A., Sabbi E.*
Discovery of Another Peculiar Radial Distribution of Blue Stragglers in Globular Clusters: The Case of 47 Tucanae
// Astrophysical Journal. III 2004. 603. 127–134.

*Ferraro F. R., Clementini G., Fusi Pecci F., Buonanno R.*
CCD-photometry of galactic globular clusters. III - NGC 6171
// Monthly Notices of the Royal Astronomical Society. X 1991. 252. 357–377.

*Ferraro F. R., Clementini G., Fusi Pecci F., Sortino R., Buonanno R.*
On the giant, horizontal and asymptotic branches of Galactic globular clusters. IV - CCD photometry of NGC 1904
// Monthly Notices of the Royal Astronomical Society. VI 1992. 256. 391–403.

*Ferraro F. R., D'Amico N., Possenti A., Mignani R. P., Paltrinieri B.*
Blue Stragglers, Young White Dwarfs, and UV-Excess Stars in the Core of 47 Tucanae
// Astrophysical Journal. XI 2001a. 561. 337–345.

*Ferraro F. R., Dalessandro E., Mucciarelli A., Beccari G., Rich R. M., Origlia L., Lanzoni B., Rood R. T., Valenti E., Bellazzini M., Ransom S. M., Cocozza G.*
The cluster Terzan 5 as a remnant of a primordial building block of the Galactic bulge
// Nature. XI 2009. 462. 483–486.

*Ferraro F. R., Lanzoni B., Dalessandro E., Beccari G., Pasquato M., Miocchi P., Rood R. T., Sigurdsson S., Sills A., Vesperini E., Mapelli M., Contreras R., Sanna N., Mucciarelli A.*
Dynamical age differences among coeval star clusters as revealed by blue stragglers
// Nature. XII 2012. 492. 393–395.

*Ferraro F. R., Massari D., Dalessandro E., Lanzoni B., Origlia L., Rich R. M., Mucciarelli A.*
The Age of the Young Bulge-like Population in the Stellar System Terzan 5: Linking the Galactic Bulge to the High-z Universe
// Astrophysical Journal. IX 2016. 828. 75.

*Ferraro F. R., Messineo M., Fusi Pecci F., de Palo M. A., Straniero O., Chieffi A., Limongi M.*
The Giant, Horizontal, and Asymptotic Branches of Galactic Globular Clusters. I. The Catalog, Photometric Observables, and Features
// Astronomical Journal. X 1999. 118. 1738–1758.

*Ferraro F. R., Pallanca C., Lanzoni B., Cadelano M., Massari D., Dalessandro E., Mucciarelli A.*

Probing the MSP Prenatal Stage: The Optical Identification of the X-Ray Burster EXO 1745-248 in Terzan 5
// Astrophysical Journal Letters. VII 2015a. 807. L1.

*Ferraro F. R., Pallanca C., Lanzoni B., Cadelano M., Massari D., Dalessandro E., Mucciarelli A.*
Probing the MSP Prenatal Stage: The Optical Identification of the X-Ray Burster EXO 1745-248 in Terzan 5
// Astrophysical Journal Letters. VII 2015b. 807. L1.

*Ferraro F. R., Paltrinieri B., Fusi Pecci F., Cacciari C., Dorman B., Rood R. T., Buonanno R., Corsi C. E., Burgarella D., Laget M.*
HST observations of blue Straggler stars in the core of the globular cluster M 3.
// Astronomy & Astrophysics. VIII 1997. 324. 915–928.

*Ferraro F. R., Paltrinieri B., Paresce F., De Marchi G.*
Very Large Telescope Observations of the Peculiar Globular Cluster NGC 6712: Discovery of a UV, H$\alpha$-Excess Star in the Core
// Astrophysical Journal Letters. X 2000. 542. L29–L32.

*Ferraro F. R., Possenti A., D'Amico N., Sabbi E.*
The Bright Optical Companion to the Eclipsing Millisecond Pulsar in NGC 6397
// Astrophysical Journal Letters. XI 2001b. 561. L93–L96.

*Ferraro F. R., Possenti A., Sabbi E., D'Amico N.*
The Helium White Dwarf Orbiting the Millisecond Pulsar in the Halo of the Globular Cluster NGC 6752
// Astrophysical Journal Letters. X 2003a. 596. L211–L214.

*Ferraro F. R., Possenti A., Sabbi E., Lagani P., Rood R. T., D'Amico N., Origlia L.*
The Puzzling Dynamical Status of the Core of the Globular Cluster NGC 6752
// Astrophysical Journal. IX 2003b. 595. 179–186.

*Ferraro F. R., Sabbi E., Gratton R., Possenti A., D'Amico N., Bragaglia A., Camilo F.*
Accurate Mass Ratio and Heating Effects in the Dual-Line Millisecond Binary Pulsar in NGC 6397
// Astrophysical Journal Letters. II 2003c. 584. L13–L16.

*Ferraro F. R., Sills A., Rood R. T., Paltrinieri B., Buonanno R.*
Blue Straggler Stars: A Direct Comparison of Star Counts and Population Ratios in Six Galactic Globular Clusters
// Astrophysical Journal. V 2003d. 588. 464–477.

*Flewelling H. A., Magnier E. A., Chambers K. C., Heasley J. N., Holmberg C., Huber M. E.,*
*Sweeney W., Waters C. Z., Chen X., Farrow D., Hasinger G., Henderson R., Long K. S., Metcalfe*
*N., Nieto-Santisteban M. A., Norberg P., Saglia R. P., Szalay A., Rest A., Thakar A. R., Tonry*
*J. L., Valenti J., Werner S., White R., Denneau L., Draper P. W., Hodapp K. W., Jedicke R., Kaiser*
*N., Kudritzki R.-P., Price P. A., Wainscoat R. J., Chastel S., McClean B., Postman M., Shiao B.*
The Pan-STARRS1 Database and Data Products
// ArXiv e-prints. XII 2016.

*Freire P. C., Camilo F., Kramer M., Lorimer D. R., Lyne A. G., Manchester R. N., D'Amico N.*
Further results from the timing of the millisecond pulsars in 47 Tucanae
// Monthly Notices of the Royal Astronomical Society. IV 2003. 340. 1359–1374.

*Freire P. C., Camilo F., Lorimer D. R., Lyne A. G., Manchester R. N., D'Amico N.*
Timing the millisecond pulsars in 47 Tucanae
// Monthly Notices of the Royal Astronomical Society. IX 2001a. 326. 901–915.

*Freire P. C., Gupta Y., Ransom S. M., Ishwara-Chandra C. H.*
Giant Metrewave Radio Telescope Discovery of a Millisecond Pulsar in a Very Eccentric Binary
System
// Astrophysical Journal Letters. V 2004. 606. L53–L56.

*Freire P. C., Kramer M., Lyne A. G., Camilo F., Manchester R. N., D'Amico N.*
Detection of Ionized Gas in the Globular Cluster 47 Tucanae
// Astrophysical Journal Letters. VIII 2001b. 557. L105–L108.

*Freire P. C. C.*
Eclipsing Binary Pulsars
// Binary Radio Pulsars. 328. VII 2005. 405.
(Astronomical Society of the Pacific Conference Series).

*Freire P. C. C., Hessels J. W. T., Nice D. J., Ransom S. M., Lorimer D. R., Stairs I. H.*
The Millisecond Pulsars in NGC 6760
// Astrophysical Journal. III 2005. 621. 959–965.

*Freire P. C. C., Ransom S. M., Bégin S., Stairs I. H., Hessels J. W. T., Frey L. H., Camilo F.*
Eight New Millisecond Pulsars in NGC 6440 and NGC 6441
// Astrophysical Journal. III 2008a. 675. 670–682.

*Freire P. C. C., Ridolfi A.*
An algorithm for determining the rotation count of pulsars
// Monthly Notices of the Royal Astronomical Society. II 2018.

*Freire P. C. C., Ridolfi A., Kramer M., Jordan C., Manchester R. N., Torne P., Sarkissian J., Heinke C. O., D'Amico N., Camilo F., Lorimer D. R., Lyne A. G.*
Long-term observations of the pulsars in 47 Tucanae - II. Proper motions, accelerations and jerks
// ArXiv e-prints. VI 2017.

*Freire P. C. C., Tauris T. M.*
Direct formation of millisecond pulsars from rotationally delayed accretion-induced collapse of massive white dwarfs
// Monthly Notices of the Royal Astronomical Society. II 2014. 438. L86–L90.

*Freire P. C. C., Wolszczan A., van den Berg M., Hessels J. W. T.*
A Massive Neutron Star in the Globular Cluster M5
// Astrophysical Journal. VI 2008b. 679. 1433–1442.

*Fruchter A. S., Stinebring D. R., Taylor J. H.*
A millisecond pulsar in an eclipsing binary
// Nature. V 1988. 333. 237–239.

*Gavriil F. P., Strohmayer T. E., Swank J. H., Markwardt C. B.*
Discovery of 442 Hz Pulsations from an X-Ray Source in the Globular Cluster NGC 6440
// Astrophysical Journal Letters. XI 2007. 669. L29–L32.

*Geffert M., Maintz G.*
First results of a photometric and astrometric study of the globular cluster M 71 (NGC 6838)
// Astronomy and Astrophysics Supplement. VI 2000. 144. 227–233.

*Gentile P. A., Roberts M. S. E., McLaughlin M. A., Camilo F., Hessels J. W. T., Kerr M., Ransom S. M., Ray P. S., Stairs I. H.*
X-Ray Observations of Black Widow Pulsars
// Astrophysical Journal. III 2014. 783. 69.

*Gieles M., Balbinot E., Yaaqib R., Henault-Brunet V., Zocchi A., Peuten M., Jonker P. G.*
Mass models of NGC 6624 without an intermediate-mass black hole
// ArXiv e-prints. IX 2017.

*Girardi L., Bressan A., Bertelli G., Chiosi C.*
Evolutionary tracks and isochrones for low- and intermediate-mass stars: From 0.15 to 7 $M_{sun}$, and from Z=0.0004 to 0.03
// Astronomy and Astrophysics Supplement. II 2000. 141. 371–383.

*Girardi L., Williams B. F., Gilbert K. M., Rosenfield P., Dalcanton J. J., Marigo P., Boyer M. L., Dolphin A., Weisz D. R., Melbourne J., Olsen K. A. G., Seth A. C., Skillman E.*

The ACS Nearby Galaxy Survey Treasury. IX. Constraining Asymptotic Giant Branch Evolution with Old Metal-poor Galaxies
// Astrophysical Journal. XII 2010. 724. 1030–1043.

*Gold T.*
Rotating Neutron Stars as the Origin of the Pulsating Radio Sources
// Nature. V 1968. 218. 731–732.

*Goldreich P., Julian W. H.*
Pulsar Electrodynamics
// Astrophysical Journal. VIII 1969. 157. 869.

*Goldsbury R., Richer H. B., Anderson J., Dotter A., Sarajedini A., Woodley K.*
The ACS Survey of Galactic Globular Clusters. X. New Determinations of Centers for 65 Clusters
// Astronomical Journal. XII 2010. 140. 1830–1837.

*Gratton R. G., Bragaglia A., Carretta E., Clementini G., Desidera S., Grundahl F., Lucatello S.*
Distances and ages of NGC 6397, NGC 6752 and 47 Tuc
// Astronomy & Astrophysics. IX 2003. 408. 529–543.

*Guillot S., Rutledge R. E.*
Rejecting Proposed Dense Matter Equations of State with Quiescent Low-mass X-Ray Binaries
// Astrophysical Journal Letters. XI 2014. 796. L3.

*Guillot S., Servillat M., Webb N. A., Rutledge R. E.*
Measurement of the Radius of Neutron Stars with High Signal-to-noise Quiescent Low-mass X-Ray Binaries in Globular Clusters
// Astrophysical Journal. VII 2013. 772. 7.

*Güver T., Özel F.*
The Mass and the Radius of the Neutron Star in the Transient Low-mass X-Ray Binary SAX J1748.9-2021
// Astrophysical Journal Letters. III 2013. 765. L1.

*Hack W., Cox C.*
Revised IDCTAB Definition: Application to HST data. VII 2001.  8.

*Hansen B. M. S., Kalirai J. S., Anderson J., Dotter A., Richer H. B., Rich R. M., Shara M. M., Fahlman G. G., Hurley J. R., King I. R., Reitzel D., Stetson P. B.*
An age difference of two billion years between a metal-rich and a metal-poor globular cluster
// Nature. VIII 2013. 500. 51–53.

*Harris W. E.*
A Catalog of Parameters for Globular Clusters in the Milky Way
// Astronomical Journal. X 1996. 112. 1487.

*Hartman J. M., Patruno A., Chakrabarty D., Kaplan D. L., Markwardt C. B., Morgan E. H., Ray P. S., van der Klis M., Wijnands R.*
The Long-Term Evolution of the Spin, Pulse Shape, and Orbit of the Accretion-powered Millisecond Pulsar SAX J1808.4-3658
// Astrophysical Journal. III 2008. 675. 1468–1486.

*Heinke C. O., Cohn H. N., Lugger P. M., Webb N. A., Ho W. C. G., Anderson J., Campana S., Bogdanov S., Haggard D., Cool A. M., Grindlay J. E.*
Improved mass and radius constraints for quiescent neutron stars in $\omega$ Cen and NGC 6397
// Monthly Notices of the Royal Astronomical Society. X 2014. 444. 443–456.

*Heinke C. O., Edmonds P. D., Grindlay J. E., Lloyd D. A., Cohn H. N., Lugger P. M.*
A Chandra X-Ray Study of the Dense Globular Cluster Terzan 5
// Astrophysical Journal. VI 2003. 590. 809–821.

*Heinke C. O., Grindlay J. E., Edmonds P. D., Cohn H. N., Lugger P. M., Camilo F., Bogdanov S., Freire P. C.*
A Deep Chandra Survey of the Globular Cluster 47 Tucanae: Catalog of Point Sources
// Astrophysical Journal. VI 2005. 625. 796–824.

*Heinke C. O., Wijnands R., Cohn H. N., Lugger P. M., Grindlay J. E., Pooley D., Lewin W. H. G.*
Faint X-Ray Sources in the Globular Cluster Terzan 5
// Astrophysical Journal. XI 2006. 651. 1098–1111.

*Hessels J., Possenti A., Bailes M., Bassa C., Freire P. C. C., Lorimer D. R., Lynch R., Ransom S. M., Stairs I. H.*
Pulsars in Globular Clusters with the SKA
// Advancing Astrophysics with the Square Kilometre Array (AASKA14). IV 2015. 47.

*Hessels J. W. T., Ransom S. M., Stairs I. H., Freire P. C. C., Kaspi V. M., Camilo F.*
A Radio Pulsar Spinning at 716 Hz
// Science. III 2006. 311. 1901–1904.

*Hessels J. W. T., Ransom S. M., Stairs I. H., Kaspi V. M., Freire P. C. C.*
A 1.4 GHz Arecibo Survey for Pulsars in Globular Clusters
// Astrophysical Journal. XI 2007. 670. 363–378.

*Hewish A., Bell S. J., Pilkington J. D. H., Scott P. F., Collins R. A.*
Observation of a Rapidly Pulsating Radio Source

// Nature. II 1968. 217. 709–713.

*Hockney R. W., Eastwood J. W.*
Computer simulation using particles. 1988.

*Holberg J. B., Bergeron P.*
Calibration of Synthetic Photometry Using DA White Dwarfs
// Astronomical Journal. IX 2006. 132. 1221–1233.

*Holtzman J. A., Burrows C. J., Casertano S., Hester J. J., Trauger J. T., Watson A. M., Worthey G.*
The Photometric Performance and Calibration of WFPC2
// Astronomical Society of the Pacific, Publications. XI 1995. 107. 1065.

*Homer L., Charles P. A., Chakrabarty D., van Zyl L.*
The optical counterpart to SAX J1808.4-3658: observations in quiescence
// Monthly Notices of the Royal Astronomical Society. VIII 2001. 325. 1471–1476.

*Huang R. H. H., Becker W., Edmonds P. D., Elsner R. F., Heinke C. O., Hsieh B. C.*
Study of Hubble Space Telescope counterparts to Chandra X-ray sources in the globular cluster M 71
// Astronomy & Astrophysics. IV 2010. 513. A16.

*Hulse R. A., Taylor J. H.*
Discovery of a pulsar in a binary system
// Astrophysical Journal Letters. I 1975. 195. L51–L53.

*Hut P.*
Binary-single star scattering. II - Analytic approximations for high velocity
// Astrophysical Journal. V 1983. 268. 342–355.

*Hut P., Murphy B. W., Verbunt F.*
The formation rate of low-mass X-ray binaries in globular clusters
// Astronomy & Astrophysics. I 1991. 241. 137–141.

*In't Zand J. J. M., Verbunt F., Strohmayer T. E., Bazzano A., Cocchi M., Heise J., van Kerkwijk M. H., Muller J. M., Natalucci L., Smith M. J. S., Ubertini P.*
A new X-ray outburst in the globular cluster NGC 6440: SAX J1748.9-2021
// Astronomy & Astrophysics. V 1999. 345. 100–108.

*In't Zand J. J. M., van Kerkwijk M. H., Pooley D., Verbunt F., Wijnands R., Lewin W. H. G.*
Identification of the Optical and Quiescent Counterparts to the Bright X-Ray Transient in NGC 6440
// Astrophysical Journal Letters. XII 2001. 563. L41–L44.

*Istrate A. G., Tauris T. M., Langer N.*
The formation of low-mass helium white dwarfs orbiting pulsars . Evolution of low-mass X-ray binaries below the bifurcation period
// Astronomy & Astrophysics. XI 2014. 571. A45.

*Ivanova N., Heinke C. O., Rasio F. A., Belczynski K., Fregeau J. M.*
Formation and evolution of compact binaries in globular clusters - II. Binaries with neutron stars
// Monthly Notices of the Royal Astronomical Society. V 2008. 386. 553–576.

*Jacoby B. A., Cameron P. B., Jenet F. A., Anderson S. B., Murty R. N., Kulkarni S. R.*
Measurement of Orbital Decay in the Double Neutron Star Binary PSR B2127+11C
// Astrophysical Journal Letters. VI 2006. 644. L113–L116.

*Janssen G. H., Stappers B. W., Kramer M., Nice D. J., Jessner A., Cognard I., Purver M. B.*
Multi-telescope timing of PSR J1518+4904
// Astronomy & Astrophysics. XI 2008. 490. 753–761.

*Johnson D. R. H., Soderblom D. R.*
Calculating galactic space velocities and their uncertainties, with an application to the Ursa Major group
// Astronomical Journal. IV 1987. 93. 864–867.

*Johnson T. J., Guillemot L., Kerr M., Cognard I., Ray P. S., Wolff M. T., Bégin S., Janssen G. H., Romani R. W., Venter C., Grove J. E., Freire P. C. C., Wood M., Cheung C. C., Casandjian J. M., Stairs I. H., Camilo F., Espinoza C. M., Ferrara E. C., Harding A. K., Johnston S., Kramer M., Lyne A. G., Michelson P. F., Ransom S. M., Shannon R., Smith D. A., Stappers B. W., Theureau G., Thorsett S. E.*
Broadband Pulsations from PSR B1821-24: Implications for Emission Models and the Pulsar Population of M28
// Astrophysical Journal. XII 2013. 778. 106.

*Kaplan D. L., Stovall K., Ransom S. M., Roberts M. S. E., Kotulla R., Archibald A. M., Biwer C. M., Boyles J., Dartez L., Day D. F., Ford A. J., Garcia A., Hessels J. W. T., Jenet F. A., Karako C., Kaspi V. M., Kondratiev V. I., Lorimer D. R., Lynch R. S., McLaughlin M. A., Rohr M. D. W., Siemens X., Stairs I. H., van Leeuwen J.*
Discovery of the Optical/Ultraviolet/Gamma-Ray Counterpart to the Eclipsing Millisecond Pulsar J1816+4510
// Astrophysical Journal. VII 2012. 753. 174.

*Kaspi V. M., Beloborodov A. M.*
Magnetars

// Annual Review of Astronomy and Astrophysics. VIII 2017. 55. 261–301.

*Kaspi V. M., Helfand D. J.*
Constraining the Birth Events of Neutron Stars
// Neutron Stars in Supernova Remnants. 271. 2002. 3.
(Astronomical Society of the Pacific Conference Series).

*Kaspi V. M., Lyne A. G., Manchester R. N., Crawford F., Camilo F., Bell J. F., D'Amico N., Stairs I. H., McKay N. P. F., Morris D. J., Possenti A.*
Discovery of a Young Radio Pulsar in a Relativistic Binary Orbit
// Astrophysical Journal. XI 2000. 543. 321–327.

*Kimmig B., Seth A., Ivans I. I., Strader J., Caldwell N., Anderton T., Gregersen D.*
Measuring Consistent Masses for 25 Milky Way Globular Clusters
// Astronomical Journal. II 2015. 149. 53.

*King A. R., Davies M. B., Beer M. E.*
Black widow pulsars: the price of promiscuity
// Monthly Notices of the Royal Astronomical Society. X 2003. 345. 678–682.

*King I. R.*
The structure of star clusters. III. Some simple dynamical models
// Astronomical Journal. II 1966. 71. 64.

*Kirk J. G., Lyubarsky Y., Petri J.*
The Theory of Pulsar Winds and Nebulae
// Astrophysics and Space Science Library. 357. 2009. 421.
(Astrophysics and Space Science Library).

*Komesaroff M. M.*
Possible Mechanism for the Pulsar Radio Emission
// Nature. II 1970. 225. 612–614.

*Kramer M., Lyne A. G., Hobbs G., Löhmer O., Carr P., Jordan C., Wolszczan A.*
The Proper Motion, Age, and Initial Spin Period of PSR J0538+2817 in S147
// Astrophysical Journal Letters. VIII 2003. 593. L31–L34.

*Kramer M., Stairs I. H., Manchester R. N., McLaughlin M. A., Lyne A. G., Ferdman R. D., Burgay M., Lorimer D. R., Possenti A., D'Amico N., Sarkissian J. M., Hobbs G. B., Reynolds J. E., Freire P. C. C., Camilo F.*
Tests of General Relativity from Timing the Double Pulsar
// Science. X 2006. 314. 97–102.

*Kuulkers E., den Hartog P. R., in't Zand J. J. M., Verbunt F. W. M., Harris W. E., Cocchi M.*
Photospheric radius expansion X-ray bursts as standard candles
// Astronomy & Astrophysics. II 2003. 399. 663–680.

*Lamers H. J. G. L. M., Gieles M.*
Clusters in the solar neighbourhood: how are they destroyed?
// Astronomy & Astrophysics. VIII 2006. 455. L17–L20.

*Lamers H. J. G. L. M., Gieles M., Bastian N., Baumgardt H., Kharchenko N. V, Portegies Zwart S.*
An analytical description of the disruption of star clusters in tidal fields with an application to Galactic open clusters
// Astronomy & Astrophysics. X 2005. 441. 117–129.

*Lanzoni B., Dalessandro E., Ferraro F. R., Miocchi P., Valenti E., Rood R. T.*
The Surface Density Profile of NGC 6388: A Good Candidate for Harboring an Intermediate-Mass Black Hole
// Astrophysical Journal Letters. X 2007. 668. L139–L142.

*Lanzoni B., Ferraro F. R., Dalessandro E., Mucciarelli A., Beccari G., Miocchi P., Bellazzini M., Rich R. M., Origlia L., Valenti E., Rood R. T., Ransom S. M.*
New Density Profile and Structural Parameters of the Complex Stellar System Terzan 5
// Astrophysical Journal. VII 2010. 717. 653–657.

*Lapenna E., Origlia L., Mucciarelli A., Lanzoni B., Ferraro F. R., Dalessandro E., Valenti E., Cirasuolo M.*
Radial Velocities from VLT-KMOS Spectra of Giant Stars in the Globular Cluster NGC 6388
// Astrophysical Journal. I 2015. 798. 23.

*Lattimer J. M., Prakash M.*
Neutron Star Structure and the Equation of State
// Astrophysical Journal. III 2001. 550. 426–442.

*Lattimer J. M., Prakash M., Masak D., Yahil A.*
Rapidly rotating pulsars and the equation of state
// Astrophysical Journal. V 1990. 355. 241–254.

*Li M., Halpern J. P., Thorstensen J. R.*
Optical Counterparts of Two Fermi Millisecond Pulsars: PSR J1301+0833 and PSR J1628-3205
// Astrophysical Journal. XI 2014. 795. 115.

*Linares M., Bahramian A., Heinke C., Wijnands R., Patruno A., Altamirano D., Homan J., Bogdanov S., Pooley D.*

The neutron star transient and millisecond pulsar in M28: from sub-luminous accretion to rotation-powered quiescence
// Monthly Notices of the Royal Astronomical Society. II 2014. 438. 251–261.

*Linares M., Chakrabarty D., Marshall H., Bahramian A., Heinke C., Sivakoff G., Patruno D. A. A., Wijnands R., Degenaar N., Sanna A.*
Swift refined location points to the neutron star transient EXO 1745-248 as the source currently active in Terzan 5
// The Astronomer's Telegram. III 2015. 7247.

*Lorimer D. R., Faulkner A. J, Lyne A. G., Manchester R. N., Kramer M., McLaughlin M. A., Hobbs G., Possenti A., Stairs I. H., Camilo F., Burgay M., D'Amico N., Corongiu A., Crawford F.*
The Parkes Multibeam Pulsar Survey - VI. Discovery and timing of 142 pulsars and a Galactic population analysis
// Monthly Notices of the Royal Astronomical Society. X 2006. 372. 777–800.

*Lorimer D. R., Kramer M.*
Handbook of Pulsar Astronomy. XII 2004.

*Lyne A., Graham-Smith F.*
Pulsar Astronomy. III 2012.

*Lyne A. G., Brinklow A., Middleditch J., Kulkarni S. R., Backer D. C.*
The discovery of a millisecond pulsar in the globular cluster M28
// Nature. VII 1987. 328. 399–401.

*Manchester R. N., Lyne A. G., Johnston S., D'Amico N., Lim J, Kniffen D. A.*
A 5.75-millisecond pulsar in the globular cluster 47 Tucanae
// Nature. VI 1990. 345. 598–600.

*Manchester R. N., Lyne A. G., Robinson C., Bailes M., D'Amico N.*
Discovery of ten millisecond pulsars in the globular cluster 47 Tucanae
// Nature. VII 1991. 352. 219–221.

*Manzato P., Pietrinferni A., Gasparo F., Taffoni G., Cordier D.*
BaSTI, a Bridge between Grid and Virtual Observatory Part 1: BaSTI inside the VO
// Astronomical Society of the Pacific, Publications. VIII 2008. 120. 922–932.

*Mardling R. A.*
Tidal Capture in Star Clusters
// Dynamical Evolution of Star Clusters: Confrontation of Theory and Observations. 174. 1996. 273.
(IAU Symposium).

*Markwardt C. B., Swank J. H.*
4U 1715-390 and NGC 6440 in Outburst
// The Astronomer's Telegram. V 2005. 495.

*Maron O., Kijak J., Kramer M., Wielebinski R.*
Pulsar spectra of radio emission
// Astronomy and Astrophysics Supplement. XII 2000. 147. 195–203.

*Massari D., Bellini A., Ferraro F. R., van der Marel R. P., Anderson J., Dalessandro E., Lanzoni B.*
Hubble Space Telescope Absolute Proper Motions Of NGC 6681 (M70) and the Sagittarius Dwarf Spheroidal Galaxy
// Astrophysical Journal. XII 2013. 779. 81.

*Massari D., Dalessandro E., Ferraro F. R., Miocchi P., Bellini A., Origlia L., Lanzoni B., Rich R. M., Mucciarelli A.*
Proper Motions in Terzan 5: Membership of the Multi-iron Subpopulations and First Constraint on the Orbit
// Astrophysical Journal. IX 2015. 810. 69.

*Massari D., Mucciarelli A., Dalessandro E., Ferraro F. R., Origlia L., Lanzoni B., Beccari G., Rich R. M., Valenti E., Ransom S. M.*
High-resolution Reddening Map in the Direction of the Stellar System Terzan 5
// Astrophysical Journal Letters. VIII 2012. 755. L32.

*Massari D., Mucciarelli A., Ferraro F. R., Origlia L., Rich R. M., Lanzoni B., Dalessandro E., Valenti E., Ibata R., Lovisi L., Bellazzini M., Reitzel D.*
Ceci N'est Pas a Globular Cluster: The Metallicity Distribution of the Stellar System Terzan 5
// Astrophysical Journal. XI 2014. 795. 22.

*Meurer G. R., Lindler D., Blakeslee J. P., Cox C., Martel A. R., Tran H. D., Bouwens R. J., Ford H. C., Clampin M., Hartig G. F., Sirianni M., de Marchi G.*
Calibration of Geometric Distortion in the ACS Detectors
// HST Calibration Workshop : Hubble after the Installation of the ACS and the NICMOS Cooling System. 2003. 65.

*Migliazzo J. M., Gaensler B. M., Backer D. C., Stappers B. W., van der Swaluw E., Strom R. G.*
Proper-Motion Measurements of Pulsar B1951+32 in the Supernova Remnant CTB 80
// Astrophysical Journal Letters. III 2002. 567. L141–L144.

*Milone A. P., Piotto G., Bedin L. R., Aparicio A., Anderson J., Sarajedini A., Marino A. F., Moretti A., Davies M. B., Chaboyer B., Dotter A., Hempel M., Marín-Franch A., Majewski S., Paust N. E. Q., Reid I. N., Rosenberg A., Siegel M.*

The ACS survey of Galactic globular clusters. XII. Photometric binaries along the main sequence
// Astronomy & Astrophysics. IV 2012a. 540. A16.

*Milone A. P., Piotto G., Bedin L. R., King I. R., Anderson J., Marino A. F., Bellini A., Gratton R., Renzini A., Stetson P. B., Cassisi S., Aparicio A., Bragaglia A., Carretta E., D'Antona F., Di Criscienzo M., Lucatello S., Monelli M., Pietrinferni A.*
Multiple Stellar Populations in 47 Tucanae
// Astrophysical Journal. I 2012b. 744. 58.

*Miocchi P., Lanzoni B., Ferraro F. R., Dalessandro E., Vesperini E., Pasquato M., Beccari G., Pallanca C., Sanna N.*
Star Count Density Profiles and Structural Parameters of 26 Galactic Globular Clusters
// Astrophysical Journal. IX 2013. 774. 151.

*Moffat A. F. J.*
A Theoretical Investigation of Focal Stellar Images in the Photographic Emulsion and Application to Photographic Photometry
// Astronomy & Astrophysics. XII 1969. 3. 455.

*Montegriffo P., Ferraro F. R., Fusi Pecci F., Origlia L.*
IR-array photometry of Galactic globular clusters - II. JK photometry of 47 TUC
// Monthly Notices of the Royal Astronomical Society. X 1995. 276. 739–752.

*Moreno E., Pichardo B., Velázquez H.*
Tidal Radii and Destruction Rates of Globular Clusters in the Milky Way due to Bulge-Bar and Disk Shocking
// Astrophysical Journal. X 2014. 793. 110.

*Mucciarelli A., Salaris M., Lanzoni B., f C., Dalessandro E., Ferraro F. R.*
New Clues on the Nature of the Companion to PSR J1740-5340 in NGC 6397 from XSHOOTER Spectroscopy
// Astrophysical Journal Letters. VIII 2013. 772. L27.

*Ng C., Bailes M., Bates S. D., Bhat N. D. R., Burgay M., Burke-Spolaor S., Champion D. J., Coster P., Johnston S., Keith M. J., Kramer M., Levin L., Petroff E., Possenti A., Stappers B. W., van Straten W., Thornton D., Tiburzi C., Bassa C. G., Freire P. C. C., Guillemot L., Lyne A. G., Tauris T. M., Shannon R. M., Wex N.*
The High Time Resolution Universe pulsar survey - X. Discovery of four millisecond pulsars and updated timing solutions of a further 12
// Monthly Notices of the Royal Astronomical Society. IV 2014. 439. 1865–1883.

*Nice D. J., Taylor J. H.*
PSR J2019+2425 and PSR J2322+2057 and the proper motions of millisecond pulsars
// Astrophysical Journal. III 1995. 441. 429–435.

*O'Donnell J. E.*
$R_{nu}$-dependent optical and near-ultraviolet extinction
// Astrophysical Journal. II 1994. 422. 158–163.

*Origlia L., Ferraro F. R., Fusi Pecci F., Oliva E.*
Infrared stellar absorption lines around 1.6$\mu$m: a new metallicity scale for old stellar populations.
// Astronomy & Astrophysics. V 1997. 321. 859–866.

*Origlia L., Lena S., Diolaiti E., Ferraro F. R., Valenti E., Fabbri S., Beccari G.*
Probing the Galactic Bulge with Deep Adaptive Optics Imaging: The Age of NGC 6440
// Astrophysical Journal Letters. XI 2008a. 687. L79.

*Origlia L., Massari D., Rich R. M., Mucciarelli A., Ferraro F. R., Dalessandro E., Lanzoni B.*
The Terzan 5 Puzzle: Discovery of a Third, Metal-poor Component
// Astrophysical Journal Letters. XII 2013. 779. L5.

*Origlia L., Rich R. M., Ferraro F. R., Lanzoni B., Bellazzini M., Dalessandro E., Mucciarelli A., Valenti E., Beccari G.*
Spectroscopy Unveils the Complex Nature of Terzan 5
// Astrophysical Journal Letters. I 2011. 726. L20.

*Origlia L., Valenti E., Rich R. M.*
High resolution infrared spectra of NGC 6440 and NGC 6441: two massive bulge globular clusters
// Monthly Notices of the Royal Astronomical Society. VIII 2008b. 388. 1419–1425.

*Ortolani S., Barbuy B., Momany Y., Saviane I., Bica E., Jilkova L., Salerno G. M., Jungwiert B.*
A Fossil Bulge Globular Cluster Revealed by very Large Telescope Multi-conjugate Adaptive Optics
// Astrophysical Journal. VIII 2011. 737. 31.

*Özel F., Psaltis D., Narayan R., Santos Villarreal A.*
On the Mass Distribution and Birth Masses of Neutron Stars
// Astrophysical Journal. IX 2012. 757. 55.

*Pallanca C.*
Cosmic-Lab: Optical companions to binary Millisecond Pulsars
// ArXiv e-prints. V 2014.

*Pallanca C., Dalessandro E., Ferraro F. R., Lanzoni B., Beccari G.*
The Optical Counterpart to the X-Ray Transient IGR J1824-24525 in the Globular Cluster M28
// Astrophysical Journal. VIII 2013a. 773. 122.

*Pallanca C., Dalessandro E., Ferraro F. R., Lanzoni B., Rood R. T., Possenti A., D'Amico N., Freire P. C., Stairs I., Ransom S. M., Bégin S.*
The Optical Companion to the Binary Millisecond Pulsar J1824-2452H in the Globular Cluster M28
// Astrophysical Journal. XII 2010. 725. 1165–1169.

*Pallanca C., Lanzoni B., Dalessandro E., Ferraro F. R., Possenti A., Salaris M., Burgay M.*
The Optical Companion to the Intermediate-mass Millisecond Pulsar J1439-5501 in the Galactic Field
// Astrophysical Journal. VIII 2013b. 773. 127.

*Pallanca C., Mignani R. P., Dalessandro E., Ferraro F. R., Lanzoni B., Possenti A., Burgay M., Sabbi E.*
The Identification of the Optical Companion to the Binary Millisecond Pulsar J0610-2100 in the Galactic Field
// Astrophysical Journal. VIII 2012. 755. 180.

*Pallanca C., Ransom S. M., Ferraro F. R., Dalessandro E., Lanzoni B., Hessels J. W. T., Stairs I., Freire P. C. C.*
Radio Timing and Optical Photometry of the Black Widow System PSR J1518+0204C in the Globular Cluster M5
// Astrophysical Journal. XI 2014. 795. 29.

*Pan Z., Hobbs G., Li D., Ridolfi A., Wang P., Freire P.*
Discovery of two new pulsars in 47 Tucanae (NGC 104)
// Monthly Notices of the Royal Astronomical Society. VI 2016. 459. L26–L30.

*Papitto A., Ferrigno C., Bozzo E., Rea N., Pavan L., Burderi L., Burgay M., Campana S., di Salvo T., Falanga M., Filipović M. D., Freire P. C. C., Hessels J. W. T., Possenti A., Ransom S. M., Riggio A., Romano P., Sarkissian J. M., Stairs I. H., Stella L., Torres D. F., Wieringa M. H., Wong G. F.*
Swings between rotation and accretion power in a binary millisecond pulsar
// Nature. IX 2013. 501. 517–520.

*Patruno A., Altamirano D., Hessels J. W. T., Casella P., Wijnands R., van der Klis M.*
Phase-Coherent Timing of the Accreting Millisecond Pulsar SAX J1748.9-2021
// Astrophysical Journal. I 2009. 690. 1856–1865.

*Patruno A., Altamirano D., Watts A., Armas Padilla M., Cavecchi Y., Degenaar N., Kalamkar M., Kaur R., Soleri P., Yang Y. J., van der Klis M., Wijnands R., Casella P., Linares M., Rea N., Heinke C. O., Pooley D.*
Detection of pulsations and identification of SAX J1748.9-2021 as the X-ray transient in NGC 6440.
// The Astronomer's Telegram. I 2010. 2407.

*Patruno A., Archibald A. M., Hessels J. W. T., Bogdanov S., Stappers B. W., Bassa C. G., Janssen G. H., Kaspi V. M., Tendulkar S., Lyne A. G.*
A New Accretion Disk around the Missing Link Binary System PSR J1023+0038
// Astrophysical Journal Letters. I 2014. 781. L3.

*Patruno A., Bult P., Gopakumar A., Hartman J. M., Wijnands R., van der Klis M., Chakrabarty D.*
Accelerated Orbital Expansion and Secular Spin-down of the Accreting Millisecond Pulsar SAX J1808.4-3658
// Astrophysical Journal Letters. II 2012. 746. L27.

*Patruno A., Jaodand A., Kuiper L., Bult P., Hessels J. W. T., Knigge C., King A. R., Wijnands R., van der Klis M.*
Radio Pulse Search and X-Ray Monitoring of SAX J1808.4-3658: What Causes Its Orbital Evolution?
// Astrophysical Journal. VI 2017. 841. 98.

*Patruno A., Watts A. L.*
Accreting Millisecond X-Ray Pulsars
// ArXiv e-prints. VI 2012.

*Pennucci T. T., Demorest P. B., Ransom S. M.*
Elementary Wideband Timing of Radio Pulsars
// Astrophysical Journal. VIII 2014. 790. 93.

*Peterson C. J., Reed B. C.*
Structural parameters and luminosities of globular clusters
// Astronomical Society of the Pacific, Publications. I 1987. 99. 20–26.

*Phinney E. S.*
Pulsars as Probes of Newtonian Dynamical Systems
// Royal Society of London Philosophical Transactions Series A. X 1992. 341. 39–75.

*Phinney E. S.*
Pulsars as Probes of Globular Cluster Dynamics
// Structure and Dynamics of Globular Clusters. 50. I 1993. 141.
(Astronomical Society of the Pacific Conference Series).

191

*Pietrinferni A., Cassisi S., Salaris M., Castelli F.*
A Large Stellar Evolution Database for Population Synthesis Studies. I. Scaled Solar Models and Isochrones
// Astrophysical Journal. IX 2004. 612. 168–190.

*Pletsch H. J., Clark C. J.*
Gamma-Ray Timing of Redback PSR J2339-0533: Hints for Gravitational Quadrupole Moment Changes
// Astrophysical Journal. VII 2015. 807. 18.

*Pooley D., Lewin W. H. G., Anderson S. F., Baumgardt H., Filippenko A. V., Gaensler B. M., Homer L., Hut P., Kaspi V. M., Makino J., Margon B., McMillan S., Portegies Zwart S., van der Klis M., Verbunt F.*
Dynamical Formation of Close Binary Systems in Globular Clusters
// Astrophysical Journal Letters. VII 2003. 591. L131–L134.

*Pooley D., Lewin W. H. G., Verbunt F., Homer L., Margon B., Gaensler B. M., Kaspi V. M., Miller J. M., Fox D. W., van der Klis M.*
Chandra Observation of the Globular Cluster NGC 6440 and the Nature of Cluster X-Ray Luminosity Functions
// Astrophysical Journal. VII 2002. 573. 184–190.

*Potekhin A. Y., Pons J. A., Page D.*
Neutron Stars - Cooling and Transport
// Space Science Reviews. X 2015. 191. 239–291.

*Prager B. J., Ransom S. M., Freire P. C. C., Hessels J. W. T., Stairs I. H., Arras P., Cadelano M.*
Using Long-term Millisecond Pulsar Timing to Obtain Physical Characteristics of the Bulge Globular Cluster Terzan 5
// Astrophysical Journal. VIII 2017. 845. 148.

*Ransom S. M., Cordes J. M., Eikenberry S. S.*
A New Search Technique for Short Orbital Period Binary Pulsars
// Astrophysical Journal. VI 2003. 589. 911–920.

*Ransom S. M., Eikenberry S. S., Middleditch J.*
Fourier Techniques for Very Long Astrophysical Time-Series Analysis
// Astronomical Journal. IX 2002. 124. 1788–1809.

*Ransom S. M., Hessels J. W. T., Stairs I. H., Freire P. C. C., Camilo F., Kaspi V. M., Kaplan D. L.*
Twenty-One Millisecond Pulsars in Terzan 5 Using the Green Bank Telescope
// Science. II 2005. 307. 892–896.

*Ray P. S., Abdo A. A., Parent D., Bhattacharya D., Bhattacharyya B., Camilo F., Cognard I., Theureau G., Ferrara E. C., Harding A. K., Thompson D. J., Freire P. C. C., Guillemot L., Gupta Y., Roy J., Hessels J. W. T., Johnston S., Keith M., Shannon R., Kerr M., Michelson P. F., Romani R. W., Kramer M., McLaughlin M. A., Ransom S. M., Roberts M. S. E., Saz Parkinson P. M., Ziegler M., Smith D. A., Stappers B. W., Weltevrede P., Wood K. S.*
Radio Searches of Fermi LAT Sources and Blind Search Pulsars: The Fermi Pulsar Search Consortium
// ArXiv e-prints. V 2012.

*Reid M. J., Menten K. M., Brunthaler A., Zheng X. W., Dame T. M., Xu Y., Wu Y., Zhang B., Sanna A., Sato M., Hachisuka K., Choi Y. K., Immer K., Moscadelli L., Rygl K. L. J., Bartkiewicz A.*
Trigonometric Parallaxes of High Mass Star Forming Regions: The Structure and Kinematics of the Milky Way
// Astrophysical Journal. III 2014a. 783. 130.

*Reid M. J., Menten K. M., Brunthaler A., Zheng X. W., Dame T. M., Xu Y., Wu Y., Zhang B., Sanna A., Sato M., Hachisuka K., Choi Y. K., Immer K., Moscadelli L., Rygl K. L. J., Bartkiewicz A.*
Trigonometric Parallaxes of High Mass Star Forming Regions: The Structure and Kinematics of the Milky Way
// Astrophysical Journal. III 2014b. 783. 130.

*Reid M. J., Menten K. M., Zheng X. W., Brunthaler A., Moscadelli L., Xu Y., Zhang B., Sato M., Honma M., Hirota T., Hachisuka K., Choi Y. K., Moellenbrock G. A., Bartkiewicz A.*
Trigonometric Parallaxes of Massive Star-Forming Regions. VI. Galactic Structure, Fundamental Parameters, and Noncircular Motions
// Astrophysical Journal. VII 2009. 700. 137–148.

*Reynolds M. T., Callanan P. J., Fruchter A. S., Torres M. A. P., Beer M. E., Gibbons R. A.*
The light curve of the companion to PSR B1957+20
// Monthly Notices of the Royal Astronomical Society. VIII 2007. 379. 1117–1122.

*Ridolfi A., Freire P. C. C., Torne P., Heinke C. O., van den Berg M., Jordan C., Kramer M., Bassa C. G., Sarkissian J., D'Amico N., Lorimer D., Camilo F., Manchester R. N., Lyne A.*
Long-term observations of the pulsars in 47 Tucanae - I. A study of four elusive binary systems
// Monthly Notices of the Royal Astronomical Society. XI 2016. 462. 2918–2933.

*Roberts M. S. E.*
Surrounded by spiders! New black widows and redbacks in the Galactic field
// Neutron Stars and Pulsars: Challenges and Opportunities after 80 years. 291. III 2013. 127–132.
(IAU Symposium).

*Roberts M. S. E., Mclaughlin M. A., Gentile P., Aliu E., Hessels J. W. T., Ransom S. M., Ray P. S.*
Intrabinary shock emission from "black widows" and "redbacks"
// Astronomische Nachrichten. III 2014. 335. 313–317.

*Robin A. C., Reylé C., Derrière S., Picaud S.*
A synthetic view on structure and evolution of the Milky Way
// Astronomy & Astrophysics. X 2003. 409. 523–540.

*Robinson C., Lyne A. G., Manchester R. N., Bailes M., D'Amico N., Johnston S.*
Millisecond pulsars in the globular cluster 47 Tucanae
// Monthly Notices of the Royal Astronomical Society. V 1995. 274. 547–554.

*Romani R. W., Shaw M. S.*
The Orbit and Companion of Probable $\gamma$-Ray Pulsar J2339-0533
// Astrophysical Journal Letters. XII 2011. 743. L26.

*Ruderman M., Shaham J., Tavani M., Eichler D.*
Late evolution of very low mass X-ray binaries sustained by radiation from their primaries
// Astrophysical Journal. VIII 1989. 343. 292–312.

*Rutledge R. E., Fox D. W., Kulkarni S. R., Jacoby B. A., Cognard I., Backer D. C., Murray S. S.*
Microsecond Timing of PSR B1821-24 with Chandra High Resolution Camera-S
// Astrophysical Journal. IX 2004. 613. 522–531.

*Ryan R. E. Jr., Deustua S., Sosey M., Anderson J., Baggett S. M., Bajaj V., Bourque M., Bowers A., Dahlen T., Durbin M., Gosmeyer C., Gunning H., Khandrika H., Mack J., MacKenty J., Martlin C., Kozhurina-Platais V., Sabbi E.*
The Updated Calibration Pipeline for WFC3/UVIS: a Reference Guide to calwf3 (version 3.3).
II 2016.

*Sabbi E., Gratton R., Ferraro F. R., Bragaglia A., Possenti A., D'Amico N., Camilo F.*
The Complex H$\alpha$ Line Profile of the Bright Companion to PSR J1740-5340 in NGC 6397
// Astrophysical Journal Letters. V 2003a. 589. L41–L44.

*Sabbi E., Gratton R. G., Bragaglia A., Ferraro F. R., Possenti A., Camilo F., D'Amico N.*
The chemical composition of the peculiar companion to the millisecond pulsar in NGC 6397
// Astronomy & Astrophysics. XII 2003b. 412. 829–836.

*Salaris M., Cassisi S., Pietrinferni A., Kowalski P. M., Isern J.*
A Large Stellar Evolution Database for Population Synthesis Studies. VI. White Dwarf Cooling Sequences
// Astrophysical Journal. VI 2010. 716. 1241–1251.

*Salaris M., Held E. V., Ortolani S., Gullieuszik M., Momany Y.*
Deep near-infrared photometry of the globular cluster 47 Tucanae. Reconciling theory and observations
// Astronomy & Astrophysics. XII 2007. 476. 243–253.

*Sanna A., Bahramian A., Bozzo E., Heinke C., Altamirano D., Wijnands R., Degenaar N., Maccarone T., Riggio A., Di Salvo T., Iaria R., Burgay M., Possenti A., Ferrigno C., Papitto A., Sivakoff G., D'Amico N., Burderi L.*
Discovery of 105 Hz coherent pulsations in the ultracompact binary IGR J16597-3704
// ArXiv e-prints. XI 2017a.

*Sanna A., Burderi L., Riggio A., Pintore F., Di Salvo T., Gambino A. F., Iaria R., Matranga M., Scarano F.*
Timing of the accreting millisecond pulsar SAX J1748.9-2021 during its 2015 outburst
// Monthly Notices of the Royal Astronomical Society. VI 2016. 459. 1340–1349.

*Sanna A., Papitto A., Burderi L., Bozzo E., Riggio A., Di Salvo T., Ferrigno C., Rea N., Iaria R.*
Discovery of a new accreting millisecond X-ray pulsar in the globular cluster NGC 2808
// Astronomy & Astrophysics. II 2017b. 598. A34.

*Sarajedini A., Bedin L. R., Chaboyer B., Dotter A., Siegel M., Anderson J., Aparicio A., King I., Majewski S., Marín-Franch A., Piotto G., Reid I. N., Rosenberg A.*
The ACS Survey of Galactic Globular Clusters. I. Overview and Clusters without Previous Hubble Space Telescope Photometry
// Astronomical Journal. IV 2007. 133. 1658–1672.

*Schlegel D. J., Finkbeiner D. P., Davis M.*
Maps of Dust Infrared Emission for Use in Estimation of Reddening and Cosmic Microwave Background Radiation Foregrounds
// Astrophysical Journal. VI 1998. 500. 525–553.

*Schönrich R., Binney J., Dehnen W.*
Local kinematics and the local standard of rest
// Monthly Notices of the Royal Astronomical Society. IV 2010. 403. 1829–1833.

*Shahbaz T., Kuulkers E.*
On the outburst amplitude of the soft X-ray transients
// Monthly Notices of the Royal Astronomical Society. III 1998. 295. L1–L5.

*Shapiro S. L., Teukolsky S. A.*
Book-Review - Black-Holes White Dwarfs and Neutron Stars
// Journal of the British Astronomical Association. X 1983. 93. 276.

*Shklovskii I. S.*
  Possible Causes of the Secular Increase in Pulsar Periods.
  // Soviet Astronomy. II 1970. 13. 562.

*Sigurdsson S., Richer H. B., Hansen B. M., Stairs I. H., Thorsett S. E.*
  A Young White Dwarf Companion to Pulsar B1620-26: Evidence for Early Planet Formation
  // Science. VII 2003. 301. 193–196.

*Sirianni M., Jee M. J., Benítez N., Blakeslee J. P., Martel A. R., Meurer G., Clampin M., De Marchi G., Ford H. C., Gilliland R., Hartig G. F., Illingworth G. D., Mack J., McCann W. J.*
  The Photometric Performance and Calibration of the Hubble Space Telescope Advanced Camera for Surveys
  // Astronomical Society of the Pacific, Publications. X 2005. 117. 1049–1112.

*Spitzer L.*
  Dynamical evolution of globular clusters. 1987.

*Stairs I. H.*
  Pulsars in Binary Systems: Probing Binary Stellar Evolution and General Relativity
  // Science. IV 2004. 304. 547–552.

*Stairs I. H., Begin S., Ransom S., Freire P., Hessels J., Katz J., Kaspi V., Camilo F.*
  New Pulsars in the Globular Cluster M28
  // American Astronomical Society Meeting Abstracts. 38. XII 2006. 1118.
  (Bulletin of the American Astronomical Society).

*Stappers B. W., Archibald A. M., Hessels J. W. T., Bassa C. G., Bogdanov S., Janssen G. H., Kaspi V. M., Lyne A. G., Patruno A., Tendulkar S., Hill A. B., Glanzman T.*
  A State Change in the Missing Link Binary Pulsar System PSR J1023+0038
  // Astrophysical Journal. VII 2014. 790. 39.

*Stappers B. W., Bessell M. S., Bailes M.*
  Detection of an Irradiated Pulsar Companion
  // Astrophysical Journal Letters. XII 1996. 473. L119.

*Stappers B. W., van Kerkwijk M. H., Bell J. F., Kulkarni S. R.*
  Intrinsic and Reprocessed Optical Emission from the Companion to PSR J2051-0827
  // Astrophysical Journal Letters. II 2001. 548. L183–L186.

*Stappers B. W., van Kerkwijk M. H., Lane B., Kulkarni S. R.*
  The Light Curve of the Companion to PSR J2051-0827
  // Astrophysical Journal Letters. I 1999. 510. L45–L48.

*Stetson P. B.*

   DAOPHOT - A computer program for crowded-field stellar photometry
   // Astronomical Society of the Pacific, Publications. III 1987. 99. 191–222.

*Strohmayer T., Keek L.*

   IGR J17062-6143 Is an Accreting Millisecond X-Ray Pulsar
   // Astrophysical Journal Letters. II 2017. 836. L23.

*Sulman B., Ransom S., Stinebring D.*

   Searching for weak, isolated pulsars in the globular cluster Terzan 5
   // American Astronomical Society Meeting Abstracts. 37. XII 2005. 1469.
   (Bulletin of the American Astronomical Society).

*Tauris T. M.*

   Spin-Down of Radio Millisecond Pulsars at Genesis
   // Science. II 2012. 335. 561.

*Tauris T. M., Langer N., Kramer M.*

   Formation of millisecond pulsars with CO white dwarf companions - II. Accretion, spin-up,
   true ages and comparison to MSPs with He white dwarf companions
   // Monthly Notices of the Royal Astronomical Society. IX 2012. 425. 1601–1627.

*Tauris T. M., Savonije G. J.*

   Formation of millisecond pulsars. I. Evolution of low-mass X-ray binaries with $P_{orb} > 2$ days
   // Astronomy & Astrophysics. X 1999. 350. 928–944.

*Tauris T. M., van den Heuvel E. P. J.*

   Formation and evolution of compact stellar X-ray sources
   // Compact stellar X-ray sources. IV 2006. 623–665.

*Taylor J. H.*

   Pulsar Timing and Relativistic Gravity
   // Philosophical Transactions of the Royal Society of London Series A. X 1992. 341. 117–134.

*Taylor J. H., Weisberg J. M.*

   Further experimental tests of relativistic gravity using the binary pulsar PSR 1913 + 16
   // Astrophysical Journal. X 1989. 345. 434–450.

*Testa V., di Salvo T., D'Antona F., Menna M. T., Ventura P., Burderi L., Riggio A., Iaria R., D'Aì
   A., Papitto A., Robba N.*

   The near-IR counterpart of <ASTROBJ>IGR J17480-2446</ASTROBJ> in <ASTROBJ>Terzan
   5</ASTROBJ>
   // Astronomy & Astrophysics. XI 2012. 547. A28.

*The NANOGrav Collaboration , Arzoumanian Z., Brazier A., Burke-Spolaor S., Chamberlin S., Chatterjee S., Christy B., Cordes J. M., Cornish N., Crowter K., Demorest P. B., Dolch T., Ellis J. A., Ferdman R. D., Fonseca E., Garver-Daniels N., Gonzalez M. E., Jenet F. A., Jones G., Jones M. L., Kaspi V. M., Koop M., Lam M. T., Lazio T. J. W., Levin L., Lommen A. N., Lorimer D. R., Luo J., Lynch R. S., Madison D., McLaughlin M. A., McWilliams S. T., Nice D. J., Palliyaguru N., Pennucci T. T., Ransom S. M., Siemens X., Stairs I. H., Stinebring D. R., Stovall K., Swiggum J. K., Vallisneri M., van Haasteren R., Wang Y., Zhu W.*
The NANOGrav Nine-year Data Set: Observations, Arrival Time Measurements, and Analysis of 37 Millisecond Pulsars
// Astrophysical Journal. XI 2015. 813. 65.

*Torres M. A. P., Jonker P. G., Britt C. T., Johnson C. B., Hynes R. I., Greiss S., Steeghs D., Maccarone T. J., Özel F., Bassa C., Nelemans G.*
Identification of 23 accreting binaries in the Galactic Bulge Survey
// Monthly Notices of the Royal Astronomical Society. V 2014. 440. 365–386.

*Torres M. A. P., Jonker P. G., Steeghs D., Roelofs G. H. A., Bloom J. S., Casares J., Falco E. E., Garcia M. R., Marsh T. R., Mendez M., Miller J. M., Nelemans G., Rodríguez-Gil P.*
Observations of the 599 Hz Accreting X-Ray Pulsar IGR J00291+5934 during the 2004 Outburst and in Quiescence
// Astrophysical Journal. I 2008. 672. 1079–1090.

*Tremou E., Sivakoff G., Bahramian A., Heinke C., Tetarenko A., Wijnands R., Degenaar N., Linares M., Miller-Jones J., Patruno A., Chomiuk L., Strader J., Altamirano D., Maccarone T., Sanna A.*
VLA observations identify the currently active source in Terzan 5 as the neutron star transient EXO 1745-248
// The Astronomer's Telegram. III 2015. 7262.

*Turk P. J., Lorimer D. R.*
An empirical Bayesian analysis applied to the globular cluster pulsar population
// Monthly Notices of the Royal Astronomical Society. XII 2013. 436. 3720–3726.

*Valenti E., Ferraro F. R., Origlia L.*
Red giant branch in near-infrared colour-magnitude diagrams - I. Calibration of photometric indices
// Monthly Notices of the Royal Astronomical Society. VII 2004. 351. 1204–1214.

*Valenti E., Ferraro F. R., Origlia L.*
Near-Infrared Properties of 24 Globular Clusters in the Galactic Bulge
// Astronomical Journal. IV 2007. 133. 1287–1301.

*Van den Heuvel E. P. J.*

    The Formation and Evolution of Relativistic Binaries

    // Physics of Relativistic Objects in Compact Binaries: From Birth to Coalescence. 359. 2009. 125.

    (Astrophysics and Space Science Library).

*Verbunt F., Freire P. C. C.*

    On the disruption of pulsar and X-ray binaries in globular clusters

    // Astronomy & Astrophysics. I 2014. 561. A11.

*Verbunt F., Hut P.*

    The Globular Cluster Population of X-Ray Binaries

    // The Origin and Evolution of Neutron Stars. 125. 1987. 187.

    (IAU Symposium).

*Verbunt F., van Kerkwijk M. H., in't Zand J. J. M., Heise J.*

    X-ray and optical follow-up observations of the August 1998 X-ray transient in NGC 6440

    // Astronomy & Astrophysics. VII 2000. 359. 960–966.

*Vesperini E., Heggie D. C.*

    On the effects of dynamical evolution on the initial mass function of globular clusters

    // Monthly Notices of the Royal Astronomical Society. VIII 1997. 289. 898–920.

*Vesperini E., McMillan S. L. W., D'Antona F., D'Ercole A.*

    Dynamical evolution and spatial mixing of multiple population globular clusters

    // Monthly Notices of the Royal Astronomical Society. III 2013. 429. 1913–1921.

*Villanova S., Moni Bidin C., Mauro F., Munoz C., Monaco L.*

    A spectroscopic study of the globular cluster M28 (NGC 6626)

    // Monthly Notices of the Royal Astronomical Society. I 2017. 464. 2730–2740.

*Weisberg J. M., Nice D. J., Taylor J. H.*

    Timing Measurements of the Relativistic Binary Pulsar PSR B1913+16

    // Astrophysical Journal. X 2010. 722. 1030–1034.

*White N. E., Kaluzienski J. L., Swank J. H.*

    The spectra of x-ray transients

    // American Institute of Physics Conference Series. 115. V 1984. 31–48.

    (American Institute of Physics Conference Series).

*Woodley K. A., Goldsbury R., Kalirai J. S., Richer H. B., Tremblay P.-E., Anderson J., Bergeron P., Dotter A., Esteves L., Fahlman G. G., Hansen B. M. S., Heyl J., Hurley J., Rich R. M., Shara M. M., Stetson P. B.*

The Spectral Energy Distributions of White Dwarfs in 47 Tucanae: The Distance to the Cluster
// Astronomical Journal. II 2012. 143. 50.

*Xing Y., Wang Z.*
Fermi Study of Gamma-ray Millisecond Pulsars: the Spectral Shape and Pulsed Emission from J0614-3329 up to 60 GeV
// Astrophysical Journal. XI 2016. 831. 143.

*Yan Z., Lin J., Yu W., Zhang W., Zhang H.*
A hard-to-soft state transition is going on in neutron star transient EXO 1745-248
// The Astronomer's Telegram. IV 2015. 7430.

*Zacharias N., Finch C. T., Girard T. M., Henden A., Bartlett J. L., Monet D. G., Zacharias M. I.*
The Fourth US Naval Observatory CCD Astrograph Catalog (UCAC4)
// Astronomical Journal. II 2013. 145. 44.

*Zhang P. F., Xin Y. L., Fu L., Zhou J. N., Yan J. Z., Liu Q. Z., Zhang L.*
Detection of gamma-ray emission from globular clusters M15, NGC 6397, 5904, 6218 and 6139 with Fermi-LAT
// Monthly Notices of the Royal Astronomical Society. VI 2016. 459. 99–107.

*Zoccali M., Renzini A., Ortolani S., Bragaglia A., Bohlin R., Carretta E., Ferraro F. R., Gilmozzi R., Holberg J. B., Marconi G., Rich R. M., Wesemael F.*
The White Dwarf Distance to the Globular Cluster 47 Tucanae and its Age
// Astrophysical Journal. VI 2001. 553. 733–743.

*van Kerkwijk M. H., Bassa C. G., Jacoby B. A., Jonker P. G.*
Optical Studies of Companions to Millisecond Pulsars
// Binary Radio Pulsars. 328. VII 2005. 357.
(Astronomical Society of the Pacific Conference Series).

*van Paradijs J., McClintock J. E.*
Absolute visual magnitudes of low-mass X-ray binaries.
// Astronomy & Astrophysics. X 1994. 290. 133–136.

*von Zeipel H.*
The radiative equilibrium of a slightly oblate rotating star
// Monthly Notices of the Royal Astronomical Society. VI 1924. 84. 684–701.

*"...from so simple a beginning*
*endless forms most beautiful and most wonderful*
*have been, and are being, evolved."*

Charles Darwin - On the origin of species